Modeling and Analysis of Lipid Bilayers with Applications to Vesicles and Lipoprotein Particles

Mohsen Maleki Karyak

Doctor of Philosophy

Department of Mechanical Engineering

McGill University

Montreal,Quebec

October 2013

A thesis submitted to McGill University in partial fulfillment of the requirements of the degree of Doctor of Philosophy

ACKNOWLEDGEMENTS

I would like to sincerely thank my advisor, teacher, and mentor, Professor Eliot Fried, for all of his generous support, encouragement, and also patience. I learned so much from him. Working with him has been a precious opportunity for me to learn the elements of high-quality research and to identify myself as a researcher. I would also like to express appreciation to my friends, including current and former group members Brian Seguin, Aisa Biria, Reza Lotfalian, Meisam Asgari, Denis Hinz, Tae-Yeon Kim, Eric Puntel, Shojaa Ramezani, Nella Rotundo, and Alex Kelly, for many motivating discussions, great comments, and the moments we spent together at McGill. I need to thank Brian Seguin for very insightful discussions, specially on the material symmetry of lipid bilayers and calculus of variations of surfaces.

I would like to thank Professor Elliot Elson and Professor Guy Genin for their hospitality and comments during my short visit to Washington University in St. Louis. Also, I greatly appreciate various discussions with Professor David Steigmann.

At McGill, I like to thank my teachers and the Mechanical Engineering Department staff, specially, the Graduate Program Coordinator, Ms. Joyce Nault. I also need to acknowledge the McGill Engineering Doctoral Award (MEDA).

Importantly, I owe my family very much. Specially, I greatly appreciate my wonderful wife, Ensieh, for all of her continuing support, encouragement, understanding, and love. I would also like to thank my dear parents for their great passion and wishes for me.

ABSTRACT

Continuum approaches for modeling lipid bilayers are developed and applied to two-phase lipid vesicles and discoidal high-density lipoprotein (HDL) particles. First, relying on a three-dimensional model, the mechanics of a lipid bilayer with spontaneous curvature is considered. Kinematics, material symmetry, stress relations, and coherency of lipid bilayer leaflets are discussed. Treating a lipid bilayer as a thin structure, the areal energy density of a lipid bilayer with spontaneous curvature is obtained using a dimension-reduction procedure. Attention is paid on the source of spontaneous curvature in the well known Canham–Helfrich energy density. Also, the effect of constitutive asymmetry of the leaflets on the areal energy density of a lipid bilayer is highlighted.

Considering a two-phase vesicle as system of coexisting spherical domains, its equilibrium is studied using a simple continuum model. Multidomain and ground-state configurations are considered. Whereas in the former case multiple budded lipid domains coexist on a vesicle, in the latter case the vesicle is composed of two large lipid domains. Variations of the net potential-energy of a multidomain vesicle with the number of lipid domains and osmotic pressure are studied. Based on an energy comparison argument, two ground-state configurations corresponding to minimum energy levels are identified: pinched-off and complete sphere configurations. The results indicate that osmotic pressure and initial excess radius play key roles in the final shape of attaining ground-state configurations. The critical values of these parameters are identified.

Lastly, the equilibrium and stability of a discoidal HDL particle are studied. A model in which the lipid bilayer and double-belt apoA-I components of discoidal HDL particle are represented by a material surface and a material curve perfectly bonded to the edge of the surface is proposed. The curvature energy and surface tension of lipid bilayer and the bending energy of apoA-I chain are included. Adopting a variational scheme, nonlinear equilibrium equations of a discoidal HDL particle in a general configuration are derived using both direct, geometrically-based and parametrized formulations. The linearized equilibrium equations of a flat circular HDL particle are obtained and its linear stability is investigated using the second variation method. An energy comparison method is applied and is found to offer a handy approach for ascertaining linear stability. Numerical results are provided for the equilibrium and stability of flat circular HDL particle. A stability plane indicating different stable and unstable regions of underlying dimensionless input parameters is provided. Possible pathways of stability change and instability mode shapes are identified. It is shown that the first transverse and planar instability modes resemble nonplanar saddle-like and planar elliptic shapes, respectively.

ABRÉGÉ

Des méthodes de milieux continus pour la modélisation de bicouches lipidiques sont développées et appliquées à des vésicules lipidiques à deux phases et à des particules discoïdes de lipoprotéines de haute densité (HDL). Tout d'abord, en s'appuyant sur un modéle tridimensionnel, la mécanique d'une bicouche lipidique possédant une courbure spontanée est considérée. La Cinématique, la symétrie matérielle, les relations de stress, et la cohérence de bicouches lipidiques sont discutées. En traitant une bicouche lipidique comme une structure mince, la densité d'énergie surfacique d'une bicouche lipidique ayant une courbure spontanée est obtenue à l'aide d'une procédure de réduction de dimension. L'attention est portée sur la source de courbure spontanée de la densité d'énergie bien connue de Canham–Helfrich. En outre, l'effet de l'asymétrie constitutive des sur la densité d'énergie surfacique d'une bicouche lipidique est mis en évidence.

Considérant une vésicule à deux phases comme système de domaines sphériques coexistants, son équilibre est étudié à l'aide d'un modèle simple de milieu continu. Des configurations multi-domaines et de l'état fondamental sont considérées. Alors que, dans le premier cas, plusieurs domaines lipidiques bourgeonnés coexistent sur une vésicule, dans le dernier cas, la vésicule est composée de deux grands domaines lipidiques. La variation de l'énergie potentielle nette d'une vésicule multi-domaine en fonction du nombre de domaines lipidiques et de la pression osmotique est étudiée. En se basant sur la comparaison de l'énergie, deux configurations de l'état fondamental correspondant à des niveaux d'énergie minimaux sont identifiés: la configuration étranglée et la sphère complète. Les résultats indiquent que la pression osmotique et le rayon excédentaire initial jouent un rôle clé dans la forme finale des configurations à l'état fondamental. Les valeurs critiques de ces paramètres sont identifiées.

Enfin, l'équilibre et la stabilité d'une particule HDL discoïde sont étudiés. Un modèle dans lequel la bicouche lipidique et les composants d'ApoA-I à double bande de la particule de HDL discoïde sont représentées par une surface de matériau et une courbe de matériau parfaitement collée sur le bord de la surface est proposé. L'énergie de courbure et la tension de surface de la bicouche lipidique ainsi que l'énergie de flexion de la chaîne apoA-I sont incluses. En adoptant un schéma variationnel, les équations d'équilibre non-linéaire d'une particule de HDL discoïdale dans une configuration générale sont calculées d'après des formulations directes, basées sur la géométrie, ou paramétrées. Les équations d'équilibre linéarisées d'une particule de HDL circulaire plane sont obtenues et sa stabilité linéaire est étudiée en utilisant la seconde méthode de variation. Une méthode de comparaison de l'énergie est appliquée et se trouve à offrir une approche pratique pour déterminer la stabilité linéaire. Des résultats numériques sont présentés pour l'équilibre et la stabilité des particules de HDL circulaires planes. Un plan de stabilité indiquant différentes régions stables et instables des paramètres d'entrée adimensionnels sous-jacents est fourni. Certaines possibilités de changement de stabilité et les formes modales d'instabilité sont identifiées. Il est démontré que les premiers modes d'instabilité transversale et plane ressemblent aux formes de selle non planes et d'ellipse plane, respectivement.

TABLE OF CONTENTS

LIST OF FIGURES

List of abbreviations:

RBC: red blood cell
HDL: high-density lipoprotein
GUV: giant unilamellar vesicle
RCT: reverse cholesterol transport
MD: molecular dynamics
PDE: partial differential equation
ODE: ordinary differential equation
HIV: human immunodeficiency virus

Contributions of authors:

1- M. Maleki, B. Seguin, and E. Fried, “Kinematics, material symmetry, and energy densities for lipid bilayers with spontaneous curvature,” *Biomechanics and Modeling in Mechanobiology*, vol. 12, pp. 997–1017, 2013:

M. Maleki developed the model and wrote the paper. **B. Seguin** contributed in the Material Symmetry section, specifically in subsection 2.6.2 discussing the representation theorem for the energy density of a lipid bilayer. He also contributed in editing the paper. **Prof. E. Fried** supervised the work and edited the paper.

2- M. Maleki and E. Fried, “Multidomain and ground state configurations of two-phase vesicles,” *Journal of The Royal Society Interface*, vol. 10, no. 83, 20130112, 2013:

M. Maleki developed the model and wrote the paper. **Prof. E. Fried** supervised the work and edited the paper.

3- M. Maleki and E. Fried, “Equilibrium of discoidal high-density lipoprotein particles,” (in preparation):

M. Maleki developed the model and wrote the paper. **Prof. E. Fried** supervised the work and edited the paper.

4- M. Maleki and E. Fried, “Stability of discoidal high-density lipoprotein particles,” *Soft Matter*, vol. 9, pp. 9991–9998, 2013:

M. Maleki developed the model and wrote the paper. **Prof. E. Fried** supervised the work and edited the paper.

CHAPTER 1
Introduction

1.1 Preface

In this chapter, first, a general background on lipid bilayers, multiphase vesicles, and high-density lipoprotein (HDL) is provided. Attention is focused on their structures, properties, and their applications. Also, various relevant definitions and terminology are introduced. Next, the motivation and objectives of the thesis are presented. For this purpose, salient aspects of the mechanical and physical modeling of lipid bilayers and of multiphase vesicles and discoidal HDL particles are reviewed and the objectives of the thesis are expressed. Finally, the organization of the thesis in the following chapters is given.

1.2 Background

1.2.1 Lipid bilayer

A lipid bilayer forms by the self-assembly of lipid molecules in aqueous solution. These structures are encountered in various biological systems. The primary example is the biomembrane—which is an essential part of the outer layer of eukaryotes and their internal organelles, red blood cells (RBC), bacteria, and viral capsids. Lipid bilayers also comprise the interior part of discoidal high-density lipoprotein (HDL) particles. Secondary examples of lipid bilayers include synthetic systems such as liposomes, giant vesicles, and supported lipid bilayers. These model membranes have found and continue to find extensive biomedical and pharmacological applications.

In addition, they provide a useful platform for studying various biophysical aspects of biomembranes.

The elementary units of lipid bilayers are phospholipid molecules [1] . A phospholipid molecule is comprised by a hydrophilic head attached to two roughly parallel hydrophobic flexible tails (Figure 1–1). The specific structure of the lipid bilayer relates to the amphiphatic property of phospholipid molecules [6]. The polar (hydrophilic) heads of phospholipid molecules are water-soluble and, hence, tend to be in contact with water. On the other hand, the nonpolar (hydrophobic) tails have a strong tendency to avoid contact with water. As a result, when present in the solution above a certain sufficient concentration and in an appropriate temperature range, phospholipid molecules spontaneously self-assemble to form lipid bilayers. In a lipid bilayer, the head groups face the solution and the tail groups are confined to the core of the bilayer where they are protected from the solution by the head groups [7] (Figure 1–2a). The typical thickness of a bilayer is on the order of few nanometers, usually about 5 nm.

For open lipid bilayers, the arrangements of the phospholipid molecules in the interior region and near the edge are completely different. In the former region, as with the molecular architecture in closed lipid bilayer, phospholipid molecules are aligned perpendicular to the midsurface of the bilayer. However, in a vicinity of the edge, they are packed so that their tails are radially aligned towards the edge (Figure 1–2b). This kind of arrangement shields the hydrophobic tails from the

---

[1] These molecules may referred to simply as “lipid molecules.”

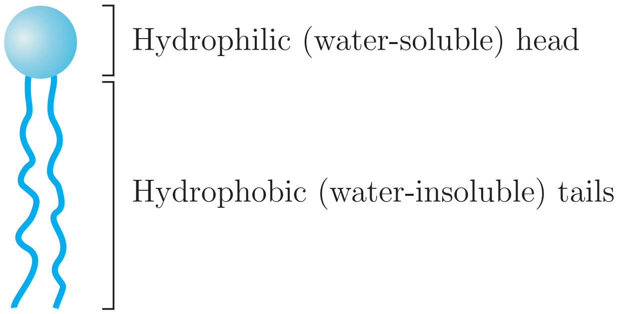

Figure 1–1: Schematic of a phospholipid showing the hydrophilic (water-soluble) head and hydrophobic (water-insoluble) tails.

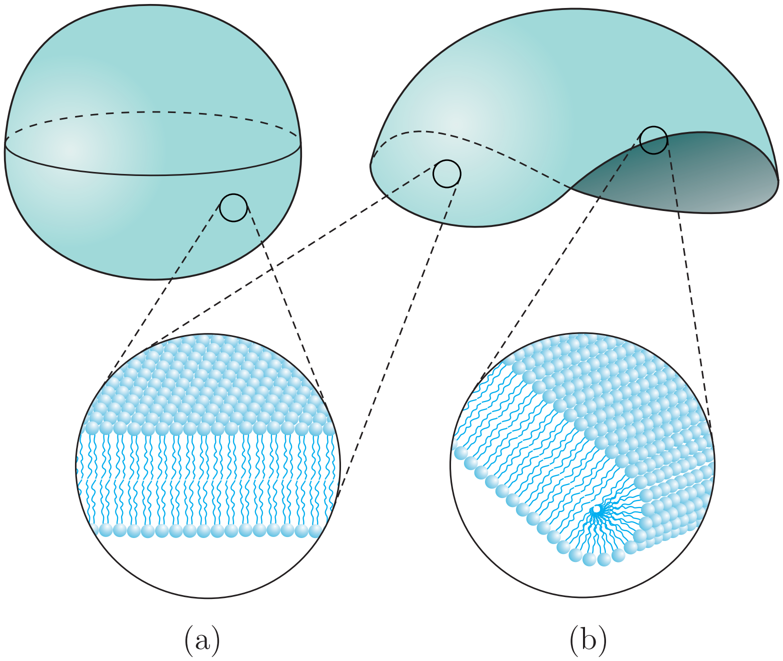

Figure 1–2: Schematic of phospholipid arrangements: (a) on a closed lipid bilayer and the interior region of an open lipid bilayer (b) around the edge of an open lipid bilayer.

aqueous solution. The highly localized change of phospholipid orientations near the edge induces an excess energy—usually known as the “edge energy”—concentrated along it [8, 9, 10, 11]. Due to this excess energy, open lipid bilayers have the tendency to close on themselves to form vesicles. The edge energy of an open lipid bilayers has a crucial role in vesicle formation—for example, using electroformation [7]. However, an open lipid bilayer may be stabilized in different ways, for example, using electric field [12] and sonication [13], and by accumulation of active chemical agents near the edge [14]. In addition, processes wherein open lipid bilayers form by the bursting of cell membrane and lipid vesicles using electroporation is currently a subject of intensive study [15].

The physical properties of lipid bilayers are very sensitive to temperature. For example, with increasing temperature, lipid bilayers usually undergo several transitions with different phases from subgel, gel, ripple, to liquid-crystalline fluid phases [16]. In most biological processes, a lipid bilayer possesses the liquid-crystalline fluid phase where molecules are statistically aligned perpendicular to the surface separating two leaflets (which is referred to as the midsurface of the bilayer) and can easily migrate laterally in each leaflet without any considerable shear renitence. Lipid molecules can also transit across the leaflets in a process known as the flip-flop diffusion. However, the time scale of flip-flop diffusion in phospholipid bilayers is on the order of hours [17] and, hence, flip-flop diffusion is much slower than lateral diffusion. Thus, for sufficiently small time scales, the lipid exchange between the leaflets may be ignored.

Lipid bilayers are very flexible biological structures. Apart from the undulations due to statistical fluctuations, they deform readily under external stimuli, such as applied forces and moments or changes of temperature or osmotic pressure in case of closed bilayers. The dominant deformational mode of lipid bilayers is bending. From the molecular point of view, the energy cost due to bending may be caused by the relative misalignment of adjacent lipid molecules. Lipid bilayers show high resistance to changes of area induced by stretching or contraction compared to changes of curvature induced by bending [18]. Due to packing constraints and intermolecular interactions, lipid molecules usually prefer to stay perpendicular to the midsurface. This, however, need not true in settings wherein the phospholipid molecules tend to be tilted, for example in the vicinity of inhomogeneities such as transmembrane proteins or other types of biological molecules [19, 20].

The conventional quantitative description of a lipid bilayer bending deformation hinges on endowing it an energy density, measured per unit area, which takes curvature changes into account. A well-known energy density proposed by Canham [21] and Helfrich [22] takes the form

$$\psi = \tfrac{1}{2}\kappa(H - H_\circ)^2 + \bar{\kappa}K, \tag{1.1}$$

in which H and K are respectively the mean and Gaussian curvatures of the midsurface of the lipid bilayer. Also, κ and $\bar{\kappa}$ are usually referred to as the splay and saddle-splay moduli which measure the respective costs of changes of H and K. The parameter $H_\circ$, which is known as the spontaneous (mean) curvature, may be viewed as the natural mean curvature of lipid bilayer.

Nonzero spontaneous curvature usually reflects an asymmetry between two sides of the lipid bilayer midsurface [23]. The asymmetry may be manifested in different

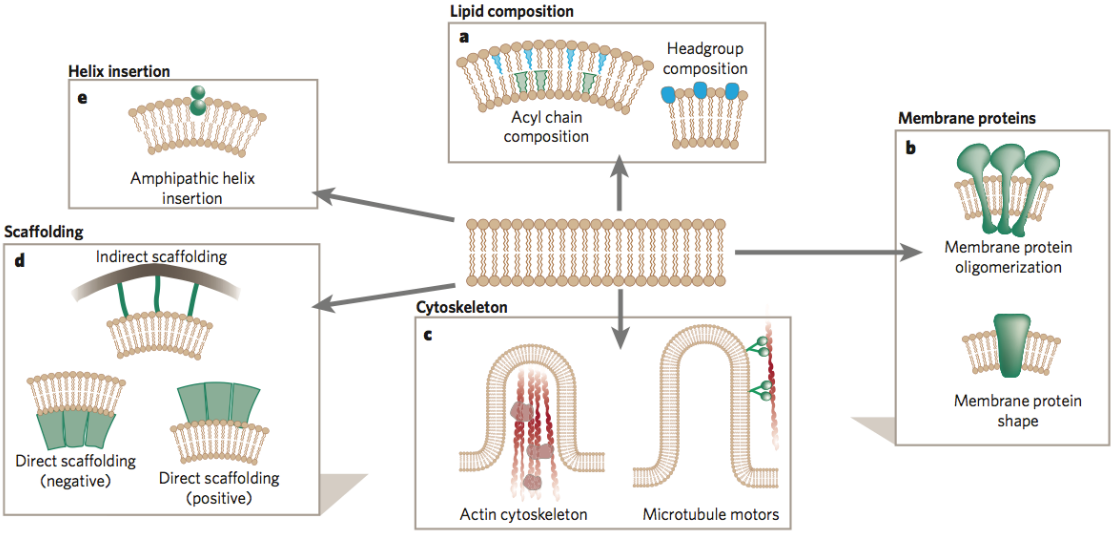

Figure 1–3: Different mechanisms inducing the natural curvature in biomembranes [1]. Reprinted by permission from Macmillan Publishers Ltd: [NATURE] (H. T. McMahon and J. L. Gallop, "Membrane curvature and mechanisms of dynamic cell membrane remodelling," *Nature*, vol. 438, no. 7068, pp. 590–596, 2005), copyright (2005).

ways. For example, a presence of different lipid molecules in two leaflets with different molecular geometries may lead to non-flat natural state [1]. Also, differences between the solutions on either side of the lipid bilayer may be another cause of asymmetry [24]. Other potential origins for asymmetry include interaction of lipid bilayer with cytoskeleton and clathrin coat, or the presence of helical or transmembrane proteins on one side of the bilayer [1, 25, 26] (Figure 1–3).

1.2.2 Multiphase lipid vesicles

A lipid vesicle or liposome is a closed lipid bilayer with no boundary. Vesicles exists in different sizes and with different numbers of lamellae [27].[2] Unilamellar vesicles consist of a single bilayer in the thickness direction (see e.g., Fig. 1–2a), while multilamellar vesicles consist of numbers of lipid bilayers stacked in the through-thickness direction. Vesicles have thicknesses of a few nanometers and their characteristic size (for example, the diameter in case of a spherical vesicle) may vary from 50 nm to tens of micometers [27]. Vesicles may be categorized according to their size. Very large vesicles are commonly known as giant vesicles. Giant unilamellar vesicles (GUVs) have received considerable attention [27]. This is due to their extensive biological, biomedical, and pharmacological applications—for example in gene therapy and drug delivery [28, 29, 30], medical diagnosis [31], immunology [32, 33], and analytical biochemistry [34, 35].

An important feature of lipid bilayers is semipermeability. For vesicles, where the lipid bilayer separates the interior and exterior solutions, the passage of large molecules (e.g., sugar molecules) or ions across the lipid bilayer occurs very slowly [23]. Asymmetric distribution of solute concentrations between the inside and outside of a vesicle then result in a nonvanishing excess pressure, known as the osmotic pressure.

GUVs can possess various shapes with different topologies [23]. Prolate, discocyte, stomatocyte, tubular, pear-shape, starfish, and toroidal GUVs have been

---

[2] If there is no chance of confusion, a "lipid vesicle" may simply be referred to as "vesicle."

observed. For example, for some of possible configurations which GUVs may adopt due to changes in the osmotic pressure, see [36]. Depending on the time scale of the shape change, the volume enclosed inside a vesicle may be assumed fixed or variable. When the deformation occurs much faster than the diffusion rate of the solvent across the lipid bilayer (which is driven by the osmotic pressure), the enclosed volume may be treated as fixed to a very good approximation. However, for long enough processes, solvent exchange across the lipid bilayer may be appreciable and, thus, typically leads to vesicular swelling or shrinking.

Apart from their extensive applications, GUVs may also serve as model systems for biophysical studies of naturally occurring biomembranes. Biomembranes are extremely complex systems composed of large number of lipid species, cholesterol, and proteins. Multicomponent GUVs, usually composed of two types of lipid molecules and cholesterol, have been widely studied. Particularly, they provide a model platforms for understanding the biological activities of the biomembranes associated with very small domains, commonly known as "lipid rafts" [37]. Lipid rafts, with typical sizes in range of 10–200 nm, are very small domains in the liquid-ordered phase surrounded by the host membrane in the liquid-disordered phase. The liquid-ordered phase is populated by saturated lipids and cholesterol while the liquid-disordered domain is primarily enriched by unsaturated lipid molecules [38]. Cholesterol is dominantly accommodated between the saturated lipids. Such arrangements allow the saturated lipids to exist in the liquid-ordered phase [39, 40]. Figure 1–4 shows a schematic of a lipid raft [2].

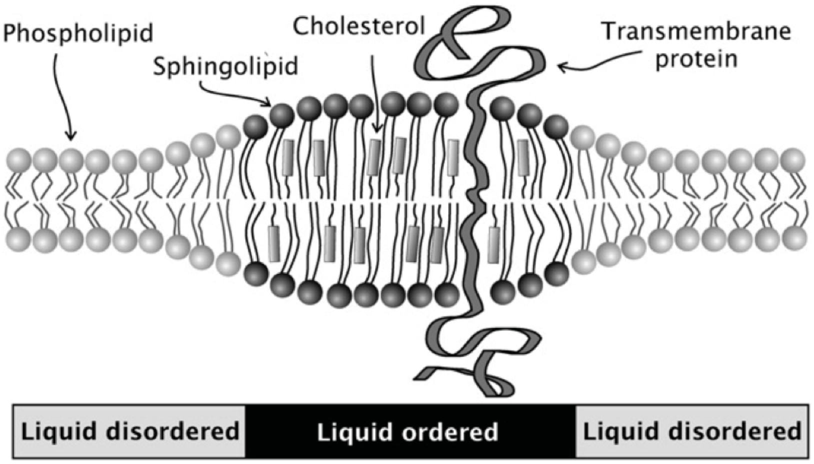

Figure 1–4: Schematic of a lipid raft in the liquid-order phase surrounded by the liquid-disordered phase [2]. Reproduced from [2] with permission of The Royal Society of Chemistry.

A lipid raft is distinct from the host membrane by a larger thickness, as saturated lipid molecules are generally longer than the unsaturated ones. Various studies have revealed the important role of lipid rafts in the sorting of membrane proteins [41, 42]. Larger rafts can be formed by the coalescence of smaller rafts. They play a crucial role in various cellular activities such as trafficking, immune responses, signaling, and endocytosis [37, 41, 42]. Another important feature of lipid rafts is linked to their role in interaction of certain pathogens, including the bird flu virus and HIV, with the cell membrane. It is widely accepted that lipid rafts may serve as gateways for these pathogens to mount attacks on cells [37, 41, 42, 43] and virus replication [44]. For a comprehensive list of diseases in which lipid rafts are involved, see [45].

The notion of a lipid raft is a controversial concept in cell biology [46, 47]. Despite their importance, lipid rafts are not fully characterized [38]. This controversy is partially due to challenges involved in the observation of lipid rafts as they are too small to be captured using conventional optical techniques. Studies of lipid domains on multicomponent GUVs composed of saturated and unsaturated lipids and cholesterol have provided an alternative platform for the description of lipid rafts on cell membranes [38, 42]. Compared to lipid rafts on cell membranes, lipid domains on model membranes can be studied much more easily under controlled experimental conditions. In addition, the characteristic size of lipid domains on model membranes is on the order of 1–10 μm, which allows for their observation using light microscopy [48]. Lipid domains on multiphase GUVs are seen in different forms. A very common mode of lipid domain formation in biphasic GUVs is shown in Fig. 1–5, where multiple domains, in liquid-ordered phase, bud from the background domain in the liquid-disordered phase. In another case, scattered domains have coalesced and a GUV is fully phase-separated into two distinct liquid-ordered and liquid-disordered regions (Figure 1–6).

Configurations of phase-separated GUVs are primarily dictated by the competition between the underlying energetics, such as the bending energy of lipid bilayer, the line tension (energy) of the phase boundary, and the volumetric energy associated with the osmotic pressure. Line tension reflects the stored energy near a phase boundary. Generally, two separate mechanical and chemical sources create line tension. The chemical contribution is a manifestation of the large gradient of dissimilar lipid species in the thin transition layer between two pure phases. The mechanical contribution accounts for energy costs due to deformation of lipid molecules

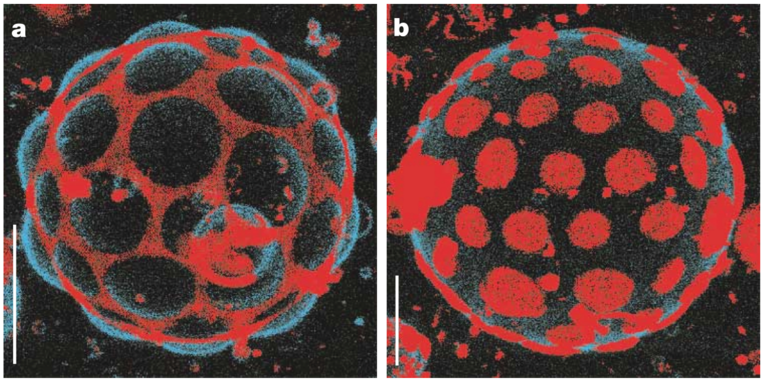

Figure 1–5: Two-phase GUVs with multiple domains [3]. Blue and red colors correspond to liquid-ordered and liquid-disordered phases, respectively [3]. The bar is 5 μm in length. Reprinted by permission from Macmillan Publishers Ltd: [NATURE] (T. Baumgart, S. T. Hess, and W. W. Webb, “Imaging coexisting fluid domains in biomembrane models coupling curvature and line tension,” *Nature*, vol. 425, no. 6960, pp. 821–824, 2003), copyright (2003).

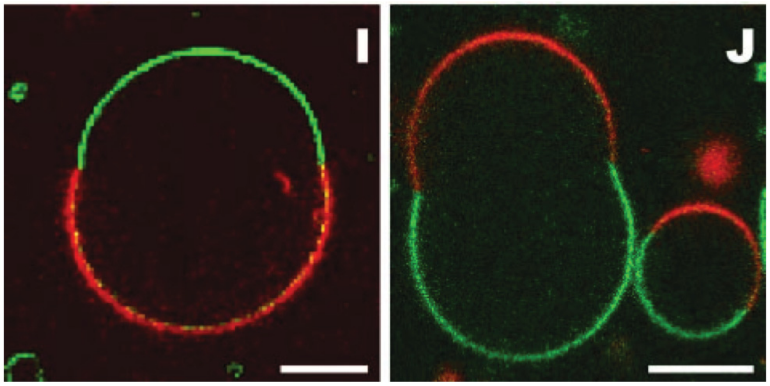

Figure 1–6: Cross section of fully-phase separated two-phase GUVs [4]. Red and green regions correspond to liquid-disordered and liquid-ordered phases, respectively. The bar is 10 μm in length. Reproduced from [4] with permission from American Society for Biochemistry and Molecular Biology.

in the transition layer, such as the splay and tilt of lipid molecules or the stretching/contraction of their tail groups. The latter deformation typically arises due to hydrophobic mismatch between two phases with different thicknesses.

1.2.3 High-density lipoprotein (HDL) particles

Lipoprotein particles are essential to cholesterol metabolism in the body [49]. Since cholesterol is not solvable in water, it must be packaged properly to circulate in the blood stream. Lipoprotein particles are responsible for the cholesterol packaging and transport in the body. A particular type of lipoprotein particles, called high-density lipoprotein (HDL) particles, collect cholesterol from tissues and deliver it to the liver for excretion into bile in a process known as "reverse cholesterol transport (RCT)." In the first step of RCT, lipid-free apolipoprotein, known as apoA-I, absorbs lipid molecules and free (unesterified) cholesterol from the blood stream to form discoidal HDL particles. Next, discoidal HDL particles transform to spheroidal HDL particles by absorbing triglycerides and more free cholesterol. In this step, free cholesterol is converted to esterified cholesterol and together with triglycerides accumulate at the core of spheroidal particles. The core of such a particle is coated by lipid monolayer and apoA-I. As spheroidal HDL particles become larger, they pick up another type of apolipoprotein, called apo-E, which has an affinity to liver receptors. Lastly, after absorption by the liver, the liver transfers cholesterol to bile and releases apoA-I to commence a new cycle.

A discoidal HDL particle consists of a lipid bilayer bounded by a double-belt apoA-I chain (Fig. 1–7). The typical diameter of discoidal HDL particles is about 10 nm [50, 51, 52, 53, 54, 55]. ApoA-I chain is very flexible and has an important role in stability of discoidal HDL particles [56]. The major part of apoA-I double-belt structure is α-helical segments which are amphipathic [56]. Hence, apoA-I and lipid bilayer form a favorable architecture of discoidal HDL particle, where α-helical segments bound to the hydrophobic core of the lipid bilayer at the edge. In this way, the hydrophobic tail groups of lipid bilayer is also protected from exposure to the aqueous solution [56].

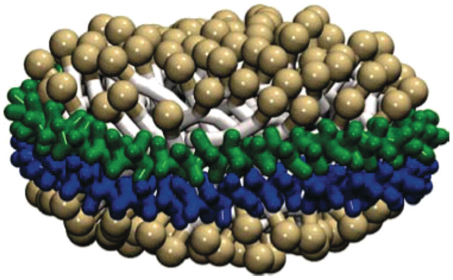

Figure 1–7: A discoidal HDL particle in the coarse-grained illustration, showing the lipid bilayer with a double-belt apoA-I chain bounding the edge of lipid bilayer [5]. Reprinted (adapted) with permission from (A. Y. Shih, A. Arkhipov, P. L. Freddolino, S. G. Sligar, and K. Schulten, "Assembly of lipids and proteins into lipoprotein particles," *The Journal of Physical Chemistry B*, vol. 111, no. 38, pp. 11095–11104, 2007). Copyright (2007) American Chemical Society.

1.3 Motivation and objectives

Mechanical and physical studies of lipid bilayers are essential for characterizing various biological structures in which they appear as components. The present thesis includes three main parts. After a fundamental study on the mechanical modeling of a lipid bilayer itself (first part), two prominent examples where lipid bilayers have crucial importance in the biological systems are addressed: multiphase vesicles (second part) and discoidal HDL particles (third part) (Figure 1–8).

In this section, the motivations and objectives of the thesis are reviewed.

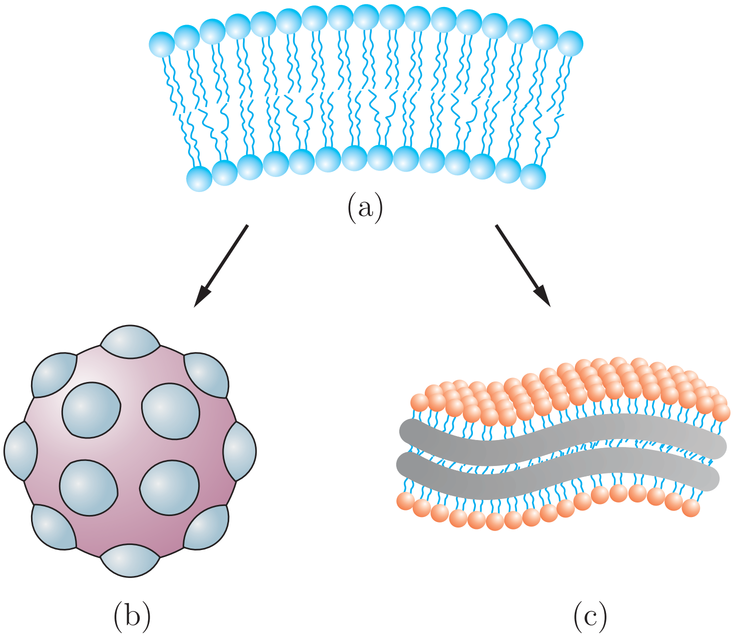

Figure 1–8: (a) Schematic cross section of a lipid bilayer. Two prominent examples where lipid bilayer is an essential element of a biological structure: (b) multiphase vesicles and (c) discoidal HDL particles.

1.3.1 Mechanical modeling of lipid bilayer

The continuum modeling of lipid bilayers has been topic of research for over forty years. Adapting the common approach in structural mechanics of elastic beams, Canham [21] showed that the famous biconcave shape of the red-blood cell (RBC) can be explained by minimization of its net bending energy. The energy density, measured per unit area of the RBC surface, was assumed to be a quadratic function of the principal curvatures of the surface. In a seminal work, Helfrich [22] proposed the energy density given in (1.1) for a lipid bilayer as a function of the mean curvature H, the square H^2 of that quantity, and the Gaussian curvature K. By including a term proportional to H in the energy density, Helfrich [22] introduced the notion of spontaneous (mean) curvature $H_\circ$. Helfrich [22] interpreted the presence of spontaneous curvature as a reflection of chemical asymmetry between the two leaflets of lipid bilayer. Using simplifying geometrical and constitutive assumptions and implementing the approach similar with bending analysis of elastic thin shells, Evans [57] studied the bending of lipid bilayers. He explained how chemical changes within the leaflets may induce bending of lipid bilayer. Studying both connected and slipping leaflets, he also emphasized the effect of leaflets coherency on the bending behavior of lipid bilayers.

The Canham–Helfrich energy density (1.1) describes the bending deformation of lipid bilayers. As mentioned earlier, lipid bilayers show very high resistance to change of the area. Such behavior has convinced many researchers to commonly assume that the area of lipid bilayer is preserved in the deformation. This, however, does not mean that area changes are completely irrelevant. Since the stretching modulus of a lipid bilayer is much larger than its bending rigidity, even very small amounts of stretch can result in considerable energy changes. Apart from certain circumstances in which lipid bilayers expand under large tension, local area changes at junctions between lipid molecules and a boundary or heterogeneity are observed. Due to the volumetric incompressibility of lipid bilayer [58, 59, 60], changes in area are accompanied by changes in thickness. For example, in the vicinity of a transmembrane protein, due to a mismatch between the lengths of hydrophobic part of the protein and the tail groups of the lipid molecules, those groups elongate/shorten to compensate for the hydrophobic mismatch. As another example, different phases of a multiphase lipid bilayer exhibit different thicknesses. The tail groups of two phases must therefore adjust their lengths at an interface to compensate for their different thicknesses (see, e.g., Fig. 1–4). Local area changes are relevant in both of these examples.

An important distinction between a lipid bilayer and an elastic shell is a consequence of their material symmetries. To understand the material symmetry of a lipid bilayer, it is necessary to identify classes of deformation which leave its constitutive response unchanged. The first important feature of a lipid bilayer is the in-plane isotropy, which means that there is no directional dependence of the mechanical response of a lipid bilayer within its tangent plane. Thus, the constitutive response of a lipid bilayer is invariant under any rigid-body rotation within the tangent plane. The second feature of a lipid bilayer is the in-plane fluidity. Consistent with the observation that lipid bilayer shows very low resistance to shear flow on the tangent plane, in-plane fluidity implies that the constitutive response of lipid bilayer is not affected under any such deformations. Consistent with the material symmetry of a lipid bilayer and adopting the Cosserat surface theory, Jenkins [61] developed the equilibrium equations of a lipid bilayer. He also discovered that the energy density of a lipid bilayer must be invariant under all two-dimensional unimodular transformations—i.e., transformations that preserve the local area and, consequently, the local mass density per unit area. Steigmann [62] provided a fundamental understanding for mechanical theory of fluid films possessing bending elasticity. Considering the set of all two-dimensional unimodular transformations as the material symmetry group, Steigmann [62] showed that the energy density must, in general, be a function of the mean and Gaussian curvatures H and K and the areal stretch J. This conclusion provides a solid theoretical basis for the problems in which lipid bilayers undergo bending and/or stretching.

Although lipid bilayers are very thin structures, they may deform in the thickness direction. In addition, the bending and stretching of a lipid bilayer are linked to through-thickness deformations. For example, when a lipid bilayer is bent, the material points located on the upper and lower leaflets experience different deformations. In particular, when one leaflet is stretched, the other leaflet shrinks. Generally, the deformation at a material point in a lipid bilayer varies in the through-thickness direction. Considering a lipid bilayer as a three-dimensional structure, Zurlo [63] and Deseri et al. [64] developed an areal energy density as a function of the mean and Gaussian curvature H and K of the midsurface, the areal stretch J of the midsurface, and the surface gradient of J. They also included chemical effects, which are important for multicomponent lipid bilayers. In their works, the derivation of areal energy density is based on a dimension reduction procedure in which a volumetric energy density is integrated through the thickness of lipid bilayer. The volumetric energy density has a hyperelastic form and is a function of three kinematical invariants. Such a volumetric energy density is derived by imposing a material symmetry describing the in-plane isotropy and fluidity of lipid bilayer.[3] Recently, relying on [63, 64], Deseri and Zurlo [65] show how the stretching response of a lipid bilayer can

---

[3] For the discussions on the material symmetry and the steps leading to derivation of the volumetric energy density, Zurlo [63] and Deseri et al. [64] refer to a paper in preparation which was and remains unavailable to this date.

be used to determination its bending moduli and the line tension arising between different phases with different thicknesses.

The physical behavior and molecular arrangement of lipid molecules in a lipid bilayer are very similar to those in a smectic liquid crystal. This has encouraged some researchers to describe the energy density and mechanics of lipid bilayer based on liquid crystal theories. Recently, Seguin and Fried [66], using a microphysical approach and, considering the lipid molecules as system of interacting rods [67], derived the Canham–Helfrich energy density (1.1). Their analysis provides expressions for the spontaneous curvature and the bending moduli based on the pair potential of lipid molecules. Just recently, using a three-dimensional liquid crystal model for a lipid bilayer, Steigmann [68] presented a dimensionally-reduced areal energy density incorporating the tilt and distension of lipid molecules. Based on the dimensionally-reduced areal energy density as a function of mean and Gaussian curvatures H and K, areal stretch J, and the surface gradient of J, Steigmann [68] derived the equilibrium equations and determined the Legendre–Hadamard condition necessary for existence of an energy minimizer.

The first objective of this thesis is a fundamental study of the mechanics of lipid bilayers with spontaneous curvature using continuum-mechanical ideas. Focus will be paid on deformation, material symmetry, and the derivation of a dimensionally-reduced areal energy density. Our approach is guided by the works of Zurlo [63] and Deseri et al. [64], who considered a lipid bilayer as a three-dimensional structure. Zurlo [63] and Deseri et al. [64] did not account for spontaneous curvature in their considerations. An important goal of this study is to provide a solid and clear theoretical basis for the concept of spontaneous curvature in the conventional Canham–Helfrich energy density (1.1). Also, the effect of leaflets asymmetry, leaflets incoherency, and the incompressibility of the lipid bilayer will be taken into account. In addition, the general stress relations within a lipid bilayer will be derived.

1.3.2 Mechanics of multiphase lipid vesicles

In view of their promising biophysical and biochemical applications, multiphase vesicles are the subject of considerable theoretical and experimental research. Both equilibrium and dynamical studies of multiphase vesicles have been performed. On the dynamical side, either in supported lipid bilayers or vesicles, most attention has been paid on the growth, clustering, and coalescence of lipid domains [69, 70, 71, 72, 73]. Studies of the equilibrium of multiphase vesicle have been primarily dedicated to fully phase separated vesicles, usually composed of two large coexisting domains (e.g., see [74, 75, 3, 76, 77, 78, 79, 80, 81]). Most analytical works on the mechanics of multiphase vesicles are concerned with solving the system of equations and associated boundary conditions for axisymmetric configurations of two-phase vesicles. The system of equations consists of a fourth-order partial differential equation, known as the shape equation, in each phase augmented by a junction condition at interfaces between two phases. As a consequence of the axisymmetry, the shape equation simplifies to an ordinary differential equation (ODE). Instead of a sharp kink-like interface between lipid phases, some researchers have considered a thin transition layer (also referred to as a boundary layer), usually exhibiting high curvature, between the phases [82, 77, 83, 84].

Numerous existing experimental observations show that, except for narrow regions surrounding their junctions, the shape of lipid domains in multiphase vesicles is essentially spherical [48, 3, 76, 72, 4, 85]. This is valid for both multidomain and fully phase separated configurations, as, e.g., observable in Figs. 1–5 and 1–6. This argument is specially more accurate for tense vesicles under an internal osmotic pressure. If considered as a spherical cap, a lipid domain is geometrically characterized only by two parameters, e.g., the radius of curvature and the opening angle. This significantly simplifies the equilibrium analysis of a multiphase vesicle; as such, instead of solving the shape equation in each domain, only the radii of curvature and opening angles must to be determined. Of course, the force balance and the geometrical compatibility at the junction must also be satisfied in equilibrium.

As introduced in Section 1.2.2, the primary energetic contributions to the net potential energy of a multiphase vesicle are the bending, lineal, and volumetric parts. The latter contribution becomes relevant when the enclosed volume of vesicle changes. Otherwise it must be imposed as a constraint. The constraint may either be considered implicitly or be included in the net potential energy using a Lagrange multiplier, representing an unknown pressure. In addition, if area changes are neglected (which is a common assumption for vesicles), the net area of each phase must be fixed among all possible configurations. Confining our attention to vesicles with spherical domains, the bending energy of each domain can easily be calculated using the Canham–Helfrich energy given in (1.1), granted knowledge of the radius of curvature. The line energy is proportional to the total length of the phase interfaces. The force balance at a junction between phases relates the line tension (i.e., the line energy per unit length of the junction) to the surface tensions of the domains and their slopes at their junction (see, e.g., [3, 86, 87] for the junction condition). Hence, the line tension in multiphase vesicles should not be viewed as an arbitrarily prescribable quantity.

Yanagisawa et al. [72] and Semrau et al. [85] considered multidomain configurations of two-phase vesicles in which each of the domains is a spherical cap. However, at interfaces between domains, they satisfied only the requirements of geometrical compatibility without considering force balance. Allain and Ben Amar [88] studied the effect of protein adsorption on the instability of a fully phase separated two-phase vesicle. Assuming that the vesicle consists of two connected spherical caps, they also derived the equilibrium equations and the necessary junction conditions at the interface of domains. Later, Allain and Ben Amar [77] studied budding and fission in two-phase vesicles composed of spherical caps. With particular attention to tense vesicles, at the first step, they used a capillary model for each lipid domain in which bending energy is ignored. Next, they refined their model by replacing the sharp kink-like interface with a smooth, thin transition layer endowed with bending energy. Employing an asymptotic method, Trejo and Ben Amar [84] studied equilibrium of a two-phase vesicle with the geometry of two connected spherical caps. A boundary layer between those caps was also considered. The results of Trejo and Ben Amar [84] concentrated on an effective line tension and the contact angles between two phases.

The second objective of this thesis is to present a simple and efficient continuum mechanical tool for studying the equilibrium of a two-phase

vesicle. Both multidomain and ground-state (fully phase separated) configurations will be studied. In view of many experimental observations, the focus will be on vesicles comprised of lipid domains with the geometry of spherical caps. The net potential energy will consist of all three relevant sources—bending, line, and volumetric. For both multidomain and the ground-state configurations, apart from the geometrical compatibility of lipid domains at their interfaces, the force balance will also be satisfied. While, consistent with relatively short time scales required for the formation of multidomain configurations, the enclosed volume of multidomain configurations will be assumed fixed, the enclosed volume at the ground-state configuration will be allowed to vary. In this case, following Seifert [23], the osmotic pressure will vary as a consequence of change of solute concentration inside the vesicle due to its volume change. Attention will be paid on the roles of osmotic pressure and the initial geometry of vesicle (specifically, its excess radius) prior to phase separation on its shape in the ground state.

1.3.3 Equilibrium and stability of discoidal HDL particles

The biological functionality of HDL particles is thought to hinge primarily on the conformation of apoA-I [89]. Despite their crucial role in the cholesterol metabolism, the structure and functionality of HDL particles still demand extensive research. In this vein, Vuorela et al. [90] state that: "*The functionality of HDL has remained elusive, and even its structure is not well understood.*"

The careful understanding and classification of the different conformations of discoidal HDL particles are subject of ongoing experimental and theoretical studies. Recent works have revealed that the flat circular shape is not the only configuration in which discoidal HDL particles are found. All-atom molecular dynamics (MD) simulations of Catte et al. [91] demonstrate the existence of nonplanar saddle-like configurations. Catte et al. [91] observed that gradual removal of lipid molecules from the surface of a discoidal HDL particle induces a transformation from a flat circular to a non-flat saddle-like configuration. Their results lead them to suggest that the midsurface of lipid bilayer of the discoidal HDL may be well represented by a minimal surface (a surface with zero mean-curvature). Saddle-like shapes of discoidal HDL particles have later been confirmed in other MD simulations and experiments [92, 93, 94, 95, 96, 94, 50]. In another experimental observation, Skar-Gislinge et al. [97] have shown that discoidal HDL particles can adopt flat elliptical shape.

MD simulations of discoidal HDL particles have provided valuable and enlightening results. Nevertheless, these simulations have practical limitations. In particular, current computational limitations make it impossible to perform simulations long enough to draw conclusions regarding equilibrium and stability. Continuum models provide a complementary alternative to studying the equilibrium and stability of discoidal HDL particles. Continuum models have been used extensively, and with considerable success, to study the equilibrium and stability of biological membranes and biomolecules; for revenant reviews, e.g., see [23, 98, 99, 100].

The third, and final, objective of this thesis is to develop a continuum model for studying the equilibrium and stability of discoidal HDL particles. The model will consist of a surface, representing the lipid bilayer, attached on its edge to a curve, representing the bounding double-belt apoA-I. From an energetic perspective, the surface will be endowed with a uniform surface tension and a bending energy in form of Canham–Helfrich (1.1). Also, the bounding curve will be considered inextensible and will be endowed with a bending energy. In view of high flexibility of apoA-I chain [56] and the amphipathic consistency of apoA-I and lipid bilayer, a condition of perfect bonding between the surface and the bounding curve will be imposed. In the first step, using a variational approach, the general nonlinear equilibrium equations of a generally-distorted discoidal HDL particle will be derived based on a direct, geometrically-based formulation. Next, on choosing a flat circular shape as a reference configuration, the equilibrium equations will be reformulated using parametrization that describes the shape of the surface and the edge of discoidal HDL particle. While the direct formulation provides a clear interpretation of equilibrium equations without relying on any particular parameterization, the parametrized formulation creates a platform for numerical investigations and, hopefully, for finding closed-form solutions for the equilibrium equations. Later, based on a small-slope approximation, a linearized formulation will be developed. That formulation will be used for understanding the equilibrium and stability of flat circular HDL particles under small deformation. Closed-form solutions will be derived for the linearized equilibrium equations. It is hypothesized that the observed nontrivial shapes of discoidal HDL particles (such as nonplanar saddle-like or planar elliptic) might represent post-buckled configurations of unstabilized flat circular shapes. To explore the veracity of this hypothesis, in the first step, it is reasonable to determine the linear stability of flat circular HDL particles under general (transverse or in-plane) perturbations. Stability will be addressed using the second variation of the energy functional. Lastly, as an alternative approach to stability, inspired by

Giomi and Mahadevan [101], an energy comparison criterion based on an assumed trial solution will be employed.

1.4 Thesis organization

The present thesis is manuscript-based including published or in preparation manuscripts.

Chapter 1 includes the introduction and comprises a background, motivation and objectives, and thesis organization.

Chapter 2 includes a fundamental continuum mechanical study of a lipid bilayer with spontaneous curvature. This chapter is reprinted from the published paper:

M. Maleki, B. Seguin, and E. Fried, "Kinematics, material symmetry, and energy densities for lipid bilayers with spontaneous curvature," *Biomechanics and Modeling in Mechanobiology*, vol. 12, pp. 997–1017, 2013.

Chapter 3 covers a continuum mechanical approach for studying two-phase vesicles in both multidomain and ground-state configurations. This chapter is reprinted from the published paper:

M. Maleki and E. Fried, "Multidomain and ground state configurations of two-phase vesicles," *Journal of The Royal Society Interface*, vol. 10, no. 83, 20130112, 2013.

Chapter 4 presents a continuum mechanical approach for dealing with the equilibrium of discoidal HDL particles under general deformation. It also includes a handy tool based on energy comparison for the linear stability of flat circular HDL particles. This chapter presents the following in preparation manuscript:

M. Maleki and E. Fried, “Equilibrium of discoidal high-density lipoprotein particles,” (in preparation).

Chapter 5 covers the linear stability of flat circular HDL particle using the variational approach. This chapter is reprinted from the published paper:

M. Maleki and E. Fried, “Stability of discoidal high-density lipoprotein particles,” *Soft Matter*, vol. 9, pp. 9991–9998, 2013.

Chapter 6 contains closing remarks, including discussions of primary conclusions, original contributions to knowledge, and directions for future work.

References appearing in all chapters are listed at the end of the thesis.

CHAPTER 2
Kinematics, material symmetry, and energy densities for lipid bilayers with spontaneous curvature

2.1 Preface

As explained in Section 1.3.1, despite their very small thickness, deformation of lipid bilayers is linked to the three-dimensional distortions within the thickness. This chapter presents a fundamental treatment for the mechanics of lipid bilayers with spontaneous curvature by considering a lipid bilayer as a three-dimensional shell-like structure with finite-size thickness. After studying the kinematics and material symmetry of a lipid bilayer, the areal energy density for lipid bilayers with spontaneous curvature is extracted. Besides other discussions (also, including the stress relations and the leaflets incoherency), an important outcome of this chapter is providing a continuum mechanical basis for the notion of spontaneous curvature in the conventional Canham–Helfrich areal energy density (1.1). This chapter is reprinted from the published paper

M. Maleki, B. Seguin, and E. Fried, “Kinematics, material symmetry, and energy densities for lipid bilayers with spontaneous curvature,” *Biomechanics and Modeling in Mechanobiology*, vol. 12, pp. 997–1017, 2013.

with kind permission from Springer Science and Business Media, and from the coauthors Prof. Eliot Fried and Dr. Brian Seguin.

2.2 Abstract

Continuum mechanical tools are used to describe the deformation, energy density, and material symmetry of a lipid bilayer with spontaneous curvature. In contrast to conventional approaches in which lipid bilayers are modeled by material surfaces, here we rely on a three-dimensional approach in which a lipid bilayer is modeling by a shell-like body with finite thickness. In this setting, the interface between the leaflets of a lipid bilayer is assumed to coincide with the midsurface of the corresponding shell-like body. The three-dimensional deformation gradient is found to involve the curvature tensors of the midsurface in the spontaneous and the deformed states, the deformation gradient of the midsurface, and the transverse deformation. Attention is also given to the coherency of the leaflets and to the area compatibility of closed lipid bilayers (i.e., vesicles). A hyperelastic constitutive theory for lipid bilayers in the liquid phase is developed. In combination, the requirements of frame-indifference and material symmetry yield a representation for the energy density of a lipid bilayer. This representation shows that three scalar invariants suffice to describe the constitutive response of a lipid bilayer exhibiting in-plane fluidity and transverse isotropy. In addition to exploring the geometrical and physical properties of these invariants, fundamental constitutively-associated kinematical quantities are emphasized. On this basis, the effect on the energy density of assuming that the lipid bilayer is incompressible is considered. Lastly, a dimension reduction argument is used to extract an areal energy density per unit area from the three-dimensional energy density. This step explains the origin of spontaneous curvature in the areal energy density. Importantly, along with a standard contribution associated with the

natural curvature of lipid bilayer, our analysis indicates that constitutive asymmetry between the leaflets of the lipid bilayer gives rise to a secondary contribution to the spontaneous curvature.

2.3 Introduction

Biomembranes are essential to the functions of cells, bacteria, and viruses [102, 103]. Basic to all biological membranes are lipid bilayers, which are thin, sheet-like structural elements composed of two adjacent monomolecular leaflets joined by weak, noncovalent bonds [104]. In the liquid phase, lipid bilayers are very flexible in bending but highly resistant to lateral stretching [18]. The architecture of lipid bilayers hinges on the amphiphatic chemical properties of the constituent phospholipid molecules [6]. Such molecules consist of hydrophilic head groups and hydrophobic tails. When suspended in aqueous solutions under suitable temperature conditions and at appropriate concentrations, they form various self-assembled complexes with hydrophobic tails facing one another and hydrophilic head groups in contact with the solution [7]. These complexes include closed bilayers, known as vesicles or liposomes, which are typically a few nanometers thick and can range between fifty nanometers and tens of micrometers in diameter [27].

Biomembranes are generally heterogeneous multicomponent systems involving hundreds of lipid species along with various proteins and hydrocarbons. The inherent complexity of such systems has driven the development of biomimetic model systems [105]. These model systems include Giant Unilaminar Vesicles (GUVs), which may be composed of as few as two lipid species and a single type of cholesterol. Aside from providing platforms for focused investigations of processes mediated by biomembranes [59, 106], GUVs are of potential value in various pharmaceutical and technological applications, including biocompatible microcapsules for targeted drug delivery and gene therapy [28, 29], adjuvants for immunization [32, 33], signal carrying and enhancement in medical diagnostics and analytical biochemistry [34, 35], and biochemical reactors [107, 108, 109, 110].

Lipid bilayers readily change shape in response to shifting osmotic and thermal conditions and applied mechanical loads [111]. Efforts to model such shape changes date back somewhat more than four decades. Canham [21] emulated the methodology commonly applied in the bending analysis of beams to yield a simplified model capable of predicting the shapes available to a red blood cell. Treating a cell membrane as a surface, Canham [21] showed that the shapes it manifests in equilibrium emerge as a consequence of bending-energy minimization. Independently, Helfrich [22] attributed a surface bending-energy to lipid bilayers. In the models of Canham [21] and Helfrich [22], energy changes induced by relative molecular misalignment are incorporated through deviations of the principal curvatures (or alternatively, the mean and Gaussian curvatures) of the surface that serves as a proxy for the lipid bilayer. Specifically, according to Canham–Helfrich theory, the bending-energy density (that is, the energy per unit surface area) is given by

$$\psi = \tfrac{1}{2}\kappa(H - H_\circ)^2 + \bar{\kappa}K, \tag{2.1}$$

where H and K are the mean and Gaussian curvatures, respectively, and $H_\circ$ is the spontaneous mean curvature, which embodies the curvature of the bilayer in its natural state. In (2.1), changes of H and K are respectively penalized by bending moduli κ and $\bar{\kappa}$, known, respectively, as the splay (or ordinary) and saddle-splay (or Gaussian) moduli. As the brothers Cosserat [112] noted in their work on elastic surfaces, Germain [113] previously derived a energy density quadratic in the mean and Gaussian curvatures equivalent to (2.1) and the particular case corresponding to zero spontaneous curvature ($H_\circ = 0$) was obtained by Poisson [114]. See also the historical remarks of Nitsche [115].

The Canham–Helfrich energy is perhaps the simplest model believed suitable to situations where the shape of the lipid bilayer is dominated by bending and the radius of curvature of the lipid bilayer is much larger than its thickness. It can nevertheless be argued that (2.1) neglects energetic contributions associated with changes of local area or thickness and merely considers the lipid bilayer as a two-dimensional fluid surface that resists curvature deviations. Moreover, the Canham–Helfrich theory does not allow for changes in overall area. This constraint is imposed by adding a term proportional to the area of the surface that models the lipid bilayer to the net bending-energy determined by integrating (2.1) over that surface. However, as is clear from the discussion of the global and local area preservation provided by Steigmann et al. [116], this approach does not rule out the local area changes. Importantly, local area or thickness changes can occur in the vicinity of phase interfaces in multi-component lipid bilayers or heterogeneities such as protein molecules [117].

In contrast to an elastic shell, a lipid bilayer in the liquid phase does not have the ability to resist in-plane shear forces. This is because the lipid molecules may move freely within a lipid bilayer. Due to the absence of preferred directionality tangent to their surfaces in the liquid phase, lipid bilayers also exhibit in-plane isotropy.

Bearing in mind that the general theory of elastic shells allows for a broad range of possible material symmetries, any shell-like model for a lipid bilayer should be consistent with the observed in-plane fluidity and isotropy. Working in the context of modern shell theory, Jenkins [61] derived the general equations governing the mechanical equilibrium for a shell with material symmetry consistent with that of a lipid bilayer. Steigmann [62] subsequently reconsidered the mechanical modeling of fluid films with bending elasticity from a fundamental perspective. By treating the lipid bilayer as a two-dimensional (inviscid) fluid and choosing the full set of two-dimensional unimodular transformations as the appropriate material symmetry group, Steigmann [62] obtained a general energy density depending not only on the mean and Gaussian curvatures H and K but also on the areal stretch J. The areal stretch J represents local expansion/contraction within the tangent plane of the bilayer. Since a lipid bilayer shows no resistance to in-plane shear forces, but rather only to the local area changes, the areal stretch J is the sole kinematical ingredient needed to reckon in-plane deformation of the lipid bilayer. A new free-energy density for biomembranes, based on treating the lipid bilayer as a three-dimensional body rather than a two-dimensional surface, was proposed by Zurlo [63] and Deseri et al. [64]. An important feature of the formulation of these authors involves the introduction of a symmetry group that describes in-plane fluidity and isotropy at the level of the bulk, three-dimensional, material. However, a proof of the corresponding representation theorem was not provided. Additionally, the analysis of Zurlo [63] and Deseri et al. [64] is based on considering a flat reference configuration, which means that spontaneous curvature is tacitly assumed to vanish. Following a dimension reduction from a three-dimensional shell-like structure to a two-dimensional material surface, Zurlo [63] and Deseri et al. [64] obtained the superficial energy density per unit area of the reference surface.

Several explanations for the existence of spontaneous curvature have been reported in the literature. Spontaneous curvature is believed to be a measure of the extent to which the upper and lower leaflets of the lipid bilayer are asymmetric [23]. Asymmetry may arise due to differences between the molecular compositions of the leaflets, different properties of the aqueous solutions adjacent to the sides of the lipid bilayer [24], or interactions with a cytoskeleton (for a review see [1]). For instance, the presence of molecules with different headgroup or tailgroup conformations can lead to spontaneous curvature [1]. Asymmetry between the upper and lower leaflets of a bilayer can also be caused by helix insertion, scaffolding, transmembrane proteins, and clathrin coating [1, 25, 26]. Importantly, the presence of different species on a lipid bilayer is not generally sufficient to generate non-zero spontaneous curvature. In fact, spontaneous curvature appears to arise only when the flip-flop diffusion of unlike molecules between two leaflets is very slow compared to other time scales underlying shape changes. Numerical models of vesicles that incorporate spontaneous curvature reveal novel predictions of equilibrium shapes that appear to agree more closely with experimental observations [27, 118, 119, 120] than otherwise.

In the present paper, continuum mechanical tools are used to study the deformation, material symmetry, and energy density of a lipid bilayer with spontaneous curvature. Attention is restricted to lipid bilayers in the liquid phase. Inspired from Zurlo [63] and Deseri et al. [64], these thin structural elements are treated as three-dimensional bodies rather than material surfaces. Specifically, the formulation encompasses bending, in-plane stretching, and thickening/thinning of the bilayer. It also enables characterizations of leaflet coherency and area compatibility; whereas leaflet coherency concerns the local coupling or sliding of upper and lower leaflets, area compatibility concerns the integrity of closed lipid bilayers (i.e., vesicles). After discussing geometry and kinematics, constitutive behavior is considered. Treating the lipid bilayer as a three-dimensional body leads not only to a more precise understanding of the deformation of lipid bilayers but also affords insight regarding the material symmetry of lipid bilayers from a bulk material perspective. In particular, stipulating that the lipid bilayer is hyperelastic and invoking suitable material symmetry requirements leads to a representation for the energy density of a lipid bilayer. In addition, the impact of imposing the notion of incompressibility is considered. Finally, dimension reduction is used to derive an areal (two-dimensional) energy density from the three-dimensional energy density. As such, it includes the Canham–Helfrich energy density as a particular case. More broadly, however, it incorporates possible asymmetry and incoherency of the leaflets.

2.4 Geometry and kinematics

2.4.1 Basic considerations

Consider a lipid bilayer, either closed or open, represented by a three-dimensional body B (Figure 1). Suppose that the lipid bilayer is in its spontaneous (natural) state. Assume that the thickness of the bilayer in that state is uniform. Allow, however, for the possibility that the upper and lower leaflets may have different, but constant, thicknesses $h_\circ^+$ and $h_\circ^-$, respectively, in which case the thickness of the bilayer in its spontaneous state is simply $h_\circ^+ + h_\circ^-$. It is useful to introduce a reference surface separating the leaflets. This surface is referred to as the *midsurface* and is denoted by $S_\circ$. The unit normal vector on $S_\circ$, directed outward from the region enclosed by the vesicle, is denoted by $\mathbb{m}$ (Figure 1). The curvature tensor of the midsurface $S_\circ$ is denoted by $\mathbb{L}_\circ$, as defined in (2.179),[1] and is referred to as the spontaneous curvature tensor. Furthermore, $H_\circ$ and $K_\circ$ denote the corresponding spontaneous mean and Gaussian curvatures, as defined in (2.180). It is assumed that $S_\circ$ does not intersect itself. Additionally, $h_\circ^+$ and $h_\circ^-$ are assumed to be sufficiently small relative to the radius of curvature of $S_\circ$ to ensure that the inner and outer surfaces of lipid bilayer S^{i} and S^{o} do not fold back on themselves. A generic material point $\mathbf{X}$ located on a material surface $S_{\xi_\circ}$ in B can then be uniquely described using its projection $\widehat{\mathbf{X}}$ onto $S_\circ$ and a local coordinate $\xi_\circ \in [-h_\circ^-, h_\circ^+]$ that reckons the normal distance between $\mathbf{X}$ and $\widehat{\mathbf{X}}$; specifically,

$$\mathbf{X} = \widehat{\mathbf{X}} + \xi_\circ \mathbb{m}(\widehat{\mathbf{X}}) = \widetilde{\mathbf{X}}(\widehat{\mathbf{X}}, \xi_\circ). \tag{2.2}$$

Consider a deformation $\boldsymbol{\chi}$ that maps the lipid bilayer in its spontaneous state into the observed space. Under $\boldsymbol{\chi}$, the reference placement of the body B, midsurface $S_\circ$, and the normal $\mathbb{m}$ to $S_\circ$ map to the observed placement $\mathcal{B}$, midsurface $\mathcal{S}_\circ$, and unit normal $\mathbb{n}$ to $\mathcal{S}_\circ$, respectively (Figure 1). The curvature tensor of the surface $\mathcal{S}_\circ$

---

[1] To streamline the presentation, the precise definitions of $\mathbb{L}_\circ$ and various other useful geometrical objects are relegated to Appendix 2.11.1.

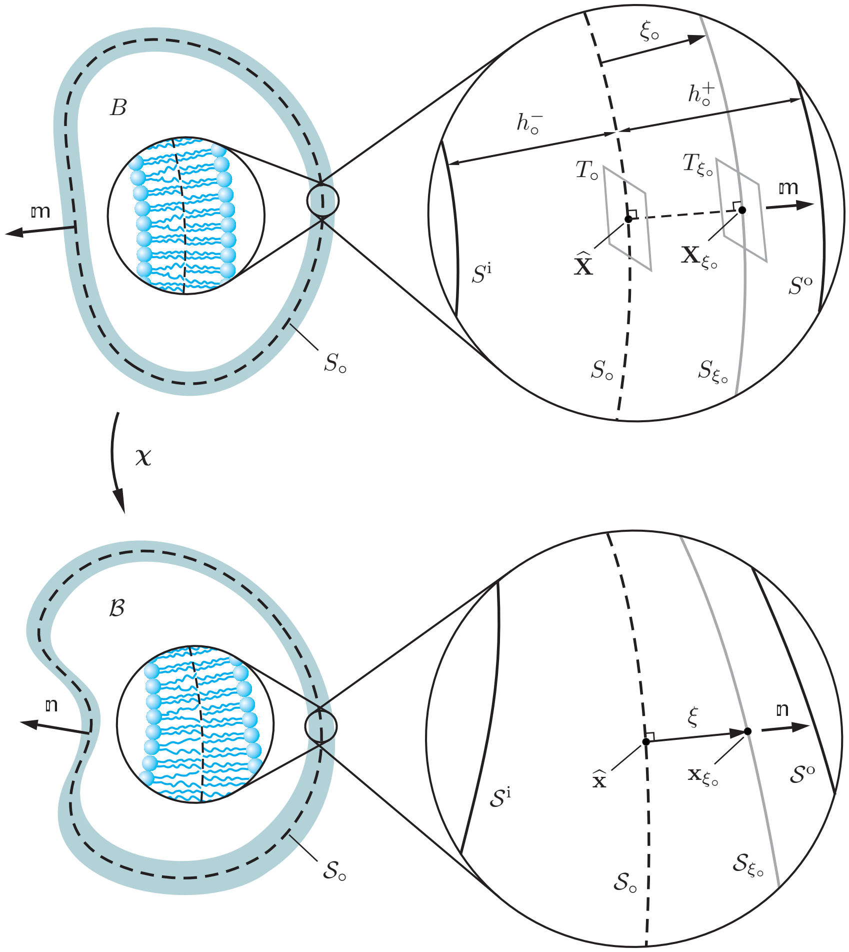

Figure 2–1: Two-dimensional schematic of a closed lipid bilayer in its spontaneous state and its deformation to a generic spatial configuration.

is $\mathbb{L}$, as defined in (2.179), with corresponding mean and Gaussian curvatures H and K, as defined in (2.181). In general, the thickness of the deformed bilayer may be nonuniform. As is customary, it is assumed that the deformation $\boldsymbol{\chi}$ is such that the images $\mathcal{S}_\circ$, $\mathcal{S}^{\mathrm{i}}$, and $\mathcal{S}^{\mathrm{o}}$ of $S_\circ$, S^{i}, and S^{o} (see Figure 1) do not fold back on themselves. Hence, there is, for each $\mathbf{x}$ in $\mathcal{B}$, a unique $\mathbf{X}$ in B such that $\mathbf{x} = \boldsymbol{\chi}(\mathbf{X})$. In view of

(2.2), the spatial point $\mathbf{x}$ can be described as

$$\mathbf{x} = \boldsymbol{\chi}(\mathbf{X}) = \widetilde{\mathbf{x}}(\widehat{\mathbf{X}}, \xi_\circ), \qquad \widehat{\mathbf{X}} \in S_\circ,\ \xi_\circ \in [-h_\circ^-, h_\circ^+]. \tag{2.3}$$

The deformation gradient describing the local distortion of B is given by

$$\mathbf{F} = \nabla \boldsymbol{\chi}(\mathbf{X}), \tag{2.4}$$

where ∇ indicates the gradient in the reference space.

Consider a material point $\mathbf{X}_{\xi_\circ}$ on $S_{\xi_\circ}$ along with a generic point $\mathbf{X}$ located at a normal elevation z from $S_{\xi_\circ}$. Since the tangent planes $T_\circ$ and $T_{\xi_\circ}$ at the points $\widehat{\mathbf{X}}$ and $\mathbf{X}_{\xi_\circ}$ are parallel (see Figure 1), the unit normal $\mathbb{m}$ on $S_\circ$ is also normal to $S_{\xi_\circ}$ and, hence, can also be viewed as a function defined on $S_{\xi_\circ}$. Thus, bearing in mind that $\mathbf{X}$ coincides with $\mathbf{X}_{\xi_\circ}$ for $z = 0$, $\mathbf{X}$ can be expressed as $\mathbf{X} = \mathbf{X}_{\xi_\circ} + z\mathbb{m}(\mathbf{X}_{\xi_\circ})$. The spatial point $\mathbf{x}$ corresponding to $\mathbf{X}$, can thus also be described via

$$\mathbf{x} = \boldsymbol{\chi}(\mathbf{X}) = \bar{\mathbf{x}}(\mathbf{X}_{\xi_\circ}, z), \tag{2.5}$$

where $\mathbf{X}_{\xi_\circ} \in S_{\xi_\circ}$ and $z \in [(-h_\circ^- - \xi_\circ), (h_\circ^+ - \xi_\circ)]$. In view of (2.5), the deformation gradient $\mathbf{F}$ for a material point located on $S_{\xi_\circ}$ can be expressed as

$$\mathbf{F} = \nabla \mathbf{x}|_{z=0} = \left(\nabla_{S_{\xi_\circ}} \bar{\mathbf{x}} + \frac{\partial \bar{\mathbf{x}}}{\partial z} \otimes \mathbb{m}\right)\Big|_{z=0}, \tag{2.6}$$

where $\nabla_{S_{\xi_\circ}}$ indicates the surface gradient on $S_{\xi_\circ}$, defined as

$$\nabla_{S_{\xi_\circ}} \bar{\mathbf{x}}|_{z=0} = (\nabla \bar{\mathbf{x}}|_{z=0})\ \mathbb{P}_{\mathbb{m}}, \tag{2.7}$$

where $\mathbb{P}_{\mathbb{m}} = \mathbf{1} - \mathbb{m} \otimes \mathbb{m}$ is the projection tensor onto the tangent plane $T_\circ$ (or, equivalently, $T_{\xi_\circ}$).

Consider a material line element $\mathrm{d}\mathbf{X}_{\xi_\circ}$ tangent to the surface $S_{\xi_\circ}$ and the corresponding line element $\mathrm{d}\mathbf{x}_{\xi_\circ}$ tangent to the spatial image $\mathcal{S}_{\xi_\circ}$ of $S_{\xi_\circ}$. According to the description of $\mathbf{x}$ in (2.3),

$$
\begin{aligned}
\mathrm{d}\mathbf{x}_{\xi_\circ} &= \mathrm{d}\widetilde{\mathbf{x}}(\widehat{\mathbf{X}}, \xi_\circ)|_{\xi_\circ=\text{constant}} \\
&= (\nabla \widetilde{\mathbf{x}}(\widehat{\mathbf{X}}, \xi_\circ)|_{\xi_\circ=\text{constant}})\, \mathrm{d}\widehat{\mathbf{X}} \\
&= (\nabla \widetilde{\mathbf{x}}(\widehat{\mathbf{X}}, \xi_\circ)|_{\xi_\circ=\text{constant}})\mathbb{P}_{\mathbb{m}}\, \mathrm{d}\widehat{\mathbf{X}} \\
&= (\nabla_{S_\circ} \widetilde{\mathbf{x}}(\widehat{\mathbf{X}}, \xi_\circ)|_{\xi_\circ=\text{constant}})\, \mathrm{d}\widehat{\mathbf{X}},
\end{aligned} \tag{2.8}
$$

where $\nabla_{S_\circ}$ indicates the surface gradient on $S_\circ$, as defined by

$$
\nabla_{S_\circ} \widetilde{\mathbf{x}}(\widehat{\mathbf{X}}, \xi_\circ)|_{\xi_\circ=\text{constant}} = (\nabla \widetilde{\mathbf{x}}(\widehat{\mathbf{X}}, \xi_\circ)|_{\xi_\circ=\text{constant}})\mathbb{P}_{\mathbb{m}}. \tag{2.9}
$$

Similarly, for the description given in (2.5) we have

$$
\begin{aligned}
\mathrm{d}\mathbf{x}_{\xi_\circ} &= (\nabla \bar{\mathbf{x}}(\mathbf{X}_{\xi_\circ}, z))|_{z=0} \mathrm{d}\mathbf{X}_{\xi_\circ} \\
&= (\nabla \bar{\mathbf{x}}(\mathbf{X}_{\xi_\circ}, z))|_{z=0} \mathbb{P}_{\mathrm{m}} \mathrm{d}\mathbf{X}_{\xi_\circ} \\
&= (\nabla_{S_{\xi_\circ}} \bar{\mathbf{x}}(\mathbf{X}_{\xi_\circ}, z)|_{z=0}) \mathrm{d}\mathbf{X}_{\xi_\circ}.
\end{aligned} \tag{2.10}
$$

Comparing (2.8) and (2.10) yields the identity

$$
(\nabla_{S_{\xi_\circ}} \bar{\mathbf{x}}|_{z=0}) \mathrm{d}\mathbf{X}_{\xi_\circ} = (\nabla_{S_\circ} \widetilde{\mathbf{x}}|_{\xi_\circ=\text{constant}}) \mathrm{d}\widehat{\mathbf{X}}. \tag{2.11}
$$

Using (2.2) and elementary properties of the curvature tensor $\mathbb{L}_\circ$ (see (2.179)) it is easy to arrive at the identity

$$\begin{aligned} \mathrm{d}\mathbf{X}_{\xi_\circ} &= d\widehat{\mathbf{X}} + \xi_\circ \mathrm{d}\mathbbm{m} \\ &= \mathrm{d}\widehat{\mathbf{X}} - \xi_\circ \mathbb{L}_\circ \mathrm{d}\widehat{\mathbf{X}}, \end{aligned} \tag{2.12}$$

which, on introducing

$$\mathbb{S}_\circ = \mathbb{P}_{\mathbbm{m}} - \xi_\circ \mathbb{L}_\circ, \tag{2.13}$$

can alternatively be written as

$$\mathrm{d}\mathbf{X}_{\xi_\circ} = \mathbb{S}_\circ \mathrm{d}\widehat{\mathbf{X}}. \tag{2.14}$$

Notice that $\mathrm{d}\widehat{\mathbf{X}}$ is a tangent line element on $S_\circ$ at the point $\widehat{\mathbf{X}}$. Since the tangent planes $T_\circ$ and $T_{\xi_\circ}$ are parallel, $\mathrm{d}\mathbf{X}_{\xi_\circ}$ and $\mathrm{d}\widehat{\mathbf{X}}$ can be viewed as elements of the same tangent space, say $T_\circ$.

The tensor $\mathbb{S}_\circ$ defined in (2.13) is fully tangential (see Appendix 2.11.1 for the definition of such a tensor) and, thus, can be viewed as a mapping from $T_\circ$ to $T_\circ$. By (2.13), the second principal invariant $I_2(\mathbb{S}_\circ)$ of $\mathbb{S}_\circ$ can be expressed as

$$\begin{aligned} I_2(\mathbb{S}_\circ) &= \tfrac{1}{2}[(I_1(\mathbb{S}_\circ))^2 - I_1(\mathbb{S}_\circ^2)] \\ &= 1 - 2\xi_\circ H_\circ + \xi_\circ^2 K_\circ. \end{aligned} \tag{2.15}$$

Let $c_{\circ 1}$ and $c_{\circ 2}$ denote the principal curvatures of $S_\circ$, so that $H_\circ = \frac{1}{2}(c_{\circ 1} + c_{\circ 2})$ and $K_\circ = c_{\circ 1} c_{\circ 2}$. Then, by (2.15),

$$I_2(\mathbb{S}_\circ) = (1 - \xi_\circ c_{\circ 1})(1 - \xi_\circ c_{\circ 2}). \tag{2.16}$$

Granted the assumption (imposed to ensure avoiding folding back of outer and inner surfaces S^{o} and S^{i} on themselves) that the thicknesses $h_\circ^+$ and $h_\circ^-$ of upper and lower leaflets are very small relative to the radius of curvature of $S_\circ$, $\xi_\circ$ must satisfy

$$\xi_\circ c_{\circ\alpha} \neq 1, \qquad \alpha = 1, 2, \tag{2.17}$$

and (2.16) implies that $I_2(\mathbb{S}_\circ) \neq 0$. Thus, as described in Appendix 2.11.2, $\mathbb{S}_\circ$ has a pseudoinverse $\mathbb{Q}_\circ$ given by

$$\mathbb{Q}_\circ = (I_2(\mathbb{S}_\circ))^{-1}(I_1(\mathbb{S}_\circ)\mathbb{P}_{\mathbb{m}} - \mathbb{S}_\circ), \tag{2.18}$$

where

$$\begin{aligned} I_1(\mathbb{S}_\circ) &= \mathrm{tr}(\mathbb{P}_{\mathbb{m}} - \xi_\circ \mathbb{L}_\circ) \\ &= 2(1 - \xi_\circ H_\circ) \end{aligned} \tag{2.19}$$

is the first principal invariant of $\mathbb{S}_\circ$, and, since, as noted above, $\mathrm{d}\mathbf{X}_{\xi_\circ}$ and $\mathrm{d}\widehat{\mathbf{X}}$ can be viewed as elements of the same tangent space, (2.14) is equivalent to

$$\mathrm{d}\widehat{\mathbf{X}} = \mathbb{Q}_\circ \mathrm{d}\mathbf{X}_{\xi_\circ}. \tag{2.20}$$

As regards $\mathbb{Q}_\circ$, it is convenient to introduce

$$\gamma_\circ(\xi_\circ) = I_2(\mathbb{S}_\circ) \tag{2.21}$$

and, thus, using (2.13), (2.15), and (2.19) in the representation (2.18) yields

$$\mathbb{Q}_\circ = (\gamma_\circ(\xi_\circ))^{-1}(\mathbb{P}_{\mathbb{m}} - 2\xi_\circ H_\circ \mathbb{P}_{\mathbb{m}} + \xi_\circ \mathbb{L}_\circ). \tag{2.22}$$

Bearing in mind (2.14), (2.11) can be expressed as

$$(\nabla_{S_{\xi_\circ}}\bar{\mathbf{x}}|_{z=0})\mathrm{d}\mathbf{X}_{\xi_\circ} = (\nabla_{S_\circ}\widetilde{\mathbf{x}}|_{\xi_\circ=\text{constant}})\mathbb{Q}_\circ\mathrm{d}\mathbf{X}_{\xi_\circ}. \tag{2.23}$$

Since (2.23) holds for an arbitrary line element $\mathrm{d}\mathbf{X}_{\xi_\circ}$, we conclude that

$$\nabla_{S_{\xi_\circ}}\bar{\mathbf{x}}|_{z=0} = (\nabla_{S_\circ}\widetilde{\mathbf{x}}|_{\xi_\circ=\text{constant}})\mathbb{Q}_\circ. \tag{2.24}$$

The second term on the far right-hand side of (2.6) includes the normal derivative $(\nabla\mathbf{x})\mathbb{m}$, as is clear from (2.176). Notice that, according to the descriptions $\mathbf{x} = \widetilde{\mathbf{x}}(\widehat{\mathbf{X}}, \xi_\circ)$ and $\mathbf{x} = \bar{\mathbf{x}}(\mathbf{X}_{\xi_\circ}, z)$, changes of $\mathbf{x}$ in the $\mathbb{m}$ direction are controlled by $\xi_\circ$ and z, respectively. Thus,

$$\begin{aligned}(\nabla\mathbf{x})\mathbb{m} &= \frac{\partial\widetilde{\mathbf{x}}}{\partial\xi_\circ}\\ &= \frac{\partial\bar{\mathbf{x}}}{\partial z},\end{aligned} \tag{2.25}$$

which, in combination with (2.6), implies that the deformation gradient $\mathbf{F}$ may be written as

$$\mathbf{F} = (\nabla_{S_\circ}\widetilde{\mathbf{x}})\mathbb{Q}_\circ + \frac{\partial\widetilde{\mathbf{x}}}{\partial\xi_\circ}\otimes\mathbb{m}. \tag{2.26}$$

2.4.2 Orientation of phospholipid molecules at the midsurface

Compatible with physical observations of amphiphilic fluid films, we assume that, due to interatomic interactions and packing requirements, the phospholipid molecules comprising the bilayer tend to remain perpendicular to the midsurface $S_\circ$. This constraint is embodied by the kinematical requirement that: *during a deformation, straight line elements perpendicular to* $S_\circ$ *remain straight and perpendicular to*

$\mathcal{S}_\circ$ (Figure 1). This assumption resembles Kirchhoff's [121] hypothesis in theories of thin plates and shells. However, at variance with that hypothesis, the kinematical constraint imposed here does not restrict the through-thickness deformation of the lipid bilayer.

To provide an analytical characterization of our constraint, it is useful to represent a generic spatial point $\mathbf{x}$ in the deformed body in the form $\mathbf{x} = \widehat{\mathbf{x}} + \xi \mathbb{n}(\widehat{\mathbf{x}})$, where ξ indicates normal distance of $\mathbf{x}$ from $\mathcal{S}_\circ$. Since $\mathbf{x}$ is the image of $\mathbf{X}$ in the observed space, and also $\mathbf{X}$ can be described by $\widehat{\mathbf{X}}$ and $\xi_\circ$ through (2.2), the out-of-plane coordinate ξ in the body can be expressed in the form

$$\xi = \widetilde{\xi}(\widehat{\mathbf{X}}, \xi_\circ). \tag{2.27}$$

Moreover, as a result of the constraint, the projection $\widehat{\mathbf{x}}$ of $\mathbf{x}$ onto $\mathcal{S}_\circ$ coincides with the placement of the spatial image of the material point $\widehat{\mathbf{X}}$ on $S_\circ$ (Figure 1). Consequently, bearing in mind (2.26) and (2.27), it transpires that

$$\mathbf{F} = (\nabla_{S_\circ}(\widehat{\mathbf{x}} + \xi \mathbb{n}))\mathbb{Q}_\circ + \frac{\partial(\widehat{\mathbf{x}} + \xi \mathbb{n})}{\partial \xi_\circ} \otimes \mathbb{m}, \tag{2.28}$$

where $\nabla_{S_\circ}(\widehat{\mathbf{x}} + \xi \mathbb{n})$ and $\partial(\widehat{\mathbf{x}} + \xi \mathbb{n})/\partial \xi_\circ$ are given by

$$\nabla_{S_\circ}(\widehat{\mathbf{x}} + \xi \mathbb{n}) = \nabla_{S_\circ}\widehat{\mathbf{x}} + \xi \nabla_{S_\circ}\mathbb{n} + \mathbb{n} \otimes \nabla_{S_\circ}\xi \tag{2.29}$$

and

$$\frac{\partial(\widehat{\mathbf{x}} + \xi \mathbb{n})}{\partial \xi_\circ} = \frac{\partial \xi}{\partial \xi_\circ}\mathbb{n}, \tag{2.30}$$

respectively.

It is now convenient to introduce some shorthand notation. Specifically, given a quantity g dependent either explicitly or implicitly on $\xi_\circ$, let

$$g|_\circ := g|_{\xi_\circ=0} \tag{2.31}$$

denote its value at the referential midsurface $S_\circ$. With this convention in mind, and according to the definition of surface gradient of a vector field provided in Appendix 2.11.1, we have

$$\begin{aligned}\nabla_{S_\circ}\widehat{\mathbf{x}} &= (\nabla\mathbf{x})|_\circ\mathbb{P}_{\mathtt{m}}\\ &= \mathbf{F}|_\circ\mathbb{P}_{\mathtt{m}}\\ &=: \mathbb{F}_\circ,\end{aligned} \tag{2.32}$$

where $\mathbb{F}_\circ$, which designates the superficial deformation gradient on the midsurface $S_\circ$, maps material line elements on $S_\circ$ to spatial line elements on $\mathcal{S}_\circ$.

Having introduced $\mathbb{F}_\circ$, the areal stretch

$$J := I_2(\mathbb{F}_\circ) \tag{2.33}$$

represents any changes in the area of the midsurface that may accompany deformation.

In general, $\mathtt{n}$ is a superficial field defined on $\mathcal{S}_\circ$—that is, $\mathtt{n}$ can be expressed as a function of points $\widehat{\mathbf{x}}$ on $\mathcal{S}_\circ$. However, $\mathtt{n}$ may be extended to all of $\mathcal{B}$. In particular, consider a normally constant extension $\mathtt{n}^e$ of $\mathtt{n}$. Then, in view of developments presented in Appendix 2.11.1,

$$\begin{aligned}\nabla_{S_\circ}\mathbb{n} &= (\nabla\mathbb{n}^e(\boldsymbol{\chi}(\mathbf{X})))|_\circ\mathbb{P}_{\mathbb{m}}\\ &= (\nabla_{\mathbf{x}}\mathbb{n}^e(\mathbf{x}))|_{\xi=0}\nabla\mathbf{x}|_\circ\mathbb{P}_{\mathbb{m}},\end{aligned} \tag{2.34}$$

where $\nabla_{\mathbf{x}}$ indicates the spatial gradient. Next, using properties of the surface gradient (see $(2.175)_1$), we have

$$\nabla_{\mathbf{x}}\mathbb{n}^e(\mathbf{x}) = \nabla_{\mathcal{S}_{\xi_\circ}}\mathbb{n}^e(\mathbf{x}) + \frac{\partial\mathbb{n}^e(\mathbf{x})}{\partial\xi}\otimes\mathbb{n}^e(\mathbf{x}), \tag{2.35}$$

and, since $\mathbb{n}^e$ does not change in the ξ-direction, we arrive at the identification

$$\begin{aligned}(\nabla_{\mathbf{x}}\mathbb{n}^e(\mathbf{x}))|_{\xi=0} &= (\nabla_{\mathcal{S}_{\xi_\circ}}\mathbb{n}^e(\mathbf{x}))|_{\xi=0}\\ &= \nabla_{\mathcal{S}_\circ}\mathbb{n}\\ &= -\mathbb{L}.\end{aligned} \tag{2.36}$$

In view of (2.32) and (2.36), $\nabla_{S_\circ}\mathbb{n}$ as defined by (2.34), can be expressed as

$$\begin{aligned}\nabla_{S_\circ}\mathbb{n} &= -\mathbb{L}(\nabla\mathbf{x})|_\circ\mathbb{P}_{\mathbb{m}}\\ &= -\mathbb{L}\mathbb{F}_\circ,\end{aligned} \tag{2.37}$$

which, in combination with (2.28), yields a useful alternative representation,

$$\mathbf{F} = (\mathbb{F}_\circ - \xi\mathbb{L}\mathbb{F}_\circ + \mathbb{n}\otimes\nabla_{S_\circ}\xi)\mathbb{Q}_\circ + \frac{\partial\xi}{\partial\xi_\circ}\mathbb{n}\otimes\mathbb{m}, \tag{2.38}$$

for the deformation gradient.

Notice that, for a trivial deformation (that is, a deformation for which $\mathbf{F} = \mathbf{1}$ everywhere on B), $\mathbb{n}$, $\mathbb{L}$, $\mathbb{F}_\circ$, and ξ are given by $\mathbb{n} = \mathbb{m}$, $\mathbb{L} = \mathbb{L}_\circ$, $\mathbb{F}_\circ = \mathbb{P}_{\mathbb{m}}$, and $\xi = \xi_\circ$. Under these circumstances, bearing in mind (2.22), (2.38) specializes to

$$
\begin{aligned}
\mathbf{F} &= (\gamma_\circ(\xi_\circ))^{-1}(\mathbb{P}_{\mathbb{m}} - \xi_\circ\mathbb{L}_\circ)(\mathbb{P}_{\mathbb{m}} - 2\xi_\circ H_\circ \mathbb{P}_{\mathbb{m}} + \xi_\circ\mathbb{L}_\circ) \\
&\qquad + \mathbb{m} \otimes \mathbb{m} \\
&= (1 - 2\xi_\circ H_\circ + {\xi_\circ}^2 K_\circ)^{-1} \\
&\quad \times (\mathbb{P}_{\mathbb{m}} - 2\xi_\circ H_\circ \mathbb{P}_{\mathbb{m}} + 2\xi_\circ^2 H_\circ \mathbb{L}_\circ - \xi_\circ^2 \mathbb{L}_\circ^2) + \mathbb{m} \otimes \mathbb{m}.
\end{aligned}
\tag{2.39}
$$

Further, on applying the Cayley–Hamilton theorem (see Appendix 2.11.2) to the spontaneous curvature tensor $\mathbb{L}_\circ$, (2.39) becomes

$$
\mathbf{F} = \mathbb{P}_{\mathbb{m}} + \mathbb{m} \otimes \mathbb{m} = \mathbf{1}, \tag{2.40}
$$

which is consistent with what must be true under a trivial deformation. Moreover, it can be immediately checked that (2.38) reduces to a result of Zurlo [63] and Deseri et al. [64] when the spontaneous curvature vanishes (in which case, (2.18) reduces to $\mathbb{Q}_\circ = \mathbb{P}_{\mathbb{m}}$).

2.4.3 Transformation of normal vectors

If the thickness of the lipid bilayer in the spatial configuration is not uniform, the unit normal vectors of its outer and inner surfaces $\mathcal{S}^{\mathrm{o}}$ and $\mathcal{S}^{\mathrm{i}}$ may differ, respectively, from the midsurface unit normal $\mathbb{n}$ and its negative $-\mathbb{n}$. In this case, let the unit normal vectors of inner and outer surfaces of bilayer in the reference and the spatial configuration be denoted by $\mathbf{m}^{\mathrm{i}} = -\mathbb{m}$, $\mathbf{m}^{\mathrm{o}} = \mathbb{m}$, and $\mathbf{n}^{\mathrm{i}}$, $\mathbf{n}^{\mathrm{o}}$, respectively. Whereas

$\mathbf{n}^{\mathrm{i}}$ and $\mathbf{n}^{\mathrm{o}}$ must transform according to

$$\mathbf{n} = \frac{\mathbf{F}^{-\top}\mathbf{m}}{|\mathbf{F}^{-\top}\mathbf{m}|}\bigg|_{\xi_\circ = h_\circ^\pm}, \tag{2.41}$$

wherein $\mathbf{n}$ and $\mathbf{m}$ take the values consistent with

$$(\mathbf{n}, \mathbf{m}) = (\mathbf{n}^{\mathrm{i}}, \mathbf{m}^{\mathrm{i}}) \quad \text{or} \quad (\mathbf{n}, \mathbf{m}) = (\mathbf{n}^{\mathrm{o}}, \mathbf{m}^{\mathrm{o}}), \tag{2.42}$$

$\mathbb{n}$ transforms according to

$$\mathbb{n} = \frac{\mathbb{F}_\circ \mathbb{e}_\circ^1 \times \mathbb{F}_\circ \mathbb{e}_\circ^2}{|\mathbb{F}_\circ \mathbb{e}_\circ^1 \times \mathbb{F}_\circ \mathbb{e}_\circ^2|}, \tag{2.43}$$

for any two linearly independent tangent vectors $\mathbb{e}_\circ^1$ and $\mathbb{e}_\circ^2$ on the midsurface $S_\circ$. Substituting (2.38) into (2.41) and invoking (2.43) shows that $\mathbf{n}$ and $\mathbb{n}$ differ unless

$$\nabla_{S_\circ}\xi|_{\xi_\circ = h_\circ^\pm} \longrightarrow 0, \tag{2.44}$$

meaning that any change of bilayer thickness on the spatial midsurface $\mathcal{S}_\circ$ must be negligibly small. However, since this need not be the case, it is important to maintain a distinction between $\mathbb{n}$ and $\mathbf{n}$. Existing two-dimensional approaches based on modeling the lipid bilayer as a material surface, as exemplified by the theory of Steigmann [62], work solely with $\mathbb{n}$.

2.4.4 Coherency of leaflets

The extent to which the upper and lower leaflets are coherent across the midsurface $S_\circ$ may influence the mechanical response of of a lipid bilayer [122, 123, 124, 23]. When lipid molecules of opposite leaflets are interdigitated, their connection is very nearly coherent [38]. If this is not the case, the leaflets may slide relative to one another. To describe leaflet coherency, consider the Hadamard compatibility condition at $S_\circ$. Let $\mathbf{F}^+$ and $\mathbf{F}^-$ denote the respective limiting values of the deformation gradient at $S_\circ$ from the outer and inner sides of the bilayer. To facilitate the calculation, we will introduce some notation. Given a quantity g with potentially different limits on either side of the referential midsurface $S_\circ$, define its jump $\llbracket g \rrbracket$ and average $\langle g \rangle$ at $S_\circ$ by

$$\llbracket g \rrbracket := g^+ - g^-, \quad \langle g \rangle := \tfrac{1}{2}(g^+ + g^-). \tag{2.45}$$

In view of (2.38), the jump $\llbracket \mathbf{F} \rrbracket$ of the deformation gradient at the midsurface (i.e., at $\xi_\circ = 0$), is given by

$$\llbracket \mathbf{F} \rrbracket = \llbracket \mathbb{F}_\circ \rrbracket + \left\llbracket \frac{\partial \xi}{\partial \xi_\circ} \right\rrbracket \Big|_\circ \mathbb{n} \otimes \mathbb{m}. \tag{2.46}$$

For $\llbracket \mathbb{F}_\circ \rrbracket = \mathbf{0}$, (2.46) represents the Hadamard condition for a coherent surface. This condition corresponds to the local interdigitation or coupling of the leaflets. However, for $\llbracket \mathbb{F}_\circ \rrbracket \neq 0$, the midsurface is an incoherent interface across which the leaflets may slide relative to one another. In general, $\llbracket \partial \xi / \partial \xi_\circ \rrbracket|_\circ$ need not vanish—as occurs if the lipid bilayer is not symmetric and its constitutive properties are discontinuous across the midsurface $S_\circ$. As mentioned earlier, a disparity between the molecular compositions of the leaflets is a potential reason for the existence of spontaneous curvature. For lipid bilayers with such induced spontaneous curvature, the jump $\llbracket \partial \xi / \partial \xi_\circ \rrbracket|_\circ$ therefore does not generally vanish.

2.4.5 Area compatibility

For closed lipid bilayers, an additional global compatibility condition becomes important. During the deformation of a vesicle, whether or not the leaflets are coherent, their bounding surfaces at the common interface (what is called here midsurface) must share the same area. Otherwise, the leaflets may loose their integrity. In view of the definition (2.33) of the areal stretch, this condition can be codified in the form

$$\int_{S_\circ} [\![J]\!] \, \mathrm{d}A_\circ = 0, \tag{2.47}$$

where, bearing in mind $(2.45)_1$, $[\![J]\!]$ denotes the jump of the areal stretch at the midsurface $S_\circ$ and $\mathrm{d}A_\circ$ represents the referential area element of $S_\circ$.

2.5 Energy densities

Any change of energy that accompanies a change in the shape of a lipid bilayer must be due to the displacement of neighboring phospholipid molecules. Various types of lipid molecules with different physical properties can be present in a lipid bilayer. As long as no phase separation occurs and, thus, the chemical energy remains fixed, any energy change can be attributed to purely mechanical phenomena. In this setting, a multi-component biomembrane can be viewed as an effectively homogenous body. For a single-component lipid bilayer, no such assumption is needed.

Molecular displacements are accompanied by changes in the amount of elastic energy stored within the lipid bilayer. This is modeled by introducing an energy density W (per unit referential volume) as a function $\hat{W}$ of the deformation gradient $\mathbf{F}$, so that the lipid bilayer is modeled as a hyperelastic material:

$$W = \hat{W}(\mathbf{F}). \tag{2.48}$$

As in the case of a conventional elastic body, we require that the energy density of a lipid bilayer has a local minimum at the spontaneous state:

$$\hat{W}(\mathbf{F}) \ \text{ has local minimum at } \mathbf{F} = \mathbf{1}. \tag{2.49}$$

Also, since the energy density of each material point may be additively scaled [125], we impose, without loss of generality, the normalization

$$\hat{W}(\mathbf{1}) = 0. \tag{2.50}$$

Zurlo [63] and Deseri et al. [64] studied the chemo-mechanical coupling of a lipid bilayer undergoing phase separation and elastic deformation. Under these circumstances, $\hat{W}$ would also be a function of species concentrations and, potentially, also their gradients, which would penalize the formation of phase interfaces on the bilayer.

Requiring the energy density in (2.48) to be frame-indifferent leads, in conventional fashion, to the conclusion that it may depend on the deformation gradient through at most the right Cauchy–Green tensor $\mathbf{C} = \mathbf{F}^{\top}\mathbf{F}$, whereby (2.48) is replaced by

$$W = \bar{W}(\mathbf{C}). \tag{2.51}$$

An important point concerning leaflet asymmetry should now be clarified. An asymmetric distribution of lipid molecules with different molecular shapes requires the shape of the lipid bilayer in its natural state to be curved [1]. This effect might be modeled by allowing for nontrivial spontaneous curvature $\mathbb{L}_{\circ}$. There is also considerable evidence pointing to marked differences between the chemical compositions of lipid molecules in the inner and outer leaflets of animal cells [126, 127, 128]. Observed differences in mechanical properties [127] might therefore be attributed to differences in molecular packing, chemical composition, or both. To encompass differences in the mechanical properties of the leaflets, it might be sufficient to allow the expression determining the energy density function $\bar{W}$ to be distinct in each leaflet.

2.6 Material symmetry

The constitutive relation (2.51), which holds for all hyperelastic materials, is very general. To incorporate the properties of a lipid bilayer, the response function $\bar{W}$ must obey certain requirements of material symmetry. Two distinguishing features of biomembranes are in-plane fluidity and in-plane isotropy. Specifically, experimental observations demonstrate unambiguously that phopholipid molecules on the surface of a lipid bilayer in the liquid phase can freely migrate. Additionally, there is no preferred direction in the tangent plane of its midsurface and therefore the lipid bilayer exhibits in-plane isotropy. In view of these observations, when modeled as three-dimensional, a lipid bilayer is like a transversely isotropic material with $\mathbb{m}$ being the axis of isotropy and $S_{\xi_\circ}$ being the surface of isotropy, where the range of $\xi_\circ$ covers the thickness of the lipid bilayer. Bearing this in mind, we next derive an appropriate representation theorem for an energy density which correctly incorporates both in-plane fluidity and transverse isotropy. To achieve this, it is necessary to determine a proper unimodular symmetry transformation $\mathbf{H}$ of the reference configuration which the leaves response of the body to deformation unchanged. As is customary, the set of all such symmetry transformations is designated by $\mathcal{G}$ and is referred to as the symmetry group.

2.6.1 Symmetry transformations

Let $\mathbf{H}$ be a a symmetry transformation. To encompass the transverse isotropy of the lipid bilayer, $\mathbf{H}$ should preserve the direction of any material line element parallel to $\mathbb{m}$. In addition, it is necessary to require that $\mathbf{H}$ preserve the length of any material line element parallel to $\mathbb{m}$. If $\mathbf{H}$ does not do so, the phospholipid molecules deform along the direction of the tail groups and, consequently, their physical characteristics will generally change. These two requirements simply imply that $\mathbf{H}$ should map any normal material line element to itself. Consistent with the in-plane fluidity of lipid bilayers, $\mathbf{H}$ should also map any material line element perpendicular to $\mathbb{m}$ to a material line element perpendicular to $\mathbb{m}$. Thus, given a unit normal vector $\mathbb{m}$, $\mathbf{H}$ should satisfy

$$\left.\begin{aligned} &\mathbf{H}\mathbb{m} = \mathbb{m}, \\ &\text{if } \ \mathbf{e}\cdot\mathbb{m} = 0, \quad \text{then } \ \mathbf{H}\mathbf{e}\cdot\mathbb{m} = 0, \\ &\det\mathbf{H} = 1. \end{aligned}\right\} \tag{2.52}$$

Under a symmetry transformation, the deformation gradient $\mathbf{F}$ becomes $\mathbf{FH}$ and, hence, the right Cauchy–Green tensor $\mathbf{C}$ becomes $\mathbf{H}^{\top}\mathbf{CH}$, while the energy measured by the response function $\bar{W}$ must be invariant:

$$\bar{W}(\mathbf{H}^{\top}\mathbf{CH}) = \bar{W}(\mathbf{C}). \tag{2.53}$$

As a first step toward determining a representation for the symmetry group $\mathcal{G}$ consistent with (2.52) and (2.53), choose two arbitrary linearly independent tangent vectors $\mathbb{e}_1$ and $\mathbb{e}_2$ satisfying $\mathbb{e}_1\cdot\mathbb{m} = \mathbb{e}_2\cdot\mathbb{m} = 0$ and, therefore, belonging to the tangent space $T_{\xi_\circ}$. Without loss of generality, $\mathbf{H}$ can be represented as

$$\mathbf{H} = \mathbb{e}_1\otimes\mathbf{f} + \mathbb{e}_2\otimes\mathbf{g} + \mathbb{m}\otimes\mathbf{h}, \tag{2.54}$$

with $\mathbf{f}$, $\mathbf{g}$, and $\mathbf{h}$ being linearly independent. Since $(\mathbb{e}_1\otimes\mathbf{f} + \mathbb{e}_2\otimes\mathbf{g} + \mathbb{m}\otimes\mathbf{h})\mathbb{m} = (\mathbf{f}\cdot\mathbb{m})\mathbb{e}_1 + (\mathbf{g}\cdot\mathbb{m})\mathbb{e}_2 + (\mathbf{h}\cdot\mathbb{m})\mathbb{m}$ and $\mathbb{e}_1$ and $\mathbb{e}_2$ are linearly independent tangent vectors, $(2.52)_1$ implies that $\mathbf{f}$ and $\mathbf{g}$ must obey

$$\mathbf{f} \cdot \mathbb{m} = \mathbf{g} \cdot \mathbb{m} = 0 \tag{2.55}$$

and, hence, must be tangent vectors and that $\mathbf{h}$ must obey

$$\mathbf{h} \cdot \mathbb{m} = 1. \tag{2.56}$$

Next, since $(\mathbb{e}_1 \otimes \mathbf{f} + \mathbb{e}_2 \otimes \mathbf{g} + \mathbb{m} \otimes \mathbf{h})\mathbf{e} = (\mathbf{f} \cdot \mathbf{e})\mathbb{e}_1 + (\mathbf{g} \cdot \mathbf{e})\mathbb{e}_2 + (\mathbf{h} \cdot \mathbf{e})\mathbb{m}$ for any tangent vector $\mathbf{e}$, on defining $\alpha_1 = \mathbf{f} \cdot \mathbf{e}$ and $\alpha_2 = \mathbf{g} \cdot \mathbf{e}$, it follows that

$$\mathbf{He} = \alpha_1 \mathbb{e}_1 + \alpha_2 \mathbb{e}_2 + (\mathbf{h} \cdot \mathbf{e})\mathbb{m}. \tag{2.57}$$

However, by $(2.52)_2$, $\mathbf{h}$ must satisfy

$$\mathbf{h} \cdot \mathbf{e} = 0, \tag{2.58}$$

which, in combination with (2.56), yields $\mathbf{h} = \mathbb{m}$. Thus, $\mathbf{H}$ must admit a representation of the form

$$\mathbf{H} = \mathbb{H} + \mathbb{m} \otimes \mathbb{m}, \tag{2.59}$$

where, bearing in mind (2.55),

$$\mathbb{H} := \mathbb{e}_1 \otimes \mathbf{f} + \mathbb{e}_2 \otimes \mathbf{g} \tag{2.60}$$

is a fully tangential tensor and therefore obeys

$$\left.\begin{aligned} &\mathbb{H}\mathbb{m} = \mathbb{H}^{\top}\mathbb{m} = \mathbf{0}, \\ &\mathbb{H} = \mathbb{P}_{\mathbb{m}}\mathbb{H} = \mathbb{H}\mathbb{P}_{\mathbb{m}} = \mathbb{P}_{\mathbb{m}}\mathbb{H}\mathbb{P}_{\mathbb{m}}. \end{aligned}\right\} \tag{2.61}$$

Notice that, granted the representation (2.59) for $\mathbf{H}$, the condition $(2.52)_3$ is equivalent to the following condition on $\mathbb{H}$:

$$I_2(\mathbb{H}) = 1. \tag{2.62}$$

2.6.2 Representation theorem for the energy density of a lipid bilayer

Observe that the right Cauchy-Green tensor $\mathbf{C}$ can be expressed in the form

$$\mathbf{C} = \mathbb{C} + \mathbb{v} \otimes \mathbb{m} + \mathbb{m} \otimes \mathbb{v} + (\mathbb{m} \cdot \mathbf{C}\mathbb{m})\mathbb{m} \otimes \mathbb{m}, \tag{2.63}$$

where $\mathbb{C}$ is a fully tangential tensor defined by

$$\mathbb{C} = (\mathbf{F}\mathbb{P}_{\mathbb{m}})^{\top}(\mathbf{F}\mathbb{P}_{\mathbb{m}}) = \mathbb{P}_{\mathbb{m}}\mathbf{C}\mathbb{P}_{\mathbb{m}} \tag{2.64}$$

and $\mathbb{v}$ is a tangent vector belonging to $T_{\xi_\circ}$ defined by

$$\mathbb{v} = \mathbf{C}\mathbb{m} - (\mathbb{m} \cdot \mathbf{C}\mathbb{m})\mathbb{m}. \tag{2.65}$$

In view of (2.51) and (2.63)–(2.65), the energy density W can be expressed as a function $\tilde{W}$ depending on $\mathbb{C}$, $\mathbb{v}$, and $\mathbb{m} \cdot \mathbf{C}\mathbb{m}$:

$$\begin{aligned} W &= \bar{W}(\mathbf{C}) \\ &= \tilde{W}(\mathbb{C}, \mathbb{v}, \mathbb{m} \cdot \mathbf{C}\mathbb{m}). \end{aligned} \tag{2.66}$$

Additionally, by (2.59) and (2.63), $\mathbf{H}^{\top}\mathbf{C}\mathbf{H}$ can be expressed as

$$\mathbf{H}^{\top}\mathbf{C}\mathbf{H} = \mathbb{H}^{\top}\mathbb{C}\mathbb{H} + \mathbb{H}^{\top}\mathbb{v} \otimes \mathbb{m} + \mathbb{m} \otimes \mathbb{H}^{\top}\mathbb{v} + (\mathbb{m} \cdot \mathbf{C}\mathbb{m})\mathbb{m} \otimes \mathbb{m}, \tag{2.67}$$

and, hence, the symmetry property (2.53) takes the form

$$\tilde{W}(\mathbb{H}^{\top}\mathbb{C}\mathbb{H}, \mathbb{H}^{\top}\mathbb{v}, \mathbb{m}\cdot\mathbf{C}\mathbb{m}) = \tilde{W}(\mathbb{C}, \mathbb{v}, \mathbb{m}\cdot\mathbf{C}\mathbb{m}). \tag{2.68}$$

Being fully tangential (see Appendix 2.11.1), $\mathbb{C}$ and $\mathbb{H}$ can be viewed as mappings of the tangent space $T_{\xi_\circ}$ to itself, in which case the transformation rule

$$\mathbb{C} \longrightarrow \mathbb{H}^{\top}\mathbb{C}\mathbb{H} \tag{2.69}$$

can be interpreted as one involving tensors that map the tangent space $T_{\xi_\circ}$ to itself. Similarly, since $\mathbb{v}$ belongs to $T_{\xi_\circ}$, the transformation rule

$$\mathbb{v} \longrightarrow \mathbb{H}^{\top}\mathbb{v} \tag{2.70}$$

can be interpreted as one involving two-dimensional referential tangent vectors belonging to $T_{\xi_\circ}$.

Consider the subgroup of the unimodular group comprised by all rotations in the tangent plane with normal vector $\mathbb{m}$. Bearing in mind that, like $\mathbb{C}$ and $\mathbb{H}$, any element of that subgroup can be viewed as a mapping of the space of two-dimensional referential tangent vectors to itself, a representation theorem due to Zheng [129] can be applied to arrive at the following representation for the energy density:

$$W = \tilde{\tilde{W}}(I_1(\mathbb{C}), I_2(\mathbb{C}), \mathbb{v}\cdot\mathbb{v}, \mathbb{v}\cdot\mathbb{C}\mathbb{v}, \mathbb{m}\cdot\mathbf{C}\mathbb{m}). \tag{2.71}$$

However, since, by (2.63),

$$\mathbb{v}\cdot\mathbb{C}\mathbb{v} = \det\mathbf{C} - (\mathbb{m}\cdot\mathbf{C}\mathbb{m})I_2(\mathbb{C}) + I_1(\mathbb{C})[\mathbb{v}\cdot\mathbb{v} - (\mathbb{m}\cdot\mathbf{C}\mathbb{m})^2], \tag{2.72}$$

(2.71) can be written as

$$W = \breve{W}(I_1(\mathbb{C}), I_2(\mathbb{C}), \mathbb{v} \cdot \mathbb{v}, \det \mathbf{C}, \mathbb{m} \cdot \mathbf{C}\mathbb{m}). \tag{2.73}$$

The five arguments of $\breve{W}$ are mutually independent. To see this, first, notice that the tensor $\mathbf{C}$ has six independent components and, hence, that the decomposition in (2.63) defines three independent quantities $\mathbb{C}$, $\mathbb{v}$, and $\mathbb{m} \cdot \mathbf{C}\mathbb{m}$. Since $\mathbb{C}$ is symmetric, it admits a spectral decomposition

$$\mathbb{C} = \omega_1 \mathbb{t}_1 \otimes \mathbb{t}_1 + \omega_2 \mathbb{t}_2 \otimes \mathbb{t}_2 \tag{2.74}$$

involving eigenvalues ω_1 and ω_2 corresponding, respectively, to eigenvectors $\mathbb{t}_1$ and $\mathbb{t}_2$ tangent to $T_{\xi_\circ}$ with the property $\mathbb{t}_1 \times \mathbb{t}_2 = \mathbb{m}$. Additionally, in terms of the basis $\{\mathbb{t}_1, \mathbb{t}_2\}$, $\mathbb{v}$ can be expressed in the form

$$\mathbb{v} = v_1 \mathbb{t}_1 + v_2 \mathbb{t}_2, \tag{2.75}$$

where v_α denote the component of $\mathbb{v}$ in the $\mathbb{t}_\alpha$ direction ($\alpha = 1, 2$). Also, since $\mathbb{m} \cdot \mathbf{C}\mathbb{m}$ indicates the component of $\mathbf{C}$ in the direction perpendicular to the tangent space $T_{\xi_\circ}$, it can be chosen independently of the remaining arguments. Put $\tau = \mathbb{m} \cdot \mathbf{C}\mathbb{m}$, bearing in mind that, since $\mathbf{C}$ is positive-definite, τ must obey $\tau > 0$. The arguments of (2.73) can then be expressed as

$$\left.\begin{aligned}
&I_1(\mathbb{C}) = \omega_1 + \omega_2,\\
&I_2(\mathbb{C}) = \omega_1\omega_2,\\
&\mathbb{v}\cdot\mathbb{v} = v_1^2 + v_2^2,\\
&\det\mathbf{C} = \omega_1\omega_2\tau - \omega_1 v_2^2 - \omega_2 v_1^2,\\
&\mathbb{m}\cdot\mathbf{C}\mathbb{m} = \tau.
\end{aligned}\right\} \tag{2.76}$$

Since ω_1, ω_2, v_1, v_2, and τ are independent, (2.76) can be used to show that the numbers $I_1(\mathbb{C})$, $I_2(\mathbb{C})$, $\det\mathbf{C}$, and $\mathbb{v}\cdot\mathbb{C}\mathbb{v}$, $\mathbb{m}\cdot\mathbf{C}\mathbb{m}$ can be varied independently.

We next show that, of the five arguments upon which $\breve{W}$ may depend, as indicated on the right-hand side of (2.73), only $I_2(\mathbb{C})$, $\det\mathbf{C}$, and $\mathbb{m}\cdot\mathbf{C}\mathbb{m}$ are invariant under any unimodular symmetry transformation $\mathbf{H}$ consistent with (2.61) and (2.62). This elucidates the distinction between the symmetry properties of a lipid bilayer with in-plane fluidity (that is, a lipid bilayer with symmetry group consisting of all fully tangential unimodular transformations $\mathbb{H}$) with those of a solid transversely isotropic about $\mathbb{m}$. Further insight regarding the symmetry properties of fluid films and transversely isotropic solids due, respectively, to Steigmann [62] and Green and Adkins [130] are particularly relevant.

To substantiate the foregoing assertion, choose orthonormal unit tangent vectors $\mathbb{e}_1$ and $\mathbb{e}_2$ spanning the tangent space $T_{\xi_\circ}$. A generic tangent vector $\mathbb{v}$ in (2.73) can be represented in the form $\mathbb{v} = \lambda_1\mathbb{e}_1 + \lambda_2\mathbb{e}_2$, with λ_1 and λ_2 being scalars. Without loss of generality, assume that $\mathbb{e}_1$ is chosen in the $\mathbb{v}$ direction, so that $\mathbb{e}_1 = \mathbb{v}/|\mathbb{v}|$. To show that $\breve{W}$ can depend at most on $I_2(\mathbb{C})$, $\det\mathbf{C}$, and $\mathbb{m}\cdot\mathbf{C}\mathbb{m}$, it sufficies to: (i) show that they are invariant under all unimodular symmetry transformations of the kind described in (2.52), and (ii) find specific tranformations under which $I_1(\mathbb{C})$ and $\mathbb{v}\cdot\mathbb{v}$ are not properly invariant. Bearing in mind $(2.52)_3$, (2.59), $(2.61)_1$, and (2.184), it is straightforward to show that, for any $\mathbf{H}$ satisfying (2.52),

$$\left.\begin{aligned} I_2(\mathbb{H}^\top\mathbb{C}\mathbb{H}) &= I_2(\mathbb{C}),\\ \det(\mathbf{H}^\top\mathbf{C}\mathbf{H}) &= \det\mathbf{C},\\ \mathbb{m}\cdot\mathbf{H}^\top\mathbf{C}\mathbf{H}\mathbb{m} &= \mathbb{m}\cdot\mathbf{C}\mathbb{m}. \end{aligned}\right\} \tag{2.77}$$

Consider, now, the tensor

$$\mathbb{H}_1 = \mathbb{e}_1\otimes\mathbb{e}_1 + \mathbb{e}_2\otimes\mathbb{e}_2 + \alpha\mathbb{e}_2\otimes\mathbb{e}_1, \qquad \alpha\in\mathbb{R} \tag{2.78}$$

which satisfies (2.61) and (2.62) for all choices of the parameter α. Then, since

$$I_1(\mathbb{H}_1^\top\mathbb{C}\mathbb{H}_1) = I_1(\mathbb{C}) + \varphi(\alpha), \tag{2.79}$$

with $\varphi(\alpha) = 2\alpha(\mathbb{e}_1\cdot\mathbb{C}\mathbb{e}_2) + \alpha^2(\mathbb{e}_2\cdot\mathbb{C}\mathbb{e}_2)$, and since

$$\mathbb{H}_1^\top\mathbb{v}\cdot\mathbb{H}_1^\top\mathbb{v} = \mathbb{v}\cdot\mathbb{v}, \tag{2.80}$$

$\breve{W}$ must obey

$$\breve{W}(I_1(\mathbb{C})+\varphi(\alpha),\cdot,\mathbb{v}\cdot\mathbb{v},\cdot,\cdot) = \breve{W}(I_1(\mathbb{C}),\cdot,\mathbb{v}\cdot\mathbb{v},\cdot,\cdot) \tag{2.81}$$

for all α. It is possible to choose α in (2.81) such that $\varphi(\alpha) = \nu I_1(\mathbb{C})$ for an arbitrary $\nu\ge 0$. Also, on defining $x := I_1(\mathbb{C})$ and $y := (1+\nu)I_1(\mathbb{C})$, fixing $I_2(\mathbb{C})$, $\mathbb{v}\cdot\mathbb{v}$, $\det\mathbf{C}$, and $\mathbb{m} \cdot \mathbf{C}\mathbb{m}$, and defining f via $f(x) := \breve{W}(x, I_2(\mathbb{C}), \mathbb{v} \cdot \mathbb{v}, \det \mathbf{C}, \mathbb{m} \cdot \mathbf{C}\mathbb{m})$, it is evident that $f(y) = f(x)$. Hence, since x and y may be chosen arbitrarily, f must be constant. It follows that $\breve{W}$ must be independent of the argument $I_1(\mathbb{C})$. Next, consider the tensor

$$\mathbb{H}_2 = \beta \mathbb{e}_1 \otimes \mathbb{e}_1 + \frac{1}{\beta} \mathbb{e}_2 \otimes \mathbb{e}_2, \qquad \beta \in \mathbb{R}, \quad \beta \neq 0, \tag{2.82}$$

which satisfies (2.61) and (2.62) for all choices of the parameter $\beta \neq 0$. Then, since

$$\mathbb{H}_2^{\top} \mathbb{v} \cdot \mathbb{H}_2^{\top} \mathbb{v} = \beta^2 \mathbb{v} \cdot \mathbb{v}, \tag{2.83}$$

$\breve{W}$ must obey

$$\breve{W}(\cdot, \beta^2 \mathbb{v} \cdot \mathbb{v}, \cdot, \cdot) = \breve{W}(\cdot, \mathbb{v} \cdot \mathbb{v}, \cdot, \cdot) \tag{2.84}$$

for all $\beta \neq 0$. On choosing β in (2.84) such that $\beta^2 = (\mathbb{v} \cdot \mathbb{v})^{-1}$, it follows that $\breve{W}$ must be independent of the argument $\mathbb{v} \cdot \mathbb{v}$. Consequently, we conclude that the energy density W of a lipid bilayer must admit a representation of the form

$$W = \Phi(\mathcal{I}_1, \mathcal{I}_2, \mathcal{I}_3), \tag{2.85}$$

with

$$\mathcal{I}_1 = I_2(\mathbb{C}),\ \mathcal{I}_2 = \det \mathbf{C},\ \mathcal{I}_3 = \mathbb{m} \cdot \mathbf{C}\mathbb{m}. \tag{2.86}$$

2.7 Kinematical discussions

With the representation (2.38) for the deformation gradient $\mathbf{F}$, the right Cauchy–Green tensor $\mathbf{C} = \mathbf{F}^{\top}\mathbf{F}$ can be expressed as

$$\begin{aligned}\mathbf{C} =&\mathbb{Q}_{\circ}\mathbb{C}_{\circ}\mathbb{Q}_{\circ} - 2\xi\mathbb{Q}_{\circ}\mathbb{F}_{\circ}^{\top}\mathbb{L}\mathbb{F}_{\circ}\mathbb{Q}_{\circ} + \xi^{2}\mathbb{Q}_{\circ}\mathbb{F}_{\circ}^{\top}\mathbb{L}^{2}\mathbb{F}_{\circ}\mathbb{Q}_{\circ}\\ &+ (\mathbb{Q}_{\circ}\nabla_{S_{\circ}}\xi)\otimes(\mathbb{Q}_{\circ}\nabla_{S_{\circ}}\xi)\\ &+ \frac{\partial\xi}{\partial\xi_{\circ}}((\mathbb{Q}_{\circ}\nabla_{S_{\circ}}\xi)\otimes\mathbb{m} + \mathbb{m}\otimes(\mathbb{Q}_{\circ}\nabla_{S_{\circ}}\xi))\\ &+ \Big(\frac{\partial\xi}{\partial\xi_{\circ}}\Big)^{2}\mathbb{m}\otimes\mathbb{m},\end{aligned}\tag{2.87}$$

where we have introduced

$$\mathbb{C}_{\circ} = \mathbb{F}_{\circ}^{\top}\mathbb{F}_{\circ}.\tag{2.88}$$

In addition, on comparing (2.64) and (2.87), it follows that the fully tangential tensor $\mathbb{C}$ can be expressed as

$$\mathbb{C} = \mathbb{Q}_{\circ}\mathbb{C}_{\circ}\mathbb{Q}_{\circ} - 2\xi\mathbb{Q}_{\circ}\mathbb{F}_{\circ}^{\top}\mathbb{L}\mathbb{F}_{\circ}\mathbb{Q}_{\circ} + \xi^{2}\mathbb{Q}_{\circ}\mathbb{F}_{\circ}^{\top}\mathbb{L}^{2}\mathbb{F}_{\circ}\mathbb{Q}_{\circ} + (\mathbb{Q}_{\circ}\nabla_{S_{\circ}}\xi)\otimes(\mathbb{Q}_{\circ}\nabla_{S_{\circ}}\xi).\tag{2.89}$$

2.7.1 The invariants $\mathcal{I}_1$, $\mathcal{I}_2$, and $\mathcal{I}_3$

Prior to formulating specific constitutive relations, it seems necessary to understand the geometric properties of the invariants $\mathcal{I}_1$, $\mathcal{I}_2$, and $\mathcal{I}_3$ entering the representation (2.85) of the generic energy density for a lipid bilayer.

The invariant $\mathcal{I}_1$

We now show that the invariant $\mathcal{I}_1 = I_2(\mathbb{C})$ controls changes in the area of infinitesimal area elements parallel to the midsurface $S_{\circ}$ (Figure 2). Toward this goal, choose linearly independent vectors $\mathbb{e}_1$ and $\mathbb{e}_2$ belonging to the tangent space

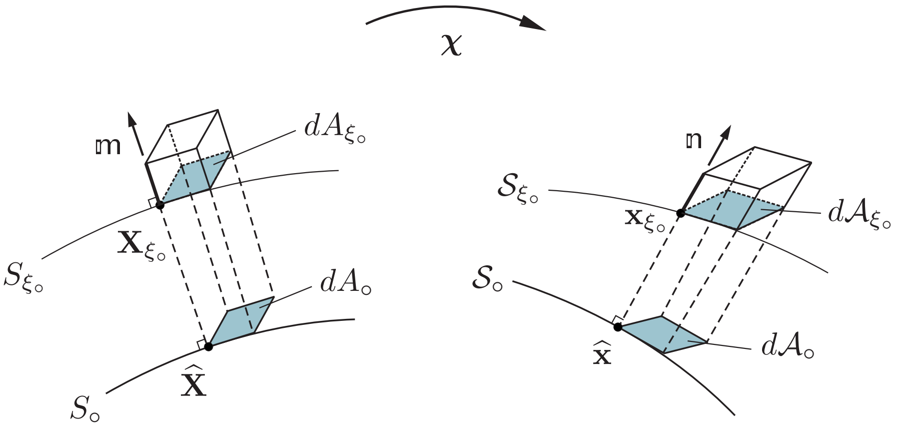

Figure 2–2: Schematic depiction of changes of volume and tangent area elements.

$T_{\xi_\circ}$ that satisfy $\mathbb{e}_1 \times \mathbb{e}_2 = \mathbb{m}$. Further, choose infinitesimal material line elements $\mathrm{d}\mathbf{X}^1_{\xi_\circ}$ and $\mathrm{d}\mathbf{X}^2_{\xi_\circ}$ directed along $\mathbb{e}_1$ and $\mathbb{e}_2$ such that they span the infinitesimal area element

$$\mathrm{d}A_{\xi_\circ} = |\mathrm{d}\mathbf{X}^1_{\xi_\circ} \times \mathrm{d}\mathbf{X}^2_{\xi_\circ}|. \tag{2.90}$$

With reference to (2.20), define elements $\mathbb{e}^1_\circ$ and $\mathbb{e}^2_\circ$ of $T_\circ$ by $\mathbb{e}^1_\circ = \mathbb{Q}_\circ \mathbb{e}_1$ and $\mathbb{e}^2_\circ = \mathbb{Q}_\circ \mathbb{e}_2$ and let the infinitesimal line elements $\mathrm{d}\widehat{\mathbf{X}}_1$ and $\mathrm{d}\widehat{\mathbf{X}}_2$, as described in (2.20), denote the images of $\mathrm{d}\mathbf{X}^1_{\xi_\circ}$ and $\mathrm{d}\mathbf{X}^2_{\xi_\circ}$ directed along $\mathbb{e}^1_\circ$ and $\mathbb{e}^2_\circ$ on $S_\circ$. Obviously, $\mathrm{d}\widehat{\mathbf{X}}_1$ and $\mathrm{d}\widehat{\mathbf{X}}_2$ span the image

$$\mathrm{d}A_\circ = |\mathrm{d}\widehat{\mathbf{X}}_1 \times \mathrm{d}\widehat{\mathbf{X}}_2| \tag{2.91}$$

of $\mathrm{d}A_{\xi_\circ}$ on $S_\circ$. The area element $\mathrm{d}\mathcal{A}_{\xi_\circ}$ corresponding to $\mathrm{d}A_{\xi_\circ}$ in the deformed body is

$$\mathrm{d}\mathcal{A}_{\xi_\circ} = |\mathbf{F}\mathbb{e}_1 \times \mathbf{F}\mathbb{e}_2|\, \mathrm{d}A_{\xi_\circ}. \tag{2.92}$$

Since $\mathbb{e}_1$ and $\mathbb{e}_2$ are tangent vectors, the deformation gradient $\mathbf{F}$ in (2.92) can be replaced by the superficial deformation gradient

$$\mathbb{F} := \mathbf{F}\mathbb{P}_{\mathbb{m}}, \tag{2.93}$$

giving

$$\mathrm{d}\mathcal{A}_{\xi_\circ} = |\mathbb{F}\mathbb{e}_1 \times \mathbb{F}\mathbb{e}_2|\, \mathrm{d}A_{\xi_\circ}, \tag{2.94}$$

whereby the area ratio $J_{\xi_\circ} = \mathrm{d}\mathcal{A}_{\xi_\circ}/\mathrm{d}A_{\xi_\circ}$ takes the form

$$\begin{aligned} J_{\xi_\circ} &= |\mathbb{F}\mathbb{e}_1 \times \mathbb{F}\mathbb{e}_2| \\ &= |\mathbb{F}^{\mathrm{c}}(\mathbb{e}_1 \times \mathbb{e}_2)| \\ &= |\mathbb{F}^{\mathrm{c}}\mathbb{m}|, \end{aligned} \tag{2.95}$$

with $\mathbb{F}^{\mathrm{c}}$ being the cofactor of $\mathbb{F}$. By (2.95),

$$\begin{aligned} J^2_{\xi_\circ} &= |\mathbb{F}^{\mathrm{c}}\mathbb{m}|^2 \\ &= \mathbb{F}^{\mathrm{c}}\mathbb{m} \cdot \mathbb{F}^{\mathrm{c}}\mathbb{m} \\ &= \mathbb{m} \cdot (\mathbb{F}^{\mathrm{c}})^{\top}\mathbb{F}^{\mathrm{c}}\mathbb{m} \\ &= \mathbb{m} \cdot (\mathbb{F}^{\top}\mathbb{F})^{\mathrm{c}}\mathbb{m} \\ &= \mathbb{m} \cdot \mathbb{C}^{\mathrm{c}}\mathbb{m}. \end{aligned} \tag{2.96}$$

By (2.183), $\mathbb{m} \cdot \mathbb{C}^{\mathrm{c}}\mathbb{m} = \mathcal{I}_1$, which with (2.96) yields

$$\mathcal{I}_1 = I_2(\mathbb{C}) = J^2_{\xi_\circ} = \Big(\frac{\mathrm{d}\mathcal{A}_{\xi_\circ}}{\mathrm{d}A_{\xi_\circ}}\Big)^2, \tag{2.97}$$

confirming the assertion that $\mathcal{I}_1$ controls changes in the area of infinitesimal area elements parallel to $S_\circ$. Evaluating (2.97) at the midsurface $S_\circ$ gives

$$J^2 = \left(\frac{\mathrm{d}\mathcal{A}_\circ}{\mathrm{d}A_\circ}\right)^2 = I_2(\mathbb{C}_\circ), \tag{2.98}$$

where J is defined in (2.33) and $\mathrm{d}\mathcal{A}_\circ$ is the image, on $\mathcal{S}_\circ$, of area element $\mathrm{d}A_\circ$.

According to the definition (2.172) of the surface gradient and the chain rule, $\nabla_{S_\circ}\xi$ in (2.89) can be replaced by $\mathbb{F}_\circ^\top \nabla_{\mathcal{S}_\circ}\xi$, where $\nabla_{\mathcal{S}_\circ}\xi = \mathbb{P}_{\mathbb{n}}\nabla_{\mathbf{x}}\xi$ is the surface gradient of ξ on $\mathcal{S}_\circ$, and

$$\mathbb{P}_{\mathbb{n}} = \mathbf{1} - \mathbb{n} \otimes \mathbb{n} \tag{2.99}$$

is the projection tensor onto the tangent plane of $\mathcal{S}_\circ$. Since $\mathbb{Q}_\circ$ is symmetric, (2.89) can be reorganized as

$$\mathbb{C} = \mathbb{Q}_\circ \mathbb{F}_\circ^\top \mathbb{K} \mathbb{F}_\circ \mathbb{Q}_\circ, \tag{2.100}$$

where we emphasize that

$$\mathbb{K} = \mathbb{P}_{\mathbb{n}} - 2\xi\mathbb{L} + \xi^2\mathbb{L}^2 + (\nabla_{\mathcal{S}_\circ}\xi) \otimes (\nabla_{\mathcal{S}_\circ}\xi) \tag{2.101}$$

is a fully tangential tensor which can be viewed as a mapping from the tangent space of $\mathcal{S}_\circ$ to itself. From $(2.184)_2$, it follows that

$$\mathcal{I}_1 = I_2(\mathbb{C}) = I_2^2(\mathbb{Q}_\circ) I_2(\mathbb{C}_\circ) I_2(\mathbb{K}). \tag{2.102}$$

The definition (2.196) of the second principal invariant I_2 and a straightforward calculation lead to

$$I_2(\mathbb{K}) = \gamma^2(\xi) + |((2H\xi - 1)\mathbb{P}_{\mathbb{n}} - \xi\mathbb{L})\nabla_{\mathcal{S}_\circ}\xi|^2, \tag{2.103}$$

with

$$\gamma(\xi) := 1 - 2\xi H + \xi^2 K. \tag{2.104}$$

In view of (2.21), (2.98) and $(2.184)_2$, (2.102) can be expressed as

$$\mathcal{I}_1 = J^2(\gamma_\circ(\xi_\circ))^{-2}(\gamma^2(\xi) + |((2H\xi - 1)\mathbb{P}_{\mathbb{n}} - \xi\mathbb{L})\nabla_{\mathcal{S}_\circ}\xi|^2). \tag{2.105}$$

The invariant $\mathcal{I}_2$

It is evident that the invariant $\mathcal{I}_2 = \det \mathbf{C} = (\det \mathbf{F})^2$ controls volume changes of infinitesimal material regions (Figure 2–2). However, it is useful to obtain $\mathcal{I}_2$ in terms of relavant kinematical quantities. According to the definition of the determinant and upon using (2.38),

$$\begin{aligned} \det \mathbf{F} &= [(\mathbf{F}\mathbb{e}_1) \times (\mathbf{F}\mathbb{e}_2)] \cdot \mathbf{F}\mathbb{m}. \\ &= \frac{\partial \xi}{\partial \xi_\circ}\Big((\mathbf{g}_\circ^1 \times \mathbf{g}_\circ^2) \cdot \mathbb{n} - \xi[(\mathbb{L}\mathbf{g}_\circ^1 \times \mathbf{g}_\circ^2) \cdot \mathbb{n} \\ &\quad + (\mathbf{g}_\circ^1 \times \mathbb{L}\mathbf{g}_\circ^2) \cdot \mathbb{n}] + \xi^2(\mathbb{L}\mathbf{g}_\circ^1 \times \mathbb{L}\mathbf{g}_\circ^2) \cdot \mathbb{n}\Big), \end{aligned} \tag{2.106}$$

where $\mathbf{g}_\circ^1 = \mathbb{F}_\circ\mathbb{e}_\circ^1$ and $\mathbf{g}_\circ^2 = \mathbb{F}_\circ\mathbb{e}_\circ^2$ are tangent to $\mathcal{S}_\circ$ and span $\mathrm{d}\mathcal{A}_\circ$.

In view of (2.183), $(2.184)_2$, and (2.21)

$$\begin{aligned}\mathbb{e}_\circ^1 \times \mathbb{e}_\circ^2 &= \mathbb{Q}_\circ \mathbb{e}_1 \times \mathbb{Q}_\circ \mathbb{e}_2 \\ &= \mathbb{Q}_\circ^{\mathrm{c}}(\mathbb{e}_1 \times \mathbb{e}_2) \\ &= \mathbb{Q}_\circ^{\mathrm{c}}\mathbb{m} \\ &= I_2(\mathbb{Q}_\circ)\mathbb{m} \\ &= (I_2(\mathbb{S}_\circ))^{-1}\mathbb{m} \\ &= (\gamma_\circ(\xi_\circ))^{-1}\mathbb{m} \end{aligned} \tag{2.107}$$

which, with (2.96) and (2.98) implies that

$$\begin{aligned}(\mathbf{g}_\circ^1 \times \mathbf{g}_\circ^2) \cdot \mathbb{n} &= |\mathbb{F}_\circ \mathbb{e}_\circ^1 \times \mathbb{F}_\circ \mathbb{e}_\circ^2| \\ &= (\gamma_\circ(\xi_\circ))^{-1}|\mathbb{F}_\circ^{\mathrm{c}}\mathbb{m}| \\ &= (\gamma_\circ(\xi_\circ))^{-1}J. \end{aligned} \tag{2.108}$$

By (2.108), (2.177), (2.181)–(2.183), and elementary properties of the trace and cofactor of $\mathbb{L}$, (2.106) simplifies to

$$\det \mathbf{F} = J\frac{\partial \xi}{\partial \xi_\circ}\frac{\gamma(\xi)}{\gamma_\circ(\xi_\circ)}, \tag{2.109}$$

and, consequently, $\mathcal{I}_2$ becomes

$$\mathcal{I}_2 = \det \mathbf{C} = J^2\Big(\frac{\partial \xi}{\partial \xi_\circ}\Big)^2\Big(\frac{\gamma(\xi)}{\gamma_\circ(\xi_\circ)}\Big)^2. \tag{2.110}$$

The invariant $\mathcal{I}_3$

Finally, it is evident that the invariant

$$\begin{aligned}\mathcal{I}_3 &= \mathbb{m} \cdot \mathbf{C}\mathbb{m} \\ &= \Big(\frac{\partial \xi}{\partial \xi_\circ}\Big)^2 \end{aligned} \tag{2.111}$$

controls the stretch of infinitesimal material fibers perpendicular to the midsurface $S_\circ$.

2.7.2 Constitutively-associated kinematical variables

In view of (2.105), (2.110), (2.111), we may use (2.196) in (2.105) to conclude that the energy density in (2.85) depends upon the referential variables

$$H_\circ, \quad K_\circ, \quad \xi_\circ, \tag{2.112}$$

and the spatial variables

$$H, \quad K, \quad \xi, \quad \frac{\partial \xi}{\partial \xi_\circ}, \quad |\nabla_{\mathcal{S}_\circ} \xi|^2, \quad (\nabla_{\mathcal{S}_\circ} \xi) \cdot \mathbb{L}(\nabla_{\mathcal{S}_\circ} \xi). \tag{2.113}$$

Consistent with existing two-dimensional theories, H and K—which are paramount importance in the areal Canham–Helfrich energy density (2.1)—represent the dependence on the curvature of the spatial midsurface $\mathcal{S}_\circ$ and the areal stretch J—which is present in the areal energy density of Steigmann [62]—embodies localized changes in the area in going from the referential midsurface $S_\circ$ to the spatial midsurface $\mathcal{S}_\circ$. In addition to through-thickness dependence via ξ, (2.85) accounts for the potential influence of transverse normal strain (and, consequently, thickness changes) via $\partial \xi / \partial \xi_\circ$

as well as both transverse shear strain and thickness nonuniformity via $|\nabla_{\mathcal{S}_\circ}\xi|^2$. Potential coupling between curvature and deviations in thickness is embodied by the quantity $(\nabla_{\mathcal{S}_\circ}\xi)\cdot\mathbb{L}(\nabla_{\mathcal{S}_\circ}\xi)$, which includes information regarding the orientation of $\nabla_{\mathcal{S}_\circ}\xi$ relative to the principal axes of the curvature tensor $\mathbb{L}$. Notice that, for example, when $\nabla_{\mathcal{S}_\circ}\xi$ coincides with one of the principal axes of $\mathbb{L}$ dependence upon the coupling term $(\nabla_{\mathcal{S}_\circ}\xi)\cdot\mathbb{L}(\nabla_{\mathcal{S}_\circ}\xi)$ is redundant. In particular, this occurs when the spatial midsurface $\mathcal{S}_\circ$ is spherical.

2.7.3 Incompressibility

Various studies suggest that lipid bilayers are very nearly incompressible [58, 59, 60]. If, to model this observation, the deformation $\boldsymbol{\chi}$ is stipulated to be isochoric, then (2.110) has the elementary consequence

$$\mathcal{I}_2 = 1. \tag{2.114}$$

Accordingly, the energy density must be independent of $\mathcal{I}_2$ and the representation (2.85) reduces to

$$W = \tilde{\Phi}(\mathcal{I}_1, \mathcal{I}_3). \tag{2.115}$$

In addition, using (2.114) in (2.110) along with (2.15), (2.21), and (2.104) yields the differential equation

$$\begin{aligned}\frac{\partial\xi}{\partial\xi_\circ} &= \frac{1}{J}\frac{\gamma_\circ(\xi_\circ)}{\gamma(\xi)}\\ &= \frac{1-2\xi_\circ H_\circ+\xi_\circ^2K_\circ}{(1-2\xi H+\xi^2K)J},\end{aligned} \tag{2.116}$$

which with (2.27) integrates to yield $\xi(1-\xi H+\frac{1}{3}\xi^2 K)J = \xi_\circ(1-\xi_\circ H_\circ+\frac{1}{3}\xi_\circ^2 K_\circ)+\phi(\widehat{\mathbf{X}})$. However, on using the condition $\xi|_\circ = 0$, the integration constant $\phi(\widehat{\mathbf{X}})$ vanishes, giving

$$\xi(1 - \xi H + \tfrac{1}{3}\xi^2 K)J = \xi_\circ(1 - \xi_\circ H_\circ + \tfrac{1}{3}\xi_\circ^2 K_\circ). \tag{2.117}$$

The relation (2.117) reveals that, for an incompressible lipid bilayer, H, K, J, and ξ are not generally independent. For instance, when J, H, and K at any point on the spatial midsurface $\mathcal{S}_\circ$ are given, (2.117) can be solved to determine the distance ξ of a spatial point on $\mathcal{S}_\circ$ corresponding to the material point at the distance $\xi_\circ$ on $S_\circ$ in the spontaneous state. In addition, the purely geometrical and kinematical result (2.117) suggests that the thickness of an incompressible lipid bilayer in its spatial configuration will not generally be uniform unless its midsurface is uniformly bent or stretched and has uniform spontaneous curvature. Zurlo [63] and Deseri et al. [64] assume that ξ is linearly proportional to $\xi_\circ$, or, alternatively, that $\partial\xi/\partial\xi_\circ$ is the ratio of thickness of the deformed and referential lipid bilayer and refer to this condition as “quasi-incompressibility.” In such a case, the incompressibility condition is only satisfied at the spatial midsurface $\mathcal{S}_\circ$ and leads to

$$\frac{\xi}{\xi_\circ} = \frac{1}{J}. \tag{2.118}$$

However, this assumption is valid only if the spontaneous mean and Gaussian curvatures $H_\circ$ and $K_\circ$ and the mean and Gaussian curvatures H and K of the spatial midsurface are very mild (or, more precisely, if ξH, $\xi^2 K$, $\xi_\circ H_\circ$, and $\xi_\circ^2 K_\circ$ are negligible in comparison with unity).

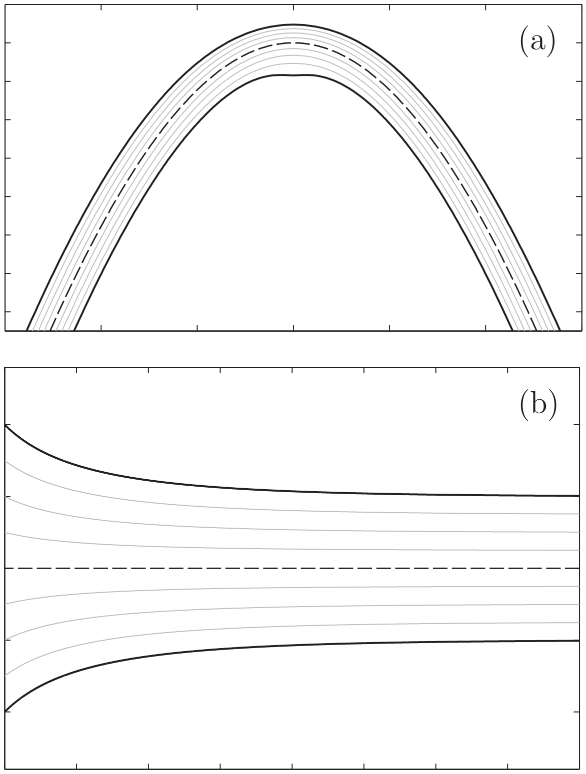

Figure 2–3: Illustrative isochoric deformations of a lipid bilayer: (a) Thickness change due to pure bending. (b) Thickness change due to pure stretching. While the dashed lines are the sptial midsurface $\mathcal{S}_\circ$, the grey lines are spatial placements of few material surfaces with constant $\xi_\circ$ in the reference configuration.

Notice that (2.117) can be viewed as a cubic equation for ξ. However, only a unique physically meaningful root of this equation is of interest. First, the root must be real. Also, to guarantee its uniqueness, the root should be an increasing function of $\xi_\circ$. In addition, to satisfy the requirement that $\xi|_\circ = 0$, the sign of ξ must match that of $\xi_\circ$. These conditions limit the range of the coefficients in (2.117). In particular, the sign of the discriminant of the cubic equation provides some information about the nature of the roots. A simpler case occurs if the lipid bilayer only has curvature in a two-dimensional space and is uniformly extended in one direction. In this circumstance, $K = 0$ (for simplicity also assume that $K_\circ = 0$) in which case (2.117) reduces to a quadratic equation with the admissible root

$$\xi = \frac{1 - \sqrt{1 - 4\xi_\circ H(1 - \xi_\circ H_\circ)/J}}{2H}, \tag{2.119}$$

which is real if and only if

$$4\xi_\circ H(1 - \xi_\circ H_\circ) \leq J. \tag{2.120}$$

For there to exist an admissible root ξ satisfying the incompressibility condition (2.117), the ratio $\xi_\circ H/J$ of the deformed lipid bilayer must be small enough to satisfy (2.120) for all $\xi_\circ \in [-h_\circ^-, h_\circ^+]$.

To provide a qualitative insight regarding incompressibility-induced changes of thickness, we restrict attention to situations where the spontaneous mean curvature $H_\circ$ vanishes and consider two illustrative examples. Figure 2–3a shows a lipid bilayer under pure bending (in which case $J = 1$) with spatial midsurface $\mathcal{S}_\circ$ having a sinusoidal shape. It is evident that the thickness of the upper (lower) leaflet decreases (increases) as the curvature H of $\mathcal{S}_\circ$ increases. Figure 2–3b shows a lipid bilayer with a flat sptial midsurface (in which case $H = 0$) subject to an areal stretch that decreases exponentially toward the left side. Notably, the thicknesses of lipid bilayer leaflets increase symmetrically as the areal stretch decreases from right to left. Thickening phenomena of this kind are well-known to occur in the presence of transmembrane proteins, in which case hydrophobic mismatch leads to stretching of the lipid molecules in the through-thickness direction (here, the left side of Figure 2–3b).

2.8 Stress relations

Consistent with the procedure pioneered by Coleman and Noll [131], the elastic Cauchy stress tensor corresponding to an energy density of the form (2.85) is given by

$$\mathbf{T} = \frac{2}{\sqrt{\mathcal{I}_2}}\mathbf{F}\Big(\sum_{i=1}^{3}\alpha_i\frac{\partial\mathcal{I}_i}{\partial\mathbf{C}}\Big)\mathbf{F}^{\top}, \tag{2.121}$$

where $\alpha_i = \partial\Phi/\partial\mathcal{I}_i$ $(i = 1, 2, 3)$. Straightforward calculations based on the definitions (2.86) lead to

$$\frac{\partial\mathcal{I}_1}{\partial\mathbf{C}} = \mathrm{tr}(\mathbb{C})\mathbb{P}_{\mathbb{m}} - \mathbb{C},\ \frac{\partial\mathcal{I}_2}{\partial\mathbf{C}} = \mathcal{I}_2\mathbf{C}^{-1},\ \frac{\partial\mathcal{I}_3}{\partial\mathbf{C}} = \mathbb{m}\otimes\mathbb{m}. \tag{2.122}$$

Using (2.122) in (2.121) results in

$$\mathbf{T} = \frac{2}{\sqrt{\mathcal{I}_2}}\Big(\alpha_1(I_1(\mathbb{B})\mathbb{B} - \mathbb{B}^2) + \alpha_2\mathcal{I}_2\mathbf{1} + \alpha_3\mathbf{F}\mathbb{m}\otimes\mathbf{F}\mathbb{m}\Big), \tag{2.123}$$

where $\mathbb{B} = \mathbb{F}\mathbb{F}^{\mathrm{T}}$. Notice that, in contrast to $\mathbb{C}$, $\mathbb{B}$ need not be a fully-tangential tensor. When the lipid bilayer is incompressible, (2.123) should be replaced by

$$\mathbf{T} = -p\mathbf{1} + 2(\tilde{\alpha}_1(I_1(\mathbb{B})\mathbb{B} - \mathbb{B}^2) + \tilde{\alpha}_3\mathbf{F}\mathbb{m}\otimes\mathbf{F}\mathbb{m}), \tag{2.124}$$

where $\tilde{\alpha}_i = \partial\tilde{\Phi}/\partial\mathcal{I}_i$ $(i = 1, 3)$, and p is an unknown Lagrange multiplier that penalizes the incompressibility.

2.9 Dimension reduction for an incompressible lipid bilayer

The derivation of two-dimensional models of shell-like structures from three-dimensional elasticity has long been a subject of interest. For a comprehensive review of this subject, see Ciarlet [132]. Simmonds [133], Stumpf and Makowski [134], Taber [135, 136, 137], and Yükseler [138] have all used the procedure to develop hyperelastic shell theories. However, Zurlo [63] and Deseri et al. [64] were the first to apply it to biomembranes. In contrast to the present work, Zurlo [63] and Deseri et al. [64] neglected spontaneous curvature.

2.9.1 General strategy

Granted that a lipid bilayer has thickness considerably smaller than its lateral dimensions, it is very reasonable to attribute to it an energy density, per unit area. The main goal of the dimension reduction described in this section is to obtain an areal energy density $\psi_\circ$ from the volumetric energy density W in accord with the condition

$$\int\limits_{D_\circ} \psi_\circ \, \mathrm{d}A_\circ = \int\limits_{P} W \, \mathrm{d}v, \tag{2.125}$$

where $\psi_\circ$ is measured per unit area on the referential midsurface $S_\circ$, $\mathrm{d}v$ is the referential volume element, $D_\circ \subset S_\circ$ is an arbitrary area on $S_\circ$, and $P \subset B$ is the material region associated with $D_\circ$, the lateral faces of which are normal to $S_\circ$ and extended to the inner and outer surfaces S^{i} and S^{o} (see Figure 2–4).

In view of (2.90), (2.91), and (2.107), we conclude that

$$\int\limits_{D_\circ} \psi_\circ \, \mathrm{d}A_\circ = \int\limits_{D_\circ} \int\limits_{-h_\circ^-}^{h_\circ^+} \Phi(\mathcal{I}_1, \mathcal{I}_2, \mathcal{I}_3)\gamma_\circ(\xi_\circ) \, \mathrm{d}\xi_\circ \mathrm{d}A_\circ. \tag{2.126}$$

Since $D_\circ$ is an arbitrary domain, (2.126) implies that

$$\psi_\circ = \int\limits_{-h_\circ^-}^{h_\circ^+} \Phi(\mathcal{I}_1, \mathcal{I}_2, \mathcal{I}_3)\gamma_\circ(\xi_\circ) \, \mathrm{d}\xi_\circ. \tag{2.127}$$

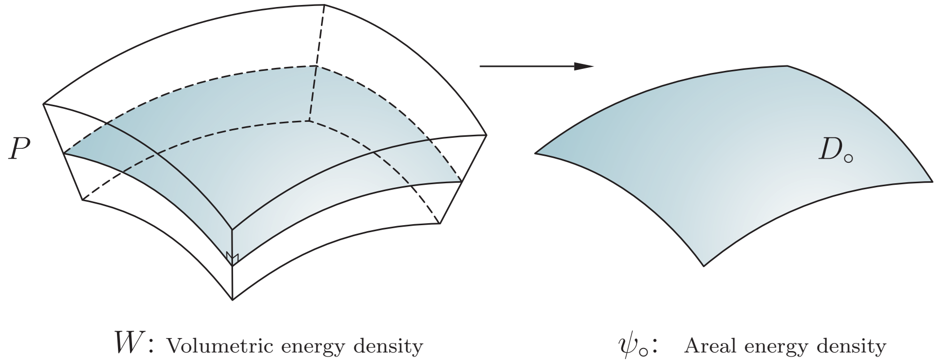

Figure 2–4: Schematic of the dimension reduction.

Regarding (2.105), (2.110), and (2.111), and bearing in mind that Φ is an arbitrary function of the invariants $\mathcal{I}_1$, $\mathcal{I}_2$, and $\mathcal{I}_3$, it is evident that the integrand of (2.127) may, in general, depend on $\xi_\circ$ in a complex manner. This makes integrating (2.127) difficult. A suitable approximate approach is to expand the integrand in (2.127) about $\xi_\circ = 0$ and truncate consistent with some desired degree of accuracy.

2.9.2 Expansion

Consistent with the consensus regarding the near incompressibility of lipid bilayers, we conduct this expansion only for an energy density of the form (2.115), in which case (2.127) is replaced by

$$\psi_\circ = \int_{-h_\circ^-}^{h_\circ^+} \tilde{\Phi}(\mathcal{I}_1, \mathcal{I}_3)\gamma_\circ(\xi_\circ)\,\mathrm{d}\xi_\circ. \tag{2.128}$$

Notice that, by (2.105), (2.111), and (2.116), the values of the invariants $\mathcal{I}_1$ and $\mathcal{I}_3$ at $S_\circ$ are

$$\mathcal{I}_1|_\circ = J^2 \tag{2.129}$$

and

$$\mathcal{I}_3|_\circ = J^{-2}. \tag{2.130}$$

In view of (2.129) and (2.130), the values of $\tilde{\Phi}$ and any of its partial derivatives at $\xi_\circ = 0$ may depend at most on the areal stretch J. Anticipating the need to expand $\tilde{\Phi}$ up to second order in $\xi_\circ$, it is therefore convenient to introduce J-dependent quantities f_0, f_1, f_3, f_{11}, f_{13}, and f_{33} via

$$\left.\begin{aligned} f_0 &= \tilde{\Phi}(\mathcal{I}_1,\mathcal{I}_3)|_\circ, \\ f_k &= \left.\frac{\partial\tilde{\Phi}(\mathcal{I}_1,\mathcal{I}_3)}{\partial\mathcal{I}_k}\right|_\circ, \quad k = 1,3, \\ f_{kl} &= \left.\frac{\partial^2\tilde{\Phi}(\mathcal{I}_1,\mathcal{I}_3)}{\partial\mathcal{I}_k\partial\mathcal{I}_l}\right|_\circ, \quad k,l = 1,3. \end{aligned}\right\} \tag{2.131}$$

Expanding $\tilde{\Phi}$ to second order in $\xi_\circ$ also requires the values of the first and second derivatives, with respect to $\xi_\circ$, of the invariants $\mathcal{I}_1$ and $\mathcal{I}_3$ at $\xi_\circ = 0$. On introducing

$$\tilde{H} = HJ^{-1} - H_\circ, \quad \tilde{K} = KJ^{-2} - K_\circ, \tag{2.132}$$

it follows that

$$\left.\begin{aligned} \mathcal{I}_1'|_\circ &= -4J^2\tilde{H}, \\ \mathcal{I}_3'|_\circ &= 4J^{-2}\tilde{H}, \\ \mathcal{I}_1''|_\circ &= -2J^2(12H_\circ\tilde{H} - 2\tilde{K} - J^{-4}|\nabla_{\mathcal{S}_\circ}J|^2), \\ \mathcal{I}_3''|_\circ &= 4J^{-2}(8\tilde{H}^2 + 6H_\circ\tilde{H} - \tilde{K}). \end{aligned}\right\} \tag{2.133}$$

Expanding $\tilde{\Phi}$ then yields

$$\psi_\circ = \int_{-h_\circ^-}^{h_\circ^+} (f_0 + \alpha_1\xi_\circ + \tfrac{1}{2}\alpha_2\xi_\circ^2 + \mathrm{o}(\xi_\circ^2))\gamma_\circ(\xi_\circ)\,\mathrm{d}\xi_\circ, \tag{2.134}$$

where α_1 and α_2 are given by

$$\alpha_1 = (f_1\mathcal{I}_1' + f_3\mathcal{I}_3')|_\circ \tag{2.135}$$

and

$$\alpha_2 = (f_1\mathcal{I}_1'' + f_3\mathcal{I}_3'' + f_{11}(\mathcal{I}_1')^2 + 2f_{13}\mathcal{I}_1'\mathcal{I}_3' + f_{33}(\mathcal{I}_3')^2)|_\circ, \tag{2.136}$$

respectively.

2.9.3 Restriction to mild areal stretch

Hereafter, we confine our attention to circumstances under which the areal stretch J of the referential midsurface $S_\circ$ is sufficiently mild to ensure that

$$h_\circ J^{-1}|\nabla_{\mathcal{S}_\circ} J| \ll 1. \tag{2.137}$$

The gradient term on the right-hand side of $(2.133)_3$ is then negligible in comparison to other terms. With this in mind, substituting (2.131), (2.135), and (2.136) in (2.134), performing the integration, and truncating yields an expression for the areal energy density $\psi_\circ$, measured per unit area of $S_\circ$, yields an expression that depends on $H_\circ$, $K_\circ$, H, K, and J. The dimension reduction therefore provides an areal energy density which includes the effects of spontaneous mean and Gaussian curvatures, deformed mean and Gaussian curvatures, and areal stretch.

In addition, an areal energy density ψ, measured per unit area in the deformed state, has the form

$$\psi = J^{-1}\psi_\circ \tag{2.138}$$

and, thus, depends on the same quantities upon which $\psi_\circ$ depends.

2.9.4 Specialization to symmetric bilayers

Suppose that the leaflets of the bilayer have identical thickness $h_\circ = h_\circ^+ = h_\circ^-$ and molecular composition, in which case they should be described by a single response function $\tilde{\Phi}$. The areal energy density $\psi_\circ$ determined by the dimension reduction argument then simplifies to

$$\psi_\circ = \psi_{\mathrm{m}} + \tfrac{1}{2}\kappa(HJ^{-1} - \bar{H}_\circ)^2 + \bar{\kappa}\tilde{K}, \tag{2.139}$$

where ψ_{m}, $\bar{H}_\circ$, κ, and $\bar{\kappa}$ are given by

$$\left.\begin{aligned} \psi_{\mathrm{m}} &= 2h_\circ(1 + \tfrac{1}{6}h_\circ^2 K_\circ)f_0 \\ &\qquad + \tfrac{4}{3}h_\circ^3 H_\circ^2(J^2(1-\nu)f_1 - J^{-2}(1+7\nu)f_3), \\ \bar{H}_\circ &= H_\circ(1+\nu), \\ \kappa &= \tfrac{32}{3}h_\circ^3 J^2\mu, \quad \bar{\kappa} = \tfrac{4}{3}h_\circ^3 J^2\eta. \end{aligned}\right\} \tag{2.140}$$

with

$$\left.\begin{aligned} \nu &= \frac{\eta}{4\mu}, \quad \eta = (f_1 - J^{-4}f_3), \\ \mu &= 2J^{-4}f_3 - 2J^{-2}f_{13} + J^{-6}f_{33} + J^2 f_{11}, \end{aligned}\right\} \tag{2.141}$$

Notice that the bending moduli κ and $\bar{\kappa}$ given in $(2.140)_{3,4}$ scale with the cube of the leaflet thickness $h_\circ$. Moreover, those moduli differ from those obtained by

Zurlo [63] and Deseri et al. [64]. The difference stems from our use of the exact incompressibility condition (2.116) in place of their use of the quasi-incompressibitlity condition (2.118). For instance, the bending moduli in (2.140) include derivatives of $\tilde{\Phi}$ with respect to $\mathcal{I}_3$, derivatives which are absent from the result of Zurlo [63] and Deseri et al. [64].

2.9.5 Alternative interpretations of the splay and saddle-splay moduli

We now provide alternative interpretations of the splay and saddle-splay moduli κ and $\bar{\kappa}$. Consider the state of stress at the spatial midsurface $\mathcal{S}_\circ$ of an incompressible lipid bilayer. Since $\mathbb{F}_\circ$ is a tangential tensor, $\mathbb{F}_\circ^\top \mathbb{n} = \mathbf{0}$ and $\mathbb{B}_\circ = \mathbb{F}_\circ \mathbb{F}_\circ^\top$ is a fully tangential tensor. Using (2.196), it can be shown that $I_2(\mathbb{B}_\circ) = I_2(\mathbb{C}_\circ) = J^2$. As a consequence of these facts, (2.124) yields

$$\begin{aligned} \mathbf{T}_\circ &:= \mathbf{T}|_{\xi=0} \\ &= -p\mathbf{1} + 2(J^2 f_1 \mathbb{P}_{\mathbb{n}} + f_3(\mathbf{F}\mathbb{m} \otimes \mathbf{F}\mathbb{m})|_\circ). \end{aligned} \tag{2.142}$$

Consistent with the kinematical assumption regarding the orientation of the phospholipid molecules, consider a deformation with the property

$$\mathbf{F}|_\circ \mathbb{m} = \phi \mathbb{n}, \quad \phi > 0, \tag{2.143}$$

where ϕ is an arbitrary constant. Also, as is customary in the theory of thin shell-like structures, assume that the normal stress $\mathbb{n} \cdot \mathbf{T}\mathbb{n}$ is very small compared to all other relevant stress components. Then, in view of (2.143) and the assumption $\mathbb{n} \cdot \mathbf{T}_\circ \mathbb{n} = 0$, (2.142) can be written as

$$\mathbf{T}_\circ = 2(f_1 J^2 - \phi^2 f_3)\mathbb{P}_{\mathbb{n}}. \tag{2.144}$$

Moreover, (2.143) reduces $\mathbf{C}$ in (2.63) to

$$\mathbf{C}|_\circ = \mathbb{C}_\circ + \phi^2 \mathbb{m} \otimes \mathbb{m}. \tag{2.145}$$

Since the deformation must be isochoric, we find that

$$\phi^2 = (I_2(\mathbb{C}_\circ))^{-1} = J^{-2}, \tag{2.146}$$

which allows us to reduce (2.144) to

$$\begin{aligned} \mathbf{T}_\circ &= 2J^2(f_1 - J^{-4} f_3)\mathbb{P}_{\mathbb{n}}, \\ &=: \Sigma \mathbb{P}_{\mathbb{n}}. \end{aligned} \tag{2.147}$$

Notice that $\mathbf{T}_\circ$ is an isotropic tensor on the tangent space of $\mathcal{S}_\circ$. Also, Σ can be considered as the in-plane tension or compression at the spatial midsurface $\mathcal{S}_\circ$. Invoking the definitions of Σ in (2.147) and η provided in $(2.141)_2$, we find that

$$\eta = \tfrac{1}{2} J^{-2} \Sigma. \tag{2.148}$$

In addition, we may define

$$\Lambda := \frac{\partial \Sigma}{\partial J}, \tag{2.149}$$

as the areal stiffness of the lipid bilayer at $\mathcal{S}_\circ$, which, with (2.141) and (2.147), can be expressed as

$$\Lambda = 4J(\mu + \eta). \tag{2.150}$$

Using (2.148), relation (2.150) becomes

$$\mu = \frac{J\Lambda - 2\Sigma}{4J^2}. \tag{2.151}$$

Then, on using (2.148) and (2.151), the splay and saddle-splay moduli defined in (2.140) can be expressed in terms of Σ and Λ as

$$\kappa = \tfrac{8}{3}h_\circ^3(J\Lambda - 2\Sigma), \quad \bar{\kappa} = \tfrac{2}{3}h_\circ^3\Sigma. \tag{2.152}$$

2.9.6 Canham–Helfrich-type energy density

In many studies, due to high in-plane resistance, the lipid bilayer is stipulated to be inextensible and this constraint is imposed by adding a suitable term to the areal energy density. Necessarily, the introduction of such a constraint is accompanied by the need for a Lagrange multiplier. In this case, the deformation of the lipid bilayer is dominated by bending. To address this limit in our setting, consider the limiting case of $J \approx 1$. Regarding the definition of ν in $(2.141)_1$, and using (2.148) and (2.151), it can be concluded that

$$\nu = \frac{\Sigma}{2(J\Lambda - 2\Sigma)}. \tag{2.153}$$

In accordance with the high in-plane resistance of the lipid bilayer, the ratio of the areal stress Σ and stiffness Λ should be very small (i.e., $\Sigma\Lambda^{-1} \approx 0$), leading to $\nu \approx 0$. Thus, the areal energy density is well approximated by

$$\psi_\circ = \psi_{\mathrm{m}} + \tfrac{1}{2}\kappa(H - H_\circ)^2 + \bar{\kappa}(K - K_\circ), \tag{2.154}$$

with

$$\psi_{\mathrm{m}} = 2h_\circ(f_0(1 + \tfrac{1}{6}h_\circ^2K_\circ) + \tfrac{2}{3}\eta h_\circ^2H_\circ^2), \tag{2.155}$$

and

$$\left.\begin{aligned}\kappa &= \tfrac{32}{3}h_\circ^3(2f_3 - 2f_{13} + f_{33} + f_{11}),\\ \bar{\kappa} &= \tfrac{4}{3}h_\circ^3(f_1 - f_3).\end{aligned}\right\} \tag{2.156}$$

Also, using the approximations $J \approx 1$ and $\Sigma\Lambda^{-1} \approx 0$ in the expression $(2.152)_1$ for the splay modulus yields

$$\kappa = \tfrac{8}{3}h_\circ^3\Lambda; \tag{2.157}$$

however, the expression $(2.152)_2$ for the saddle-splay modulus remains unchanged with these approximations.

Assuming that the lipid bilayer is very thin, the membranal energy given in (2.155) reduces to $\psi_{\mathrm{m}} = 2h_\circ f_0$. Since f_0 only depends on J, the membranal energy can be represented as $\psi_{\mathrm{m}} = \varphi_\circ(J)$. Therefore, it is natural to introduce an effective surface tension

$$\sigma := \frac{\mathrm{d}\varphi_\circ}{\mathrm{d}J} \tag{2.158}$$

and an effective areal stiffness

$$\lambda := \frac{\mathrm{d}^2\varphi_\circ}{\mathrm{d}J^2}, \tag{2.159}$$

for the lipid bilayer. On using the definitions of η, Σ, and Λ in $(2.141)_2$, (2.147), and (2.149), respectively, and performing straitforward differentiation, it is possible to verify that

$$\eta = \tfrac{1}{2}J^{-1}\frac{\mathrm{d}f_0}{dJ},\ \Sigma = J\frac{\mathrm{d}f_0}{\mathrm{d}J},\ \Lambda = \Sigma J^{-1} + J\frac{\mathrm{d}^2 f_0}{\mathrm{d}J^2}, \tag{2.160}$$

which, in view of the approximations $J \approx 1$ and $\Sigma\Lambda^{-1} \approx 0$, and $(2.152)_2$ and (2.157), yields

$$\kappa = \tfrac{4}{3}h_\circ^2\frac{\mathrm{d}^2\varphi_\circ}{\mathrm{d}J^2},\ \bar{\kappa} = \tfrac{1}{3}h_\circ^2\frac{\mathrm{d}\varphi_\circ}{\mathrm{d}J}; \tag{2.161}$$

thus, on referring to (2.158) and (2.159), the splay and saddle-splay moduli can be expressed as

$$\kappa = \tfrac{4}{3}h_\circ^2\lambda, \quad \bar{\kappa} = \tfrac{1}{3}h_\circ^2\sigma. \tag{2.162}$$

From relations (2.162) it is evident that κ and $\bar{\kappa}$ are directly proportional to the effective areal stiffness and surface tension of the lipid bilayer, respectively.

When the bilayer is in a state of pure bending (i.e., $J = 1$), $\mathcal{I}_1$, and $\mathcal{I}_3$ are both equal to unity on the spatial midsurface $\mathcal{S}_\circ$, and thus $\mathcal{S}_\circ$ corresponds to the natural state—that is,

$$\tilde{\Phi}(\mathcal{I}_1, \mathcal{I}_3)\big|_{\xi_\circ = 0; J = 1} = 0, \tag{2.163}$$

whereby $f_0 = 0$. Thus, $\psi_{\rm m} = 0$, and

$$\psi_\circ = \tfrac{1}{2}\kappa(H - H_\circ)^2 + \bar{\kappa}(K - K_\circ). \tag{2.164}$$

Since the areal energy density is determinable only up to an arbitrary additive constant, (2.164) is equivalent to the the Canham–Helfrich energy density (2.1).

When the lipid bilayer is assumed inextensible, the areal energy density (2.164) should be considered, while the inextensibility constraint should be penalized by considering a Lagrange multiplier.

2.9.7 Effect of asymmetric chemistry of the leaflets

Now suppose that, due to possible trans-bilayer asymmetric chemistry of the leaflets [126, 127, 128, 1], the response functions $\tilde{\Phi}^+$ and $\tilde{\Phi}^-$ in the upper and lower leaflets differ. This situation is very probable when the spontaneous curvature is induced due to asymmetric distribution of lipid molecules with different molecular shapes across the midsurface of the lipid bilayer [1].

The dimension reduction then leads to an energy density of the form

$$\psi_\circ = \psi_\mathrm{m} + \tfrac{1}{2}\kappa(HJ^{-1} - \hat{H}_\circ)^2 + \bar{\kappa}\tilde{K}, \tag{2.165}$$

where ψ_m, $\hat{H}_\circ$, κ, and $\bar{\kappa}$ are given by

$$\left.\begin{aligned}
\psi_\mathrm{m} &= 2h_\circ(\langle f_0\rangle - \tfrac{1}{2}\llbracket f_0\rrbracket h_\circ H_\circ + \tfrac{1}{6}h_\circ^2\langle f_0\rangle K_\circ) \\
&\quad + \tfrac{4}{3}h_\circ^3 H_\circ^2(J^2(1-\hat{\nu})\langle f_1\rangle - J^{-2}(1+7\hat{\nu})\langle f_3\rangle) \\
&\quad - \kappa\hat{\nu}H_\circ H_\mathrm{c}, \\
\hat{H}_\circ &= H_\circ(1+\hat{\nu}) + H_\mathrm{c}, \\
\kappa &= \tfrac{32}{3}h_\circ^3\langle\mu\rangle J^2, \quad \bar{\kappa} = \tfrac{4}{3}h_\circ^3\langle\eta\rangle J^2,
\end{aligned}\right\} \tag{2.166}$$

with

$$H_\mathrm{c} = 2\frac{h_\circ^2 J^2}{\kappa}\llbracket\eta\rrbracket, \ \hat{\nu} = \frac{\langle\eta\rangle}{4\langle\mu\rangle}, \tag{2.167}$$

In addition, for the approximation $J \approx 1$, the counterpart of (2.154) takes the form

$$\psi_\circ = \psi_\mathrm{m} + \tfrac{1}{2}\kappa(H - (H_\circ + H_\mathrm{c}))^2 + \bar{\kappa}(K - K_\circ), \tag{2.168}$$

where ψ_m, H_c, κ, and $\bar{\kappa}$ are given by

$$\left.\begin{aligned}
\psi_\mathrm{m} &= 2h_\circ\langle f_0\rangle, \\
H_\mathrm{c} &= 2\frac{h_\circ^2}{\kappa}\llbracket f_1 - f_3\rrbracket, \\
\kappa &= \tfrac{32}{3}h_\circ^3\langle 2f_3 - 2f_{13} + f_{33} + f_{11}\rangle, \\
\bar{\kappa} &= \tfrac{4}{3}h_\circ^3\langle f_1 - f_3\rangle.
\end{aligned}\right\} \tag{2.169}$$

If, moreover, the lipid bilayer is in a state of pure bending then (2.168) reduces to

$$\psi_\circ = \tfrac{1}{2}\kappa(H - (H_\circ + H_\mathrm{c}))^2 + \bar{\kappa}(K - K_\circ). \tag{2.170}$$

Let H_c denote the *constitutively-induced spontaneous mean curvature* and introduce the *net spontaneous curvature* $H_\mathrm{sp} = H_\circ + H_\mathrm{c}$. The net spontaneous mean curvature H_sp for an asymmetric lipid bilayer is then seen to incorporate two contributions: (i) a geometrical contribution $H_\circ$, which stems from the spontaneous geometry of the lipid bilayer, due to asymmetric distribution of phospholipid molecules with different molecular shapes or due to other possible sources [1, 24]; (ii) a constitutive contribution H_c, which stems from differences between the constitutive properties of the leaflets.

Also, notice that the alternative representations of κ and $\bar{\kappa}$ in (2.152), (2.157), (2.161), and (2.162) remain valid under the present circumstances, except that Σ, Λ, and $\varphi_\circ$ should be replaced by $\langle\Sigma\rangle$, $\langle\Lambda\rangle$, and $\varphi_\circ = 2h_\circ\langle f_0\rangle$, respectively.

2.9.8 Effect of the incoherency between the leaflets

The areal energy density obtained by dimension reduction may be generalized to include the effect of incoherency between the leaflets. In such case, the invariants $\mathcal{I}_k^+$ and $\mathcal{I}_k^-$ $(k = 1, 3)$ and the areal stretches J^+ and J^- in the upper and lower leaflets differ. The integration in (2.128) must therefore be performed piecewise. Being very similar to the steps leading to (2.134), the steps involved are not shown. The final form of the areal energy density depends, as before, on $H_\circ$, $K_\circ$, H, and K; however, instead of J, it includes dependence on both J^+ and J^-.

2.9.9 Remarks

- The Canham–Helfrich energy density is an acceptable areal energy density when (i) the leaflets have identical thickness and the same response function (ii) the ratio of the thickness to the principal radii of curvature is very small, and (iii) the lipid bilayer has pure bending or it is inextensible.
- In contrast to the classical Canham–Helfrich energy density (2.1), our theory predicts that the spontaneous Gaussian curvature should be included in the areal energy density in a manner analogous to the spontaneous mean curvature. Moreover, in contrast to (2.1), the energy density (2.164) vanishes at the spontaneous state. This issue is not important in the case of homogeneous lipid bilayers because the energy density can be additively scaled by any constant. However, for heterogeneous lipid bilayers, such as multi-phase GUVs (e.g., see Baumgart et al. [76]), where the saddle-splay modulus or the spontaneous curvature are nonuniform, this distinction should be considered.
- As long as the response function $\tilde{\Phi}$ is known, the bending moduli κ and $\bar{\kappa}$ cannot be be arbitrary chosen. Rather, they derive from the response function $\tilde{\Phi}$. This is consistent with the conclusions of Zurlo [63] and Deseri et al. [64].
- The bending moduli κ and $\bar{\kappa}$ scale with the cube of the leaflet thickness $h_\circ$. This is in harmony with the deformation of a thin elastic sheet, for example, as described by the classical Föppl–von Kármán theory, where the bending rigidity is proportional to the cube of the sheet thickness. In addition, just as the bending rigidity of an isotropic homogeneous elastic sheet is linearly proportional to its Young modulus, the splay modulus κ is linearly proportional to

the in-plane stiffness of the lipid bilayer. In contrast, the saddle-splay modulus $\bar{\kappa}$ is linearly scaled with the surface tension in the lipid bilayer.

- The membranal energy ψ_{m} includes not only a term proportional to $h_\circ$ but also a secondary term proportional to $h_\circ^3$. This term also contains the spontaneous mean and Gaussian curvatures of the lipid bilayer. However, as long as the lipid bilayer is very thin, the contribution of this secondary term is negligible.
- Ostensibly, the areal energy density $\psi_\circ$ obtained from the dimension reduction argument should provide a basis for formulating variational problems to determine minimum energy configurations of lipid bilayers. However, to generate well-posed variational problems, the areal energy density $\psi_\circ$ should at very least satisfy the Legendre–Hadamard condition and thereby guarantee that the second (weak) variation of the underlying functional is positive. For example, based on the established Legendre–Hadamard condition for elastic surfaces of second-grade (see, for instance, Hilgers and Pipkin [139]), Steigmann [62] and Agrawal and Steigmann [78] derived the Legendre–Hadamard condition relevant to a lipid bilayer with an areal energy density depending generically on H, K, and J—which encompasses the result of the dimension reduction obtained here. If, in the present context, the assumption of mild areal stretch embodied by (2.137) does not hold, then, as is the case in the work of Zurlo [63] and Deseri et al. [64], the areal energy density $\psi_\circ$ will include an extra contribution proportional to $|\nabla_{\mathcal{S}_\circ} J|^2$. However, there is no reason to expect that the Legendre–Hadamard conditions for an areal energy density depending on H, K, J, and $|\nabla_{\mathcal{S}_\circ} J|$ should always be satisfied by the areal energy density arising

from the dimensional reduction argument, even if the three-dimensional energy density $\tilde{\Phi}$ leading to $\psi_\circ$ satisfies the appropriate three-dimensional Legendre–Hadamard condition. To see this consider, for example, a flat lipid bilayer, in which the energetic contribution of curvature is absent, so that

$$\psi_\circ = \varphi_\circ(J) + \frac{2}{3} h_\circ^3 J^{-2} f_1 |\nabla_{\mathcal{S}_\circ} J|^2. \tag{2.171}$$

The approach of Hilgers and Pipkin (1993) can then be used to show that the Legendre–Hadamard condition is satisfied only if $f_1 > 0$. A precise understanding of the sign of f_1 depends on the specific structure of the response function $\tilde{\Phi}$ and the value of areal stretch J on the midsurface. Nevertheless, in view of (2.147), it can be observed that f_1 may depend on the in-plane stress at the midsurface of the lipid bilayer. As long as f_1 is positive, the second variation of $\psi_\circ$ is positive and the equilibrium configuration of the lipid bilayer is stable (locally, at least). However, if f_1 is negative, due to a possible contraction in the lipid bilayer, then the Legendre–Hadamard condition is violated, implying that the configuration of the lipid bilayer is unstable. One way to cure this problem is to add a term to $\psi_\circ$, as Hilgers and Pipkin [140] did in their study of the equilibrium of elastic membranes with strain-gradient energies.

2.10 Summary

A continuum approach to modeling the deformation of lipid bilayers with spontaneous curvature was provided. In a departure from prevailing tradition, a lipid bilayer was modeled by a three-dimensional body. Apart from a kinematical constraint incorporating natural aspects of the behavior of lipid molecules, no further restrictions were imposed on the deformation. In this context, a general representation for the deformation gradient was derived. That representation involves the curvature tensor of the midsurface in the spontaneous (or reference) state, the curvature tensor of the midsurface in the deformed state, the deformation gradient of the midsurface, and changes in transverse thickness. The coherency of the leaflets that comprise a lipid bilayer, which entails considering local coupling or sliding of those leaflets, was explored, as was the topic of area compatibility.

Geometry and kinematics aside, the material symmetry of lipid bilayers that exhibit in-plane fluidity and transverse isotropy was studied. Moreover, modeling the bilayer as a hyperelastic material, a representation theorem for the energy density was developed. Three invariants were found to be sufficient to describe the constitutive behavior of a lipid bilayer. It was shown that these invariants describe local strecth of area elements parallel to the midsurface, volume change, and through-thickness stretching. Explicit expressions for these invariants were determined and presented in terms of fundamental kinematical quantities. Among these kinematical quantities are the referential and spatial midsurface curvatures, the areal stretch of the mid-surface, the transverse normal and shear strains (which, in the present setting, control thickness change and nonuniformity, respectively), and a coupling term between the surface gradient of the transverse deformation and the midsurface curvature tensor.

The special case of a lipid bilayer that—in accord with experimental observations—is incompressible was considered. Under this constraint, transverse deformation (with respect to the midsurface) of the lipid bilayer is coupled to midsurface deformation.

This purely geometrical and kinematical consideration suggests that when the midsurface of an incompressible lipid bilayer has nonuniform bending and/or stretching or when the spontaneous curvature is nonuniform, its thickness in the deformed state is, in general, nonuniform.

Granted that the lipid bilayer is sufficiently thin, a dimension reduction argument was used to extract an areal (two-dimensional) energy density from the volumetric energy density. The conditions under which a Canham–Helfrich-type energy density is derivable were discussed. An energy density for lipid bilayer with asymmetric leaflets was also obtained and it was shown that, for such a medium, the spontaneous curvature can be interpreted as combination of two contributions. The first contribution represents the preferred geometry (i.e., the spontaneous shape) of the lipid bilayer. The second contribution—which may be called the constitutively-induced spontaneous curvature—arises due to differences between the response functions of the leaflets. Lastly, the general form of the areal energy density for a lipid bilayer with incoherent leaflets was considered.

2.11 Appendices

2.11.1 Superficial fields

A field defined only on a surface is called superficial. For instance, $\mathbb{m}$ is a superficial unit vector field defined on the midsurface $S_\circ$. The three-dimensional gradient of such a field is undefined. However, a smooth extension of a superficial field to a three-dimensional neighborhood of the surface on which it is defined provides a means for defining its three-dimensional gradient (on the relevant neighborhood). The normally constant extension, in which a superficial field is stipulated to be constant along lines perpendicular to the surface on which it is defined, provides the simplest such extension [141]. For example, consider a scalar-valued superficial field f defined on $S_\circ$ and let f^{e} denote a smooth extension of f to a neighborhood of $S_\circ$. This extension can be used to define the surface gradient $\nabla_{S_\circ} f$ of f on $S_\circ$ in terms of the three-dimensional gradient ∇f^{e} of f^{e} by

$$\nabla_{S_\circ} f = \mathbb{P}_{\mathbb{m}} \nabla f^{\mathrm{e}}, \tag{2.172}$$

where

$$\mathbb{P}_{\mathbb{m}} = \mathbf{1} - \mathbb{m} \otimes \mathbb{m} \tag{2.173}$$

is the projection tensor onto the tangent space $T_\circ$ of $S_\circ$. Notice that ∇f^{e} in (2.172) must be evaluated at points on the surface $S_\circ$. It should be mentioned that $\nabla_{S_\circ} f$ as determined by (2.172) is independent of the particular features of the extension f^{e}. It is easily shown that $\nabla_{S_\circ} f$ is tangent to the surface $S_\circ$. Similarly, the surface gradient $\nabla_{S_\circ} \mathbf{g}$ and surface divergence $\mathrm{div}_{S_\circ} \mathbf{g}$ of vector-valued superficial field $\mathbf{g}$ are defined as

$$\left.\begin{aligned} \nabla_{S_\circ} \mathbf{g} &= (\nabla \mathbf{g}^{\mathrm{e}}) \mathbb{P}_{\mathbb{m}}, \\ \mathrm{div}_{S_\circ} \mathbf{g} &= \mathrm{tr}(\nabla_{S_\circ} \mathbf{g}) = \mathbb{P}_{\mathbb{m}} \cdot \nabla \mathbf{g}^{\mathrm{e}}, \end{aligned}\right\} \tag{2.174}$$

where $\mathbf{g}^{\mathrm{e}}$ is a smooth extension of $\mathbf{g}$. Here, as with ∇f^{e} in (2.172), $\nabla \mathbf{g}^{\mathrm{e}}$ is evaluated at the point on $S_\circ$. Additionally, in a suitably determined neighborhood of $S_\circ$, the gradient $\nabla \mathbf{g}$ and divergence $\mathrm{div}\, \mathbf{g}$ of a vector field $\mathbf{g}$ defined on a three-dimensional region containing $S_\circ$ decomposes according to

$$\left.\begin{aligned} \nabla \mathbf{g} &= \nabla_{S_\circ} \mathbb{g} + \frac{\partial \mathbf{g}}{\partial \mathbb{m}} \otimes \mathbb{m}, \\ \operatorname{div} \mathbf{g} &= \operatorname{div}_{S_\circ} \mathbb{g} + \frac{\partial \mathbf{g}}{\partial \mathbb{m}} \cdot \mathbb{m}, \end{aligned}\right\} \tag{2.175}$$

where $\mathbb{g} = \mathbf{g}|_{S_\circ}$ is the restriction of $\mathbf{g}$ to $S_\circ$ and

$$\frac{\partial \mathbf{g}}{\partial \mathbb{m}} = (\nabla \mathbf{g})\mathbb{m} \tag{2.176}$$

is the normal derivative of $\mathbf{g}$.

A superficial tensor field $\mathbb{G}$, besides being defined only on a surface, must satisfy

$$\mathbb{G}\mathbb{m} = \mathbf{0}. \tag{2.177}$$

For example, the surface gradient $\nabla_{S_\circ}\mathbb{g}$ of superficial vector field $\mathbb{g}$ is a superficial tensor field. If $\mathbb{G}$ also obeys

$$\mathbb{G}^\top \mathbb{m} = \mathbf{0}, \tag{2.178}$$

then $\mathbb{G}$ is said to be a fully tangential tensor field. For example, the projection tensor $\mathbb{P}_{\mathbb{m}}$ is fully tangential.

Other examples of fully tangential tensor fields are the curvature tensors $\mathbb{L}_\circ$ and $\mathbb{L}$ of the surfaces $S_\circ$ and $\mathcal{S}_\circ$, as defined by

$$\mathbb{L}_\circ = -\nabla_{S_\circ}\mathbb{m}, \ \ \mathbb{L} = -\nabla_{\mathcal{S}_\circ}\mathbb{n}. \tag{2.179}$$

$\mathbb{L}_\circ$ and $\mathbb{L}$ each possess at most two nontrivial scalar invariants. Convenient choices for these are the mean and Gaussian curvatures. Specifically, while

$$\left.\begin{aligned} H_\circ &= \tfrac{1}{2}I_1(\mathbb{L}_\circ) = \tfrac{1}{2}\mathrm{tr}(\mathbb{L}_\circ), \\[1em] K_\circ &= I_2(\mathbb{L}_\circ) = \tfrac{1}{2}[(\mathrm{tr}(\mathbb{L}_\circ))^2 - \mathrm{tr}(\mathbb{L}_\circ^2)], \end{aligned}\right\} \tag{2.180}$$

define the mean and Gaussian curvatures $H_\circ$ and $K_\circ$ of the surface $S_\circ$,

$$\left.\begin{aligned} H &= \tfrac{1}{2}I_1(\mathbb{L}) = \tfrac{1}{2}\mathrm{tr}(\mathbb{L}), \\[1em] K &= I_2(\mathbb{L}) = \tfrac{1}{2}[(\mathrm{tr}(\mathbb{L}))^2 - \mathrm{tr}(\mathbb{L}^2)], \end{aligned}\right\} \tag{2.181}$$

define the analogous quantities for $\mathcal{S}_\circ$.

A useful property of any fully tangential tensor $\mathbb{A}$ is the relation

$$\mathbb{A}^{\mathrm{c}} = \mathbb{A}^2 - I_1(\mathbb{A})\mathbb{A} + I_2(\mathbb{A})\mathbf{1} \tag{2.182}$$

determining its cofactor $\mathbb{A}^{\mathrm{c}}$, where $I_1(\mathbb{A})$ and $I_2(\mathbb{A})$ are first two principal invariants of $\mathbb{A}$. A simple, but useful consequence of (2.182) is that

$$\mathbb{A}^{\mathrm{c}}\mathbb{m} = I_2(\mathbb{A})\mathbb{m}. \tag{2.183}$$

Notice that $I_2(\mathbb{A})$ can be viewed as the determinant of a two-dimensional matrix representation of $\mathbb{A}$. Having this in mind, other useful identities can be established, including

$$I_2(\mathbb{A}^{\top}) = I_2(\mathbb{A}), \quad I_2(\mathbb{A}\mathbb{B}) = I_2(\mathbb{A})I_2(\mathbb{B}), \tag{2.184}$$

with $\mathbb{B}$ also being a fully tangential tensor.

2.11.2 Pseudoinverse of a fully tangential tensor

Let $\mathbb{A}$ be a fully tangential tensor. Then

$$\mathbb{A}\mathbb{m} = \mathbb{A}^{\top}\mathbb{m} = \mathbf{0} \tag{2.185}$$

and

$$\mathbb{A} = \mathbb{P}_{\mathbb{m}}\mathbb{A} = \mathbb{A}\mathbb{P}_{\mathbb{m}}. \tag{2.186}$$

Since the determinant of $\mathbb{P}_{\mathbb{m}}$ vanishes, (2.186) implies that the determinant of $\mathbb{A}$ must also vanish. Consequently, as a mapping from three-dimensional vector space to itself, $\mathbb{A}$ is not invertible. However, from (2.186), $\mathbb{A}$ maps any vector from the tangent space $T_{\circ}$ to a vector in $T_{\circ}$. If $\mathbb{A}$, considered as a mapping from $T_{\circ}$ to $T_{\circ}$, is one-to-one and, thus, invertible, then there exists a tensor $\mathbb{A}^{\dagger}$ satisfying

$$\mathbb{A}\mathbb{A}^{\dagger} = \mathbb{A}^{\dagger}\mathbb{A} = \mathbb{P}_{\mathbb{m}}. \tag{2.187}$$

In view of (2.187), $\mathbb{A}^{\dagger}$ provides an inverse for $\mathbb{A}$ as a mapping from $T_{\circ}$ to $T_{\circ}$. However, $\mathbb{A}^{\dagger}$ does not provide an inverse of $\mathbb{A}$ considered as a mapping from three-dimensional vector space to itself. Thus, $\mathbb{A}^{\dagger}$ may be thought of as a *pseudoinverse* of $\mathbb{A}$.

To obtain the pseudoinverse $\mathbb{A}^{\dagger}$ of a fully tangential tensor $\mathbb{A}$ that is a one-to-one mapping from $T_{\circ}$ to $T_{\circ}$, consider the Cayley–Hamilton equation

$$\mathbb{A}^3 - I_1(\mathbb{A})\mathbb{A}^2 + I_2(\mathbb{A})\mathbb{A} = \mathbf{0}, \tag{2.188}$$

for $\mathbb{A}$. (Notice that, since $\mathbb{A}$ is fully tangential, its third principal invariant $I_3(\mathbb{A})$ obeys $I_3(\mathbb{A}) = \det\mathbb{A} = 0$. Hence, a term proportional to $I_3(\mathbb{A})$ is absent from (2.188).) On applying the left-hand side of (2.188) to an arbitrary vector $\mathbf{t}$ and introducing the vector $\mathbb{u} = \mathbb{A}\mathbf{t}$, it follows that

$$(\mathbb{A}^2 - I_1(\mathbb{A})\mathbb{A} + I_2(\mathbb{A})\mathbb{P}_{\mathbb{m}})\mathbb{u} = \mathbf{0}. \tag{2.189}$$

Since $\mathbb{u}$ is a tangent vector and, thus, $\mathbb{P}_{\mathbb{m}}\mathbb{u} = \mathbb{u}$, keeping 2.185 and (2.186) in mind, (2.189) yields

$$\begin{aligned} \mathbb{u} &= \mathbb{A}[(I_2(\mathbb{A}))^{-1}(I_1(\mathbb{A})\mathbb{P}_{\mathbb{m}} - \mathbb{A})]\mathbb{u} \\ &= [(I_2(\mathbb{A}))^{-1}(I_1(\mathbb{A})\mathbb{P}_{\mathbb{m}} - \mathbb{A})]\mathbb{A}\mathbb{u}. \end{aligned} \tag{2.190}$$

Since, for any invertible tensor $\mathbf{T}$,

$$\mathbf{T}\mathbf{T}^{-1}\mathbb{u} = \mathbf{T}^{-1}\mathbf{T}\mathbb{u}, \tag{2.191}$$

it follows from (2.190) that

$$\mathbb{A}^{\dagger} = (I_2(\mathbb{A}))^{-1}(I_1(\mathbb{A})\mathbb{P}_{\mathbb{m}} - \mathbb{A}) \tag{2.192}$$

provides a pseudoinverse of the fully tangential tensor $\mathbb{A}$ that is one-to-one as a mapping from $T_\circ$ to $T_\circ$.

In view of (2.192), a fully tangential tensor $\mathbb{A}$ is pseudoinvertible if and only if

$$I_2(\mathbb{A}) \neq \mathbf{0}. \tag{2.193}$$

Granted that $\mathbb{A}$ is fully tangential, $\mathbb{A}^{\dagger}$ defined by (2.192) is also fully tangential—that is, $\mathbb{A}^{\dagger}$ defined by (2.192) obeys

$$\mathbb{A}^{\dagger}\mathbb{m} = (\mathbb{A}^{\dagger})^{\top}\mathbb{m} = \mathbf{0}, \tag{2.194}$$

and

$$\mathbb{A}^{\dagger} = \mathbb{P}_{\mathbb{m}}\mathbb{A}^{\dagger} = \mathbb{A}^{\dagger}\mathbb{P}_{\mathbb{m}}. \tag{2.195}$$

Also multiplying (2.192) by $\mathbb{A}$ and using (2.187), while invoking (2.193), yields the relation

$$\mathbb{A}^2 - I_1(\mathbb{A})\mathbb{A} + I_2(\mathbb{A})\mathbb{P}_{\mathbb{m}} = \mathbf{0}, \tag{2.196}$$

which can be viewed as the Cayley–Hamilton equation for a fully tangential tensor (see also Simmonds [133] for a discussion of the Cayley–Hamilton equation for a linear mapping of two-dimensional vector space into itself). Finally, using (2.196) in (2.182) leads to

$$\mathbb{A}^{\mathrm{c}} = I_2(\mathbb{A})\mathbb{m} \otimes \mathbb{m}. \tag{2.197}$$

CHAPTER 3
Multidomain and ground-state configurations of two-phase vesicles

3.1 Preface

Chapter 2 was devoted to a continuum approach to mechanics of lipid bilayers with spontaneous curvature, leading to an areal energy density describing the bending of lipid bilayers. Prominent examples of biological structures composed of lipid bilayers are lipid vesicles. These vesicles, with very good approximation, can be modeled as fluid surfaces endowed with elastic bending energy. In this chapter, mechanical equilibria of two-phase vesicles are studied. Two general classes of configurations, namely multidomain and ground-state configurations, are studied. The present chapter shows how different underlying physical parameters contribute to the attainment of equilibrium configurations of two-phase vesicles. This chapter is reproduced from the published paper

M. Maleki and E. Fried, "Multidomain and ground state configurations of two-phase vesicles," *Journal of The Royal Society Interface*, vol. 10, no. 83, 20130112, 2013.
with permission from the Royal Society, and from the coauthor Prof. Eliot Fried.

3.2 Abstract

A simple model is used to study the equilibrium of lipid domains on two-phase vesicles. Two classes of configurations are considered, multidomain and ground-state configurations. For multidomain configurations, the vesicle has a finite number of

identical lipid domains. For ground-state configurations, the vesicle is fully phase separated into two coexisting domains. Whereas the volume enclosed by a vesicle with multidomains is fixed, the volume enclosed by a vesicle in a ground state is allowed to vary with the osmotic pressure. Guided by experimental observations, all domains are assumed to be spherical caps. In a multidomain configuration, the line tension is found to decrease with the number of domains present, with possible exceptions when the number of domains is very small. The importance of a critical osmotic pressure and a critical excess radius on ground-state configurations is explored. Emphasis is placed on understanding the variations of these critical quantities with relevant parameters.

3.3 Introduction

It is widely believed that lipids and proteins on the cell membrane interact to form very small stable regions called rafts [37]. Usually in the size range of 10–200 nm, rafts are domains in the liquid-ordered phase, enriched by saturated lipids and cholesterol, and surrounded by the background cell membrane in the liquid-disordered phase [38]. Rafts are crucial in protein sorting [41, 42]. They also coalesce to form larger regions that serve as platforms for cellular functions such as signaling, trafficking, endocytosis, and immune responses [37, 41, 42]. Moreover, it has been shown that pathogens such as viruses use rafts as gateways during attacks on cells [37, 41, 42, 43]. Despite many experimental and theoretical investigations, a definitive understanding of the size, stability, and lifetime of rafts remains elusive [38].

A major difficulty encountered in studying rafts is their observation. Nanoscopic rafts on the cell membrane are much smaller than the resolution of optical microscopes. Model membranes, namely Giant Unilamellar Vesicles (GUVs) composed of unsaturated phospholipids, saturated sphingolipids, and cholesterol, have a composition similar to the dominant composition of the cell membrane. On vesicles, phase separation provides a practical pathway for characterizing rafts in biological membranes [38, 42]. On GUVs, raft-like lipid domains, usually in the size range of 1–10 μm, are observable via conventional light microscopy [48]. The size and distribution of lipid domains arise due to competition between different energetic influences such as bending energy and line tension. Line tension is a manifestation of energetic interactions between phases at their interface.

Phase separation on GUVs and supported bilayers has been studied extensively both theoretically and experimentally. A significant part of the relevant literature focuses on studying microdomains from a nonequilibrium perspective, addressing issues such as growth dynamics and the recycling mechanism [69, 70, 71, 72, 73]. Numerous studies have also been devoted to understanding equilibrium configurations of multiphase vesicles [142, 74, 75, 143, 48, 3, 76, 77, 72, 78, 79, 144, 80, 81]. For recent reviews, see [145, 146]. Most theoretical works in this area involve solving an Euler–Lagrange equation (known as the shape equation), which hold in each domain, associated with boundary conditions at the interface between the domains.

Experimental observations on multiphase vesicles in the liquid phase reveal configurations in which the phase separated domains on vesicle very closely resemble spherical caps, usually in the liquid-ordered phase, surrounded by a spherical background, usually in the liquid-disordered phase [48, 3, 76, 72, 4, 85]. Configurations including both multiple ordered domains or only one large ordered domain are commonly observed. Such piecewise spherical configurations are more likely to be observed for vesicle under tension, due to osmotic pressure. These observations regarding the geometry of multiphase vesicles seem to have convinced more than a few researchers [72, 85] to confine attention to models in which the domains are taken to be spherical. This assumption obviates the need to solve the shape equation and thus significantly simplifies the calculations. The net potential energy becomes a function of the geometrical parameters, namely the radii of curvatures of the domains and contact angles, and equilibrium configurations result from minimizing with respect to those parameters.

Although the results of Yanagisawa et al. [72] and Semrau et al. [85] compare favorably with experimental observations and, thus, support the applicability of models based on piecewise spherical configurations, more careful attention to the conditions at interfaces remains necessary. In particular, while Yanagisawa et al. [72] and Semrau et al. [85] consider geometrical compatibility at interfaces they do not require satisfaction of the force balance. Force balance at an interface on a piecewise spherical vesicle relates the surface tensions of the adjacent areas and the line tension of the interface [76, 3, 77, 88, 86]. Notably, the interfacial force balance has been previously used to estimate of the line tension from experimental data [3, 86, 87]—from which it follows that the line tension in such modeling cannot generally be chosen arbitrarily, as it must be compatible with force balance. In addition, piecewise spherical models can overlook potentially important energetic information. This may occur on replacing thin transition layer with very high curvature by a sharp interface endowed with a (given constant) line tension. Comprehensive discussions of such transition (or boundary) layers appear for example in the works of Fournier and Ben Amar [82], Allain and Ben Amar [77], Das and Jenkins [83], and Trejo and Ben Amar [84]. The energy stored in a transition layer consists of two general sources. The first source is the chemical energy due to very high gradients of lipid species concentrations. The second source is the mechanical energy due to distortion and misalignment of lipid molecules. For example, the stretching/contraction of different lipid molecules with different hydrophobic tails, splay and tilt of lipid molecules are all mechanical sources of this kind. Then, representing the energy of a transition layer by a sharp interface endowed with line tension is very delicate and requires evaluation of the underlying energies at the boundary layer. Comprehensive studies of the line tension in multiphase lipid membranes have been undertaken [147, 148, 149, 150, 84]. In particular, Fournier and Ben Amar [82], Towles and Dan [150], and Trejo and Ben Amar [84] demonstrate that the line tension may be influenced by the contact angle at the junction between two phases. Questions regarding the suitability of taking the line tension to be constant therefore arise.

In a study of the instability of the vesicle due to protein adsorption, Allain and Ben Amar [88] obtain the equilibrium equations and associated interface conditions for a biphasic vesicle composed of two spherical caps. Working with the same geometrical assumptions, Allain and Ben Amar [77] develop a model for the budding and the fission of biphasic vesicles under tension. In accord with the property of tense vesicles, they implement a capillary solution in which the bending energies of two spherical caps are negligible in comparison to the line and the osmotic-pressure induced energies. They then improve the capillary solution by replacing the sharp interface (across which the slope is discontinuous) with a smooth boundary layer where the bending energy of the lipid domains is considered. Their analysis leads to an effective line tension which takes the elasticity of the boundary layer into account. Further discussion of their work appears at the end of the section in which we present our numerical results. Trejo and Ben Amar [84] use an asymptotic approach to explore the equilibrium of a biphasic vesicle composed of two spherical domains connected by a boundary layer. They conduct a detailed analysis taking into account various macroscopic and microscopic energetics, including local area-difference elasticity and the thickness change of the membrane. Within the spherical caps, which are referred to as "outer layers," they account for bending energy. In addition, they take the volume of the vesicle to be fixed. The analysis of Trejo and Ben Amar [84] focuses on understanding the contact angle and effective line tension at a junction separating the phases.

In this paper, we first discuss the local equilibrium of piecewise spherical vesicles, the junction conditions, and different energetics. Next, we consider two different classes of equilibrium configurations, multidomain and ground-state configurations. Our analysis of multidomain configurations builds on the works of Yanagisawa et al. [72] and Semrau et al. [85]. Although our analysis accounts only for the bending and line energies, by ensuring that the interfacial force balance is satisfied, we provide a more complete physical description. As a natural consequence of this and consistent with the works of Baumgart et al. [3], Tian et al. [86], and Hutchison et al. [87], we view the line tension as a dependent variable that can be obtained by satisfying the interfacial force balance. In contrast, the osmotic pressure is considered as the independent parameter that influences the surface tension in the domains. For multidomain configurations, we assume that the volume of the vesicle is fixed. Although the osmotic pressure does not change the volume of the system (and, hence, has no energetic contribution), we find that it influences the net potential-energy of the system through modulation of the line energy. For instance, Akimov et al. [148] discuss how the line tension increases with the surface tension. Importantly, our results show that line tension decreases with the number of domains, despite possible exceptions that may occur for very small numbers of domains. We next focus on ground-state configurations, which represent equilibria resulting from the coalescence of multiple domains into a single domain. In contrast to our treatment of multidomain configurations, we allow the volume enclosed by the vesicle in a ground-state configuration to change. In so doing, we explore the effect of osmotic pressure and initial excess radius of a vesicle on its equilibrium configuration. We determine critical values of the osmotic pressure and the initial excess radius and investigate their effect on the final shape of a vesicle in a ground-state configuration. Finally, we discuss and compare our approach to ground state configurations with that of Allain and Ben Amar [77].

3.4 Formulation

3.4.1 Local equilibrium of spherical vesicles

Consider a vesicle with superficial energy density $\psi = \bar{\psi}(H, K)$, where H and K are the mean and Gaussian curvatures, respectively. The shape equation for such membrane is (see alternative expressions provided, for example, by Steigmann [62] and Steigmann et al. [116])

$$\begin{aligned}(2H^2 - K)\bar{\psi}_H + \tfrac{1}{2}\Delta_s\bar{\psi}_H + 2KH\bar{\psi}_K + 2\Delta_s(\bar{\psi}_K H) - \operatorname{div}_s(\mathbb{L}\nabla_s\bar{\psi}_K)\\ - 2\nabla_s\bar{\psi}_K\cdot\nabla_s H - 2\bar{\psi}_K\Delta_s H - 2H(\bar{\psi}+\sigma) = p,\end{aligned} \tag{3.1}$$

where $\bar{\psi}_H$ and $\bar{\psi}_K$ represent the partial derivatives of $\bar{\psi}$ with respect to H and K, ∇_s and div_s indicate the surface gradient and divergence, and $\mathbb{L}$, σ, and p respectively denote the curvature tensor, surface tension, and osmotic pressure.

Assume now that the vesicle is spherical with radius R, so that

$$H = -\frac{1}{R}, \quad K = \frac{1}{R^2}, \tag{3.2}$$

and the shape equation (3.1) specializes to

$$\frac{1}{R^2}\bar{\psi}_H - \frac{1}{R^3}\bar{\psi}_K + \frac{2}{R}(\bar{\psi} + \sigma) = p. \tag{3.3}$$

Suppose, further, that $\bar{\psi}$ is of the Canham–Helfrich [21, 22] form, but with zero spontaneous curvature, so that

$$\bar{\psi} = \tfrac{1}{2}\kappa H^2 + \overline{\kappa}K, \tag{3.4}$$

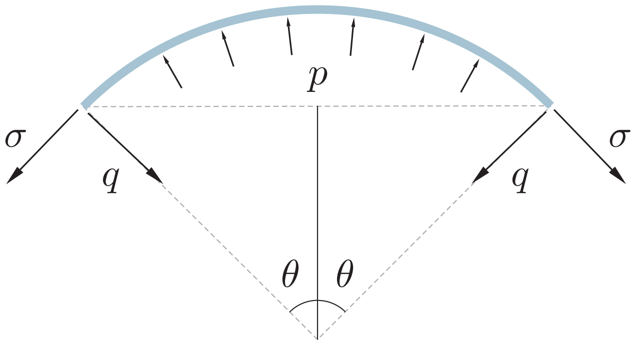

Figure 3–1: A two-dimensional cross section of a spherical cap under pressure p, surface tension σ, and transverse shear force q.

where κ and $\bar{\kappa}$ are the splay and saddle-splay moduli. Substituting (3.4) in (3.3) yields

$$\sigma = \tfrac{1}{2}pR, \tag{3.5}$$

which is the classical Young–Laplace equation. The reduction of the shape equation to the Young–Laplace equation in the absence of the spontaneous curvature is also discussed by Allain and Ben Amar [88], Baumgart et al. [76] and Idema and Storm [81]. A generalization of (3.5) that incorporates spontaneous curvature is provided by Ou-Yang and Helfrich [151, 152]. Trejo and Ben Amar [84] provide a similar relation which, in addition to considering spontaneous curvature, accounts for variations in membrane thickness.

Consider now a spherical cap, with arbitrary opening angle 2θ, cut from a spherical vesicle and subject to uniform pressure p, as depicted in Figure 3–1. Suppose that, in addition to the surface tension σ, the bilayer supports a transverse shear force q.

The force balance in the vertical direction then requires that

$$p\big(\pi(R\sin\theta)^2\big) = \sigma\sin\theta(2\pi R\sin\theta) + q\cos\theta(2\pi R\sin\theta), \tag{3.6}$$

which upon using (3.5) yields $q = 0$. Thus, a spherical bilayer described by the Canham–Helfrich bending energy (in the absence of the spontaneous curvature) under uniform pressure cannot support transverse shear force.

3.4.2 Junction condition

Consider a two-phase vesicle, composed of phases α and β, as depicted in Figure 3–2. Suppose that the domains occupied by phases α and β are spherical caps, with respective radii of curvature R_α and R_β. Denote the radius of curvature of the junction between the phases by ρ. As a consequence of force balance at the junction in the direction perpendicular to the plane in which the junction resides, it follows that

$$\sigma_\alpha\sin\theta_\alpha = \sigma_\beta\sin\theta_\beta, \tag{3.7}$$

where σ_α and σ_β are the surface tensions in phases α and β, respectively, and the angles θ_α and θ_β are as indicated in Figure 3–2. In view of (3.5) and the geometrical relation

$$R_\alpha\sin\theta_\alpha = R_\beta\sin\theta_\beta = \rho, \tag{3.8}$$

(3.7) is satisfied identically. Further, the balance of force in the plane within which the junction resides yields

$$-(\sigma_\alpha\cos\theta_\alpha + \sigma_\beta\cos\theta_\beta)\rho = \tau. \tag{3.9}$$

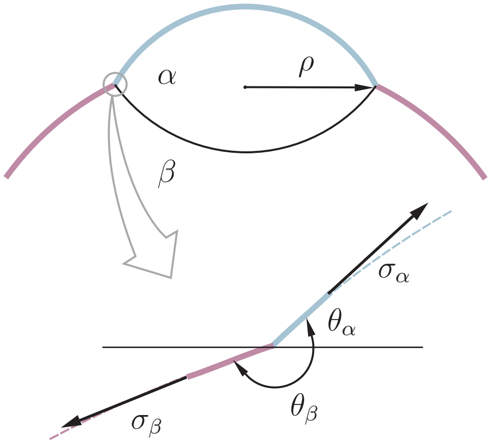

Figure 3–2: A junction between spherical caps occupied by two phases α and β.

The surface tensions σ_α and σ_β are determined by the Young–Laplace equation (3.5) through

$$\sigma_\alpha = \tfrac{1}{2}pR_\alpha, \quad \sigma_\beta = \tfrac{1}{2}pR_\beta. \tag{3.10}$$

In view of (3.8) and (3.10), (3.9) can be written as

$$\cot\theta_\alpha - \cot\phi = -\frac{2\tau}{p\rho^2}, \tag{3.11}$$

with $\phi = \pi - \theta_\beta$. Equation (3.11) or equivalent versions of that equation were derived previously by Baumgart et al. [3, 76], Allain and Ben Amar [88, 77], Tian et al. [86], and Hutchison et al. [87].

3.4.3 Geometrical relations

Consider a vesicle consisting of N identical spherical caps of phase α surrounded by a background phase β with constant radius of curvature R_β. Straightforward calculations show that the net areas A_α and A_β occupied by the phases α and β are given by

$$\left.\begin{aligned} A_\alpha &= 2\pi N\rho^2(1+\cos\theta_\alpha)^{-1}, \\ A_\beta &= 4\pi R_\beta^2 - 2\pi N\rho^2(1+\cos\phi)^{-1}. \end{aligned}\right\} \tag{3.12}$$

Since the interface separating each domain of phase α from phase β has length $2\pi\rho$, the total length s of the interface between the phases is

$$s = 2\pi N\rho. \tag{3.13}$$

Further, the volume enclosed by the vesicle is

$$V = \tfrac{4\pi}{3}R_\beta^3 + \tfrac{\pi}{3}N\rho^3\Big[\tfrac{(1-\cos\theta_\alpha)^2(2+\cos\theta_\alpha)}{\sin^3\theta_\alpha} - \tfrac{(1-\cos\phi)^2(2+\cos\phi)}{\sin^3\phi}\Big]. \tag{3.14}$$

In view of (3.12), the net area A of the vesicle is simply

$$A = A_\alpha + A_\beta. \tag{3.15}$$

Let R_a and R_v be defined such that

$$A = 4\pi R_\mathrm{a}^2, \quad V = \tfrac{4}{3}\pi R_\mathrm{v}^3, \tag{3.16}$$

Notice that the areal inextensibility of the vesicle requires that R_a be fixed.

Since a sphere encloses the maximum volume for a given area, it is evident that $R_\mathrm{a} > R_\mathrm{v}$ and it seems reasonable to work with the excess radius

$$\zeta = \frac{R_\mathrm{a} - R_\mathrm{v}}{R_\mathrm{v}} \tag{3.17}$$

introduced by Yanagisawa et al. [72]. Consideration of (3.17) shows that ζ measures of the extent to which the lipid domains of phase α are allowed to bud outward from phase β. An alternative to this measure is the reduced volume $V/\big((4\pi/3)R_{\mathrm{a}}^3\big)$ used by Seifert et al. [153], Jülicher and Lipowsky [74] and Baumgart et al. [76].

Species conservation requires that the net area occupied by each phase be fixed. On defining the ratio $\xi = A_\alpha/A$ of the net area of phase α to the net area of the vesicle, it follows that

$$\xi = \text{constant}. \tag{3.18}$$

Further, by $(3.12)_1$ and $(3.16)_1$,

$$\xi = \frac{N\tilde{\rho}^2}{2(1+\cos\theta_\alpha)}, \tag{3.19}$$

where

$$\tilde{\rho} = \frac{\rho}{R_{\mathrm{a}}} \tag{3.20}$$

is a dimensionless version of the radius of curvature of the junction between the phases. Next, using (3.12), (3.8), and (3.19) in (3.15) gives

$$\frac{2}{\sin^2\phi} - \frac{N}{1+\cos\phi} = \frac{2(1-\xi)}{\tilde{\rho}^2}, \tag{3.21}$$

which can be solved for ϕ to yield

$$\phi = \cos^{-1}\left(\frac{\sqrt{N^2+4a(a+N-2)}-N}{2a}\right), \tag{3.22}$$

with

$$a = \frac{2(1-\xi)}{\tilde{\rho}^2}. \tag{3.23}$$

3.4.4 Energetics

The net potential-energy Ψ of the system can be expressed as

$$\Psi = \Psi_b + \Psi_l + \Psi_v, \tag{3.24}$$

where Ψ_b and Ψ_l are bending and line contributions. Assuming that the compositions of phases α and β are uniform, the bending moduli and the line tension must also be uniform and it follows that

$$\left.\begin{aligned} \Psi_b &= \frac{\hat{\kappa}_\alpha A_\alpha}{2R_\alpha^2} + \frac{\hat{\kappa}_\beta A_\beta}{2R_\beta^2}, \\ \Psi_l &= \tau s, \end{aligned}\right\} \tag{3.25}$$

where $\hat{\kappa}_\alpha = \kappa_\alpha + 2\bar{\kappa}_\alpha$ and $\hat{\kappa}_\beta = \kappa_\beta + 2\bar{\kappa}_\beta$ serve as effective bending-moduli. Notice that this reduction stems from the assumption that the domains occupied by phases α and β are spherical.

The volumetric (or pressure) contribution Ψ_v to (3.24), defined by

$$\Psi_v = -\int_{V_\circ}^{V_\mathrm{f}} p \,\mathrm{d}V, \tag{3.26}$$

is relevant only if the volume of the vesicle changes. In (3.26), $V_\circ$ and V_f represent the initial and final volumes of the vesicle. Also, the osmotic pressure p is viewed as a known (that is, experimentally controllable) input.

3.4.5 Scaling

To streamline the presentation and interpretation of results, we work exclusively with dimensionless quantities. Specifically, we introduce:

$$\left.\begin{aligned} &\tilde{R}_\alpha = \frac{R_\alpha}{R_{\mathrm{a}}}, \quad \tilde{R}_\beta = \frac{R_\beta}{R_{\mathrm{a}}}, \quad \tilde{A}_\alpha = \frac{A_\alpha}{R_{\mathrm{a}}^2}, \\ &\tilde{A}_\beta = \frac{A_\beta}{R_{\mathrm{a}}^2}, \quad \tilde{V} = \frac{V}{R_{\mathrm{a}}^3}, \quad \tilde{s} = \frac{s}{R_{\mathrm{a}}}, \\ &\tilde{\Psi} = \frac{\Psi}{\hat{\kappa}_\alpha}, \quad \tilde{p} = \frac{pR_{\mathrm{a}}^3}{\hat{\kappa}_\alpha}, \quad \tilde{\tau} = \frac{\tau R_{\mathrm{a}}}{\hat{\kappa}_\alpha}. \end{aligned}\right\} \tag{3.27}$$

Accordingly, the dimensionless net potential-energy $\tilde{\Psi}$ of the system can be expressed as

$$\tilde{\Psi} = \tilde{\Psi}_b + \tilde{\Psi}_l + \tilde{\Psi}_v, \tag{3.28}$$

where $\tilde{\Psi}_b$, $\tilde{\Psi}_l$, and $\tilde{\Psi}_v$ are dimensionless counterparts of Ψ_b, Ψ_l, and Ψ_p given by

$$\left.\begin{aligned} &\tilde{\Psi}_b = \frac{\tilde{A}_\alpha}{2\tilde{R}_\alpha^2} + \frac{\tilde{\kappa}_\beta \tilde{A}_\beta}{2\tilde{R}_\beta^2}, \\ &\tilde{\Psi}_l = \tilde{\tau}\tilde{s}, \\ &\tilde{\Psi}_v = -\int_{\tilde{V}_\circ}^{\tilde{V}_{\mathrm{f}}} \tilde{p}\,\mathrm{d}\tilde{V}, \end{aligned}\right\} \tag{3.29}$$

with

$$\tilde{\kappa}_\beta = \frac{\hat{\kappa}_\beta}{\hat{\kappa}_\alpha} \tag{3.30}$$

being the dimensionless effective bending-modulus of phase β.

In view of (3.27), the junction condition (3.11) can be expressed alternatively as

$$\tilde{\tau} = -\frac{1}{2}\tilde{p}\tilde{\rho}^2(\cot\theta_\alpha - \cot\phi). \tag{3.31}$$

Baumgart et al. [3], Tian et al. [86], and Hutchison et al. [87] use counterparts of (3.31) to evaluate the line tension using experimental data. If θ_α, θ_β, and $\tilde{\rho}$ are held fixed, it is evident from (3.31) that the dimensionless line tension scales linearly with the dimensionless osmotic pressure and, consequently, with the surface tension.

For brevity, the adjective "dimensionless" is suppressed from here on.

3.4.6 Equilibrium configurations

In this section, we consider two distinct classes of equilibrium configurations. The first of these classes emerges when a uniform multispecies vesicle undergoing phase separation is transformed to a multidomain vesicle (see the transformation from (a) to (b) depicted in Figure 3–3). In the second class of configurations, the lipid domains have coalesced into a single domain (see the transformation from (b) to (c) depicted in Figure 3–3).

Multidomain configurations

Granted that osmotic-pressure driven solvent transport across the vesicle occurs much more slowly than the phase separation process leading to multiple lipid domains, when considering multidomain configurations we assume that the volume enclosed by the vesicle is fixed. In view of (3.14), we must therefore satisfy the condition

$$\tfrac{4\pi}{3}R_\beta^3 + \tfrac{\pi}{3}N\rho^3\left[\tfrac{(1-\cos\theta_\alpha)^2(2+\cos\theta_\alpha)}{\sin^3\theta_\alpha} - \tfrac{(1-\cos\phi)^2(2+\cos\phi)}{\sin^3\phi}\right] = V_\circ. \tag{3.32}$$

Additionally, the conservation of lipid species and the areal inextensibility of the vesicle demand satisfaction of (3.19) and (3.21). Solving (3.32), (3.19), and (3.21) for a given number N of domains determines the unknowns $\tilde{\rho}$, θ_α, and ϕ. Also, for a

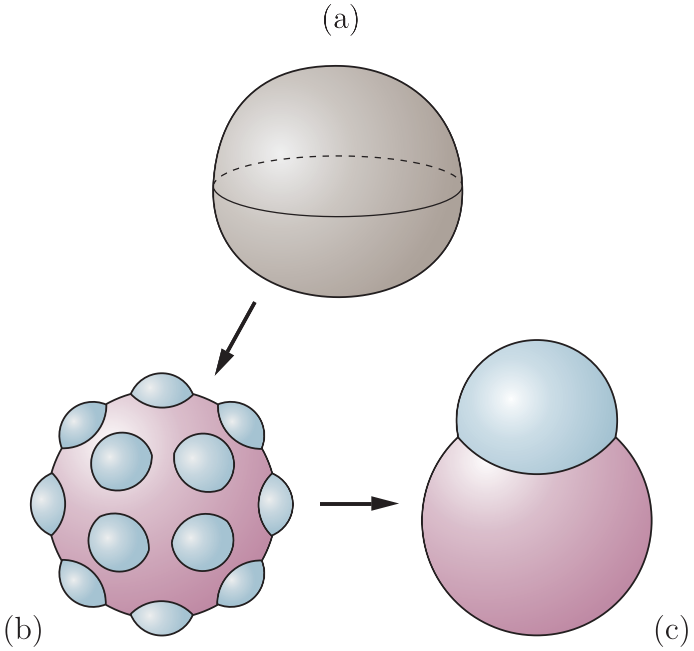

Figure 3–3: Schematic of a phase separation process: (a) a multispecies membrane before phase separation, (b) a multidomain configuration, and (c) a ground-state (or fully phase separated) configuration.

given osmotic pressure $\tilde{p}$, the line tension $\tilde{\tau}$ can be obtained from (3.11), as is needed to determine the line energy $\tilde{\Psi}_l$.

Ground-state configurations

After a sufficiently long time, scattered lipid domains may coalesce into a single domain. We refer to such a state as a 'ground-state configuration.' Yanagisawa et al. [72] and Semrau et al. [85] observe that the net potential-energy of a multidomain configuration decreases with the number of domains. Consistent with this, it seems reasonable to expect that ground-state configurations should correspond to minima of the net potential-energy $\tilde{\Psi}$.

Lipid domains usually coalesce very slowly. One reason for this is that coalescence can be resisted by an interdomain repulsive forces that become significant when two domains approach one another sufficiently closely [72, 85, 144]. In view of this fact and because the time required to reach a ground-state configuration is likely to be long enough to allow for solvent transport across the membrane owing to osmotic pressure, it seems reasonable to allow the volume of the vesicle in a ground-state configuration to vary. This stands in contrast to our treatment of multidomain configurations. In particular, the volume enclosed by the vesicle in a ground-state configuration is determined as a consequence of energy minimization.

When the volume enclosed by the vesicle is allowed to vary, the volumetric energy Ψ_v defined in (3.26) must be considered in addition to the bending and line energies Ψ_b and Ψ_l. Moreover, it is important to account for the dependence of the osmotic pressure on the solute concentration. If the osmotic pressure is assumed to be linearly proportional to the solute concentration, we may consider the interior fluid as an ideal solution [23]. For the sake of simplicity, we neglect the ion concentration in the exterior region. Then, since the pressure vanishes in the fluid surrounding the vesicle, the osmotic pressure p and the pressure in the fluid enclosed by the vesicle coincide. Thus,

$$pV = p_\circ V_\circ, \tag{3.33}$$

where $p_\circ$ is the initial osmotic pressure—that is, the osmotic pressure in the vesicle before phase separation and also in a multidomain configuration. Using (3.33) in (3.26) yields

$$\Psi_v = -p_\circ V_\circ \ln\left(\frac{\tilde{V}}{\tilde{V}_\circ}\right), \tag{3.34}$$

which, since $p_\circ$ and $V_\circ$ are both constant, can be additively scaled according to

$$\Psi_v = -p_\circ V_\circ \ln \tilde{V}. \tag{3.35}$$

In view of (3.27), the energy $\tilde{\Psi}_v$ therefore reads

$$\tilde{\Psi}_v = -\tilde{p}_\circ \tilde{V}_\circ \ln \tilde{V}. \tag{3.36}$$

Also using $(3.16)_2$, (3.17), and (3.27), we have

$$\tilde{V}_\circ = \frac{4\pi}{3(1+\zeta_\circ)^3}, \tag{3.37}$$

in which

$$\zeta_\circ = \left(\frac{R_\mathrm{a} - R_\mathrm{v}}{R_\mathrm{v}}\right)_\circ \tag{3.38}$$

is the initial excess radius of the vesicle. Substituting (3.37) in (3.36) gives

$$\tilde{\Psi}_v = -\tfrac{4}{3}\pi \Pi_\circ \ln \tilde{V}, \tag{3.39}$$

where

$$\Pi_\circ = \frac{\tilde{p}_\circ}{(1+\zeta_\circ)^3} \tag{3.40}$$

denotes the reduced osmotic pressure. Seifert [23] and Allain and Ben Amar [77] perform similar calculations and explore the importance of the volumetric energy with varying pressure.

Using (3.33), the osmotic pressure can be expressed alternatively as

$$\tilde{p} = \tfrac{4}{3}\pi \Pi_\circ / \tilde{V}. \tag{3.41}$$

As for multidomain configurations, the conservation of lipid species and the constraint of areal inextensibility require satisfaction of (3.19) and (3.21). In addition, the line tension depends on the solution through the junction condition (3.11). At equilibrium, the net potential-energy $\tilde{\Psi}$ is minimized. Solving the three equations (3.11), (3.19), and (3.21), while requiring that the net potential-energy be minimized delivers the ground-state configuration.

The capillary approximation for the ground-state configuration

For sufficiently large values of the osmotic pressure, the net potential-energy of a vesicle is dominated by the osmotic pressure effect, rendering the bending energy negligible. Under such conditions, Allain and Ben Amar [77] adopt and study a capillary approximation in which the net potential-energy of a mutiphase vesicle includes only the line and volumetric contributions. In terms of the dimensionless quantities defined in $(3.29)_{2,3}$, this approximation leads to

$$\tilde{\Psi}_{\text{cap}} = \tilde{\Psi}_l + \tilde{\Psi}_v. \tag{3.42}$$

On invoking $(3.29)_2$, (3.31), (3.41), and (3.39) and introducing the purely geometrical quantity

$$g = \pi \frac{\tilde{\rho}^3}{\tilde{V}} (\cot \theta_\alpha - \cot \phi) + \ln \tilde{V}, \tag{3.43}$$

(3.42) simplifies to

$$\tilde{\Psi}_{\text{cap}} = -\tfrac{4}{3}\pi \Pi_\circ g, \tag{3.44}$$

showing that $\tilde{\Psi}_{\text{cap}}$ scales linearly with $\Pi_\circ$. Modulo a different nondimensionalization, (3.44) is equivalent to the expression given by Allain and Ben Amar [77].

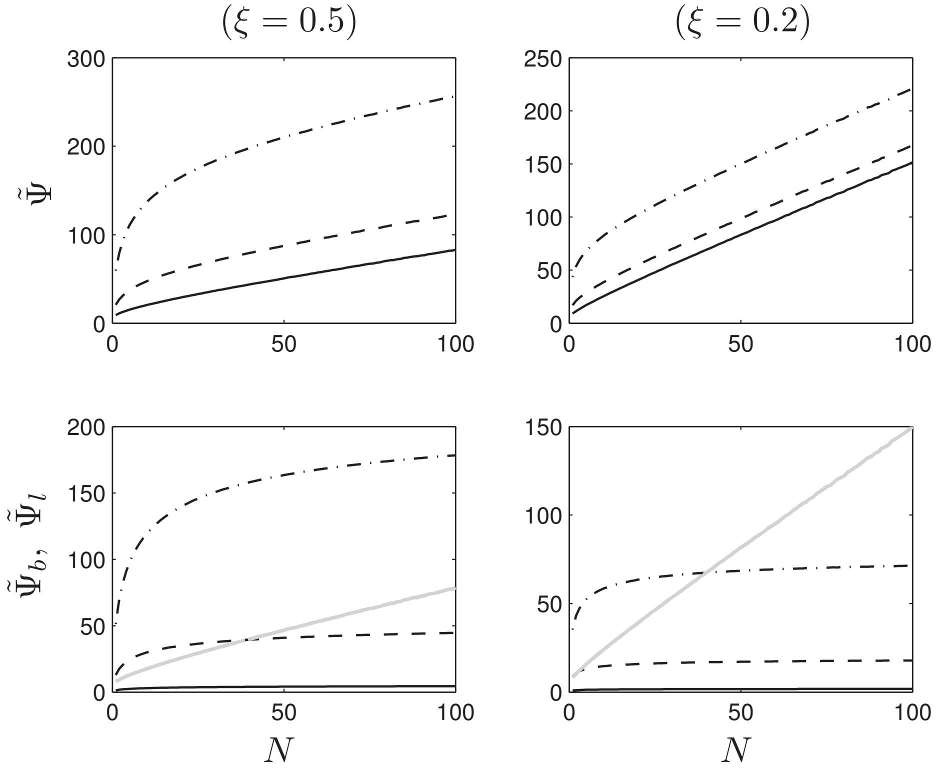

Figure 3–4: Variations of the net potential-energy $\tilde{\Psi}$ (upper row), bending energy $\tilde{\Psi}_b$ (gray lines in the lower row), and line energy $\tilde{\Psi}_l$ (black lines in the lower row) with the number N of lipid domains, for the excess radius ζ equal to $\zeta = 0.02$, different values of the area ratio ξ and the osmotic pressures $\tilde{p}$ (solid line: $\tilde{p} = 1$; dashed line: $\tilde{p} = 10$; dash-dotted line: $\tilde{p} = 40$).

3.5 Numerical results

We next explore various features of multidomain and ground-state configurations. Without loss of generality, we take $\hat{\kappa}_\alpha/\hat{\kappa}_\beta = 1.25$. Further, for simplicity, we take the ratio of the effective bending moduli equal to the value of the ratio of the splay moduli reported by Baumgart et al. [3].

3.5.1 Multidomain configurations

The variations of the net potential-energy $\tilde{\Psi}$, the bending energy $\tilde{\Psi}_b$, and the line energy $\tilde{\Psi}_l$ with the number N of lipid domains for different values of the area ratio ξ and the osmotic pressure $\tilde{p}$ are depicted in Figure 3–4. Notably, $\tilde{\Psi}$ increases with N and achieves an absolute minimum at $N = 1$, verifying that ground state configurations correspond to minimizers of the net potential energy. For sufficiently large values of N, $\tilde{\Psi}$ increases almost linearly with N, consistent with a result due to Yanagisawa et al. [72]. In addition, $\tilde{\Psi}$ increases with the osmotic pressure $\tilde{p}$. The net potential-energy $\tilde{\Psi}$ behaves consistently for different area ratios ξ, except that for smaller values (e.g., $\xi = 0.2$) it is less sensitive to the osmotic pressure $\tilde{p}$. The bending and line energies $\tilde{\Psi}_b$ and $\tilde{\Psi}_l$ increase with the number N of domains. Thus, there is no competition between these contributions to the net potential-energy $\tilde{\Psi}$. Importantly, $\tilde{\Psi}_b$ is independent of $\tilde{p}$. This is because the geometry of a multidomain configuration is completely dictated by the geometrical constraints—i.e., by (3.19), (3.21), and (3.32). Also, the ratio $\tilde{\tau}/\tilde{p}$ of the line tension to the osmotic pressure is determined from (3.11) and, therefore, is independent of $\tilde{p}$. However, in view of (3.11), $\tilde{\tau}$ and, accordingly, $\tilde{\Psi}_l$ varies linearly with $\tilde{p}$. For this reason, $\tilde{\Psi}_l$, as apposed to $\tilde{\Psi}_b$, increases with $\tilde{p}$, and naturally is the source of the dependence of $\tilde{\Psi}$ on $\tilde{p}$. As $\tilde{p}$ increases, the energy difference between configurations with high and low numbers of domains increases, especially for higher values of the area ratio ξ. This potentially favors higher tendency for domain coarsening when $\tilde{p}$ increases. We believe that this argument is consistent with the experimental observation of Morales-Penningston et al. [146] which reveals the osmotic pressure increase can induce the coalescence of small domains. According to these authors, this process is accompanied by swelling of the vesicles into spheres composed most often of two large domains.

The variations of the characteristic size $\tilde{\rho}$, the slopes θ_α and ϕ, and the ratio $\tilde{\tau}/\tilde{p}$ of the line tension to the osmotic pressure with the number N of the domains are depicted in Figure 3–5 for different values of the area ratio ξ and the excess radius ζ. For smaller values of the excess radius (e.g., $\zeta = 0.02$), the results show that $\tilde{\rho}$ decreases with N, which is not very surprising since the net area occupied by phase α is fixed. Also, both θ_α and ϕ decrease with N, while $\theta_\alpha > \phi$ indicates that the domains are dimpled from the vesicle toward the exterior region. In addition, the ratio $\tilde{\tau}/\tilde{p}$ decreases with N, meaning that for $\tilde{p}$ fixed $\tilde{\tau}$ decreases with the number N of domains. As the excess radius increases (from $\zeta = 0.02$ to $\zeta = 0.07$), $\tilde{\rho}$ decreases, θ_α increases, and ϕ is essentially unchanged. This behavior seems reasonable because, for larger values of the excess radius, domains have more latitude to bud from the vesicle with higher slope θ_α and smaller neck $\tilde{\rho}$. For smaller area ratios ξ (e.g., $\xi = 0.2$), the influence of ζ on the ratio $\tilde{\tau}/\tilde{p}$ is more tangible. Moreover, for larger excess radius (e.g., $\zeta = 0.07$), the solution experiences a jump between $N = 1$ and $N = 2$. This is because the configuration of the vesicle for a constant net area A, the net area A_α of the domains, and volume V enclosed by the vesicle dramatically changes between $N = 1$ and $N = 2$. However, as N increases, the vesicle geometry and net potential-energy become less sensitive to the number N of domains. As such, no perceptible jump of the solution occurs for $N > 2$.

3.5.2 Ground-state configurations

In this section, we explore the consequences of regarding the reduced osmotic pressure $\Pi_\circ$ as a control parameter. (For brevity, the adjective 'reduced' is dropped hereafter in referring to $\Pi_\circ$.) Under these circumstances, θ_α and ϕ are determined from (3.19) and (3.22) in terms of $\tilde{\rho}$. Accordingly, using (3.14) and (3.27), the volume $\tilde{V}$ is calculated. Next, the osmotic pressure $\tilde{p}$ is provided by (3.41). Finally, (3.31) is used to obtain the line tension $\tilde{\tau}$.

The variations of the net potential-energy $\tilde{\Psi}$, the slopes θ_α and ϕ, and the line tension $\tilde{\tau}$ with the domain size $\tilde{\rho}$ are depicted in Figure 3–6 for the area ratio $\xi = 0.5$ along with two values $\Pi_\circ = 1$ and $\Pi_\circ = 10$ of the osmotic pressure. For the smaller value of $\Pi_\circ$, the results show that $\tilde{\Psi}$ decreases monotonically with $\tilde{\rho}$, achieving an absolute minimum at $\tilde{\rho} = 1$. This corresponds to a ground-state configuration in which the vesicle is composed of two spherical caps (in this case, two hemispheres) of phases α and β with identical radii (see also from the second row of Figure 3–6, which indicates that $\theta_\alpha = \phi = \pi/2$ at $\tilde{\rho} = 1$). For the higher value of $\Pi_\circ$, the results show that $\tilde{\Psi}$ possesses a local minimum at $\tilde{\rho} = 0$ and, much like what arises at lower osmotic pressures, an absolute minimum at $\tilde{\rho} = 1$. The size $\tilde{\rho} = 0$ corresponds to a ground-state configuration wherein the domain occupied phase α is about to pinch off from the vesicle (see also the second row of Figure 3–6, which shows that $\theta_\alpha = \pi$ and $\phi = 0$ at $\tilde{\rho} = 0$). The other ground-state configuration occurs at $\tilde{\rho} = 1$, corresponding to the complete sphere configuration. In the third row, we see how the line tension $\tilde{\tau}$ changes with the domain size $\tilde{\rho}$. Importantly, at the ground-state configurations arising for $\tilde{\rho} = 0$ and $\tilde{\rho} = 1$, the model predicts that the line tension vanishes. This result is consistent with the observation that, by (3.11), $\tilde{\tau}$ vanishes for $\tilde{\rho} = 0$ and $\tilde{\rho} = 1$. As it might seem unreasonable to allow $\tilde{\tau}$ to vanish, we will return to this issue shortly.

On the basis of Figure 3–6, we notice that the structure of the net potential-energy curve is strongly influenced by the value of the osmotic pressure $\Pi_\circ$. For $\Pi_\circ = 1$, $\tilde{\Psi}$ has an absolute minimum at $\tilde{\rho} = 1$. However, for $\Pi_\circ = 10$, in addition to an absolute minimum at $\tilde{\rho} = 1$, $\tilde{\Psi}$ has a local minimum at $\tilde{\rho} = 0$. Notice that $\tilde{\rho} = 1$ is the locus of the absolute minimum only for $\xi = 0.5$. Regardless of the value of the area ratio ξ, numerical results verify that the location of the absolute minimum of $\tilde{\Psi}$ corresponds to a configuration in which the vesicle resembles a complete sphere composed of two spherical caps of the phases α and β with the same radii of curvature and identical slopes (i.e., $\theta_\alpha = \phi$) at their interface. Under these conditions, the geometrical relations (3.19) and (3.21) simply imply that the size $\tilde{\rho}$ corresponding a completely spherical ground-state configuration is

$$\tilde{\rho} = 2\sqrt{\xi(1-\xi)}. \tag{3.45}$$

Importantly, the transition from the case where $\tilde{\Psi}$ exhibits a single absolute minimum at $\tilde{\rho} = 2\sqrt{\xi(1-\xi)}$ to that wherein $\tilde{\Psi}$ exhibits two minima (specifically, one local minimum at $\tilde{\rho} = 0$ and one absolute minimum at $\tilde{\rho} = 2\sqrt{\xi(1-\xi)}$) occurs for $\Pi_\circ$ in excess of a critical value Π_c. Figure 3–7 shows the variation of Π_c with ξ. The circles in the figure indicate the distinct values of Π_c determined by numerical trial and error for various choices of ξ. The graph of Π_c versus ξ seems to be almost symmetric about the line $\xi \approx 0.5$. The critical value Π_c is very large for ξ close to either zero or unity and achieves a minimum at approximately $\xi = 0.5$, for which $\Pi_\mathrm{c} \approx 1.8$. For $\Pi_\circ < \Pi_\mathrm{c}$, the only ground-state configuration is a complete sphere. For $\Pi_\circ > \Pi_\mathrm{c}$, two ground-state configurations, one a complete sphere and the other pinched-off, exist. Although the pinched-off configuration can be considered as metastable relative to the complete sphere configuration, it qualifies as an equilibrium configuration as long as $\tilde{\Psi}$ does not pass the energy barrier between the two configurations.

We propose that the initial excess radius $\zeta_\circ$ is a key parameter that determines which configuration, the pinched-off or the complete sphere, is likely to be selected as the ground state. Figure 3–8 shows the variations of the net potential-energy $\tilde{\Psi}$ and the excess radius ζ with the size $\tilde{\rho}$ of the domain for $\Pi_\circ = 10 > \Pi_\mathrm{c}$ and two choices $\xi = 0.5$ and $\xi = 0.2$ of ξ. Notably, $\tilde{\Psi}$ has an absolute maximum at a critical size $\tilde{\rho}_\mathrm{c}$. For this value of $\tilde{\rho}$, the excess radius is ζ_c; this justifies referring to ζ_c as the critical excess radius. We propose that the ground-state configuration is pinched-off for initial excess radii greater than ζ_c (i.e., $\zeta_\circ > \zeta_\mathrm{c}$). Otherwise, for $\zeta_\circ < \zeta_\mathrm{c}$, the ground-state configuration is a complete sphere. In fact, $\zeta_\circ$ serves as an initial value which, depending on its value compared to the critical excess radius, leads to different ground-state configurations.

The variations of the critical excess radius ζ_c and the critical domain size $\tilde{\rho}_\mathrm{c}$ with the initial osmotic pressure $\tilde{p}_\circ$ are depicted in Figure 3–9 for two choices $\xi = 0.5$ and $\xi = 0.2$ of the area ratio ξ. Obviously, $\tilde{p}_\circ$ exceeds the critical value exhibited in Figure 3–7. The critical excess radius ζ_c attains a maximum at the critical pressure (equal to 2.5 and 4.4 for $\xi = 0.5$ and $\xi = 0.2$, respectively). It also decreases with $\tilde{p}_\circ$. In addition, schematic representations of the corresponding ground-state configurations are shown above and below the critical excess radius line.

Returning to the consideration of Figure 3–6, the present model predicts zero line tension for the two possible ground-state configurations corresponding to $\tilde{\rho} = 0$ and $\tilde{\rho} = 2\sqrt{\xi(1-\xi)}$. In practice, however, it seems likely that, consistent with the results of Towles and Dan [150] and Trejo and Ben Amar [84], the line tension should have a positive nonzero lower bound. To rule out the vanishing of the line tension without recourse to any fundamental analysis of its nature, we may simply stipulate that it be greater than some chosen value. To illustrate the outcome of this strategy, we take the lower bound to be $\tilde{\tau}/\Pi_\circ = 0.1$. Accordingly, only values of $\tilde{\rho}$ for which $\tilde{\tau}/\Pi_\circ$ exceeds 0.1 must be considered. Instead of adopting pinched-off or complete sphere configurations, the ground-states then consist of a budded configuration (in which two spherical phases are connected by a very narrow neck) and a very slightly budded spherical domain of phase α on an otherwise spherical vesicle, as shown in Figure 3–10. Both of these configurations are commonly observed in experiments [3, 76, 4].

It is important to investigate the extent to which including the bending energy in the net potential-energy influences the equilibrium configurations of a two-phase vesicle. With this aim, we next compare the net potential-energy given in (3.28) with the energy, given in (3.42), arising in the capillary limit. The variations of $\tilde{\Psi}/\Pi_\circ$ and $\tilde{\Psi}_{\text{cap}}/\Pi_\circ$ with $\tilde{\rho}$ are depicted in Figure 3–11 for different values for the osmotic pressure $\Pi_\circ$ and two different choices $\xi = 0.5$ and $\xi = 0.2$ of the area ratio ξ. To allow comparisons of the results for different values of the osmotic pressure in the same plot, the net potential-energies have been divided by $\Pi_\circ$. Notice from (3.44) that $\tilde{\Psi}_{\mathrm{cap}}/\Pi_\circ = -\frac{4}{3}\pi g$, implying that $\tilde{\Psi}_{\mathrm{cap}}/\Pi_\circ$ is independent of $\Pi_\circ$. Comparing the curves associated with each osmotic pressure value with the curve corresponding to the capillary approximation indicates that the bending energy is significant for the lower values of the osmotic pressure. Including the bending energy also changes the structure of the net potential-energy function. From Figure 3–11, the capillary approximation to the net potential-energy function has a fixed local maximum and a global minimum at $\tilde{\rho} = 2\sqrt{\xi(1-\xi)}$. However, including the bending energy alters the structure of the net potential-energy function. It is noteworthy that the critical osmotic pressure Π_{c} arises only in the presence of the bending energy. Finally, as Figure 3–11 reveals (in agreement with an observation of Allain and Ben Amar [77]), for sufficiently large values of the osmotic pressure the bending energy has a negligible contribution and the capillary approximation is acceptable.

As part of their study, Allain and Ben Amar [77] apply a methodology similar to that presented in Section 2 to consider the capillary limit of equilibrium of a two-phase vesicle composed of two spherical caps. By neglecting the bending energy of the domains and taking the osmotic pressure to be constant while varying the volume enclosed by the vesicle, they arrive at a net potential-energy that, apart from the geometrical parameters, depends only on the dimensionless quantity τ/pR_{a}^2. If this quantity is taken to be a control parameter, their equations deliver two solutions for the equilibrium configurations. Allain and Ben Amar [77] present a plot similar to those in the third row of Figure 3–6 or that in Figure 3–10 (with horizontal and vertical axis interchanged). For any given τ/pR_{a}^2, only the lowest energy solution is kept, while ruling out the remaining solution as unstable. The importance of a critical value of τ/pR_a^2, corresponding to the maximum value of $\tilde{\tau}$ in Figure 3–6 or $\tilde{\tau}/\Pi_\circ$ in Figure 3–10, is addressed as well. For this critical value, the neck size $\tilde{\rho}$ is finite (cf., e.g., Figure 3–10, where $\tilde{\rho} \approx 0.5$). Allain and Ben Amar [77] mention that if τ/pR_a^2 exceeds this critical value then no solution exists for the equilibrium configuration, but two disconnected spheres of each phases can provide a solution. However, a more detailed analysis would be needed to explain such a discontinuous transition. Indeed, Allain and Ben Amar [77] state that "*The transition is a dynamical process and has similarities with the breaking of a soap film between two rings (the catenoid instability) [41]. Nevertheless, complete fission requires a microscopic reorganization, such as hemifission [42] which occurs at small scales and is out of reach of the present treatment. A detailed analysis may be found in [43] for example. It is why we cannot predict if the two daughter vesicles remain connected by a small filament of lipids or prefer to separate.*" After discussing the capillary solution, Allain and Ben Amar [77] replace the sharp interface between the domains with a smooth boundary layer in which the bending energy of the boundary layer is incorporated.

A subtle difference between our approach to ground-state configurations and the approach of Allain and Ben Amar [77] should be clarified. Since we consider the bending energy of the domains, our solution cannot be characterized by the single ratio τ/pR_a^2. Indeed, we consider $\Pi_\circ$ as a control parameter. Since the volume of the vesicle is allowed to change, we allow the system to take on different values for $\tilde{\rho}$ between $0 \leq \tilde{\rho} \leq 2\sqrt{\xi(1-\xi)}$, spanning from the pinched-off to the complete sphere configurations. Next, for each value of $\Pi_\circ$ and each set of $\tilde{\rho}$, θ_α, and ϕ, the line tension $\tilde{\tau}$ is calculated from (3.31). As our numerical results show, $\tilde{\rho} = 2\sqrt{\xi(1-\xi)}$

correspond to equilibrium configurations for $\Pi_\circ < \Pi_c$. For $\Pi_\circ > \Pi_c$, we have two equilibrium configurations corresponding to $\tilde{\rho} = 0$ and $\tilde{\rho} = 2\sqrt{\xi(1-\xi)}$. In this case, we do not rule out the configuration with larger net potential-energy. Rather, since there is an energy barrier between the two configurations, and as long as the energetic fluctuations are not large enough compared to the height of this barrier, we believe that both configurations are possible; consistent with this, we regard $\tilde{\rho} = 2\sqrt{\xi(1-\xi)}$ as stable and $\tilde{\rho} = 0$ as metastable. However, as mentioned previously, in view of other studies indicating a positive non-zero lower bound for the line tension [150, 84], by setting a lower bound for $\tilde{\tau}/\Pi_\circ$, we may exclude the extreme cases corresponding to $\tilde{\rho} = 0$ and $\tilde{\rho} = 2\sqrt{\xi(1-\xi)}$ in which $\tilde{\tau} = 0$. Also, as shown, the initial excess radius $\zeta_\circ$ of the vesicle has a strong influence on the nature of the final configuration adopted in any ground state.

3.6 Summary

A simple model was used to study the equilibrium of the domains on a two-phase vesicle. Multidomain and ground-state configurations were considered. In a multidomain configuration, the vesicle is covered by identical partially budded lipid domains. In a ground-state configuration, the vesicle is composed of two coexisting lipid domains. Inspired by experimental observations in which lipid domains appear to be closely approximated by spherical caps, we assumed that all domains have constant radii and, for multidomain configurations, the host phase is assumed to have constant radius.

For multidomain configurations, we studied the net potential-energy, the shape of the domains as characterized by their size and slope at the junction, and the line tension at the junctions for various sets of input parameters. In contrast to Yanagisawa et al. [72] and Semrau et al. [85], we ensured that force is balanced at the domain junctions. In this sense, our work is consistent with studies of fully phase-separated configurations conducted by Baumgart et al. [3, 76], Allain and Ben Amar [77], and Tian et al. [86]. Since the area of the each phase and the volume of the vesicle are fixed, the geometry of the vesicle is independent of the osmotic pressure. But, as a result of the force balance at the domain junctions, the line tension depends linearly on the osmotic pressure. Thus, although the osmotic pressure increase does not energetically contribute by itself (because the volume is fixed), it increases the line tension and consequently the net potential-energy of the system. Consistent with observations of Morales-Penningston et al. [146], this result suggests a preference for domain coalescence at sufficiently high osmotic pressures. Also, the numerical results showed that the line tension decreases by increase of number of domains. However, while this observation is valid for more than three domains, it might not hold in the transition from a pair of domains to a single domain.

A vesicle in a ground-state configuration was assumed to be formed by coalescence of distributed domains of a vesicle in the multidomain configuration. Since the characteristic time needed to attain such a configuration may be comparable to or greater than that associated with solvent transport across the membrane, we allowed the volume enclosed the vesicle to be nonconstant. This stands in contrast to our study of multidomain configurations, which generally form on a time scale short compared to that associated with solvent transport across the membrane. Allowing for variations of the volume enclosed by the vesicle requires that a volumetric contribution involving the osmotic pressure be included in the net potential-energy. In this context, we considered the consequences of following Seifert [23] and invoking the van't Hoff [154] relation, wherein the osmotic pressure is linearly proportional to the solute concentration. Treating the osmotic pressure as a control parameter, the dependence of net potential-energy as a function of the size of domain was shown to depend on whether the osmotic pressure $\Pi_\circ$ is below or above a critical value Π_c. For osmotic pressures below Π_c, the net potential-energy has an absolute minimum at a configuration in which the vesicle resembles a complete sphere divided into two domains of identical radius. For osmotic pressures above Π_c, aside from a complete sphere configuration like that arising for osmotic pressures below Π_c, the net potential-energy possesses a local minimum, corresponding to two pinched-off spheres of pure phase. These two configurations are separated by an energy barrier which allows both configurations be possible, at least in the absence of energy fluctuations sufficiently large to induce transitions from well to well. We proposed a criterion for determining which of these ground-state configurations will prevail based on comparing the value of the excess radius of the vesicle prior to phase separation (or in a multidomain configuration) to a critical excess radius. We also showed that this critical excess radius decreases by increase of the osmotic pressure $\tilde{p}_\circ$. Motivated by works of Towles and Dan [150] and Trejo and Ben Amar [84], we considered a positive non-zero lower bound for the line tension, leading to slight modifications of two possible ground-state configurations.

Finally, we studied the effect of the bending energy of the phases. The results revealed that, for sufficiently small values of the osmotic pressure, the bending energy can significantly influence the ground-state configuration of a two-phase vesicle.

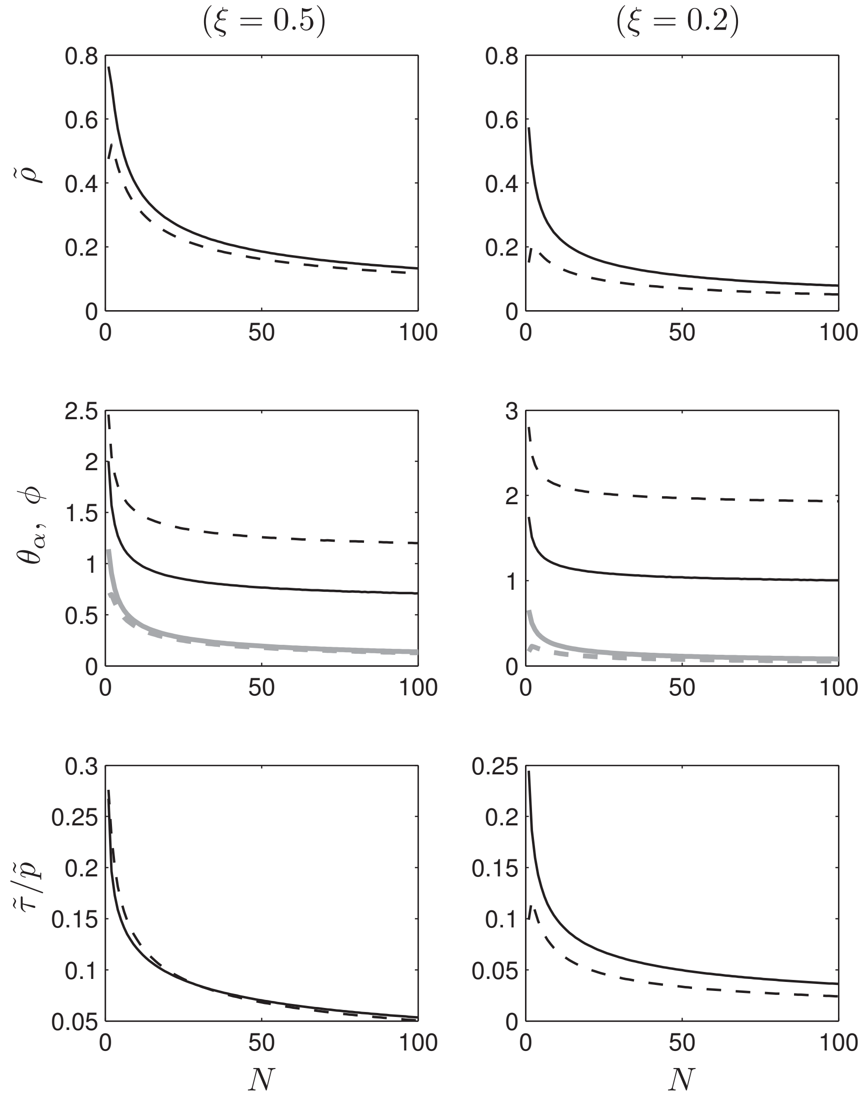

Figure 3–5: Variations of the characteristic domain size $\tilde{\rho}$ (first row), slopes θ_α (black lines in the second row), and ϕ (gray lines in the second row), and ratio $\tilde{\tau}/\tilde{p}$ of the line tension to the osmotic pressure (third row) with the number N of domains for different values of the area ratio ξ and the excess radius ζ (solid line: $\zeta = 0.02$; dashed line: $\zeta = 0.07$).

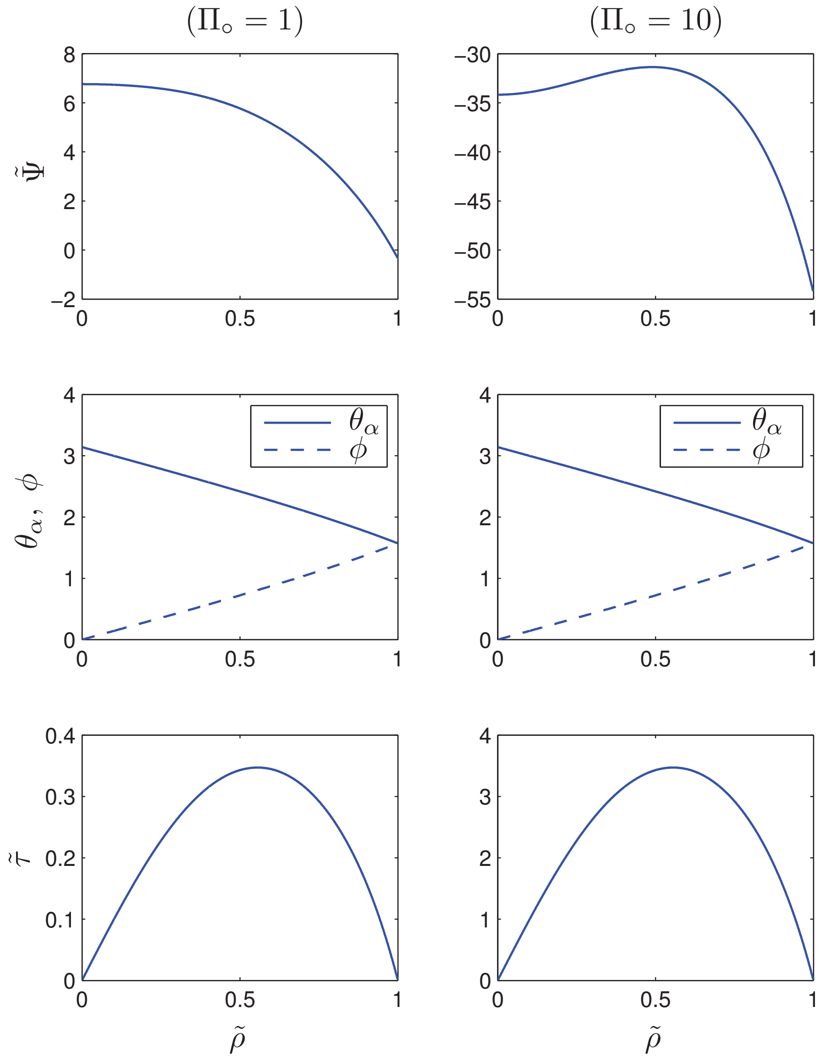

Figure 3–6: Variations of the net potential-energy $\tilde{\Psi}$ (first row), the slopes θ_α and ϕ (second row), and the line tension $\tilde{\tau}$ (third row) with the domain size $\tilde{\rho}$ for the area ratio ξ equal to $\xi = 0.5$, and two values $\Pi_\circ = 1$ and $\Pi_\circ = 10$ of the osmotic pressure $\Pi_\circ$.

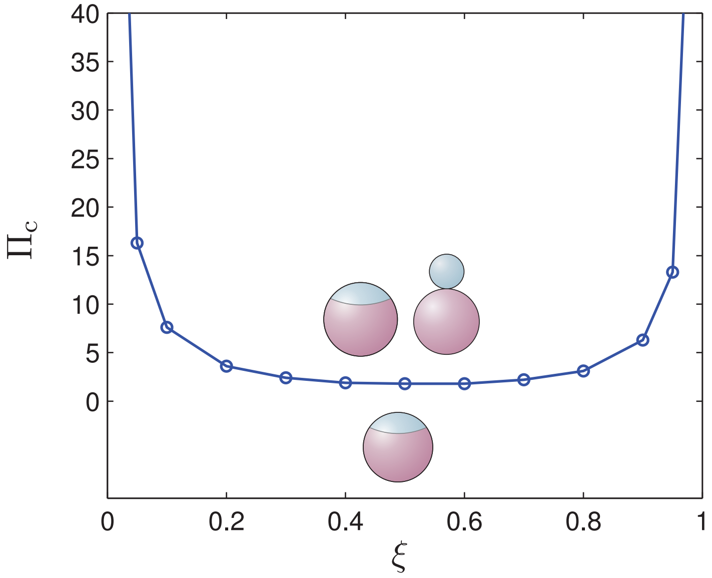

Figure 3–7: Variation of the critical osmotic pressure Π_c with the area ratio ξ.

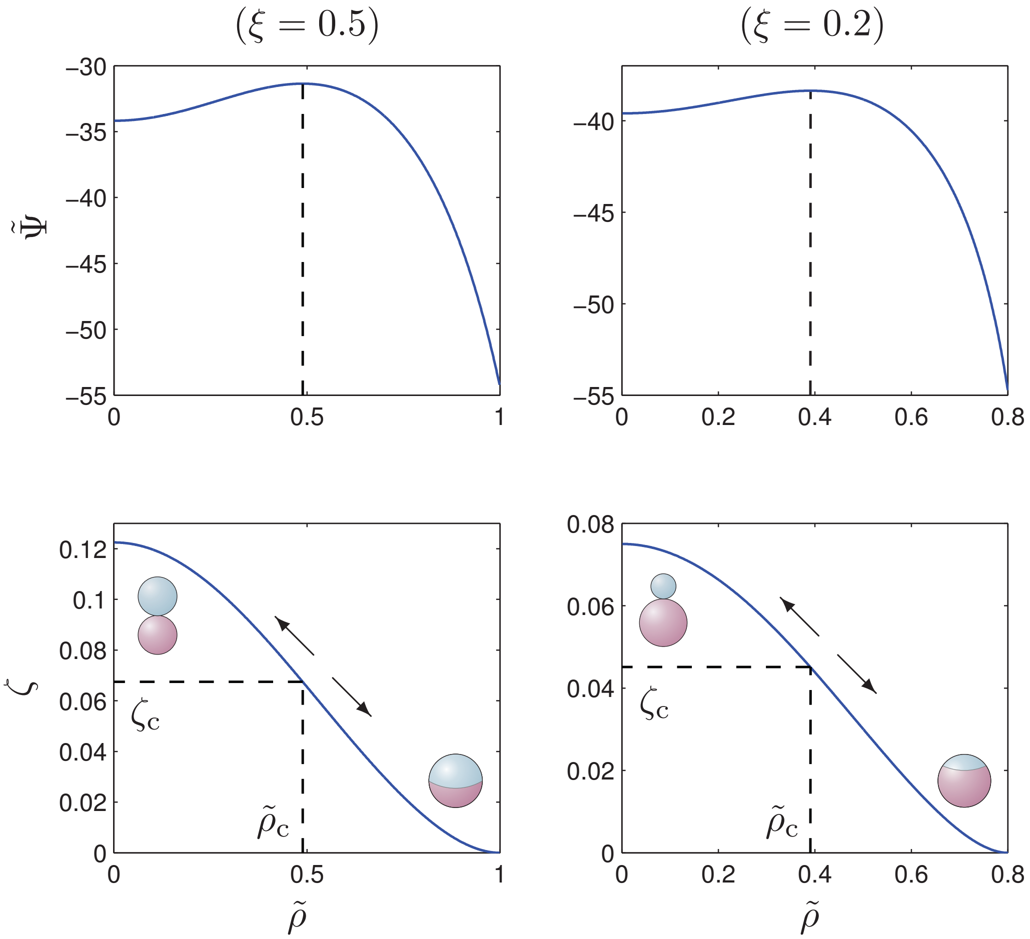

Figure 3–8: Variation of the net potential energy $\tilde{\Psi}$ (upper row) and the excess radius ζ (lower row) with the size of the domain $\tilde{\rho}$ for $\Pi_\circ = 10$ and two values $\xi = 0.5$ and $\xi = 0.2$ of the area ratio ξ.

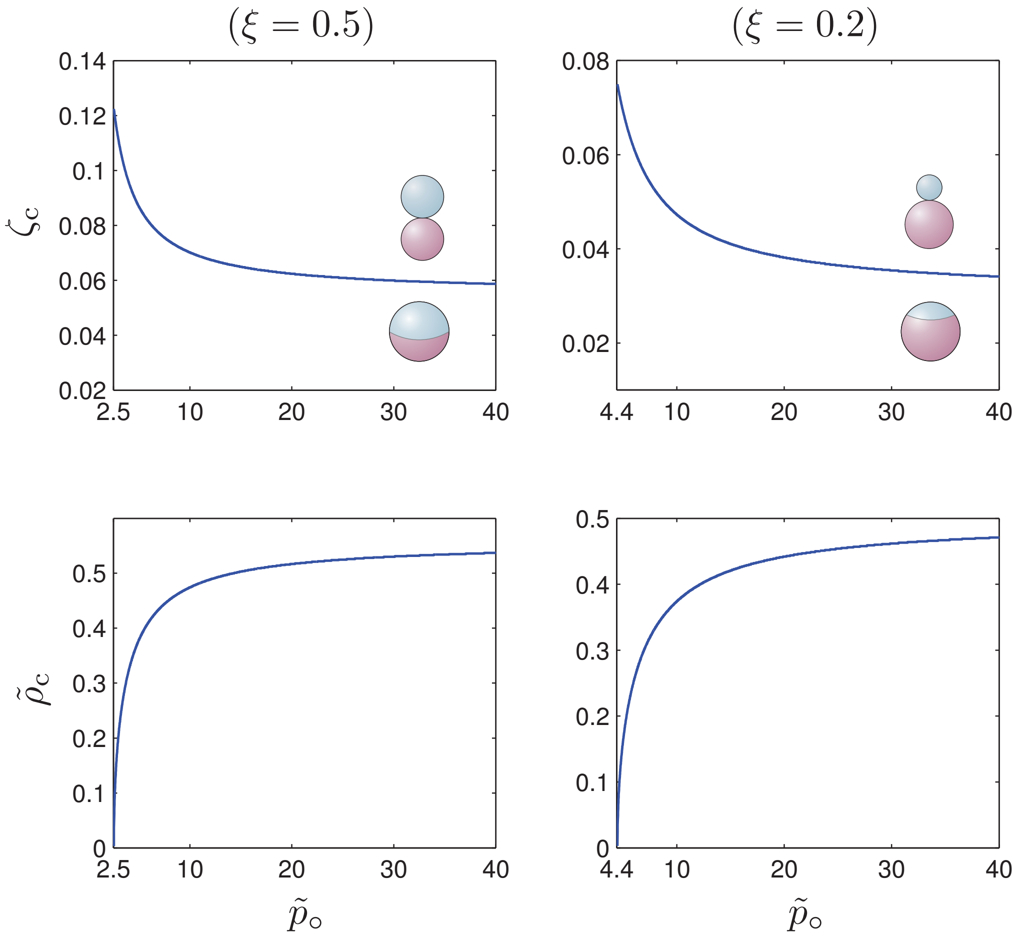

Figure 3–9: Variations of the critical excess radius ζ_c (upper row) and the critical domain size $\tilde{\rho}_c$ (lower row) with the initial osmotic pressure $\tilde{p}_\circ$ for two values $\xi = 0.5$ and $\xi = 0.2$ of the area ratio ξ.

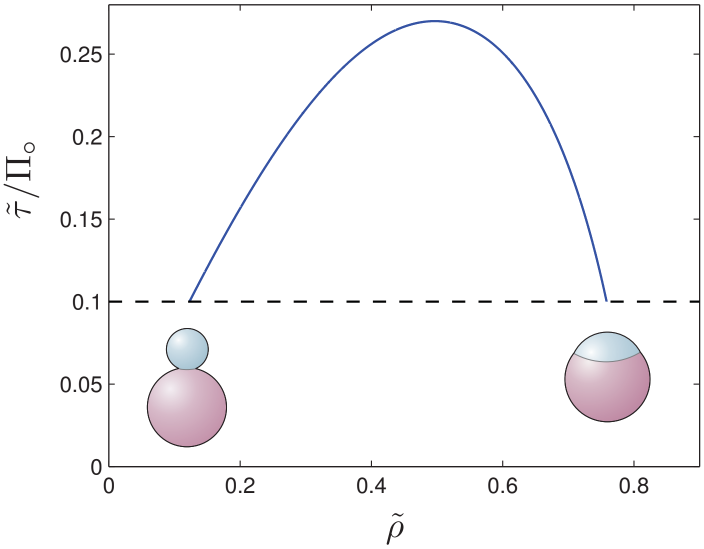

Figure 3–10: Variation of the line tension (scaled by $\Pi_\circ$) by the domain size $\tilde{\rho}$ for the area ratio equal to $\xi = 0.2$ when a lower bound is considered. The shapes of the ground-state configurations are also depicted schematically.

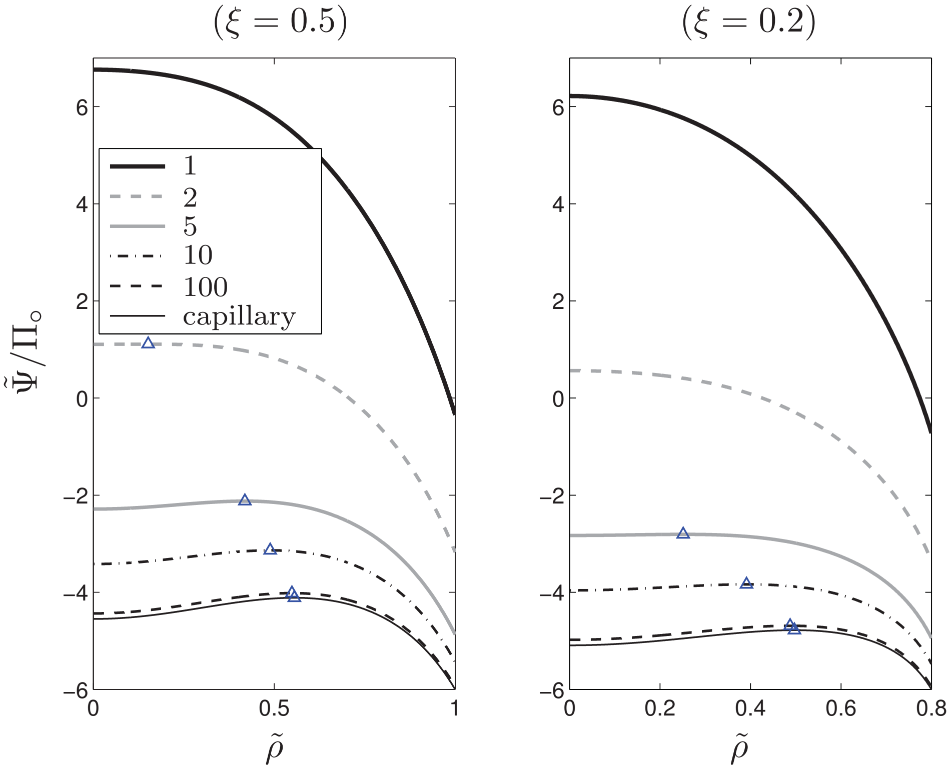

Figure 3–11: Variation of $\tilde{\Psi}/\Pi_\circ$ with $\tilde{\rho}$ for different values of the osmotic pressure $\Pi_\circ$, and two choices $\xi = 0.5$ and $\xi = 0.2$ of the area ratio ξ. The first five lines from the top correspond to the net potential-energy (with bending energy taken into consideration) and the first line from the bottom corresponds to the value of $\tilde{\Psi}/\Pi_\circ$ under the capillary approximation—namely, $\tilde{\Psi}_{\text{cap}}/\Pi_\circ$. The triangles show the local maxima of the curves.

CHAPTER 4
Equilibrium of discoidal high-density lipoprotein particles

4.1 Preface

Besides multiphase vesicles of the kind considered in Chapter 3, another object of interest, in which the lipid bilayer is an essential element, is a discoidal high-density lipoprotein (HDL) particle. In a discoidal HDL particle, an open lipid bilayer, in a discoidal shape, is bound on its edge to a flexible double-belt apoA-I chain. In this chapter, continuum approaches and variational tools are implemented to describe the equilibrium of discoidal HDL particles in general configurations. Both geometrically-based and parametrized formulations are provided. Also, a small-slope approximation is used to obtain linearized conditions of equilibrium. The linearized formulation presented in this chapter paves the road for a comprehensive stability analysis performed in Chapter 5. Nevertheless, here, a simple method is considered to deal with the linear stability of flat circular HDL particles. This chapter presents the (currently in preparation) manuscript

M. Maleki and E. Fried, "Equilibrium of discoidal high-density lipoprotein particles," (in preparation).

with permission from the coauthor Prof. Eliot Fried.

4.2 Abstract

The equilibrium conditions of a discoidal high-density lipoprotein (HDL) particle with a general configuration are studied using the continuum mechanics tools and variational approach. The discoidal HDL particle consisting of a lipid bilayer looped by a double-belt apoA-I chain is modelled as an open fluid surface endowed with curvature elasticity and surface tension perfectly bonded on its edge to an inextensible one-dimensional elastic filament with bending energy. First, relying on vanishing the first variation of the underlying energy functional, the general equilibrium equations on the surface and the edge of a discoidal HDL particle are derived and interpreted using a direct, geometrically-based formulation. The problem is next reformulated using parameterization of the surface and the boundary, and the equilibrium equations are derived alternatively in the parametrized form. Next, considering a flat circular HDL particle, the linearized equilibrium conditions are derived using small-slope deformation approximation. Lastly, a handy energy comparison method is used to examine the linear stability of flat circular HDL particle with respect to planar elliptical and transverse saddle-like perturbations. Numerical results reveal that the energy comparison method is an efficient tool for the planar stability and, in specific ranges of the physical parameters values, for the transverse stability.

4.3 Introduction

Over the past few decades, considerable attention has been paid to high-density lipoprotein (HDL) particles, as they are essential to the cholesterol metabolism in the human body. Studying their biological functions is crucial for controlling atherosclerosis. The primary building blocks of an HDL particle are lipid molecules

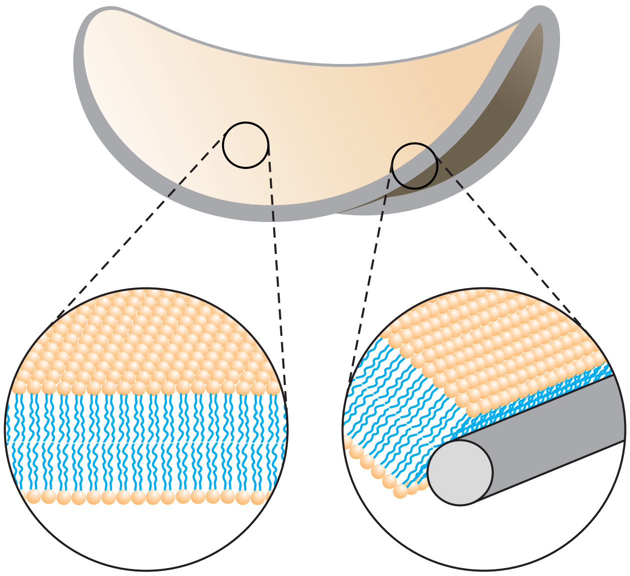

Figure 4–1: Schematic of a generic configuration of a discoidal HDL particle composed of a lipid bilayer bound at its edge by an apoA-I chain. The left inset depicts the arrangement of the lipid molecules at a generic point away from the edge of the particle. The right inset depicts the arrangement of the lipid molecules and the apoA-I chain at a generic point on the edge of the particle.

and apolipoprotein A-I (apoA-I) chains. In a process known as “reverse cholesterol transport” (RCT), HDL particles collect and carry cholesterol from cells and bloodstream for delivery to liver. RCT involves a sequence of steps during which an HDL particle undergoes various shape transitions from discoidal to spheroidal shapes. Importantly, shape transitions of HDL particles are accompanied by significant changes in the conformation of apoA-I chains. As Davidson and Silva [89] observe, the conformation of apoA-I influences its biological functionality and, hence, that understanding its conformational diversity is important. A discoidal HDL particle consists of an open lipid bilayer bound at its edge by a pair of apoA-I chains.

The major part of double-belt apoA-I structure is composed of amphipathic α-helical polypeptide. As a result, α-helical segments of apoA-I attach to the hydrophobic tail groups of the lipids at the edge of the bilayer in a way that the lipid tails groups are shielded from the surrounding solution (Figure 4–1) [56]. Experimental studies and numerical simulations have recently been devoted to understanding the assembly and conformation of discoidal HDL particles. Experiments and all-atom molecular dynamics (MD) simulations reported by Catte et al. [91] reveal that depleting a flat, circular discoidal HDL particle of lipid molecules results in a shape change to a non-planar saddle-like configuration. The saddle-like discoidal HDL particles have been later confirmed by MD simulations [92, 93, 94] and experimentally [95, 96, 94, 50]. Another interesting study due to Skar-Gislinge et al. [97] showed that the discoidal HDL particle may be flat and elliptical. Motivated by the experimental and MD simulation studies, Maleki and Fried [155] studied the linear stability of a discoidal HDL particle is a flat, circular configuration. Their analysis revealed that the first in-plane and transverse unstable modes correspond to planar elliptical and nonplanar saddle-like perturbations.

Although the model of Maleki and Fried [155] explains the equilibrium and stability of a flat, circular HDL particle, it is unable to capture the large distortions observed in experiments and MD simulations. In the present paper, a nonlinear theory for studying the equilibria of a discoidal HDL particle subject to arbitrary—small or large—distortions is developed. Within this theory, the lipid bilayer and double-belt apoA-I chain that comprise a discoidal HDL particle are identified with an open surface and its boundary curve, respectively. An implicit consequence of these identifications is that the lipid bilayer and the apoA-I are perfectly bonded at their interface, which is consistent with high flexibility of apoA-I in adapting different conformations [56]. Aside from supporting a uniform tension, the surface is endowed with curvature elasticity as embodied by a free-energy density of the type familiar from Canham–Helfrich–Evans [21, 22, 57] theory for lipid bilayers. Like the surface tension, the associated splay and saddle-splay moduli are taken to be uniform and spontaneous curvature is neglected. The boundary curve is treated as a twist-free, inextensible, elastic filament, endowed with a bending energy density in a quadratic form of the curvature of the lipid bilayer boundary and derivative of the curvature with respect to the arclength of the boundary. In view of the potential high curvature kinks along apoA-I chains [156, 157, 56], the latter dependency is considered to take the effect of large curvature change into account. For simplicity, we consider uniform rigidity coefficients. Variational arguments are applied to the net potential-energy arising from these assumptions, leading to conditions that describe nontrivial equilibria.

The paper is organized as follows. Necessary mathematical preliminaries, including the differential geometry of the surface (i.e., the lipid bilayer) and its boundary (i.e., the apoA-I chain), are presented in Section 4.4. The assumptions underlying the energetics of a discoidal HDL particle are presented in Section 4.5. A direct, geometrically-based derivation of the Euler–Lagrange equations for the surface and its boundary is presented in Section 4.6. Relying on a parametrization of the surface and its boundary, a reformulation of the variational description of the problem is presented in Section 4.7. Aside from providing a potentially useful platform for continuum-based numerical simulations, the parametrized description leads naturally to a small-slope approximation of the equilibrium conditions, a comprehensive derivation of which appears in Section 4.8. These approximate conditions coincide with those used by Maleki and Fried [155] to study the equilibrium and linear stability of a flat, circular discoidal HDL particle. An energy comparison method is used to obtain a handy criterion for the in-plane and transverse (linear) stability of a flat, circular discoidal HDL particle. Lastly, numerical results are provided in Section 4.9.

4.4 Preliminaries

4.4.1 Two-dimensional representation of a discoidal HDL particle

Consider a discoidal HDL particle consisting of a lipid bilayer and an apoA-I chain. Identify the bilayer with a smooth, open, orientable surface $\mathcal{S}$. Further, consistent with the aforementioned arguments about the flexibility of double-belt apoA-I structure and its affinity with the tail groups of lipid bilayer due to their hydrophobic compatibility [56], assume that the bilayer and the chain are perfectly bonded at their interface, and identify the chain with the boundary $\mathcal{C} = \partial\mathcal{S}$ (Figure 4–2) of $\mathcal{S}$. Smoothness of $\mathcal{S}$ naturally results in the smoothness of $\mathcal{C}$. In addition, we exclude the circumstances wherein either $\mathcal{S}$ or $\mathcal{C}$ can have self intersection.

Let $\boldsymbol{n}$ denote a unit-vector valued orientation on $\mathcal{S}$ and let $\boldsymbol{e}$ denote a unit tangent to $\mathcal{C}$, defined such that, on restricting $\boldsymbol{n}$ to $\mathcal{C}$,

$$\boldsymbol{\nu} = \boldsymbol{e} \times \boldsymbol{n} \tag{4.1}$$

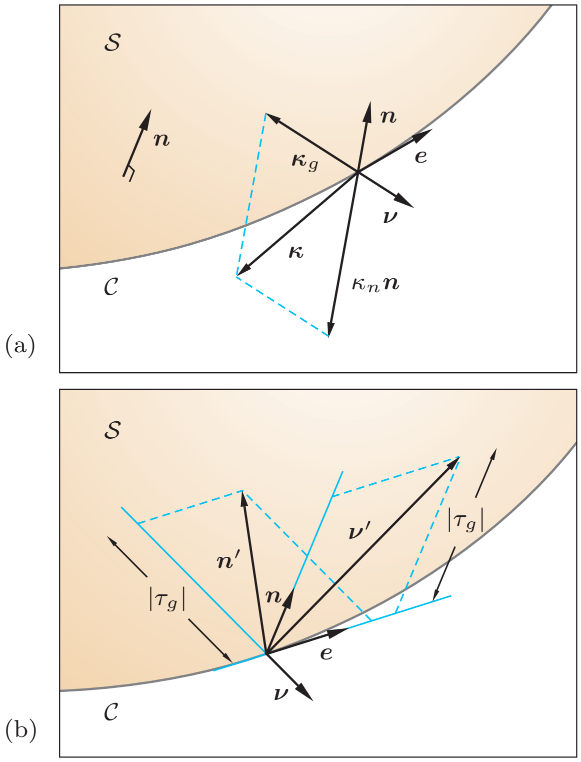

Figure 4–2: (a) Schematic of a portion of a discoidal HDL particle modeled as a surface $\mathcal{S}$ with boundary $\mathcal{C} = \partial\mathcal{S}$. A Darboux frame is shown at a generic point on $\mathcal{C}$. The curvature vector $\boldsymbol{\kappa}$ and its components $\kappa_n\boldsymbol{n}$ and $\boldsymbol{\kappa}_g$ in the normal and tangent to the surface directions are also depicted. In addition, the unit normal $\boldsymbol{n}$ is depicted at a generic point on $\mathcal{S}$. (b) Geometrical interpretation of the geodesic torsion τ_g at the boundary $\mathcal{C}$ of a discoidal HDL particle.

is the unit tangent-normal of $\mathcal{C}$, directed outward from $\mathcal{S}$. The vector triad $\{\boldsymbol{e}, \boldsymbol{n}, \boldsymbol{\nu}\}$, which is orthonormal and positively-oriented, is commonly referred to as the Darboux frame (Figure 4–2) of $\mathcal{C}$.

4.4.2 Superficial fields, differential operators, and useful identities

Fields that are defined exclusively on $\mathcal{S}$ are called superficial. A superficial vector-field $\boldsymbol{g}$ is tangential if

$$\boldsymbol{g} \cdot \boldsymbol{n} = 0. \tag{4.2}$$

Similarly, a superficial tensor-field $\boldsymbol{A}$ is tangential if

$$\boldsymbol{A}\boldsymbol{n} = \boldsymbol{0} \tag{4.3}$$

and fully-tangential if

$$\boldsymbol{A}\boldsymbol{n} = \boldsymbol{A}^{\top}\boldsymbol{n} = \boldsymbol{0}. \tag{4.4}$$

A useful example of a fully-tangential superficial tensor field is the perpendicular projector

$$\boldsymbol{P} = \boldsymbol{1} - \boldsymbol{n} \otimes \boldsymbol{n}. \tag{4.5}$$

Let f be a smooth superficial scalar-field. Consider a point $\boldsymbol{x}$ in the interior of $\mathcal{S}$ and a unit vector $\boldsymbol{m}$ tangent to $\mathcal{S}$ at $\boldsymbol{x}$, so that

$$|\boldsymbol{m}| = 1 \qquad \text{and} \qquad \boldsymbol{m} \cdot \boldsymbol{n}(\boldsymbol{x}) = 0. \tag{4.6}$$

The surface gradient $\nabla_{\mathcal{S}} f$ of f is the unique tangential superficial vector-field defined such that

$$\lim_{h \to 0} \frac{f(\boldsymbol{x} + h\boldsymbol{m}) - f(\boldsymbol{x}) - h[\nabla_{\mathcal{S}} f(\boldsymbol{x})] \cdot \boldsymbol{m}}{h} = 0. \tag{4.7}$$

Analogously, the surface gradient of a smooth superficial vector field $\boldsymbol{g}$ is the unique tangential superficial tensor-field $\nabla_{\mathcal{S}}\boldsymbol{g}$ defined such that

$$\lim_{h\to 0}\frac{\boldsymbol{g}(\boldsymbol{x}+h\boldsymbol{m})-\boldsymbol{g}(\boldsymbol{x})-h[\nabla_{\mathcal{S}}\boldsymbol{g}(\boldsymbol{x})]\boldsymbol{m}}{h}=\boldsymbol{0}. \tag{4.8}$$

Alternatively, given smooth extensions f^{e} and $\boldsymbol{g}^{\mathrm{e}}$ of f and $\boldsymbol{g}$ to some neighborhood of $\mathcal{S}$, $\nabla_{\mathcal{S}}f$ and $\nabla_{\mathcal{S}}\boldsymbol{g}$ are related to the conventional three-dimensional gradients ∇f^{e} and $\nabla\boldsymbol{g}^{\mathrm{e}}$ of f^{e} and $\boldsymbol{g^e}$ by

$$\nabla_{\mathcal{S}}f=\boldsymbol{P}\nabla f^{\mathrm{e}} \qquad \text{and} \qquad \nabla_{\mathcal{S}}\boldsymbol{g}=(\nabla\boldsymbol{g}^{\mathrm{e}})\boldsymbol{P}, \tag{4.9}$$

where ∇f^{e} and $\nabla\boldsymbol{g}^{\mathrm{e}}$ are necessarily evaluated on $\mathcal{S}$. Importantly, as Fried and Gurtin [141] explain, $\nabla_{\mathcal{S}}f$ and $\nabla_{\mathcal{S}}\boldsymbol{g}$ are independent of the strategy used to extend f and $\boldsymbol{g}$.

In view of the foregoing definitions, the surface divergence $\mathrm{div}_{\mathcal{S}}\boldsymbol{g}$ of $\boldsymbol{g}$ and the surface Laplacian $\Delta_{\mathcal{S}}f$ of f are given by

$$\mathrm{div}_{\mathcal{S}}\boldsymbol{g}=\mathrm{tr}\,(\nabla_{\mathcal{S}}\boldsymbol{g})=\boldsymbol{P}\cdot\nabla\boldsymbol{g}^{\mathrm{e}}. \tag{4.10}$$

and

$$\Delta_{\mathcal{S}}f=\mathrm{div}_{\mathcal{S}}\,(\nabla_{\mathcal{S}}f)=\mathrm{tr}\,(\nabla_{\mathcal{S}}\nabla_{\mathcal{S}}f). \tag{4.11}$$

Given a superficial scalar field f and superficial vector fields $\boldsymbol{g}$ and $\boldsymbol{h}$, Gurtin and Murdoch [158] establish the following useful identities

$$\left.\begin{aligned}\mathrm{div}_{\mathcal{S}}\,(f\boldsymbol{g})&=f\,\mathrm{div}_{\mathcal{S}}\boldsymbol{g}+\boldsymbol{g}\cdot\nabla_{\mathcal{S}}f,\\ \nabla_{\mathcal{S}}(\boldsymbol{g}\cdot\boldsymbol{h})&=(\nabla_{\mathcal{S}}\boldsymbol{h})^{\top}\boldsymbol{h}+(\nabla_{\mathcal{S}}\boldsymbol{h})^{\top}\boldsymbol{g}.\end{aligned}\right\} \tag{4.12}$$

4.4.3 Differential geometry of the surface

Like the perpendicular projector $\boldsymbol{P}$, the curvature tensor $\boldsymbol{L}$ of $\mathcal{S}$, defined as

$$\boldsymbol{L} = -\nabla_{\mathcal{S}}\boldsymbol{n} \tag{4.13}$$

is both fully-tangential and symmetric; that is, $\boldsymbol{L}$ satisfies

$$\boldsymbol{L}\boldsymbol{n} = \boldsymbol{0} \qquad \text{and} \qquad \boldsymbol{L} = \boldsymbol{L}^{\top}. \tag{4.14}$$

The mean and Gaussian curvatures H and K of $\mathcal{S}$ may be represented in terms of the scalar invariants $\operatorname{tr}\boldsymbol{L}$ and $\operatorname{tr}(\boldsymbol{L}^2)$ of $\boldsymbol{L}$ via

$$\left.\begin{aligned} H &= \tfrac{1}{2}\operatorname{tr}\boldsymbol{L} = -\tfrac{1}{2}\operatorname{div}_{\mathcal{S}}\boldsymbol{n}, \\ K &= \tfrac{1}{2}\big((\operatorname{tr}\boldsymbol{L})^2 - \operatorname{tr}(\boldsymbol{L}^2)\big), \end{aligned}\right\} \tag{4.15}$$

Eliminating $\operatorname{tr}\boldsymbol{L}$ between $(4.15)_1$ and $(4.15)_2$ yields the useful corollary

$$\operatorname{tr}(\boldsymbol{L}^2) = 2(2H^2 - K). \tag{4.16}$$

4.4.4 Surface divergence theorem

With reference to the definition (4.1) of the unit tangent-normal $\boldsymbol{\nu}$, the surface divergence theorem implies that [158]

$$\int_{\mathcal{C}} \boldsymbol{g}\cdot\boldsymbol{\nu} = \int_{\mathcal{S}} (\operatorname{div}_{\mathcal{S}}\boldsymbol{g} + 2H\boldsymbol{g}\cdot\boldsymbol{n}). \tag{4.17}$$

4.4.5 Differential geometry of the boundary curve

Let a prime represent differentiation with respect to the arclength s along $\mathcal{C}$. The arclength derivatives of the elements $\boldsymbol{e}$, $\boldsymbol{n}$, and $\boldsymbol{\nu}$ of the Darboux frame then obey

$$\left.\begin{aligned} \boldsymbol{e}' &= \kappa_n\boldsymbol{n} - \kappa_g\boldsymbol{\nu}, \\ \boldsymbol{n}' &= -\kappa_n\boldsymbol{e} - \tau_g\boldsymbol{\nu}, \\ \boldsymbol{\nu}' &= \kappa_g\boldsymbol{e} + \tau_g\boldsymbol{n}, \end{aligned}\right\} \tag{4.18}$$

where

$$\kappa_n = \boldsymbol{e}' \cdot \boldsymbol{n} = -\boldsymbol{n}' \cdot \boldsymbol{e}, \quad \kappa_g = -\boldsymbol{e}' \cdot \boldsymbol{\nu} = \boldsymbol{\nu}' \cdot \boldsymbol{e}, \tag{4.19}$$

and

$$\tau_g = \boldsymbol{\nu}' \cdot \boldsymbol{n} = -\boldsymbol{n}' \cdot \boldsymbol{\nu} \tag{4.20}$$

are, respectively, the normal curvature, geodesic curvatures, and geodesic torsion of $\mathcal{C}$. Geometrical interpretations of κ_n, κ_g, and τ_g are provided in Figure 4–2.

The differentiation properties (4.18) provide a representation

$$\boldsymbol{\kappa} = \boldsymbol{e}' = \kappa_n\boldsymbol{n} - \kappa_g\boldsymbol{\nu} \tag{4.21}$$

for the curvature vector $\boldsymbol{\kappa}$ of $\mathcal{C}$ and suggest introducing a geodesic curvature vector

$$\boldsymbol{\kappa}_g = \boldsymbol{\kappa} - \kappa_n\boldsymbol{n} = -\kappa_g\boldsymbol{\nu} \tag{4.22}$$

for $\mathcal{C}$. In view of (4.21) and (4.22), $\kappa_n\boldsymbol{n}$ and $\boldsymbol{\kappa}_g = -\kappa_g\boldsymbol{\nu}$ are the normal and tangential components of the curvature vector $\boldsymbol{\kappa}$ and the magnitude $\kappa = |\boldsymbol{e}'| = |\boldsymbol{\kappa}|$ of $\boldsymbol{\kappa}$, which is also known as the scalar curvature of $\mathcal{C}$, is determined by κ_n and κ_g through

$$\kappa = \sqrt{\kappa_n^2 + \kappa_g^2}, \tag{4.23}$$

where, using (4.21) and (4.22), the normal and geodesic curvatures κ_n and κ_g can alternatively be expressed as

$$\kappa_n = \boldsymbol{\kappa} \cdot \boldsymbol{n}, \quad \kappa_g = -\boldsymbol{\kappa} \cdot \boldsymbol{\nu}. \tag{4.24}$$

Since $\boldsymbol{n}'$ is simply the derivative of $\boldsymbol{n}$ in $\boldsymbol{e}$ direction, using the definition of the curvature tensor $\boldsymbol{L}$ in (4.13) yields

$$\boldsymbol{n}' = (\nabla_{\mathcal{S}} \boldsymbol{n})\boldsymbol{e} = -\boldsymbol{L}\boldsymbol{e}. \tag{4.25}$$

Using (4.25) in $(4.19)_1$ and (4.20) leads to representations

$$\kappa_n = -\boldsymbol{n}' \cdot \boldsymbol{e} = -\boldsymbol{e} \cdot (\nabla_{\mathcal{S}} \boldsymbol{n})\boldsymbol{e} = \boldsymbol{e} \cdot \boldsymbol{L}\boldsymbol{e} \tag{4.26}$$

and

$$\tau_g = -\boldsymbol{n}' \cdot \boldsymbol{\nu} = -\boldsymbol{\nu} \cdot (\nabla_{\mathcal{S}} \boldsymbol{n})\boldsymbol{e} = \boldsymbol{e} \cdot \boldsymbol{L}\boldsymbol{\nu} \tag{4.27}$$

for the normal curvature and geodesic torsion in terms of the restriction to $\mathcal{C}$ of the curvature tensor $\boldsymbol{L}$ of $\mathcal{S}$. In contrast, it is evident from $(4.19)_2$ that the geodesic curvature κ_g cannot be expressed in terms of $\boldsymbol{n}'$ and, thus, cannot be represented in terms of the restriction of $\boldsymbol{L}$ to $\mathcal{C}$. Hence, κ_g must be viewed as a geometric quantity which is independent of $\boldsymbol{L}$.

4.5 Energetics of a discoidal HDL particle

Consider a discoidal HDL particle comprised by a lipid bilayer and an apoA-I chain. Assume that the particle is thermally and chemically isolated and free of applied forces and moments. Then net potential-energy of the particle must then be the sum of the free-energy of the bilayer and the free-energy of the chain. Moreover, a stable equilibrium configuration of the particle must minimize that sum. Having identified the bilayer and chain with an open surface $\mathcal{S}$ and its boundary $\mathcal{C} = \partial\mathcal{S}$, any study of the equilibrium configurations available to the particle rests on providing suitable model expressions for the free-energy densities of $\mathcal{S}$ and $\mathcal{C}$.

4.5.1 Free-energy density of the lipid bilayer

The prevailing approach to modeling lipid bilayers as surfaces dates to the seminal works of Canham [21], Helfrich [22], and Evans [57], who independently recognized the critical importance of bending elasticity. For a surface with mean and Gaussian curvatures H and K, the Canham–Helfrich–Evans free-energy density has the general form $\frac{1}{2}\mu(H - H_\circ)^2 + \bar{\mu}K$, with μ and $\bar{\mu}$ the splay and saddle-splay moduli and $H_\circ$ the spontaneous (mean) curvature. However, as there is currently no compelling evidence to suggest that discoidal HDL particles possess spontaneous curvature, it seems reasonable to take $H_\circ = 0$ and work with the resulting specialization,

$$\psi = \tfrac{1}{2}\mu H^2 + \bar{\mu}K, \tag{4.28}$$

of the Canham–Helfrich–Evans expression.

Additionally, following Farago and Pincus [159], $\mathcal{S}$ is endowed with a uniform surface tension σ, so that its net free-energy per unit area is

$$\sigma + \psi. \tag{4.29}$$

Farago and Pincus [159] discuss that the surface tension σ can be viewed as a unified quantity in two different possible processes. In the first process, the number of lipid molecules are fixed and the surface tension is induced as a result of change of area per unit molecule. Consistent with this viewpoint, considering the discoidal HDL particle as a closed system, we consider σ as a uniform and constant tension. In the second process discussed by Farago and Pincus [159], when the system is not closed and the exchange of lipid molecules is allowed, σ plays the role of the chemical potential of lipid molecules when they are added or removed from the lipid bilayer. For this case, change of the net area is a result of change of net number of lipid molecules on its surface. However, confining our attention to a chemically-isolated discoidal HDL particle, such treatment does not apply to our case. Apart from the former porcess where the area of lipid bilayer is not fixed, the presented formulation may also be applied to another possible case, when the area of lipid bilayer is locally inextensible. Areal inextensibility of lipid bilayer is a common assumption in mechanical modeling of giant unilamellar vesicles (GUVs) [27, 23]. For this example, σ plays the role of an unknown Lagrange multiplier which penalizes the areal inextensibility of lipid bilayer. By adapting such assumption, the equilibrium equations is augmented by the constraint equations by which the unknown Lagrange multiplier can be determined. Steigmann et al. [116] show that the Lagrange multiplier σ must be uniform on the surface of lipid bilayer to guarantee its tangential equilibrium. An important difference between a GUV and discoidal HDL particle is the considerable size difference. The typical diameter of a spherical GUV is in order of few micrometers while the latter has the typical diameter of about 10 nm. However, they both have same thickness—i.e., the thickness of a lipid bilayer. From the structural point of view, GUVs are very thin structures whose typical radii of curvature are usually much larger than their thickness. Naturally, deformation of GUVs is primarily dominated by bending and, hence, the area change has very minor contribution. However, generalization of such reasoning for lipid bilayer in discoidal HDL particles does not seem trivial and requires careful study. This is particularly because discoidal HDL particles are much thicker than GUVs (comparing their ratio of thickness to the lateral characteristic length), and also the radii of curvature in the observed non-flat configurations of discoidal HDL particles are comparable with their thickness (e.g., see [91] and [94]). For example, relying on the assumption of volumetric incompressibility of lipid bilayer [58, 59, 60], Maleki et al. [160] show how the thickness of lipid bilayer, radii of curvatures (or alternatively, the mean and Gaussian curvatures) and areal stretch of lipid bilayer midsurface may depend on each others. It can be observed that when the radii of curvature of the lipid bilayer midsurface are much larger than its thickness, no coupling arises between the bending and stretching. The presented formulation in this paper can be applied for either scenarios, i.e., whether or not the area of lipid bilayer is locally persevered in deformation of a discoidal HDL particle. However, for the constrained case, as mentioned earlier, the equilibrium conditions must be augmented by the areal inextensibility constraint equation.

4.5.2 Free-energy density of the apoA-I chain

The bounding double-belt apoA-I chain is a flexible structure which can easily conform to the boundary of the discoidal lipid bilayer by bending. A mechanical model with minimal complexity which can efficiently describe the energetics of the apoA-I double-belt chain relies on the energy density φ (per unit arclength of $\mathcal{C}$) which takes the change of curvature κ of $\mathcal{C}$ into account. Additionally, in view of the observed large variation of the curvature across apoA-I chain around very localized kink-like regions [156, 157], we may augment φ with an additional term depending on the arclength derivative κ' of κ. A simple expression of such energy density can have the quadratic form of [155]

$$\varphi = \tfrac{1}{2}\alpha\kappa^2 + \tfrac{1}{2}\beta(\kappa')^2, \tag{4.30}$$

where $\alpha > 0$ is the bending modulus of $\mathcal{C}$. In addition, $\beta \geq 0$ is the constant generalized bending modulus which penalizes nonuniformity of the curvature κ along $\mathcal{C}$. Notice that since $\mathcal{C}$ is closed, inclusion of a coupling term proportional to $\kappa\kappa' = \frac{1}{2}(\kappa^2)'$ in φ is irrelevant because it is ruled out after integrating φ over $\mathcal{C}$.

4.5.3 Net potential-energy of a discoidal HDL particle

Granted that the particle is isolated, both thermally and chemically, and is not subject to externally applied forces and moments, the net potential-energy of a discoidal HDL takes the form

$$\mathcal{E} = \int_{\mathcal{S}} (\sigma + \psi) + \int_{\mathcal{C}} \varphi. \tag{4.31}$$

The inextensibility of apoA-I chain can be incorporated by working with the augmented net potential-energy (e.g., see [101] for a similar augmentation)

$$\mathcal{F} = \mathcal{E} + \int_{\mathcal{C}} \lambda, \tag{4.32}$$

where λ is an unknown Lagrange multiplier.

Since $\mathcal{S}$ is a smooth, orientable open surface with smooth boundary $\mathcal{C}$, applying the Gauss–Bonnet theorem to (4.31) leads to

$$\mathcal{F} = \mathcal{F}_a + \mathcal{F}_l + 2\pi\bar{\mu}, \tag{4.33}$$

where

$$\mathcal{F}_a = \int_{\mathcal{S}} (\sigma + \tfrac{1}{2}\mu H^2) \tag{4.34}$$

and

$$\mathcal{F}_l = \int_{\mathcal{C}} (\tfrac{1}{2}\alpha\kappa^2 + \tfrac{1}{2}\beta(\kappa')^2 - \bar{\mu}\kappa_g + \lambda) \tag{4.35}$$

represent effective measures of areal and lineal potential energy.

4.6 Direct formulation

In this section, a direct, geometrically-based approach is employed to address the equilibrium of a discoidal HDL particle.

4.6.1 Variation of the net potential-energy

At equilibrium, the first variation $\dot{\mathcal{F}}$ of the energy functional $\mathcal{F}$ must vanish. Consider a general variation $\boldsymbol{v}$ defined on $\mathcal{S}$ and $\mathcal{C}$. Any such variation may be decomposed into a sum [116]

$$\boldsymbol{v} = \boldsymbol{v}_t + U\boldsymbol{n}. \tag{4.36}$$

of tangential and normal variations $\boldsymbol{v}_t = \boldsymbol{P}_{\boldsymbol{n}}\boldsymbol{v}$ and $U\boldsymbol{n}$. It is advantageous to consider separately the first variations $\dot{\mathcal{F}}_a$ and $\dot{\mathcal{F}}_l$ of $\mathcal{F}_a$ and $\mathcal{F}_l$ in (4.33).

Areal contribution

Using the variation of superficial integral in (4.188) and keeping in mind that σ is uniform, it follows from (4.34) that the variation $\dot{\mathcal{F}}_a$ of the areal contribution (4.34) to the net potential energy $\mathcal{F}$ takes the form

$$\dot{\mathcal{F}}_a = \int_{\mathcal{S}} \big(\mu H\dot{H} + (\sigma + \tfrac{1}{2}\mu H^2)(\operatorname{div}_{\mathcal{S}}\boldsymbol{v}_t - 2HU)\big). \tag{4.37}$$

Since σ is constant,

$$\sigma(\operatorname{div}_{\mathcal{S}}\boldsymbol{v}_t - 2HU) = -2\sigma HU + \operatorname{div}_{\mathcal{S}}(\sigma\boldsymbol{v}_t). \tag{4.38}$$

Further, substituting the expression for variation $\dot{H}$ of the mean curvature H provided in (4.181) and using the identity $(4.12)_1$ yields

$$\begin{aligned} &H\dot{H} + \tfrac{1}{2}H^2(\operatorname{div}_{\mathcal{S}}\boldsymbol{v}_t - 2HU) \\ &\qquad = \big(\tfrac{1}{2}\triangle_{\mathcal{S}}H + H(H^2-K)\big)U - \tfrac{1}{2}\operatorname{div}_{\mathcal{S}}\big((\nabla_{\mathcal{S}}H)U - H^2\boldsymbol{v}_t - H\nabla_{\mathcal{S}}U\big). \end{aligned} \tag{4.39}$$

Thus, by the surface divergence theorem (4.17), it follows that

$$\begin{aligned}\dot{\mathcal{F}}_a &= \int_{\mathcal{S}} \tfrac{1}{2}\big(\mu\triangle_{\mathcal{S}}H + 2\mu H(H^2-K) - 4\sigma H\big)U \\ &\quad + \int_{\mathcal{C}} \Big[\tfrac{1}{2}\mu\big(H^2\boldsymbol{\nu}\cdot\boldsymbol{v}_t + H\nabla_{\mathcal{S}}U\cdot\boldsymbol{\nu} - (\nabla_{\mathcal{S}}H)\cdot\boldsymbol{\nu}U\big) + \sigma\boldsymbol{v}_t\cdot\boldsymbol{\nu}\Big]. \qquad (4.40)\end{aligned}$$

Lineal contribution

Consider the variation $\dot{\mathcal{F}}_l$ of the lineal contribution $\mathcal{F}_l$ in the net potential-energy $\mathcal{F}$. In view of (4.35) the general expression (4.212) for the variation of an integral over $\mathcal{C}$, it follows that

$$\dot{\mathcal{F}}_l = \int_{\mathcal{C}} \big[\alpha\kappa\dot{\kappa} + \beta\kappa'\dot{\overline{\kappa'}} - \bar{\mu}\dot{\kappa}_g + \big(\tfrac{1}{2}\alpha\kappa^2 + \tfrac{1}{2}\beta\kappa'^2 - \bar{\mu}\kappa_g + \lambda\big)\boldsymbol{v}'\cdot\boldsymbol{e}\big]. \qquad (4.41)$$

Substituting the expressions (4.201), (4.202), and (4.209) for the variations $\dot{\kappa}$, $\dot{\overline{\kappa'}}$, and $\dot{\kappa}_g$ in (4.41), integrating by parts, using (4.25) and the properties $\boldsymbol{\nu}\cdot\boldsymbol{n} = \boldsymbol{\nu}\cdot\boldsymbol{e} = 0$ and $\boldsymbol{\nu}\cdot\boldsymbol{\nu} = 1$, results in

$$\begin{aligned}\dot{\mathcal{F}}_l &= \int_{\mathcal{C}} \big[\boldsymbol{a}'\cdot\boldsymbol{n} - (\boldsymbol{a}\cdot\boldsymbol{e})\kappa_n + \big(\alpha\kappa^2 - \beta\big(\kappa\kappa'' - \kappa'^2\big)\big)\kappa_n \\ &\quad - (\tfrac{1}{2}\alpha\kappa^2 + \tfrac{1}{2}\beta\kappa'^2 - \bar{\mu}\kappa_g + \lambda)\kappa_n + \bar{\mu}c\big]U + \int_{\mathcal{C}} \bar{\mu}\kappa_n(\nabla_{\mathcal{S}}U\cdot\boldsymbol{\nu}) \\ &\quad + \int_{\mathcal{C}} \Big[\boldsymbol{P_n}\boldsymbol{a}' - \big(\boldsymbol{a}'\cdot\boldsymbol{e} + \boldsymbol{a}\cdot\boldsymbol{\kappa}\big)\boldsymbol{e} - (\boldsymbol{a}\cdot\boldsymbol{e})\boldsymbol{\kappa}_g + \big(\alpha\kappa^2 - \beta\big(\kappa\kappa'' - \kappa'^2\big)\big)'\boldsymbol{e} \\ &\quad + \big(\alpha\kappa^2 - \beta\big(\kappa\kappa'' - \kappa'^2\big)\big)\boldsymbol{\kappa}_g - (\tfrac{1}{2}\alpha\kappa^2 + \tfrac{1}{2}\beta\kappa'^2 - \bar{\mu}\kappa_g + \lambda)'\boldsymbol{e} \\ &\quad - (\tfrac{1}{2}\alpha\kappa^2 + \tfrac{1}{2}\beta\kappa'^2 - \bar{\mu}\kappa_g + \lambda)\boldsymbol{\kappa}_g + \bar{\mu}\kappa_n\boldsymbol{L}\boldsymbol{\nu} + \bar{\mu}\boldsymbol{b}\Big]\cdot\boldsymbol{v}_t, \qquad (4.42)\end{aligned}$$

where $\boldsymbol{a}$, $\boldsymbol{b}$, and c are defined by

$$\left.\begin{aligned} \boldsymbol{a} &= \alpha\boldsymbol{\kappa}' - \beta\big((\kappa^{-1}\kappa''' - \kappa^{-2}\kappa''\kappa')\boldsymbol{\kappa} + \kappa^{-1}\kappa''\boldsymbol{\kappa}'\big), \\ \boldsymbol{b} &= -(\tau_g\boldsymbol{L}\boldsymbol{e} + \kappa_g'\boldsymbol{e} + \kappa_g\boldsymbol{\kappa}_g), \end{aligned}\right\} \tag{4.43}$$

and

$$c = \tau_g' - \kappa_g\kappa_n. \tag{4.44}$$

4.6.2 Euler–Lagrange equations

Stipulating that the the variation

$$\dot{\mathcal{F}} = \dot{\mathcal{F}}_a + \dot{\mathcal{F}}_l \tag{4.45}$$

of the net potential-energy $\mathcal{F}$ to be stationary delivers the Euler–Lagrange equations. Since, the variations U, $\boldsymbol{v}_t$, and $\nabla_{\mathcal{S}}U\cdot\boldsymbol{\nu}$ are independent fields, the fundamental lemma of calculus of variations can then be used to obtain the governing Euler–Lagrange equations. These consist of the shape equation

$$\mu\triangle_{\mathcal{S}}H + 2\mu H(H^2 - K) - 4\sigma H = 0, \tag{4.46}$$

which must hold on $\mathcal{S}$, and the boundary conditions

$$\begin{multline} -\tfrac{1}{2}\mu(\nabla_{\mathcal{S}}H)\cdot\boldsymbol{\nu} + \boldsymbol{a}'\cdot\boldsymbol{n} - (\boldsymbol{a}\cdot\boldsymbol{e})\kappa_n + \big(\alpha\kappa^2 - \beta\big(\kappa\kappa'' - \kappa'^2\big)\big)\kappa_n \\ - (\tfrac{1}{2}\alpha\kappa^2 + \tfrac{1}{2}\beta\kappa'^2 - \bar{\mu}\kappa_g + \lambda)\kappa_n + \bar{\mu}c = 0, \end{multline} \tag{4.47}$$

$$\tfrac{1}{2}\mu H + \bar{\mu}\kappa_n = 0, \tag{4.48}$$

$$
\begin{aligned}
&(\tfrac{1}{2}\mu H^2+\sigma)\boldsymbol{\nu}+\boldsymbol{P_n}\boldsymbol{a}'-\big(\boldsymbol{a}'\cdot\boldsymbol{e}+\boldsymbol{a}\cdot\boldsymbol{\kappa}\big)\boldsymbol{e}\\
&\qquad-(\boldsymbol{a}\cdot\boldsymbol{e})\boldsymbol{\kappa}_g+\big(\alpha\kappa^2-\beta\big(\kappa\kappa''-\kappa'^2\big)\big)'\boldsymbol{e}+\big(\alpha\kappa^2-\beta\big(\kappa\kappa''-\kappa'^2\big)\big)\boldsymbol{\kappa}_g\\
&\qquad-(\tfrac{1}{2}\alpha\kappa^2+\tfrac{1}{2}\beta\kappa'^2-\bar{\mu}\kappa_g+\lambda)'\boldsymbol{e}-(\tfrac{1}{2}\alpha\kappa^2+\tfrac{1}{2}\beta\kappa'^2-\bar{\mu}\kappa_g+\lambda)\boldsymbol{\kappa}_g\\
&\qquad\qquad+\bar{\mu}\kappa_n\boldsymbol{L}\boldsymbol{\nu}+\bar{\mu}\boldsymbol{b}=\boldsymbol{0},
\end{aligned}
\tag{4.49}
$$

must be satisfied on $\mathcal{C}$. Using (4.43) and (4.44) in (4.47) yields

$$
\begin{aligned}
&-\tfrac{1}{2}\mu(\nabla_{\mathcal{S}}H)\cdot\boldsymbol{\nu}+\alpha(\kappa_n''-2\kappa_g'\tau_g-\tau_g'\kappa_g+\tfrac{1}{2}\kappa_n^3-\kappa_n\tau_g^2+\tfrac{1}{2}\kappa_g^2\kappa_n)\\
&\qquad+\bar{\mu}\tau_g'-\kappa_n\lambda+\beta\big[-\big(\kappa^{-1}\kappa''''-2\kappa^{-2}\kappa'''\kappa'+2\kappa^{-3}(\kappa')^2\kappa''-\kappa^{-2}(\kappa'')^2\big)\kappa_n\\
&-2(\kappa^{-1}\kappa'''-\kappa^{-2}\kappa''\kappa')(\kappa_n'-\kappa_g\tau_g)-\kappa^{-1}\kappa''\big(\kappa_n''-\kappa_g\tau_g'-\kappa_n^3-\kappa_n\tau_g^2-2\kappa_g'\tau_g-\kappa_g^2\kappa_n\big)\\
&\qquad\qquad-2\kappa_n\kappa\kappa''+\tfrac{1}{2}(\kappa')^2\kappa_n\big]=0.
\end{aligned}
\tag{4.50}
$$

Also, (4.49) is a vectorial (tangential) equation including two independent scalar equations. Using (4.43) in boundary conditions (4.49) and dot producting it with $\boldsymbol{\nu}$ and $\boldsymbol{e}$ respectively lead to

$$
\begin{aligned}
&(\tfrac{1}{2}\mu H^2+\sigma)+\alpha(-\kappa_g''-\tau_g'\kappa_n-2\tau_g\kappa_n'+\tau_g^2\kappa_g-\tfrac{1}{2}\kappa_g\kappa^2)+\lambda\kappa_g+\bar{\mu}K\\
&\qquad+\beta\big[\big(\kappa^{-1}\kappa''''-2\kappa^{-2}\kappa'''\kappa'+2\kappa^{-3}(\kappa')^2\kappa''-\kappa^{-2}(\kappa'')^2\big)\kappa_g\\
&+2(\kappa^{-1}\kappa'''-\kappa^{-2}\kappa''\kappa')(\kappa_g'+\kappa_n\tau_g)-\kappa^{-1}\kappa''(-\kappa_g''-\tau_g'\kappa_n-2\tau_g\kappa_n'+\tau_g^2\kappa_g+\kappa_g\kappa_n^2+\kappa_g^3)\\
&\qquad\qquad+2\kappa_g\kappa''\kappa-\tfrac{1}{2}\kappa_g(\kappa')^2\big]=0,
\end{aligned}
\tag{4.51}
$$

and

$$
\lambda=\text{constant}.
\tag{4.52}
$$

The shape equation (4.46) governs the local curvature of the lipid bilayer. In addition, the boundary conditions (4.48), (4.50), (4.51), and (4.52) must be satisfied on $\mathcal{C}$. We may also interpret the physical meanings of the boundary conditions (4.48), (4.50), (4.51), and (4.52) by checking their energetic kinematical conjugates in (4.45). As a result, (4.50) explains the equilibrium of the boundary curve $\mathcal{C}$ in the normal $\boldsymbol{n}$ direction. Also, (4.48) governs the slope of $\mathcal{S}$ in $\boldsymbol{\nu}$ direction at its boundary $\mathcal{C}$ and, thus, implies the balance of bending moments at the boundary of $\mathcal{S}$ in that direction. Equation (4.51) describes the shape of $\mathcal{C}$ in the tangent plane of $\mathcal{S}$ at $\mathcal{C}$—i.e., the plane spanned by $\boldsymbol{e}$ and $\boldsymbol{\nu}$. The boundary condition (4.51) can be viewed as lineal analogous of the shape equation (4.46). Lastly, (4.52) implies that the Lagrange multiplier λ must be uniform on $\mathcal{C}$ for forces to be balanced in the direction $\boldsymbol{e}$ tangent to $\mathcal{C}$ of $\mathcal{S}$. Consistent with the absence of external forces or moments applied to $\mathcal{C}$, the boundary conditions (4.48), (4.50), (4.51), and (4.52) are homogeneous.

The derived equilibrium equations are accompanied by the local inextensibility constraint of $\mathcal{C}$. However, since λ is uniform on $\mathcal{C}$, we may also use the global form of that constraint, which implies that

$$L = L_{\circ}, \tag{4.53}$$

where L is the perimeter of $\mathcal{C}$ and $L_{\circ}$ is the corresponding reference value.

4.6.3 Planar disk

Consider the limiting case in which the shape of a discoidal HDL particle has a flat circular configuration of radius R. This configuration may be considered as the reference configuration (Figure 4–3a). In such case, the shape equation (4.46) is trivially satisfied on the surface and, on the boundary, the only nonvanishing equation is (4.51) as

$$-\frac{\alpha}{2R^3} + \frac{\lambda}{R} + \sigma = 0. \tag{4.54}$$

Equation (4.54) is consistent with the a result obtained by Giomi and Mahadevan [101] in studying a soap film looped by an inextensible elastic circular curve. A more special case is when the bounding loop has negligible bending energy. Then, (4.54) reduces to

$$\frac{\lambda}{R} + \sigma = 0. \tag{4.55}$$

Equation (4.55) can be viewed as a two-dimensional Young–Laplace equation. In addition,

$$\lambda = -\sigma R \tag{4.56}$$

indicates that λ has the nature of the line tension—or, the compression in this case.

4.6.4 Discoidal HDL particles with locally-preserved area

Following the discussions in Section 4.5.1, we may use the presented formulation in Section 4.6 and the following Section 4.7 for the possible case that the area of lipid bilayer is locally preserved. Under this circumstance, as opposed to our current treatment of σ by assuming it as a uniform constant input, we need to consider σ as an unknown Lagrange multiplier on $\mathcal{S}$ and to include its spatial derivative in the calculations. In doing so, in the absence of external force and moments of the surface of lipid bilayer, consistent with the result of Steigmann et al. [116], we conclude that σ must be uniform on $\mathcal{S}$ as a consequence of local tangential equilibrium of lipid

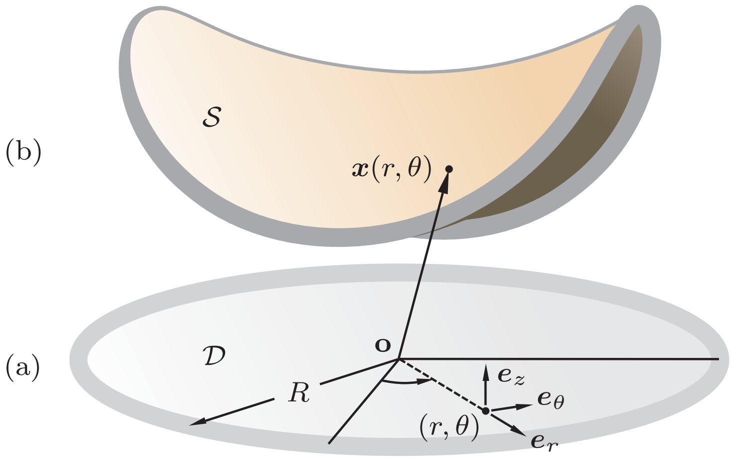

Figure 4–3: Schematic of a reference flat circular HDL particle and a generic configuration of a discoidal HDL particle in the observed space. The polar coordinate is used for parametrization of the surface $\mathcal{S}$ and the boundary $\mathcal{C}$ of the discoidal HDL particle.

bilayer. Now, since σ is uniform on $\mathcal{S}$, the constraint equation may advantageously be used in its global form as

$$A = A_\circ, \tag{4.57}$$

where A is the area of $\mathcal{S}$ and $A_\circ$ is the corresponding reference value. Equation (4.57) along with the existing derived equilibrium conditions suffice description of the equilibrium state and determination of σ.

4.7 Parameterized formulation

In this section, we reformulate the problem by parametrization of the surface $\mathcal{S}$ and its boundary $\mathcal{C}$. Parametrized reformulation of the problem is particularly crucial towards finding closed-form solutions for the equilibrium equations, and more practically, for implementation of numerical approaches, such as finite element method.

Consider a circular disk $\mathcal{D}$ of radius R as a reference configuration. Using the polar coordinate (r, θ), the domain $\mathcal{D}$ can be expressed as

$$\mathcal{D} = \{(r, \theta) : 0 \leq r \leq R, 0 \leq \theta \leq 2\pi\}. \tag{4.58}$$

We view $\mathcal{S}$ as the deformed configuration or image of $\mathcal{D}$ as

$$\mathcal{S} = \{\boldsymbol{x} \in \mathbb{R}^3 : \boldsymbol{x} = \boldsymbol{x}(r, \theta), (r, \theta) \in \mathcal{D}\}, \tag{4.59}$$

and $\mathcal{C}$, the image of $\partial\mathcal{D}$, as

$$\mathcal{C} = \{\boldsymbol{x} \in \mathbb{R}^3 : \boldsymbol{x} = \boldsymbol{x}(R, \theta), 0 \leq \theta \leq 2\pi\}. \tag{4.60}$$

The areal and lineal parts $\mathcal{F}_a$ and $\mathcal{F}_l$ of the energy functional $\mathcal{F}$ in (4.33) can be expressed parametrically as

$$\mathcal{F}_a = \int_0^{2\pi} \int_0^R (\sigma + \tfrac{1}{2}\mu H^2)|\boldsymbol{x}_r \times \boldsymbol{x}_\theta| \, \mathrm{d}r \, \mathrm{d}\theta \tag{4.61}$$

and

$$\mathcal{F}_l = \int_0^{2\pi} (\tfrac{1}{2}\alpha\kappa^2 + \tfrac{1}{2}\beta(\kappa')^2 - \bar{\mu}\kappa_g + \lambda)|\boldsymbol{x}_\theta| \, \mathrm{d}\theta, \tag{4.62}$$

where subscripts r and θ indicate the partial derivative with respect to r and θ, respectively.

4.7.1 Parameterized geometrical quantities

In this section, geometrical quantities which are used in the following formulation have been presented in terms of parametrization (4.59) and (4.60).

Areal quantities

Parametric expressions of the mean and Gaussian curvature H and K are

$$H = \frac{\boldsymbol{n} \cdot (\boldsymbol{x}_\theta \times \boldsymbol{n}_r + \boldsymbol{n}_\theta \times \boldsymbol{x}_r)}{2|\boldsymbol{x}_r \times \boldsymbol{x}_\theta|} \tag{4.63}$$

and

$$K = \frac{(\boldsymbol{n} \cdot \boldsymbol{x}_{rr})(\boldsymbol{n} \cdot \boldsymbol{x}_{\theta\theta}) - |\boldsymbol{n} \cdot \boldsymbol{x}_{r\theta}|^2}{|\boldsymbol{x}_r \times \boldsymbol{x}_\theta|^2}, \tag{4.64}$$

where the normal $\boldsymbol{n}$ is given by

$$\boldsymbol{n} = \frac{\boldsymbol{x}_r \times \boldsymbol{x}_\theta}{|\boldsymbol{x}_r \times \boldsymbol{x}_\theta|}. \tag{4.65}$$

Lineal quantities

The curvature κ, curvature derivative κ', the normal curvature κ_n, and the geodesic curvature κ_g are

$$\left.\begin{aligned} \kappa &= \left.\frac{|\boldsymbol{x}_\theta \times \boldsymbol{x}_{\theta\theta}|}{|\boldsymbol{x}_\theta|^3}\right|_{r=R}, \quad \kappa' = \left.\frac{\kappa_\theta}{|\boldsymbol{x}_\theta|}\right|_{r=R}, \\ \kappa_n &= \left.\frac{\boldsymbol{x}_{\theta\theta} \cdot \boldsymbol{n}}{|\boldsymbol{x}_\theta|^2}\right|_{r=R}, \quad \kappa_g = \left.\frac{\boldsymbol{n} \cdot (\boldsymbol{x}_\theta \times \boldsymbol{x}_{\theta\theta})}{|\boldsymbol{x}_\theta|^3}\right|_{r=R}. \end{aligned}\right\} \tag{4.66}$$

Also, the lineal inextensibility of $\mathcal{C}$ can be expressed as

$$|\boldsymbol{x}_\theta|_{r=R} = R. \tag{4.67}$$

Two useful consequences of (4.67) are

$$(\boldsymbol{x}_\theta \cdot \boldsymbol{x}_{\theta\theta})_{r=R} = 0, \quad |\boldsymbol{x}_\theta \times \boldsymbol{x}_{\theta\theta}|_{r=R} = R|\boldsymbol{x}_{\theta\theta}|_{r=R}. \tag{4.68}$$

In view of the constraint (4.67) and the subsequent results (4.68), the lineal quantities in (4.66) take the form

$$\left.\begin{aligned} \kappa &= \frac{|\boldsymbol{x}_{\theta\theta}|_{r=R}}{R^2}, \quad \kappa' = \frac{\big(|\boldsymbol{x}_{\theta\theta}|_\theta\big)_{r=R}}{R^3}, \\ \kappa_n &= \frac{(\boldsymbol{x}_{\theta\theta}\cdot\boldsymbol{n})_{r=R}}{R^2}, \quad \kappa_g = \frac{\boldsymbol{n}\cdot(\boldsymbol{x}_\theta\times\boldsymbol{x}_{\theta\theta})}{R^3}\bigg|_{r=R}. \end{aligned}\right\} \tag{4.69}$$

4.7.2 Variation of the net potential-energy

Areal contribution

Since the integration domain $\mathcal{D}$ in (4.61) is fixed, only the variation of its integrant must be calculated. Then

$$\dot{\mathcal{F}}_a = \int_0^{2\pi}\int_0^R \big[\mu H\dot{H}|\boldsymbol{x}_r\times\boldsymbol{x}_\theta| + (\sigma+\tfrac{1}{2}\mu H^2)\overline{|\boldsymbol{x}_r\times\boldsymbol{x}_\theta|}^{\boldsymbol{\cdot}}\big]\,\mathrm{d}r\,\mathrm{d}\theta. \tag{4.70}$$

Substitution of the variations $\dot{H}$ and $\dot{\overline{|\boldsymbol{x}_r \times \boldsymbol{x}_\theta|}}$ from (4.216) and (4.213) in (4.70) results

$$
\begin{aligned}
\dot{\mathcal{F}}_a = \int_0^{2\pi}\int_0^R \bigg[\bigg\{ &\tfrac{1}{2}\mu H A^{-1}|\boldsymbol{x}_\theta|^2\boldsymbol{n}\cdot\boldsymbol{v}_{rr} + \tfrac{1}{2}\mu H A^{-1}\Big[A(\boldsymbol{n}\times\boldsymbol{n}_\theta) \\
&- 3\boldsymbol{n}\cdot(\boldsymbol{x}_\theta\times\boldsymbol{n}_r)(\boldsymbol{x}_\theta\times\boldsymbol{n}) - 3\boldsymbol{n}\cdot(\boldsymbol{n}_\theta\times\boldsymbol{x}_r)(\boldsymbol{x}_\theta\times\boldsymbol{n}) + \boldsymbol{x}_r(\boldsymbol{n}\cdot\boldsymbol{x}_{\theta\theta} - \boldsymbol{x}_\theta\cdot\boldsymbol{n}_\theta) \\
&+ \boldsymbol{x}_\theta(\boldsymbol{x}_\theta\cdot\boldsymbol{n}_r - \boldsymbol{n}\cdot\boldsymbol{x}_{r\theta}) + \big(\boldsymbol{x}_\theta\cdot\boldsymbol{x}_{r\theta} - \boldsymbol{x}_r\cdot\boldsymbol{x}_{\theta\theta} - A_rA^{-1}|\boldsymbol{x}_\theta|^2 + A_\theta A^{-1}(\boldsymbol{x}_r\cdot\boldsymbol{x}_\theta)\big)\boldsymbol{n} \\
&- |\boldsymbol{x}_\theta|^2\boldsymbol{n}_r + (\boldsymbol{x}_r\cdot\boldsymbol{x}_\theta)\boldsymbol{n}_\theta\Big]\cdot\boldsymbol{v}_r - \mu H A^{-1}(\boldsymbol{x}_r\cdot\boldsymbol{x}_\theta)\boldsymbol{n}\cdot\boldsymbol{v}_{r\theta} \\
&+ \tfrac{1}{2}\mu H A^{-1}\Big[A(\boldsymbol{n}_r\times\boldsymbol{n}) + 3\boldsymbol{n}\cdot(\boldsymbol{x}_\theta\times\boldsymbol{n}_r)(\boldsymbol{x}_r\times\boldsymbol{n}) + 3\boldsymbol{n}\cdot(\boldsymbol{n}_\theta\times\boldsymbol{x}_r)(\boldsymbol{x}_r\times\boldsymbol{n}) \\
&+ \boldsymbol{x}_r(\boldsymbol{x}_r\cdot\boldsymbol{n}_\theta - \boldsymbol{x}_{r\theta}\cdot\boldsymbol{n}) + \boldsymbol{x}_\theta(\boldsymbol{x}_{rr}\cdot\boldsymbol{n} - \boldsymbol{x}_r\cdot\boldsymbol{n}_r) + \big(\boldsymbol{x}_r\cdot\boldsymbol{x}_{r\theta} - \boldsymbol{x}_\theta\cdot\boldsymbol{x}_{rr} \\
&+ A_rA^{-1}(\boldsymbol{x}_\theta\cdot\boldsymbol{x}_r) - A_\theta A^{-1}|\boldsymbol{x}_r|^2\big)\boldsymbol{n} + (\boldsymbol{x}_r\cdot\boldsymbol{x}_\theta)\boldsymbol{n}_r - |\boldsymbol{x}_r|^2\boldsymbol{n}_\theta\Big]\cdot\boldsymbol{v}_\theta \\
&+ \tfrac{1}{2}\mu H A^{-1}|\boldsymbol{x}_r|^2\boldsymbol{n}\cdot\boldsymbol{v}_{\theta\theta}\bigg\} + (\sigma + \tfrac{1}{2}\mu H^2)\big((\boldsymbol{x}_\theta\times\boldsymbol{n})\cdot\boldsymbol{v}_r - (\boldsymbol{x}_r\times\boldsymbol{n})\cdot\boldsymbol{v}_\theta\big)\bigg]\,\mathrm{d}r\,\mathrm{d}\theta,
\end{aligned}
\tag{4.71}
$$

where $A = |\boldsymbol{x}_r \times \boldsymbol{x}_\theta|$ indicates the areal Jacobian. Implementing integration by parts changes (4.71) to

$$
\dot{\mathcal{F}}_a = \dot{\mathcal{F}}_a^{\mathcal{S}} + \dot{\mathcal{F}}_a^{\mathcal{C}}, \tag{4.72}
$$

where

$$\begin{aligned}
\dot{\mathcal{F}}_a^{\mathcal{S}} = \int_0^{2\pi}\int_0^R \Big[&\big(\tfrac{1}{2}\mu H A^{-1}|\boldsymbol{x}_\theta|^2\boldsymbol{n}\big)_{rr} - \Big(\tfrac{1}{2}\mu H A^{-1}\Big[A(\boldsymbol{n}\times\boldsymbol{n}_\theta) \\
&- 3\boldsymbol{n}\cdot(\boldsymbol{x}_\theta\times\boldsymbol{n}_r)(\boldsymbol{x}_\theta\times\boldsymbol{n}) - 3\boldsymbol{n}\cdot(\boldsymbol{n}_\theta\times\boldsymbol{x}_r)(\boldsymbol{x}_\theta\times\boldsymbol{n}) + \boldsymbol{x}_r(\boldsymbol{n}\cdot\boldsymbol{x}_{\theta\theta} - \boldsymbol{x}_\theta\cdot\boldsymbol{n}_\theta) \\
&+ \boldsymbol{x}_\theta(\boldsymbol{x}_\theta\cdot\boldsymbol{n}_r - \boldsymbol{n}\cdot\boldsymbol{x}_{r\theta}) + \big(\boldsymbol{x}_\theta\cdot\boldsymbol{x}_{r\theta} - \boldsymbol{x}_r\cdot\boldsymbol{x}_{\theta\theta} - A_rA^{-1}|\boldsymbol{x}_\theta|^2 + A_\theta A^{-1}(\boldsymbol{x}_r\cdot\boldsymbol{x}_\theta)\big)\boldsymbol{n} \\
&- |\boldsymbol{x}_\theta|^2\boldsymbol{n}_r + (\boldsymbol{x}_r\cdot\boldsymbol{x}_\theta)\boldsymbol{n}_\theta\Big]\Big)_r - \big(\mu H A^{-1}(\boldsymbol{x}_r\cdot\boldsymbol{x}_\theta)\boldsymbol{n}\big)_{r\theta} \\
&- \Big(\tfrac{1}{2}\mu H A^{-1}\Big[A(\boldsymbol{n}_r\times\boldsymbol{n}) + 3\boldsymbol{n}\cdot(\boldsymbol{x}_\theta\times\boldsymbol{n}_r)(\boldsymbol{x}_r\times\boldsymbol{n}) + 3\boldsymbol{n}\cdot(\boldsymbol{n}_\theta\times\boldsymbol{x}_r)(\boldsymbol{x}_r\times\boldsymbol{n}) \\
&+ \boldsymbol{x}_r(\boldsymbol{x}_r\cdot\boldsymbol{n}_\theta - \boldsymbol{x}_{r\theta}\cdot\boldsymbol{n}) + \boldsymbol{x}_\theta(\boldsymbol{x}_{rr}\cdot\boldsymbol{n} - \boldsymbol{x}_r\cdot\boldsymbol{n}_r) + \big(\boldsymbol{x}_r\cdot\boldsymbol{x}_{r\theta} - \boldsymbol{x}_\theta\cdot\boldsymbol{x}_{rr} \\
&+ A_rA^{-1}(\boldsymbol{x}_\theta\cdot\boldsymbol{x}_r) - A_\theta A^{-1}|\boldsymbol{x}_r|^2\big)\boldsymbol{n} + (\boldsymbol{x}_r\cdot\boldsymbol{x}_\theta)\boldsymbol{n}_r - |\boldsymbol{x}_r|^2\boldsymbol{n}_\theta\Big]\Big)_\theta \\
&+ \big(\tfrac{1}{2}\mu H A^{-1}|\boldsymbol{x}_r|^2\boldsymbol{n}\big)_{\theta\theta} - \big((\sigma + \tfrac{1}{2}\mu H^2)(\boldsymbol{x}_\theta\times\boldsymbol{n})\big)_r + \big((\sigma + \tfrac{1}{2}\mu H^2)(\boldsymbol{x}_r\times\boldsymbol{n})\big)_\theta\Big]\cdot\boldsymbol{v}\,\mathrm{d}r\,\mathrm{d}\theta,
\end{aligned} \tag{4.73}$$

and

$$\begin{aligned}
\dot{\mathcal{F}}_a^{\mathcal{C}} = \int_0^{2\pi} \Big[&- \big(\tfrac{1}{2}\mu H A^{-1}|\boldsymbol{x}_\theta|^2\boldsymbol{n}\big)_r + \tfrac{1}{2}\mu H A^{-1}\Big[A(\boldsymbol{n}\times\boldsymbol{n}_\theta) \\
&- 3\boldsymbol{n}\cdot(\boldsymbol{x}_\theta\times\boldsymbol{n}_r)(\boldsymbol{x}_\theta\times\boldsymbol{n}) - 3\boldsymbol{n}\cdot(\boldsymbol{n}_\theta\times\boldsymbol{x}_r)(\boldsymbol{x}_\theta\times\boldsymbol{n}) + \boldsymbol{x}_r(\boldsymbol{n}\cdot\boldsymbol{x}_{\theta\theta} - \boldsymbol{x}_\theta\cdot\boldsymbol{n}_\theta) \\
&+ \boldsymbol{x}_\theta(\boldsymbol{x}_\theta\cdot\boldsymbol{n}_r - \boldsymbol{n}\cdot\boldsymbol{x}_{r\theta}) + \big(\boldsymbol{x}_\theta\cdot\boldsymbol{x}_{r\theta} - \boldsymbol{x}_r\cdot\boldsymbol{x}_{\theta\theta} - A_rA^{-1}|\boldsymbol{x}_\theta|^2 + A_\theta A^{-1}(\boldsymbol{x}_r\cdot\boldsymbol{x}_\theta)\big)\boldsymbol{n} \\
&- |\boldsymbol{x}_\theta|^2\boldsymbol{n}_r + (\boldsymbol{x}_r\cdot\boldsymbol{x}_\theta)\boldsymbol{n}_\theta\Big] + \big(\mu H A^{-1}(\boldsymbol{x}_r\cdot\boldsymbol{x}_\theta)\boldsymbol{n}\big)_\theta + (\sigma + \tfrac{1}{2}\mu H^2)(\boldsymbol{x}_\theta\times\boldsymbol{n})\Big]\cdot\boldsymbol{v}\,\mathrm{d}\theta \\
&+ \int_0^{2\pi} \big(\tfrac{1}{2}\mu H A^{-1}|\boldsymbol{x}_\theta|^2\boldsymbol{n}\big)\cdot\boldsymbol{v}_r\,\mathrm{d}\theta.
\end{aligned} \tag{4.74}$$

Lineal contribution

Analogous to the areal integral of $\mathcal{F}_a$, since the integration domain $\partial\mathcal{D}$ of the lineal contribution $\mathcal{F}_l$ of the net-potential energy $\mathcal{F}$ is constant, variation $\dot{\mathcal{F}}_l$ only demands including the variation of the integrand as

$$\dot{\mathcal{F}}_l = \int_0^{2\pi} \left[(\alpha\kappa\dot{\kappa} + \beta\kappa'\dot{\overline{\kappa'}} - \bar{\mu}\dot{\kappa}_g)|\boldsymbol{x}_\theta| + (\tfrac{1}{2}\alpha\kappa^2 + \tfrac{1}{2}\beta\kappa'^2 - \bar{\mu}\kappa_g + \lambda)\dot{\overline{|\boldsymbol{x}_\theta|}}\right] \mathrm{d}\theta. \tag{4.75}$$

Substitution of variations $\dot{\overline{|\boldsymbol{x}_\theta|}}$, $\dot{\kappa}$, $\dot{\overline{\kappa'}}$, and $\dot{\kappa}_g$ from (4.218), (4.221), (4.223), and (4.225) into (4.75) and using κ, κ', and κ_g given in (4.69) yield

$$\begin{aligned}
\dot{\mathcal{F}}_l = \int_0^{2\pi} \Bigg\{ \Bigg(& -\frac{3\alpha}{2R^5}|\boldsymbol{x}_{\theta\theta}|^2\boldsymbol{x}_\theta - \frac{\beta}{2R^7}\big(5(|\boldsymbol{x}_{\theta\theta}|_\theta)^2\boldsymbol{x}_\theta + 4|\boldsymbol{x}_{\theta\theta}|_\theta|\boldsymbol{x}_{\theta\theta}|\boldsymbol{x}_{\theta\theta}\big) \\
& - \frac{\bar{\mu}}{R^2}\Big[A^{-1}\big[(\boldsymbol{x}_r\cdot\boldsymbol{x}_\theta)\boldsymbol{x}_{\theta\theta} - (\boldsymbol{x}_r\cdot\boldsymbol{x}_{\theta\theta})\boldsymbol{x}_\theta + \big(\boldsymbol{n}\cdot(\boldsymbol{x}_\theta\times\boldsymbol{x}_{\theta\theta})\big)(\boldsymbol{x}_r\times\boldsymbol{n})\big] \\
& \qquad + (\boldsymbol{x}_{\theta\theta}\times\boldsymbol{n}) - \frac{2}{R^2}\big(\boldsymbol{n}\cdot(\boldsymbol{x}_\theta\times\boldsymbol{x}_{\theta\theta})\big)\boldsymbol{x}_\theta\Big] + \frac{\lambda}{R}\boldsymbol{x}_\theta\Bigg)\cdot\boldsymbol{v}_\theta \\
& + \left(\frac{\alpha}{R^3}\boldsymbol{x}_{\theta\theta} + \frac{\beta}{R^5}\left[\frac{|\boldsymbol{x}_{\theta\theta}|_\theta\boldsymbol{x}_{\theta\theta\theta}}{|\boldsymbol{x}_{\theta\theta}|} - \frac{(|\boldsymbol{x}_{\theta\theta}|_\theta)^2\boldsymbol{x}_{\theta\theta}}{|\boldsymbol{x}_{\theta\theta}|^2} - \frac{2|\boldsymbol{x}_{\theta\theta}|_\theta|\boldsymbol{x}_{\theta\theta}|\boldsymbol{x}_\theta}{R^2}\right] - \frac{\bar{\mu}}{R^2}(\boldsymbol{n}\times\boldsymbol{x}_\theta)\right)\cdot\boldsymbol{v}_{\theta\theta} \\
& + \frac{\beta}{R^5}\frac{|\boldsymbol{x}_{\theta\theta}|_\theta\boldsymbol{x}_{\theta\theta}}{|\boldsymbol{x}_{\theta\theta}|}\cdot\boldsymbol{v}_{\theta\theta\theta} + \frac{\bar{\mu}}{R^2}A^{-1}\Big[R^2\boldsymbol{x}_{\theta\theta} + \big(\boldsymbol{n}\cdot(\boldsymbol{x}_\theta\times\boldsymbol{x}_{\theta\theta})\big)(\boldsymbol{x}_\theta\times\boldsymbol{n})\Big]\cdot\boldsymbol{v}_r\Bigg\}\,\mathrm{d}\theta.
\end{aligned} \tag{4.76}$$

Implementing integration by parts leads to

$$
\begin{aligned}
\dot{\mathcal{F}}_l = \int_0^{2\pi} \bigg[\bigg(&\frac{\alpha}{R^5}\Big(\frac{3}{2}\big(|\boldsymbol{x}_{\theta\theta}|^2\boldsymbol{x}_\theta\big)_\theta + R^2\boldsymbol{x}_{\theta\theta\theta\theta}\Big) + \frac{\beta}{2R^7}\Big[\big(5(|\boldsymbol{x}_{\theta\theta}|_\theta)^2\boldsymbol{x}_\theta + 4|\boldsymbol{x}_{\theta\theta}|_\theta|\boldsymbol{x}_{\theta\theta}|\boldsymbol{x}_{\theta\theta}\big)_\theta \\
&+ 2R^2\Big(\frac{|\boldsymbol{x}_{\theta\theta}|_\theta\boldsymbol{x}_{\theta\theta\theta}}{|\boldsymbol{x}_{\theta\theta}|} - \frac{(|\boldsymbol{x}_{\theta\theta}|_\theta)^2\boldsymbol{x}_{\theta\theta}}{|\boldsymbol{x}_{\theta\theta}|^2} - \frac{2|\boldsymbol{x}_{\theta\theta}|_\theta|\boldsymbol{x}_{\theta\theta}|\boldsymbol{x}_\theta}{R^2}\Big)_{\theta\theta} - 2R^2\Big(\frac{|\boldsymbol{x}_{\theta\theta}|_\theta\boldsymbol{x}_{\theta\theta}}{|\boldsymbol{x}_{\theta\theta}|}\Big)_{\theta\theta\theta}\Big] \\
&+ \frac{\bar{\mu}}{R^2}\Big[A^{-1}\big[(\boldsymbol{x}_r \cdot \boldsymbol{x}_\theta)\boldsymbol{x}_{\theta\theta} - (\boldsymbol{x}_r \cdot \boldsymbol{x}_{\theta\theta})\boldsymbol{x}_\theta + \big(\boldsymbol{n} \cdot (\boldsymbol{x}_\theta \times \boldsymbol{x}_{\theta\theta})\big)(\boldsymbol{x}_r \times \boldsymbol{n})\big] \\
&+ (\boldsymbol{x}_{\theta\theta} \times \boldsymbol{n}) - \frac{2}{R^2}\big(\boldsymbol{n} \cdot (\boldsymbol{x}_\theta \times \boldsymbol{x}_{\theta\theta})\big)\boldsymbol{x}_\theta - (\boldsymbol{n} \times \boldsymbol{x}_\theta)_\theta\Big]_\theta - \frac{(\lambda\boldsymbol{x}_\theta)_\theta}{R}\bigg) \cdot \boldsymbol{v} \\
&+ \frac{\bar{\mu}}{R^2}A^{-1}\Big[R^2\boldsymbol{x}_{\theta\theta} + \big(\boldsymbol{n} \cdot (\boldsymbol{x}_\theta \times \boldsymbol{x}_{\theta\theta})\big)(\boldsymbol{x}_\theta \times \boldsymbol{n})\Big] \cdot \boldsymbol{v}_r\bigg]\,\mathrm{d}\theta. \qquad (4.77)
\end{aligned}
$$

4.7.3 Euler–Lagrange equations

Using the decomposition (4.72), the variation of the energy functional $\mathcal{F}$ given in (4.33) reads

$$\dot{\mathcal{F}} = \dot{\mathcal{F}}_a^{\mathcal{S}} + (\dot{\mathcal{F}}_a^{\mathcal{C}} + \dot{\mathcal{F}}_l), \qquad (4.78)$$

with $\dot{\mathcal{F}}_a^{\mathcal{S}}$, $\dot{\mathcal{F}}_a^{\mathcal{C}}$, and $\dot{\mathcal{F}}_l$ given in (4.73), (4.74), and (4.77). Since variables $\boldsymbol{v}$ and $\boldsymbol{v}_r$ are independent, according to the fundamental lemma of calculus of variations, the following Euler–Lagrange equation must hold on $\mathcal{S}$

$$
\begin{aligned}
&\big(\tfrac{1}{2}\mu H A^{-1}|\boldsymbol{x}_\theta|^2\boldsymbol{n}\big)_{rr} - \Big(\tfrac{1}{2}\mu H A^{-1}\big[A(\boldsymbol{n}\times\boldsymbol{n}_\theta) - 3\boldsymbol{n}\cdot(\boldsymbol{x}_\theta\times\boldsymbol{n}_r)(\boldsymbol{x}_\theta\times\boldsymbol{n}) \\
&\quad - 3\boldsymbol{n}\cdot(\boldsymbol{n}_\theta\times\boldsymbol{x}_r)(\boldsymbol{x}_\theta\times\boldsymbol{n}) + \boldsymbol{x}_r(\boldsymbol{n}\cdot\boldsymbol{x}_{\theta\theta} - \boldsymbol{x}_\theta\cdot\boldsymbol{n}_\theta) + \boldsymbol{x}_\theta(\boldsymbol{x}_\theta\cdot\boldsymbol{n}_r - \boldsymbol{n}\cdot\boldsymbol{x}_{r\theta}) \\
&+ \big(\boldsymbol{x}_\theta\cdot\boldsymbol{x}_{r\theta} - \boldsymbol{x}_r\cdot\boldsymbol{x}_{\theta\theta} - A_r A^{-1}|\boldsymbol{x}_\theta|^2 + A_\theta A^{-1}(\boldsymbol{x}_r\cdot\boldsymbol{x}_\theta)\big)\boldsymbol{n} - |\boldsymbol{x}_\theta|^2\boldsymbol{n}_r + (\boldsymbol{x}_r\cdot\boldsymbol{x}_\theta)\boldsymbol{n}_\theta\big]\Big)_r \\
&\quad - \big(\mu H A^{-1}(\boldsymbol{x}_r\cdot\boldsymbol{x}_\theta)\boldsymbol{n}\big)_{r\theta} - \Big(\tfrac{1}{2}\mu H A^{-1}\big[A(\boldsymbol{n}_r\times\boldsymbol{n}) + 3\boldsymbol{n}\cdot(\boldsymbol{x}_\theta\times\boldsymbol{n}_r)(\boldsymbol{x}_r\times\boldsymbol{n}) \\
&\quad + 3\boldsymbol{n}\cdot(\boldsymbol{n}_\theta\times\boldsymbol{x}_r)(\boldsymbol{x}_r\times\boldsymbol{n}) + \boldsymbol{x}_r(\boldsymbol{x}_r\cdot\boldsymbol{n}_\theta - \boldsymbol{x}_{r\theta}\cdot\boldsymbol{n}) + \boldsymbol{x}_\theta(\boldsymbol{x}_{rr}\cdot\boldsymbol{n} - \boldsymbol{x}_r\cdot\boldsymbol{n}_r) \\
&+ \big(\boldsymbol{x}_r\cdot\boldsymbol{x}_{r\theta} - \boldsymbol{x}_\theta\cdot\boldsymbol{x}_{rr} + A_r A^{-1}(\boldsymbol{x}_\theta\cdot\boldsymbol{x}_r) - A_\theta A^{-1}|\boldsymbol{x}_r|^2\big)\boldsymbol{n} + (\boldsymbol{x}_r\cdot\boldsymbol{x}_\theta)\boldsymbol{n}_r - |\boldsymbol{x}_r|^2\boldsymbol{n}_\theta\big]\Big)_\theta \\
&+ \big(\tfrac{1}{2}\mu H A^{-1}|\boldsymbol{x}_r|^2\boldsymbol{n}\big)_{\theta\theta} - \big((\sigma + \tfrac{1}{2}\mu H^2)(\boldsymbol{x}_\theta\times\boldsymbol{n})\big)_r + \big((\sigma + \tfrac{1}{2}\mu H^2)(\boldsymbol{x}_r\times\boldsymbol{n})\big)_\theta = \mathbf{0},
\end{aligned}
\tag{4.79}
$$

and the following boundary conditions must hold on $\mathcal{C}$

$$
\begin{aligned}
&\frac{\alpha}{R^5}\Big(\frac{3}{2}\big(|\boldsymbol{x}_{\theta\theta}|^2\boldsymbol{x}_\theta\big)_\theta + R^2\boldsymbol{x}_{\theta\theta\theta\theta}\Big) + \frac{\beta}{2R^7}\Big[\big(5(|\boldsymbol{x}_{\theta\theta}|_\theta)^2\boldsymbol{x}_\theta + 4|\boldsymbol{x}_{\theta\theta}|_\theta|\boldsymbol{x}_{\theta\theta}|\boldsymbol{x}_{\theta\theta}\big)_\theta \\
&\quad + 2R^2\Big(\frac{|\boldsymbol{x}_{\theta\theta}|_\theta\boldsymbol{x}_{\theta\theta\theta}}{|\boldsymbol{x}_{\theta\theta}|} - \frac{(|\boldsymbol{x}_{\theta\theta}|_\theta)^2\boldsymbol{x}_{\theta\theta}}{|\boldsymbol{x}_{\theta\theta}|^2} - \frac{2|\boldsymbol{x}_{\theta\theta}|_\theta|\boldsymbol{x}_{\theta\theta}|\boldsymbol{x}_\theta}{R^2}\Big)_{\theta\theta} - 2R^2\Big(\frac{|\boldsymbol{x}_{\theta\theta}|_\theta\boldsymbol{x}_{\theta\theta}}{|\boldsymbol{x}_{\theta\theta}|}\Big)_{\theta\theta\theta}\Big] \\
&\qquad + \frac{\bar{\mu}}{R^2}\Big[A^{-1}\big[(\boldsymbol{x}_r\cdot\boldsymbol{x}_\theta)\boldsymbol{x}_{\theta\theta} - (\boldsymbol{x}_r\cdot\boldsymbol{x}_{\theta\theta})\boldsymbol{x}_\theta + \big(\boldsymbol{n}\cdot(\boldsymbol{x}_\theta\times\boldsymbol{x}_{\theta\theta})\big)(\boldsymbol{x}_r\times\boldsymbol{n})\big] \\
&\qquad\quad + (\boldsymbol{x}_{\theta\theta}\times\boldsymbol{n}) - \frac{2}{R^2}\big(\boldsymbol{n}\cdot(\boldsymbol{x}_\theta\times\boldsymbol{x}_{\theta\theta})\big)\boldsymbol{x}_\theta - (\boldsymbol{n}\times\boldsymbol{x}_\theta)_\theta\Big]_\theta - \frac{(\lambda\boldsymbol{x}_\theta)_\theta}{R} \\
&\quad - \big(\tfrac{1}{2}\mu H A^{-1}|\boldsymbol{x}_\theta|^2\boldsymbol{n}\big)_r + \tfrac{1}{2}\mu H A^{-1}\Big[A(\boldsymbol{n}\times\boldsymbol{n}_\theta) - 3\boldsymbol{n}\cdot(\boldsymbol{x}_\theta\times\boldsymbol{n}_r)(\boldsymbol{x}_\theta\times\boldsymbol{n}) \\
&\quad - 3\boldsymbol{n}\cdot(\boldsymbol{n}_\theta\times\boldsymbol{x}_r)(\boldsymbol{x}_\theta\times\boldsymbol{n}) + \boldsymbol{x}_r(\boldsymbol{n}\cdot\boldsymbol{x}_{\theta\theta} - \boldsymbol{x}_\theta\cdot\boldsymbol{n}_\theta) + \boldsymbol{x}_\theta(\boldsymbol{x}_\theta\cdot\boldsymbol{n}_r - \boldsymbol{n}\cdot\boldsymbol{x}_{r\theta}) \\
&+ \big(\boldsymbol{x}_\theta\cdot\boldsymbol{x}_{r\theta} - \boldsymbol{x}_r\cdot\boldsymbol{x}_{\theta\theta} - A_r A^{-1}|\boldsymbol{x}_\theta|^2 + A_\theta A^{-1}(\boldsymbol{x}_r\cdot\boldsymbol{x}_\theta)\big)\boldsymbol{n} - |\boldsymbol{x}_\theta|^2\boldsymbol{n}_r + (\boldsymbol{x}_r\cdot\boldsymbol{x}_\theta)\boldsymbol{n}_\theta\Big] \\
&\qquad\qquad + \big(\mu H A^{-1}(\boldsymbol{x}_r\cdot\boldsymbol{x}_\theta)\boldsymbol{n}\big)_\theta + (\sigma + \tfrac{1}{2}\mu H^2)(\boldsymbol{x}_\theta\times\boldsymbol{n}) = \mathbf{0},
\end{aligned}
\tag{4.80}
$$

$$\frac{\bar{\mu}}{R^2}A^{-1}\Big[R^2\boldsymbol{x}_{\theta\theta} + \big(\boldsymbol{n}\cdot(\boldsymbol{x}_\theta \times \boldsymbol{x}_{\theta\theta})\big)(\boldsymbol{x}_\theta \times \boldsymbol{n})\Big] + \tfrac{1}{2}\mu H A^{-1}|\boldsymbol{x}_\theta|^2\boldsymbol{n} = \boldsymbol{0}. \tag{4.81}$$

Lengthy calculations can verify that the only nonvanishing component of (4.79) is the normal component which corresponds the shape equation (4.46) derived using the direct formulation. In doing such verification, the parametric description of the surface Laplacian $\triangle_{\mathcal{S}}$ operator given by [1]

$$\begin{aligned}\triangle_{\mathcal{S}} = {} & \big[A^{-1}(\boldsymbol{x}_\theta \times \boldsymbol{n})\cdot\big(A^{-1}(\boldsymbol{x}_\theta \times \boldsymbol{n})\big)_r + A^{-1}(\boldsymbol{n}\times\boldsymbol{x}_r)\cdot\big(A^{-1}(\boldsymbol{x}_\theta \times \boldsymbol{n})\big)_\theta\big]\frac{\partial}{\partial r} \\ & + \big[A^{-1}(\boldsymbol{x}_\theta \times \boldsymbol{n})\cdot\big(A^{-1}(\boldsymbol{n}\times\boldsymbol{x}_r)\big)_r + A^{-1}(\boldsymbol{n}\times\boldsymbol{x}_r)\cdot\big(A^{-1}(\boldsymbol{n}\times\boldsymbol{x}_r)\big)_\theta\big]\frac{\partial}{\partial\theta} \\ & + A^{-2}|\boldsymbol{x}_\theta|^2\frac{\partial^2}{\partial r^2} + A^{-2}|\boldsymbol{x}_r|^2\frac{\partial^2}{\partial\theta^2} - 2A^{-2}(\boldsymbol{x}_r\cdot\boldsymbol{x}_\theta)\frac{\partial^2}{\partial r\partial\theta},\end{aligned} \tag{4.82}$$

and the mean and Gaussian curvatures in (4.63) and (4.64) are necessary. Also, it can be verified that the vectorial equation (4.80) is the parametrized analog of (4.50), (4.51), and (4.52). Lastly, upon the dot product of the vectorial equation (4.81) with $\boldsymbol{x}_\theta$ and $\boldsymbol{x}_r$, and in view of the conditions (4.67) and $(4.68)_1$, it follows that the tangential components of (4.81) vanish and it reduces to its normal component given by

$$\tfrac{1}{2}\mu H + \bar{\mu}\frac{\boldsymbol{x}_{\theta\theta}\cdot\boldsymbol{n}}{R^2} = 0, \tag{4.83}$$

---

[1] For brevity, the derivations leading to (4.82) are not provided here. Also, it can be shown that the surface Laplacian operator in (4.82) and what is known as the Laplace–Beltrami operator (e.g., used in [151] and [161]) are equivalent. Again, we avoid providing such verification due to space limitations.

which, regarding the parametric description of the normal curvature κ_n in $(4.69)_3$, coincides with (4.48) obtained previously using the direct formulation.

4.7.4 Dimensionless formulation

It is very desirable to express the results in a nondimensional format. Towards this goal, we may choose the following change of variables

$$\boldsymbol{x}(r,\theta) = R\boldsymbol{\xi}(\rho,\theta), \quad r = R\rho. \tag{4.84}$$

In view of the change of variables (4.84), $\mathcal{R}$, the dimensionless counterpart of the domain $\mathcal{D}$ may be defined as

$$\mathcal{R} = \{(\rho,\theta) \in \mathbb{R}^2 : 0 \le \rho \le 1, 0 \le \theta \le 2\pi\}. \tag{4.85}$$

In addition, consider the following dimensionless quantities

$$\big(\mathcal{H}, \eta, \bar{\eta}, \nu, \iota, \epsilon\big) := \Big(\frac{\mathcal{F}R}{\alpha}, \frac{\mu R}{\alpha}, \frac{\bar{\mu} R}{\alpha}, \frac{\sigma R^3}{\alpha}, \frac{\lambda R^2}{\alpha}, \frac{\beta}{\alpha R^2}\Big). \tag{4.86}$$

In view of the dimensionless group (4.86), the decomposition of the energy functional $\mathcal{F}$ in (4.33), the expressions (4.61) and (4.62) of the areal and lineal contributions $\mathcal{F}_a$ and $\mathcal{F}_l$ of $\mathcal{F}$, the dimensionless augmented net potential-energy $\mathcal{H}$ can be expressed as

$$\mathcal{H} = \mathcal{H}_a + \mathcal{H}_l + 2\pi\bar{\eta}, \tag{4.87}$$

where

$$\mathcal{H}_a = \int_0^{2\pi} \int_0^1 (\nu + \tfrac{1}{2}\eta R^2 H^2)|\boldsymbol{\xi}_\rho \times \boldsymbol{\xi}_\theta| \,\mathrm{d}\rho \,\mathrm{d}\theta, \tag{4.88}$$

and

$$\mathcal{H}_l = \int_0^{2\pi} \big(\tfrac{1}{2}R^2\kappa^2 + \tfrac{1}{2}\epsilon R^4(\kappa')^2 - \bar{\eta}R\kappa_g + \iota\big)|\boldsymbol{\xi}_\theta|_{\rho=1}\,\mathrm{d}\theta. \tag{4.89}$$

Hereafter, the adjective 'dimensionless' is suppressed for the sake of brevity.

4.8 Component-wise description and small-slope formulation

In this section, we aim to furnish a small-slope deformation approximation to study the linearized equilibrium equation and stability of a discoidal HDL particle. To this end, first, it is very useful to express the problem based on component-wise displacement field. The position of a generic point on $\mathcal{S}$ can be expressed as

$$\boldsymbol{\xi}(\rho,\theta) = \mathbf{o} + (\rho + u(\rho,\theta))\boldsymbol{e}_r + v(\rho,\theta)\boldsymbol{e}_\theta + w(\rho,\theta)\boldsymbol{e}_z, \tag{4.90}$$

where $\mathbf{o}$ indicates the origin of the reference disk and u, v, and w are the displacement components in $\boldsymbol{e}_r$, $\boldsymbol{e}_\theta$, and $\boldsymbol{e}_z$ directions, respectively (Figure 4–3). In addition, the inextensibility constraint (4.67) can be expressed as

$$|\boldsymbol{\xi}_\theta(1,\theta)| = 1, \quad 0 \le \theta \le 2\pi. \tag{4.91}$$

Straightforward calculations lead to

$$\left.\begin{aligned}
&\boldsymbol{\xi}_\rho = (1+u_\rho)\boldsymbol{e}_r + v_\rho\boldsymbol{e}_\theta + w_\rho\boldsymbol{e}_z, \quad \boldsymbol{\xi}_\theta = (u_\theta - v)\boldsymbol{e}_r + (\rho + u + v_\theta)\boldsymbol{e}_\theta + w_\theta\boldsymbol{e}_z,\\
&\boldsymbol{\xi}_\rho \times \boldsymbol{\xi}_\theta = C^\rho\boldsymbol{e}_r + C^\theta\boldsymbol{e}_\theta + C^z\boldsymbol{e}_z, \quad |\boldsymbol{\xi}_\rho \times \boldsymbol{\xi}_\theta| = \sqrt{(C^\rho)^2 + (C^\theta)^2 + (C^z)^2},\\
&\boldsymbol{n} = \frac{C^\rho\boldsymbol{e}_r + C^\theta\boldsymbol{e}_\theta + C^z\boldsymbol{e}_z}{\sqrt{(C^\rho)^2 + (C^\theta)^2 + (C^z)^2}}, \quad |\boldsymbol{\xi}_\theta|_{\rho=1} = \sqrt{(u_\theta - v)^2 + (1 + u + v_\theta)^2 + w_\theta^2}\Big|_{\rho=1},
\end{aligned}\right\} \tag{4.92}$$

where

$$C^\rho = C_1^\rho + C_2^\rho, \quad C^\theta = C_1^\theta + C_2^\theta, \quad C^z = \rho + C_1^z + C_2^z, \tag{4.93}$$

with

$$\left.\begin{aligned}
&C_1^\rho = -w_\rho \rho, \quad C_2^\rho = w_\theta v_\rho - w_\rho (u + v_\theta), \\
&C_1^\theta = -w_\theta, \quad C_2^\theta = w_\rho (u_\theta - v) - w_\theta u_\rho, \\
&C_1^z = u_\rho \rho + u + v_\theta, \quad C_2^z = u_\rho (u + v_\theta) - v_\rho (u_\theta - v).
\end{aligned}\right\} \tag{4.94}$$

To develop the linearized equilibrium equations and boundary conditions, it is necessary that all terms in the net potential-energy are kept up to the second order of u, v, w, and their partial derivatives. In view of the definitions of the curvature κ and the geodesic curvature κ_g in $(4.66)_{1,4}$ and relations (4.90) and (4.92), after lengthy but straightforward derivations, expressions of the terms $|\boldsymbol{\xi}_\rho \times \boldsymbol{\xi}_\theta|$, $R^2 H^2$, $|\boldsymbol{\xi}_\theta|_{\rho=1}$, $R^2 \kappa^2$, $R^4 \kappa'^2$ and $R\kappa_g$, appearing in the net potential-energy $\mathcal{H}$ in (4.87), expanded up to the second order of u, v, and w, are given as [2]

$$|\boldsymbol{\xi}_\rho \times \boldsymbol{\xi}_\theta| = \rho + [\rho u_\rho + u + v_\theta] + \left[u_\rho (u + v_\theta) - v_\rho (u_\theta - v) + \frac{\rho w_\rho^2}{2} + \frac{w_\theta^2}{2\rho}\right], \tag{4.95}$$

$$R^2 H^2 = \tfrac{1}{4}[\Delta w]^2, \tag{4.96}$$

$$|\boldsymbol{\xi}_\theta|_{\rho=1} = 1 + [u + v_\theta]_{\rho=1} + \frac{1}{2}\left[(u_\theta - v)^2 + w_\theta^2\right]_{\rho=1}, \tag{4.97}$$

---

[2] Derivations leading to (4.95)–(4.100) can effectively be optimized using proper decomposition of the relevant terms based on the order of u, v, and w, similar to what presented in (4.93). The middle-step calculations are avoided due to the space limit.

$$R^2\kappa^2 = 1 - 2[u + u_{\theta\theta}]_{\rho=1} + \Big[-3(u_\theta - v)^2 + 10(u + v_\theta)^2 + 8(-u - 2v_\theta + u_{\theta\theta})(u + v_\theta) + (-u - 2v_\theta + u_{\theta\theta})^2 + 2(u_\theta - v)(2u_\theta - v + v_{\theta\theta}) + w_{\theta\theta}^2 - 2w_\theta^2\Big]_{\rho=1}, \quad (4.98)$$

$$R^4\kappa'^2 = [(u_\theta + u_{\theta\theta\theta})^2]_{\rho=1}, \quad (4.99)$$

$$R\kappa_g = 1 - [u + u_{\theta\theta}]_{\rho=1} + \Big[-\frac{3}{2}(u_\theta - v)^2 + 3(u + v_\theta)^2 + 2(u + v_\theta)(-u - 2v_\theta + u_{\theta\theta}) + (u_\theta - v)(2u_\theta - v + v_{\theta\theta}) - w_\theta^2 - w_\rho w_{\theta\theta} - \frac{w_\rho^2}{2}\Big]_{\rho=1}, \quad (4.100)$$

where $\Delta = \frac{1}{\rho}()_\rho + ()_{\rho\rho} + \frac{1}{\rho^2}()_{\theta\theta}$ is the two-dimensional Laplacian in the polar coordinate. Also, each bracket [ ] contains the terms with the same order of the displacement components u, v, and w. Substitution of (4.95)–(4.100) in the net potential-energy (4.87) and keeping the terms with the relevant orders result

$$\mathcal{H}_a = \int_0^{2\pi}\int_0^1 \frac{\eta}{8}[\Delta w]^2 \rho \,\mathrm{d}\rho\,\mathrm{d}\theta + \int_0^{2\pi}\int_0^1 \nu\Big\{\rho + [\rho u_\rho + u + v_\theta] + \Big[u_\rho(u + v_\theta) - v_\rho(u_\theta - v) + \frac{\rho w_\rho^2}{2} + \frac{w_\theta^2}{2\rho}\Big]\Big\}\,\mathrm{d}\rho\,\mathrm{d}\theta, \quad (4.101)$$

and

$$\begin{aligned}\mathcal{H}_l = \int_0^{2\pi} \frac{1}{2}\Big\{ 1 + \big[-u - 2u_{\theta\theta} + v_\theta\big] + \Big[-\frac{5}{2}(u_\theta - v)^2 \\ - 2(u + u_{\theta\theta})(u + v_\theta) + 10(u + v_\theta)^2 + 8(-u - 2v_\theta + u_{\theta\theta})(u + v_\theta) \\ + (-u - 2v_\theta + u_{\theta\theta})^2 + 2(u_\theta - v)(2u_\theta - v + v_{\theta\theta}) - \frac{3}{2}w_\theta^2 + w_{\theta\theta}^2\Big]\Big\}\,\mathrm{d}\theta \\ + \int_0^{2\pi} \frac{\epsilon}{2}[u_\theta + u_{\theta\theta\theta}]^2\,\mathrm{d}\theta - \int_0^{2\pi} \bar{\eta}\Big\{1 - \frac{w_\theta^2}{2} - w_\rho w_{\theta\theta} - \frac{w_\rho^2}{2}\Big\}\,\mathrm{d}\theta \\ + \int_0^{2\pi} \iota\Big\{1 + [u + v_\theta] + \frac{1}{2}\big[(u_\theta - v)^2 + w_\theta^2\big]\Big\}\,\mathrm{d}\theta. \quad (4.102)\end{aligned}$$

4.8.1 Equilibrium equations and boundary conditions

The first variation of the net potential-energy (4.87) yields

$$\dot{\mathcal{H}} = \dot{\mathcal{H}}^{\mathcal{S}} + \dot{\mathcal{H}}^{\mathcal{C}}, \tag{4.103}$$

where

$$\dot{\mathcal{H}}^{\mathcal{S}} = \int_0^{2\pi}\int_0^1 \Big[\frac{\eta}{4}\Delta^2 w - \nu\Delta w\Big]\dot{w}\rho\,\mathrm{d}\rho\,\mathrm{d}\theta, \tag{4.104}$$

and

$$\begin{aligned}\dot{\mathcal{H}}^{\mathcal{C}} = \frac{\eta}{4}\int_0^{2\pi}\big[(\Delta w)\dot{w}_\rho - (\Delta w)_\rho \dot{w}\big]\,\mathrm{d}\theta + \nu\int_0^{2\pi}\big[(1 + u + v_\theta)\dot{u} - (u_\theta - v)\dot{v} + w_\rho\dot{w}\big]\,\mathrm{d}\theta \\ + \frac{1}{2}\int_0^{2\pi}\Big\{\big[-1 + (2u + 5u_{\theta\theta} + 2u_{\theta\theta\theta\theta} - v_\theta)\big]\dot{u} + (u_\theta - v)\dot{v} + (3w_{\theta\theta} + 2w_{\theta\theta\theta\theta})\dot{w}\Big\}\,\mathrm{d}\theta \\ - \epsilon\int_0^{2\pi}[u_{\theta\theta} + 2u_{\theta\theta\theta\theta} + u_{\theta\theta\theta\theta\theta\theta}]\dot{u}\,\mathrm{d}\theta - \bar{\eta}\int_0^{2\pi}\big[(w_{\theta\theta} - w_{\rho\theta\theta})\dot{w} + (-w_{\theta\theta} - w_\rho)\dot{w}_\rho\big]\,\mathrm{d}\theta \\ + \int_0^{2\pi}\Big\{\big[\iota - \big(\iota(u_\theta - v)\big)_\theta\big]\dot{u} + \big[-\iota_\theta - \iota(u_\theta - v)\big]\dot{v} - (\iota w_\theta)_\theta\dot{w}\Big\}\,\mathrm{d}\theta. \quad (4.105)\end{aligned}$$

The Euler–Lagrange equations resulting from the requirement $\dot{\mathcal{H}} = 0$ are the partial-differential equation (PDE)

$$\Delta^2 w - \zeta^2 \Delta w = 0 \qquad \text{on } \mathcal{R}, \tag{4.106}$$

with $\zeta = 2\sqrt{\nu/\eta}$, and boundary conditions

$$\begin{aligned}\dot{u}: \quad &\Big[(\iota + \nu - \tfrac{1}{2}) + \nu(u + v_\theta) + \tfrac{1}{2}(2u + 5u_{\theta\theta} + 2u_{\theta\theta\theta\theta} - v_\theta) \\ &\qquad - \epsilon\big(u_{\theta\theta} + 2u_{\theta\theta\theta\theta} + u_{\theta\theta\theta\theta\theta\theta}\big) - \big(\iota(u_\theta - v)\big)_\theta\Big]_{\rho=1} = 0, \end{aligned} \tag{4.107}$$

$$\dot{v}: \quad \big[\iota_\theta + (\iota + \nu - \tfrac{1}{2})(u_\theta - v)\big]_{\rho=1} = 0, \tag{4.108}$$

$$\begin{aligned}\dot{w}: \quad &\Big[-\frac{\eta}{4}(\Delta w)_\rho + \nu w_\rho + \tfrac{1}{2}(3w_{\theta\theta} + 2w_{\theta\theta\theta\theta}) \\ &\qquad - \bar{\eta}(w_{\theta\theta} - w_{\rho\theta\theta}) - (\iota w_\theta)_\theta\Big]_{\rho=1} = 0, \end{aligned} \tag{4.109}$$

$$\dot{w}_\rho: \quad \Big[\frac{\eta}{4}\Delta w + \bar{\eta}(w_\rho + w_{\theta\theta})\Big]_{\rho=1} = 0. \tag{4.110}$$

Also, the linearized form of the inextensibility constraint (4.91) is expressed as

$$(u + v_\theta)_{\rho=1} = 0. \tag{4.111}$$

The equilibrium equation (4.106) is the linearized counterpart of the general shape equations (4.79) and (4.46). In addition, boundary conditions (4.107)–(4.110) are linearized version of the general boundary conditions (4.80) and (4.81) in the parametrized form or (4.48), (4.50), (4.51), and (4.52) using the direct formulation. Equation (4.106) reveals that, up to the small-slope approximation, the displacement components u and v do not play any role in the shape equation. Moreover, u and v

are absent in the boundary conditions (4.109) and (4.110). Thus, using the system of equations (4.106), (4.109), and (4.110), the transverse displacement can be determined independently. In addition, the boundary conditions (4.107) and (4.108), and the constraint (4.111) suffice the in-plane equilibrium. This clearly signifies the decoupling of in-plane and transverse equilibria in the linearized formulation.

Notice that all equations (4.106)–(4.111) must be trivially satisfied at the reference configuration under which the solution is trivial ($u = v = w = 0$). Equation (4.107) results

$$\iota = \tfrac{1}{2} - \nu, \tag{4.112}$$

which determines the Lagrange multiplier up to zeroth order—i.e., at the trivial solution. Notice that zeroth order coefficient $(\iota + \nu - \tfrac{1}{2}) = 0$ suffices the linear equation (4.108). Hence, it follows

$$\iota = \text{constant}, \tag{4.113}$$

implying that the tangential force balance in of the boundary in $\boldsymbol{e}_\theta$ direction requires the constancy of the Lagrange multiplier ι along the apoA-I belt. Equation (4.113) is analog of the condition (4.52) in the direction formulation.

Using the relations (4.112) and (4.113) and the inextensibility condition (4.111), the boundary conditions (4.107), (4.109), and (4.110) take the form

$$\dot{u}: \quad \big[u + 2u_{\theta\theta} + u_{\theta\theta\theta\theta} + \nu(u_{\theta\theta} + u) - \epsilon(u_{\theta\theta} + 2u_{\theta\theta\theta\theta} + u_{\theta\theta\theta\theta\theta\theta})\big]_{\rho=1} = 0, \tag{4.114}$$

$$\dot{w}: \quad \Big[-\frac{\eta}{4} w_{\rho\rho\rho} - \frac{\eta}{4} w_{\rho\rho} + (\frac{\eta}{4} + \nu) w_\rho + (\bar{\eta} - \frac{\eta}{4}) w_{\rho\theta\theta} + w_{\theta\theta\theta\theta} + \big(\nu + 1 - \bar{\eta} + \frac{\eta}{2}\big) w_{\theta\theta} \Big]_{\rho=1} = 0, \quad (4.115)$$

$$\dot{w}_\rho: \quad \Big[\frac{\eta}{4} w_{\rho\rho} + \big(\frac{\eta}{4} + \bar{\eta}\big) w_\rho + \big(\frac{\eta}{4} + \bar{\eta}\big) w_{\theta\theta} \Big]_{\rho=1} = 0. \quad (4.116)$$

4.8.2 Solving the equilibrium equations and boundary conditions

In this section, we aim to present the solution of the equilibrium equation (4.106) and the associated boundary conditions (4.114)–(4.116).

In-plane equilibrium

The boundary condition (4.114) suffices the in-plane equilibrium of the boundary $\mathcal{C}$. Also, in view of the constraint (4.111), the tangent displacement $v(1, \theta)$ of the boundary can be obtained as

$$v(1, \theta) = -\int u(1, \theta) \, \mathrm{d}\theta. \quad (4.117)$$

Ordinary-differential equation (ODE) (4.114) with constant coefficients admits the general solution

$$u(1, \theta) = U \sin(m\theta) \quad (m \in \mathbb{Z}), \quad (4.118)$$

which is consistent with the periodicity condition $u(1, \theta) = u(1, \theta + 2\pi k)$, $\forall k \in \mathbb{Z}$. Substituting the general solution (4.118) into the ODE (4.114) delivers the characteristic equation

$$(m^2 - 1)\big[(m^2 - 1) + m^2(m^2 - 1)\epsilon - \nu\big] = 0. \quad (4.119)$$

Excluding the solution $m = 1$ corresponding to the in-plane rigid body translation, (4.119) results the critical surface tension

$$\nu^{\mathrm{i}}_m = m^2 - 1 + m^2(m^2 - 1)\epsilon, \tag{4.120}$$

for each mode number m of the in-plane deformation. The first nontrivial mode is $m = 2$ attributed to an elliptical distortion of the boundary. Since ϵ, defined in (4.86), is non-negative, the lowest critical value ν^{i}_m is associated with $m = 2$ given as

$$\nu^{\mathrm{i}}_{\mathrm{c}} = \nu^{\mathrm{i}}_2 = 3 + 12\epsilon. \tag{4.121}$$

In the absence of the curvature derivative effect (i.e., for $\epsilon = 0$), $\nu^{\mathrm{i}}_{\mathrm{c}} = 3$ retrieves the critical value obtained by Chen and Fried [162] for stability and bifurcation of a circular soap film spanning an inextensible, elastic filament.

Transverse equilibrium

The system of equations (4.106), (4.115), and (4.116) suffices the transverse equilibrium. It can be shown that fourth-order PDE (4.106) has the general solution (see Section 4.11.2 of Appendix for the proof)

$$\begin{aligned} w(\rho,\theta) = c_0 + a_0 I_0(\zeta\rho) + \sum_{n=1}^{\infty} \big(c_n\rho^n + a_n I_n(\zeta\rho)\big)\cos(n\theta) \\ + \sum_{n=1}^{\infty} \big(d_n\rho^n + b_n I_n(\zeta\rho)\big)\sin(n\theta), \end{aligned} \tag{4.122}$$

with I_i, $i \in \mathbb{N}$ being the modified Bessel function of the first kind. Notice that c_0 can be neglected as it represents a rigid body translation which has no physical role. Substitution of the general solution (4.122) in the boundary conditions (4.115), and

(4.116) results

$$\left.\begin{aligned} &A_0^1 a_0 = A_0^2 a_0 = 0, \\ &[A]_n [a_n \ c_n]^\top = [A]_n [b_n \ d_n]^\top = [0 \ 0]^\top \quad (n \in \mathbb{N}), \end{aligned}\right\} \tag{4.123}$$

where A_0^1 and A_0^2 are two coefficients and $[A]_n$ is a 2×2 matrix provided in (4.251). Notice that A_0^1, A_0^2, and $[A]_n$ are functions of η, $\bar{\eta}$, and ν.

We may consider ν as the control parameter and η and $\bar{\eta}$ as the known input. Then, since we have two independent equations in $(4.123)_1$ for one unknown a_0, in general, it can be concluded that $a_0 = 0$. Thus, it follows that the axisymmetric solution (i.e., $n = 0$), except at the trivial solution, does not exist. Also, the terms including c_1 and d_1 in (4.122) are associated with rigid body rotations about the diameter of the reference domain $\mathcal{R}$ and have no physical importance. Moreover, to satisfy the conditions $(4.123)_2$ for $n = 1$, the requirements $a_1 = b_1 = 0$ must exist. Hence, the first nontrivial mode for the transverse deformation w corresponds to $n = 2$ which represents a saddle-like mode shape.

Conditions $(4.123)_2$ define the eigenvalue problem

$$\det[A]_n = 0, \quad n \geq 2, \tag{4.124}$$

leading to the dispersion relation

$$\begin{aligned}
\Big[-\frac{\eta}{4}\big(\zeta^3 I_n'''(\zeta)+\zeta^2 I_n''(\zeta)\big)+(\frac{\eta}{4}+\nu)\zeta I_n'(\zeta)&\\
+(\frac{\eta}{4}-\bar{\eta})n^2\zeta I_n'(\zeta)+n^4 I_n(\zeta)-(\nu+1-\bar{\eta}+\frac{\eta}{2})n^2 I_n(\zeta)\Big]\big[\bar{\eta}n(1-n)\big]&\\
-\Big[-\frac{\eta}{4}n(n-1)^2+(\frac{\eta}{4}+\nu)n+(\frac{\eta}{4}-\bar{\eta})n^3+n^4-(\nu+1-\bar{\eta}+\frac{\eta}{2})n^2\Big]&\\
\Big[\frac{\eta}{4}\zeta^2 I_n''(\zeta)+(\frac{\eta}{4}+\bar{\eta})\big(\zeta I_n'(\zeta)-n^2 I_n(\zeta)\big)\Big]&=0. \quad (4.125)
\end{aligned}$$

In addition, granted satisfaction of (4.125), $(4.123)_2$ results

$$c_n=\gamma_n a_n, \quad d_n=\gamma_n b_n, \tag{4.126}$$

where

$$\gamma_n=-A_n^{(1,1)}/A_n^{(1,2)}=-A_n^{(2,1)}/A_n^{(2,2)}. \tag{4.127}$$

Using $(4.251)_{5,6}$, γ_n can be expressed as

$$\gamma_n=\frac{\frac{\eta}{4}\zeta^2 I_n''(\zeta)+(\frac{\eta}{4}+\bar{\eta})\big(\zeta I_n'(\zeta)-n^2 I_n(\zeta)\big)}{\bar{\eta}n(n-1)}. \tag{4.128}$$

Accordingly, w can be written as

$$w(\rho,\theta)=\sum_{n=1}^{\infty}\omega_n(\rho)\Theta_n(\theta), \tag{4.129}$$

where

$$\left.\begin{aligned}\omega_n(\rho)&=I_n(\zeta\rho)+\gamma_n\rho^n,\\ \Theta_n(\theta)&=a_n\cos(n\theta)+b_n\sin(n\theta).\end{aligned}\right\} \tag{4.130}$$

Since $\sin(n\theta)$ and $\cos(n\theta)$ are orthogonal functions, the deformation w for each mode number n is decoupled from the remaining modes. Hence, each mode n can be studied separately.

We denote the root of the dispersion relation (4.125), resulting the critical surface tension for each transverse mode n, by ν_n^{t}. Numerical solution of the dispersion relation (4.125) is given in the numerical results Section 4.9.

4.8.3 Energy comparison method

In this section, we implement a simple method based on an energy comparison to study the stability of a flat circular disk due to a very small perturbation from the trivial solution $u = v = w = 0$. Such method can be viewed as a handy stability analysis compared to more sophisticated ones such as the one presented by Maleki and Fried [155] using the second variation of the energy functional. Towards this goal, we will consider the net potential-energy $\mathcal{H}$ given in (4.87) for a circular HDL particle under very small in-plane or transverse perturbations. Recently, similar approach has been efficiently employed by Giomi and Mahadevan [101] in studying the stability of a circular soap film bounded by a twist-free, inextensible elastic frame.

Because the transverse and in-plane deformations are—up to the small-slope approximation—decoupled, we will apply the energy comparison for each deformation type separately. Obviously, such method directly depends on the excitation or the test function. In theory, there are infinite number of candidates for the excitation function. However, we may use functions which are as simple as possible and, at the same time, mimic realistic deformations inspired from, for example, experimental observations. In view of (4.87) and (4.112), the net potential-energy $\mathcal{H}_{\mathrm{trivial}}$ at the trivial deformation is

$$\mathcal{H}_{\text{trivial}} = \pi(2-\nu). \tag{4.131}$$

The sign of the energy difference $\Delta\mathcal{H} = \mathcal{H} - \mathcal{H}_{\text{trivial}}$ is used to interpret the stability. If $\Delta\mathcal{H} > 0$, the trivial configuration is stable; if $\Delta\mathcal{H} = 0$, it is at the critical status; if $\Delta\mathcal{H} < 0$, it is unstable.

In-plane stability

The net potential-energy $\mathcal{H}_{\text{i}} := \mathcal{H}|_{w=0}$ for a general in-plane deformation is given by

$$\begin{aligned}\mathcal{H}_{\text{i}} = &\int_0^{2\pi}\int_0^1 \nu\big[\rho + \rho u_\rho + u + v_\theta + u_\rho(u+v_\theta) - v_\rho(u_\theta - v)\big]\,\mathrm{d}\rho\,\mathrm{d}\theta \\ &+ \int_0^{2\pi} \frac{1}{2}\big[1 - u - 2u_{\theta\theta} + v_\theta - \frac{5}{2}(u_\theta - v)^2 - 2(u+u_{\theta\theta})(u+v_\theta) \\ &+ 10(u+v_\theta)^2 + 8(-u-2v_\theta+u_{\theta\theta})(u+v_\theta) + (-u-2v_\theta+u_{\theta\theta})^2 \\ &+ 2(u_\theta - v)(2u_\theta - v + v_{\theta\theta})\big]\,\mathrm{d}\theta + \int_0^{2\pi}\frac{\epsilon}{2}[u_\theta + u_{\theta\theta\theta}]^2\,\mathrm{d}\theta \\ &+ \int_0^{2\pi}\iota\big[1 + u + v_\theta + \frac{1}{2}(u_\theta - v)^2\big]\,\mathrm{d}\theta. \end{aligned} \tag{4.132}$$

By straightforward calculations, imposing the constraint (4.111), and implementing the zeroth order equilibrium equation (4.112), (4.132) can be simplified as

$$\begin{aligned}\mathcal{H}_{\text{i}} = &\nu\int_0^{2\pi}\frac{1}{2}(u^2 - u_\theta^2)\,\mathrm{d}\theta + \int_0^{2\pi}\Big(-u_\theta^2 + \frac{u^2}{2} + \frac{u_{\theta\theta}^2}{2}\Big)\,\mathrm{d}\theta \\ &+ \frac{\epsilon}{2}\int_0^{2\pi}\big(u_\theta^2 + u_{\theta\theta\theta}^2 + 2u_\theta u_{\theta\theta\theta}\big)\,\mathrm{d}\theta + \pi(2-\nu). \end{aligned} \tag{4.133}$$

Consider the excitation function in the form of radial displacement given in (4.118). Substitution of (4.118) in (4.133) results

$$\Delta\mathcal{H}_{\mathrm{i}} = \frac{\pi}{2}U^2(m^2-1)\big[m^2-1-\nu+m^2(m^2-1)\epsilon\big]. \tag{4.134}$$

The sign of the energy difference $\Delta\mathcal{H}_{\mathrm{i}}$ determines the following stability criteria

$$\left.\begin{aligned} \nu < \nu_m^{\mathrm{i}} &: \quad \text{stable} \\ \nu > \nu_m^{\mathrm{i}} &: \quad \text{unstable} \end{aligned}\right\} \tag{4.135}$$

where the critical value ν_m^{i} for the surface tension is

$$\nu_m^{\mathrm{i}} = (m^2-1) + m^2(m^2-1)\epsilon. \tag{4.136}$$

Surprisingly, ν_m^{i} in (4.141) exactly coincides with the critical value given in (4.120).

The first unstable mode $m = 2$ corresponds to planar elliptical perturbation. As recently emphasized by Maleki and Fried [155], the observed planar elliptical shapes for discoidal HDL particles in experiment [97] might represent stabilized post-buckled configuration of initially unstable flat circular shape whose linear stability is characterized by (4.135).

Transverse stability

The net potential-energy $\mathcal{H}_\mathrm{t} := \mathcal{H}|_{u=v=0}$ for a general transverse deformation is given by

$$\begin{aligned}\mathcal{H}_\mathrm{t} = \int_0^{2\pi}\int_0^1 \frac{\eta}{8}[\Delta w]^2\rho\,\mathrm{d}\rho\,\mathrm{d}\theta + \int_0^{2\pi}\int_0^1 \nu\Big[\rho + \frac{\rho w_\rho^2}{2} + \frac{w_\theta^2}{2\rho}\Big]\,\mathrm{d}\rho\,\mathrm{d}\theta \\ + \int_0^{2\pi} \frac{1}{2}\Big[1 - \frac{3}{2}w_\theta^2 + w_{\theta\theta}^2\Big]\,\mathrm{d}\theta - \int_0^{2\pi} \bar{\eta}\Big[1 - \frac{w_\theta^2}{2} - w_\rho w_{\theta\theta} - \frac{w_\rho^2}{2}\Big]\,\mathrm{d}\theta \\ + \int_0^{2\pi} \iota\Big[1 + \frac{w_\theta^2}{2}\Big]\,\mathrm{d}\theta + 2\pi\bar{\eta}. \end{aligned} \quad (4.137)$$

Now, in view of various experiments and numerical simulations [91, 92, 93, 95, 96, 94, 50], consider a saddle-like excitation function as

$$w(\rho,\theta) = c_n\rho^n\cos n\theta. \quad (4.138)$$

Substituting (4.138) in (4.137) results

$$\mathcal{H}_\mathrm{t} = \pi(2-\nu) + \frac{\pi}{2}c_n^2 n(n-1)\big[n(n+1) - \nu - 2n\bar{\eta}\big], \quad (4.139)$$

or alternatively,

$$\Delta\mathcal{H}_\mathrm{t} = \frac{\pi}{2}c_n^2 n(n-1)\big[n(n+1) - \nu - 2n\bar{\eta}\big]. \quad (4.140)$$

Based on the sign of coefficient of $\Delta\mathcal{H}_\mathrm{t}$ in (4.140), the following stability criteria

$$\left.\begin{aligned} \nu < \nu_n^\mathrm{t}: &\quad \text{stable} \\ \nu > \nu_n^\mathrm{t}: &\quad \text{unstable} \end{aligned}\right\} \quad (4.141)$$

describe the transverse stability of the trivial solution, where critical value ν_n^{t} for the surface tension is given by as

$$\nu_n^{\mathrm{t}} = n(n+1) - 2n\bar{\eta}. \tag{4.142}$$

Excluding the modes $n = 0$ and $n = 1$ corresponding to the rigid body translation in $\boldsymbol{e}_z$ direction and the rigid body rotation about the diameter of the region $\mathcal{R}$, the first nontrivial mode corresponds to $n = 2$. Obviously, in contrast with the in-plane stability, the critical surface tension ν_n^{t} in (4.142) and the root of the dispersion relation (4.125) are not equal. In addition, ν_n^{t} in (4.142) does not depend on the splay modulus η, because the saddle-like perturbation (4.138) corresponds to a minimal surface with $H = 0$. Thus, in view of the Canham–Helfrich–Evans energy (4.28), the spay modulus μ and, subsequently, its dimensionless form η do not play any role in the stability of the discoidal HDL particle under the saddle-like perturbation (4.138).

4.9 Numerical results

Generating analytical solution based on the system of equations (4.79), (4.80) and (4.83) for a general large deformation, except for simple geometries such as the axisymmetric case, seems very challenging. However, excluding the trivial, axisymmetric, flat, circular shape, none of the existing experimental or MD simulations indicate any axisymmetric configurations for discoidal HDL particles. Alternative approach for dealing with the complicated geometries of the discoidal HDL particles, e.g. the saddle-like shape with large deformation, could be the continuum-based numerical methods, including the finite element method. As the finite element solutions use a variational setting (particularly the weak form of the Euler–Lagrange equations) and rely on the parametrization of the problem, they can directly benefit from the formulation provided in Section 4.7.

In this section, we exclusively provide some numerical results based on the analysis described in Section 4.8 presenting the small-slope formulation. Particular numerical result of the interest in the small-slope regime is numerical solution of the dispersion relation (4.125) which can deliver the critical surface tension ν_n^{t} for each transverse mode n. According to Maleki and Fried [155], the root of dispersion relation (4.125) indicates the condition under which the the stability of a flat circular discoidal HDL particle changes. We also numerically investigate the stability analysis based on the energy comparison method discussed in Section 4.8.3.

Considering the dimensionless surface tension ν as the control parameter, we need to provide the input parameters for the dimensionless bending moduli η and $\bar{\eta}$. Regarding the dimensionless group in (4.86), determining the dimensionless parameters η and $\bar{\eta}$ hinges on knowing the radius R of the circular flat discoidal HDL particle, splay and saddle-splay mouldi μ and $\bar{\mu}$ of the lipid bilayer, and the bending rigidity α of the apoA-I chain. Consistent with the existing literature [50, 51, 52, 53, 54], the representative diameter $2R \approx 10$ nm is considered as the characteristic size of the reference flat circular discoidal HDL particle. Also, the typical value $\mu \approx 0.5 \times 10^{-19}$J is considered for the splay modulus of the lipid bilayer [163]. We do not consider any specific value for the saddle-splay modulus $\bar{\mu}$ as its value and sign have been subject of controversy. Nevertheless, we consider both positive and negative values for its dimensionless form $\bar{\eta}$ with relatively wide range of magnitudes. Since, as far as we know, no data exists for the bending rigidity or the persistence length of apoA-I chain, we use the data for the persistence length 36 nm of an apolipoprotein C-II chain [164], which is the apolipoprotein element of other types of lipoproteins. The corresponding bending rigidity is (36 nm)k_BT, while k_B and T indicate the Boltzmann's constant and the absolute temperature, respectively. Considring a double-belt structure for the apoA-I chain around the discoidal HDL particle, the approximate value $\alpha \sim (70\text{ nm})k_BT$ is assumed for the bending rigidity of the boundary. Finally, with these input parameters, we have considered the approximate value $\eta = 1$ in part of the results, while we also consider other choices for η in another part. In general, the flexibility in choosing the input parameters η and $\bar{\eta}$ are useful because, as mentioned earlier, there seems no definitive value exists for the bending rigidity α of the apoA-I.

The solid lines in Fig. 4–4 depict variation of the root ν_n^{t} of the dispersion relation (4.125) with the saddle-splay modulus $\bar{\eta}$ for the fixed value $\eta = 1$ of the splay modulus and first few transverse modes $n = 1$ to $n = 4$. The dashed lines correspond to the critical values of ν_n^{t} predicted by the energy comparison method given in (4.142). Maleki and Fried [155], using the second variation test, indicate that the domains confined between the solid lines and the horizontal axis is stable and the outside domains are unstable. The stability criteria (4.141) of the energy comparison method indicate that the domains confined between the dashed lines and the horizontal axis are stable and the domains above the dashed lines are unstable. Considering the solid lines as the benchmarks for the stability analysis, it is notable that the energy comparison method—which might be viewed as a handy approach—provides very

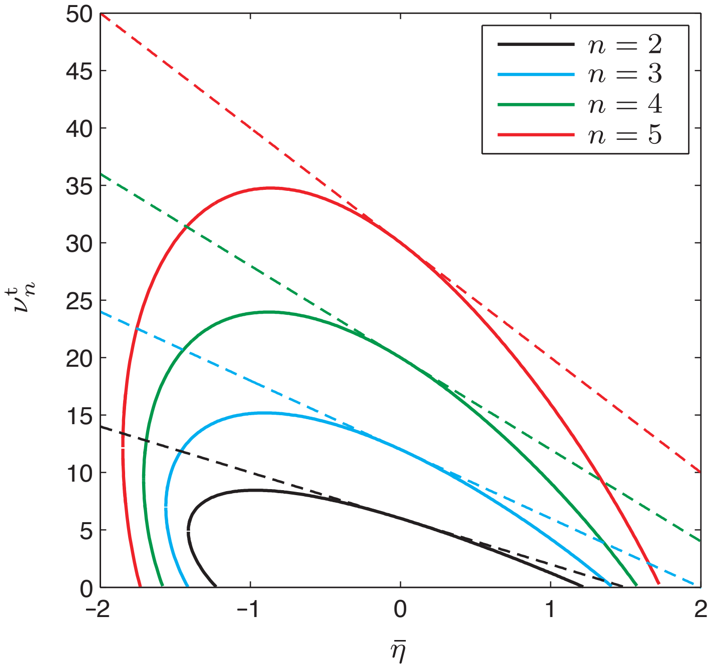

Figure 4–4: Variation of the numerically-determined critical surface tension ν_n^{t}, i.e. the root of dispersion relation (4.125), with the saddle-splay modulus $\bar{\eta}$ (the solid lines). The splay modulus is kept fixed at $\eta = 1$. The first four transverse modes $n = 1$ to $n = 4$ are considered. The dashed lines correspond to ν_n^{t} given by the energy comparison method in (4.142).

good stability criteria for small magnitudes of $\bar{\eta}$ and becomes a fairly good tool for larger magnitudes of $\bar{\eta}$.

Figure 4–5 shows variation of the critical surface tension ν_2^{t} with the splay modulus η for the first nontrivial transverse mode $n = 2$ and two values of the saddle-splay modulus $\bar{\eta} = -1$ and $\bar{\eta} = 1$. Also, the dashed lines show the corresponding values of the energy comparison method given by (4.142). It can be observed that the behaviors of ν_2^{t}–η diagrams for positive and negative $\bar{\eta}$ are different. Particularly, for $\bar{\eta} > 0$, the critical surface tension ν_2^{t} monotonically increases with the splay

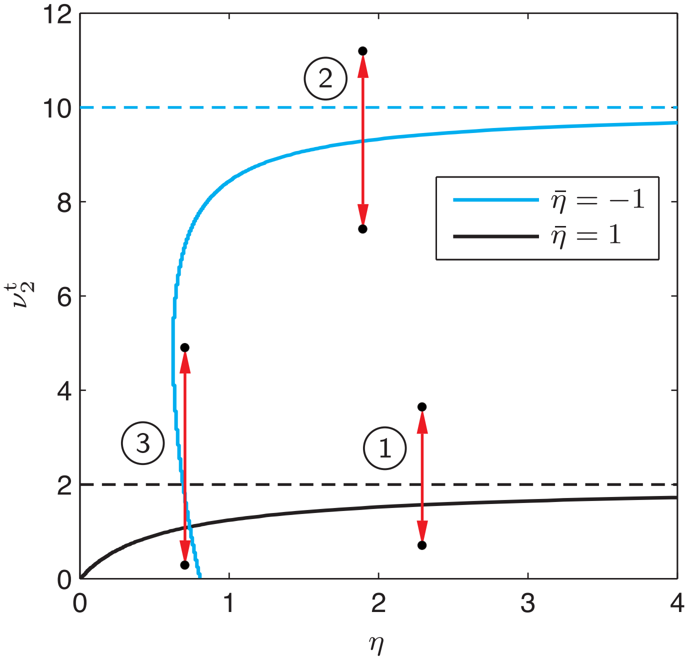

Figure 4–5: Variation of the critical surface tension ν_2^{t}, shown by solid lines, with η for two positive and negative values of $\bar{\eta}$. The dashed lines correspond to the value $\nu_n^{\mathrm{t}} = n(n+1) - 2n\bar{\eta}$ predicted by the energy comparison method in (4.142). Also, various potential pathways of the stability change are shown using red arrows.

modulus η. However, for $\bar{\eta} < 0$, ν_2^{t} first increases with decreasing η and then, at some point, it starts to monotonically increase with η. This confirms the previous observation of Maleki and Fried [155] that, for negative saddle-splay modulus $\bar{\eta}$, the dispersion relation (4.125) can have two roots. The stability analysis of Maleki and Fried [155] can be applied to verify that the domains confined by the solid lines and the horizontal axis indicate the stable domains while the domains above the solid lines correspond to unstable domain. Thus, the solid lines define the change of stability.

Catte et al. [91], using the MD simulations, showed that gradual depletion of the lipid molecules from the surface of a discoidal HDL particle, while the keeping the length of the apoA-I belt fixed, leads to shape transition from flat circular to nonplanar saddle-like shape. Decreasing the number of lipid molecules in a constant area increases the distance between adjacent lipid molecules and elevates the tension in the lipid bilayer. Such effect may be compared with stretching of a lipid bilayer under which the spacing between the molecules increases due to the area increase. However, for the stretching case, the number of lipid molecules remains constant. First two red arrows in Fig. 4–5, labeled with by numbers 1 and 2, show two possible pathways in which the change of surface tension ν can induce the change of stability of a flat, circular discoidal HDL particle. Particularly, increasing enough the surface tension (a process equivalent to the lipid depletion in the MD simulations of Catte et al. [91]), for example, from the bottom points of the arrows to the top ones, makes a flat circular discoidal HDL particle unstable under the saddle-like perturbations. In fact, the observed saddle-like shapes may represent the post-buckled configurations of a flat circular discoidal HDL particle. For $\bar{\eta} < 0$, however, there also exist a reverse mechanism, labeled with number 3, in which the surface tension decrease may induce the instability. However, the range of values of η for which such reverse mechanism exists is very smaller than the rest of the range of values of η.

Lastly, the stability criteria (4.141) of the energy comparison method predict that the domains below the dashed lines in Fig. 4–5 are stable while the domains above them are unstable. It is noteworthy that the energy comparison method serves as an efficient tool for larger values of η, where the solid and dashed lines tend towards each other.

4.10 Conclusions

A comprehensive continuum mechanical framework with a variational approach was developed to study the equilibrium of a discoidal HDL particle with a general configuration. The model relies on the simplifying assumptions including identifying the lipid bilayer with a smooth open surface $\mathcal{S}$ and the bounding double-belt apoA-I chain with the boundary $\mathcal{C} = \partial\mathcal{S}$ of $\mathcal{S}$. Consistent with high flexibility of apoA-I chain and amphipathic properties of apoA-I and lipid molecules, a perfect bonding was assumed between apoA-I chain and the lipid bilayer edge. Lipid bilayer was endowed with the bending energy density ψ (per unit area of $\mathcal{S}$) in form of Canham [21], Helfrich [22], and Evans [57], and a uniform surface tension σ. The double-belt apoA-I chain was modeled as an inextensible, twist-free, elastic filament with bending elasticity, endowed with an energy density (per unit length of $\mathcal{C}$) with a quadratic expression depending on the curvature κ of $\mathcal{C}$ and its derivative κ' with respect to the arclength of $\mathcal{C}$ [155].

First, mathematical preliminaries including definitions, conventions, identities and differential geometry discussions used through the paper were introduced. After constructing the energy functional comprising areal and lineal parts, using its first variation, the general equilibrium conditions (i.e., the Euler–Lagrange equations) were derived based on a direct, geometrically-based formulation. Taking the advantage of the direct formulation, clear physical interpretations of the equilibrium conditions were given. Conventionally, on the lipid bilayer, the shape equation governs the local curvature of $\mathcal{S}$. On the boundary $\mathcal{C}$, four distinct scalar equilibrium equations were identified. Three of them describes the force balance in the directions of the unit normal $\boldsymbol{n}$ of $\mathcal{S}$ restricted on $\mathcal{C}$, unit tangent-normal $\boldsymbol{\nu}$ of $\mathcal{C}$, and unit tangent $\boldsymbol{e}$ of $\mathcal{C}$. The latter equation reduces to condition implying that the Lagrange multiplier introduced due to the inextensibility of apoA-I chain to be uniform on $\mathcal{C}$. It is also mentioned that how the presented formulation can be applied to the case in which the lipid bilayer is considered locally inextensible.

Following the direct formulation, the problem was reformulated based on parametrization of $\mathcal{S}$ and $\mathcal{C}$. Using the parametrization is an important step for developing analytical solutions for equilibrium equations. In addition, numerical approaches, such as finite element method, rely on the parametrization of the problem domain. As a natural choice, the flat circular configuration of a discoidal HDL particle and polar coordinates within that configuration were used to parametrize a general configuration. The parametric form of the of equilibrium equations on $\mathcal{S}$ and $\mathcal{C}$ were derived using the first variation of the energy functional.

Adapting the component-wise version of the parametrized reformulation, a small-slope deformation theory (which is recently introduced in the brief format by Maleki and Fried [155]) was derived in details. As shown by Maleki and Fried [155], the small-slope approximation is necessary for derivation of the linearized equilibrium equations and, additionally, in studying the linear stability of a flat circular HDL particle. In the linearized formulation, the equilibrium of a flat circular HDL particle in the transverse and in-plane directions are decoupled. The equilibrium equations on the boundary $\mathcal{C}$ deliver two distinct dispersion relations, each associated with the transverse and planar deformational modes. The roots of the dispersion relations correspond to the critical (or buckling) conditions [155]. Comparing with the more comprehensive stability analysis introduced in Maleki and Fried [155], an alternative handy stability analysis was employed based on an energy comparison method. In this approach, the sign of the energy change from the flat circular configuration (i.e., the trivial state) to slightly perturbed configuration is used as a criterion to determine the nature of the stability of a flat circular HDL particle. Consistent with the observed flat elliptical or nonplanar saddle-like configurations of discoidal HDL particles, two separate planar elliptical and nonplanar saddle-like modes were chosen for the infinitesimal perturbations.

Lastly, numerical results for the linearized formulation were provided. The results corresponded to the solutions of the dispersion relation for the transverse deformation and showed the variation of the critical dimensionless surface tension with the dimensionless splay and saddle-splay moduli. As studied by Maleki and Fried [155], the curves associated with the roots of the dispersion relations correspond to the change of stability and separate domains of the physical input parameters where a circular flat HDL particle is stable or unstable. In addition, comparison between the handy energy comparison method and the recently developed analysis based on the second variation [155] was made. Interestingly, they have completely similar results for the planar stability. For the transverse stability, the numerical results indicate that the energy comparison method serves as an efficient tool for small magnitudes of dimensionless saddle-splay modulus or large values of dimensionless splay modulus.

4.11 Appendices

4.11.1 Variations of various quantities

In this section, variations of different quantities are derived for both direct and parametrized formulations introduced in Sections 4.6 and 4.7. For the direct formulation, we adapt the variational approach developed by Fosdick and Virga [165] and later extended by Rosso and Virga [166] who derived variations of various relevant quantities. For the sake of completeness and being self-consistent, this section contains derivations of all variations used in this paper.

Variation of a field

Consider an arbitrary field ϱ defined on the discoidal HDL particle represented by the surface $\mathcal{S}$ and the boundary $\mathcal{C}$. Suppose that the surface $\mathcal{S}$ and the boundary $\mathcal{C}$ undergo very small perturbation which maps them to $\mathcal{S}_\varepsilon$ and $\mathcal{C}_\varepsilon = \partial\mathcal{S}_\varepsilon$, respectively. The small scalar number $\varepsilon \geq 0$ is called the perturbation parameter which is used for labelling the virtual placement of the body—i.e., the discoidal HDL particle. The conventional method for describing variations of superficial or lineal quantities relies on a virtual velocity $\boldsymbol{v}$—which we simply refer it to as the 'variation'—restrictively defined on $\mathcal{S}$ and $\mathcal{C}$. However, guided by Fosdick and Virga [165], we implement an alternative approach based on the assumption that $\mathcal{S}$ is a surface embedded in an arbitrary material region $\mathcal{P}$—i.e., $\mathcal{S} \subset \mathcal{P}$. Notice that the only requirement for the arbitrary material region $\mathcal{P}$ is that it must include $\mathcal{S}$ and $\mathcal{C}$. Now, the virtual deformation $\boldsymbol{\chi}_\varepsilon$ can be defined as a mapping from an arbitrary point $\boldsymbol{x}$ in $\mathcal{P}$ to its image in $\mathcal{P}_\varepsilon$ as

$$\boldsymbol{x}_\varepsilon = \boldsymbol{\chi}_\varepsilon(\boldsymbol{x}) = \boldsymbol{x} + \varepsilon\boldsymbol{v} + o(\varepsilon). \tag{4.143}$$

On $\mathcal{S}$, the variation $\boldsymbol{v}$ can advantageously be decomposed as sum of tangential and normal components $\boldsymbol{v}_t = \boldsymbol{P}\boldsymbol{v}$ and $U\boldsymbol{n}$ as (4.36).

Consistent with the variational description (4.143), the first variation of an arbitrary field ϱ defined on $\mathcal{S}$ and $\mathcal{C}$ can be given as

$$\dot{\varrho} = \lim_{\varepsilon \to 0} \frac{\varrho_\varepsilon - \varrho}{\varepsilon}. \tag{4.144}$$

Using (4.143), the virtual deformation gradient $\boldsymbol{F}_\varepsilon = \nabla \boldsymbol{\chi}_\varepsilon$ is derived as

$$\boldsymbol{F}_\varepsilon = \nabla \boldsymbol{\chi}_\varepsilon(\boldsymbol{x}) = \mathbf{1} + \varepsilon \nabla \boldsymbol{v} + o(\varepsilon), \tag{4.145}$$

where ∇ is the gradient with respect to the spatial points $\boldsymbol{x}$. Based on the definition (4.144) of the first variation, variation of $\boldsymbol{F}$ is obtained as

$$\begin{aligned} \dot{\boldsymbol{F}} &= \lim_{\varepsilon \to 0} \frac{\boldsymbol{F}_\varepsilon - \mathbf{1}}{\varepsilon} \\ &= \lim_{\varepsilon \to 0} \frac{\mathbf{1} + \varepsilon \nabla \boldsymbol{v} + o(\varepsilon) - \mathbf{1}}{\varepsilon} = \nabla \boldsymbol{v}. \end{aligned} \tag{4.146}$$

Notice that the virtual deformation gradient

$$\boldsymbol{F} := \lim_{\varepsilon \to 0} \boldsymbol{F}_\varepsilon = \mathbf{1} \tag{4.147}$$

indicates no variation. Also, trivial, but useful, consequence of (4.147) is

$$\boldsymbol{F}^{-1} = \boldsymbol{F}^{\top} = \boldsymbol{F}^{-\top} = \mathbf{1}. \tag{4.148}$$

Differentiating the identity $\boldsymbol{F}_\varepsilon {\boldsymbol{F}_\varepsilon}^{-1} = \mathbf{1}$ with respect to ε at $\varepsilon = 0$, it follows that

$$\left(\dot{\overline{\boldsymbol{F}_\varepsilon}} \boldsymbol{F}_\varepsilon^{-1} + \boldsymbol{F}_\varepsilon \dot{\overline{\boldsymbol{F}_\varepsilon^{-1}}} \right)_{\varepsilon = 0} = \mathbf{0}, \tag{4.149}$$

which, in view of the commutation of the variation and the transposition, can be rearranged as

$$\overset{\cdot}{\overline{\boldsymbol{F}^{-1}}} = (\overset{\cdot}{\overline{\boldsymbol{F}_{\varepsilon}^{-1}}})_{\varepsilon=0} = -\boldsymbol{F}^{-1}\dot{\boldsymbol{F}}\boldsymbol{F}^{-1}. \tag{4.150}$$

Lastly, upon substitution of $\boldsymbol{F}^{-1}$ from (4.148) and using $\dot{\boldsymbol{F}}$ from (4.146), $\overset{\cdot}{\overline{\boldsymbol{F}^{-1}}}$ in (4.150) is expressed as

$$\overset{\cdot}{\overline{\boldsymbol{F}^{-1}}} = -\nabla \boldsymbol{v}. \tag{4.151}$$

Again, using the commutation of the variation and the transposition, variation $\overset{\cdot}{\overline{\boldsymbol{F}^{-\top}}}$ can be derived by transposition of (4.151), given by

$$\overset{\cdot}{\overline{\boldsymbol{F}^{-\top}}} = -(\nabla \boldsymbol{v})^{\top}. \tag{4.152}$$

Variation of the volumetric virtual Jacobian $J_{\varepsilon} = \det \boldsymbol{F}_{\varepsilon}$ can be determined by differentiation of $(\det \boldsymbol{F}_{\varepsilon})$ with respect to ε at $\varepsilon = 0$ as

$$\begin{aligned} \dot{J} = \big(\overset{\cdot}{\overline{\det \boldsymbol{F}_{\varepsilon}}}\big)_{\varepsilon=0} &= \big[(\det \boldsymbol{F}_{\varepsilon})\operatorname{tr}(\dot{\boldsymbol{F}}_{\varepsilon}\boldsymbol{F}_{\varepsilon}^{-1})\big]_{\varepsilon=0} \\ &= (\det \boldsymbol{F})\operatorname{tr}(\dot{\boldsymbol{F}}\boldsymbol{F}^{-1}), \end{aligned} \tag{4.153}$$

where, upon substitution of $\boldsymbol{F}$, $\boldsymbol{F}^{-1}$, and $\dot{\boldsymbol{F}}$ from (4.147), (4.148), and (4.146), it follows

$$\dot{J} = \operatorname{tr}(\nabla \boldsymbol{v}) = \operatorname{div} \boldsymbol{v}. \tag{4.154}$$

Obviously, the volumetric Jacobian in the limit of zero variation is unity, i.e.

$$J := \lim_{\varepsilon \to 0} J_{\varepsilon} = 1. \tag{4.155}$$

Areal quantities

- **Unit normal:**

The unit normal $\boldsymbol{n}_\varepsilon$ to $\mathcal{S}_\varepsilon$ convects under the virtual deformation $\boldsymbol{\chi}_\varepsilon$ as

$$\boldsymbol{n}_\varepsilon = \frac{\boldsymbol{F}_\varepsilon^{-\top}\boldsymbol{n}}{|\boldsymbol{F}_\varepsilon^{-\top}\boldsymbol{n}|}. \tag{4.156}$$

Variation $\dot{\boldsymbol{n}}$ of the unit normal $\boldsymbol{n}$ can easily be determined upon differentiation of the right-hand side of (4.156) with respect to ε at $\varepsilon = 0$ as

$$\dot{\boldsymbol{n}} = \left[\frac{|\boldsymbol{F}_\varepsilon^{-\top}\boldsymbol{n}|\dot{\overline{(\boldsymbol{F}_\varepsilon^{-\top}\boldsymbol{n})}} - \dot{\overline{|\boldsymbol{F}_\varepsilon^{-\top}\boldsymbol{n}|}}(\boldsymbol{F}_\varepsilon^{-\top}\boldsymbol{n})}{|\boldsymbol{F}_\varepsilon^{-\top}\boldsymbol{n}|^2}\right]_{\varepsilon=0}. \tag{4.157}$$

Substitution of $\boldsymbol{F}^{-\top} = \mathbf{1}$ from (4.148) in (4.157) yields

$$\dot{\boldsymbol{n}} = \dot{\overline{\boldsymbol{F}^{-\top}}}\boldsymbol{n} - \dot{\overline{|\boldsymbol{F}_\varepsilon^{-\top}\boldsymbol{n}|}}_{\varepsilon=0}\boldsymbol{n}. \tag{4.158}$$

Using the identity $|\boldsymbol{F}_\varepsilon^{-\top}\boldsymbol{n}|^2 = (\boldsymbol{F}_\varepsilon^{-\top}\boldsymbol{n}) \cdot (\boldsymbol{F}_\varepsilon^{-\top}\boldsymbol{n})$, it follows

$$\dot{\overline{|\boldsymbol{F}_\varepsilon^{-\top}\boldsymbol{n}|}}_{\varepsilon=0} = \frac{(\dot{\overline{\boldsymbol{F}^{-\top}}}\boldsymbol{n}) \cdot (\boldsymbol{F}^{-\top}\boldsymbol{n})}{|\boldsymbol{F}^{-\top}\boldsymbol{n}|}, \tag{4.159}$$

which, using $\boldsymbol{F}^{-\top}$ and $\dot{\overline{\boldsymbol{F}^{-\top}}}$ from (4.148) and (4.152), results

$$\dot{\overline{|\boldsymbol{F}_\varepsilon^{-\top}\boldsymbol{n}|}}_{\varepsilon=0} = -\boldsymbol{n} \cdot (\nabla\boldsymbol{v})\boldsymbol{n}. \tag{4.160}$$

Substitution of $\overline{|\boldsymbol{F}_\varepsilon^{-\top}\boldsymbol{n}|}^{\boldsymbol{\cdot}}|_{\varepsilon=0}$ and $\overline{\boldsymbol{F}^{-\top}}^{\boldsymbol{\cdot}}$ from (4.160) and (4.152) into the expression of $\dot{\boldsymbol{n}}$ in (4.158) yields

$$\begin{aligned}\dot{\boldsymbol{n}} &= -(\nabla \boldsymbol{v})^\top \boldsymbol{n} + [\boldsymbol{n} \cdot (\nabla \boldsymbol{v})\boldsymbol{n}]\boldsymbol{n} \\ &= -(\boldsymbol{1} - \boldsymbol{n} \otimes \boldsymbol{n})(\nabla \boldsymbol{v})^\top \boldsymbol{n} = -[(\nabla \boldsymbol{v})\boldsymbol{P}]^\top \boldsymbol{n} \\ &= -(\nabla_{\mathcal{S}} \boldsymbol{v})^\top \boldsymbol{n}. \end{aligned} \tag{4.161}$$

Since $\boldsymbol{n}$ is unit vector, $\dot{\boldsymbol{n}}$ must be orthogonal to $\boldsymbol{n}$—i.e., $\dot{\boldsymbol{n}} \cdot \boldsymbol{n} = 0$. This can be easily verified using the second-line expression of $\dot{\boldsymbol{n}}$ in (4.161) as $\dot{\boldsymbol{n}} \cdot \boldsymbol{n} = -\big([(\nabla \boldsymbol{v})\boldsymbol{P}]^\top \boldsymbol{n}\big) \cdot \boldsymbol{n} = -(\nabla \boldsymbol{v})\boldsymbol{P}\boldsymbol{n} \cdot \boldsymbol{n} = 0$, because $\boldsymbol{P}\boldsymbol{n} = \boldsymbol{0}$.

- **Projection tensor:**

Variation of the projection tensor $\boldsymbol{P}$ can be determined using the definition (4.5) as

$$\boldsymbol{P}_\varepsilon = \boldsymbol{1} - \boldsymbol{n}_\varepsilon \otimes \boldsymbol{n}_\varepsilon. \tag{4.162}$$

Differentiating $\boldsymbol{P}_\varepsilon$ in (4.162) with respect to ε at $\varepsilon = 0$ results

$$\dot{\boldsymbol{P}} = -\dot{\boldsymbol{n}} \otimes \boldsymbol{n} - \boldsymbol{n} \otimes \dot{\boldsymbol{n}}, \tag{4.163}$$

which, by substituting $\dot{\boldsymbol{n}}$ from (4.161), can be expressed as

$$\dot{\boldsymbol{P}} = (\nabla_{\mathcal{S}} \boldsymbol{v})^\top \boldsymbol{n} \otimes \boldsymbol{n} + \boldsymbol{n} \otimes (\nabla_{\mathcal{S}} \boldsymbol{v})^\top \boldsymbol{n}. \tag{4.164}$$

- **Curvature tensor:**

Based on the definition of the curvature tensor $\boldsymbol{L}$ in (4.13) and the definition $(4.9)_2$ of the surface gradient of a vector-valued superficial field, the perturbed curvature tensor $\boldsymbol{L}_\varepsilon$ can be expressed as

$$\boldsymbol{L}_\varepsilon = -(\nabla \boldsymbol{n}^{\mathrm{e}})_\varepsilon \boldsymbol{P}_\varepsilon, \tag{4.165}$$

where $\boldsymbol{n}^{\mathrm{e}}$ denotes the extension of $\boldsymbol{n}$. Straightforward differentiation of (4.165) leads

$$\dot{\boldsymbol{L}} = -(\dot{\overline{\nabla \boldsymbol{n}^{\mathrm{e}}}})\boldsymbol{P} - (\nabla \boldsymbol{n}^{\mathrm{e}})\dot{\boldsymbol{P}}. \tag{4.166}$$

According to the definition (4.144) of the first variation and using the variation $\dot{\overline{\boldsymbol{F}^{-1}}}$ from (4.151), it follows

$$\begin{aligned}
\dot{\overline{\nabla \boldsymbol{n}^{\mathrm{e}}}} &= \lim_{\varepsilon \to 0} \frac{\nabla_\varepsilon \boldsymbol{n}^{\mathrm{e}}_\varepsilon - \nabla \boldsymbol{n}^{\mathrm{e}}}{\varepsilon} \\
&= \lim_{\varepsilon \to 0} \frac{(\nabla_\varepsilon \boldsymbol{n}^{\mathrm{e}}_\varepsilon - \nabla_\varepsilon \boldsymbol{n}^{\mathrm{e}}) + (\nabla_\varepsilon \boldsymbol{n}^{\mathrm{e}} - \nabla \boldsymbol{n}^{\mathrm{e}})}{\varepsilon} \\
&= \nabla \dot{\overline{\boldsymbol{n}^{\mathrm{e}}}} + (\nabla \boldsymbol{n}^{\mathrm{e}})\ \dot{\overline{\boldsymbol{F}^{-1}}} \\
&= \nabla \dot{\overline{\boldsymbol{n}^{\mathrm{e}}}} - (\nabla \boldsymbol{n}^{\mathrm{e}})\nabla \boldsymbol{v}.
\end{aligned} \tag{4.167}$$

Substitution of $\dot{\overline{\nabla \boldsymbol{n}^{\mathrm{e}}}}$ and $\dot{\boldsymbol{P}}$ from (4.167) and (4.164) into (4.166) yields

$$\begin{aligned}
\dot{\boldsymbol{L}} &= -\nabla \dot{\overline{\boldsymbol{n}^{\mathrm{e}}}} \boldsymbol{P} + (\nabla \boldsymbol{n}^{\mathrm{e}})\nabla \boldsymbol{v}\boldsymbol{P} \\
&\quad - \nabla \boldsymbol{n}[(\nabla_{\mathcal{S}} \boldsymbol{v})^{\top} \boldsymbol{n} \otimes \boldsymbol{n} + \boldsymbol{n} \otimes (\nabla_{\mathcal{S}} \boldsymbol{v})^{\top} \boldsymbol{n}] \\
&= -\nabla_{\mathcal{S}} \dot{\boldsymbol{n}} + (\nabla \boldsymbol{n}^{\mathrm{e}})\nabla_{\mathcal{S}} \boldsymbol{v} - \nabla \boldsymbol{n}^{\mathrm{e}}(\boldsymbol{n} \otimes \boldsymbol{n})\nabla_{\mathcal{S}} \boldsymbol{v} \\
&\quad + \boldsymbol{L}(\nabla_{\mathcal{S}} \boldsymbol{v})^{\top} \boldsymbol{n} \otimes \boldsymbol{n} \\
&= -\nabla_{\mathcal{S}} \dot{\boldsymbol{n}} + (\nabla \boldsymbol{n}^{\mathrm{e}})\boldsymbol{P}\nabla_{\mathcal{S}} \boldsymbol{v} + \boldsymbol{L}(\nabla_{\mathcal{S}} \boldsymbol{v})^{\top} \boldsymbol{n} \otimes \boldsymbol{n} \\
&= -\nabla_{\mathcal{S}} \dot{\boldsymbol{n}} - \boldsymbol{L}\nabla_{\mathcal{S}} \boldsymbol{v} + \boldsymbol{L}(\nabla_{\mathcal{S}} \boldsymbol{v})^{\top} \boldsymbol{n} \otimes \boldsymbol{n}.
\end{aligned} \tag{4.168}$$

Lastly, using $\dot{\boldsymbol{n}}$ from (4.161) in (4.168) results in

$$\dot{\boldsymbol{L}} = \boldsymbol{L}[(\nabla_{\mathcal{S}}\boldsymbol{v})^{\top}\boldsymbol{n} \otimes \boldsymbol{n} - \nabla_{\mathcal{S}}\boldsymbol{v}] + \nabla_{\mathcal{S}}[(\nabla_{\mathcal{S}}\boldsymbol{v})^{\top}\boldsymbol{n}]. \tag{4.169}$$

- **Mean curvature:**

Regarding the definition (4.15) of the mean curvature H, its variation $\dot{H}$ is given by

$$\dot{H} = \tfrac{1}{2}\dot{\overline{\operatorname{tr}\boldsymbol{L}}} = \tfrac{1}{2}\operatorname{tr}\dot{\boldsymbol{L}}, \tag{4.170}$$

which, using the variation $\dot{\boldsymbol{L}}$ in (4.169) and properties of the curvature tensor $\boldsymbol{L}$ in (4.14), takes the form

$$\begin{aligned}\operatorname{tr}\dot{\boldsymbol{L}} &= \boldsymbol{L}^{\top}\boldsymbol{n} \cdot (\nabla_{\mathcal{S}}\boldsymbol{v})^{\top}\boldsymbol{n} - \operatorname{tr}(\boldsymbol{L}\nabla_{\mathcal{S}}\boldsymbol{v}) + \operatorname{tr}[\nabla_{\mathcal{S}}((\nabla_{\mathcal{S}}\boldsymbol{v})^{\top}\boldsymbol{n})] \\ &= -\operatorname{tr}(\boldsymbol{L}\nabla_{\mathcal{S}}\boldsymbol{v}) + \operatorname{tr}[\nabla_{\mathcal{S}}((\nabla_{\mathcal{S}}\boldsymbol{v})^{\top}\boldsymbol{n})]. \end{aligned} \tag{4.171}$$

Now, according to the decomposition (4.36), we separately consider the normal and tangential contributions of the variation $\boldsymbol{v}$ to the mean curvature H.

First, consider the normal variation $\boldsymbol{v} = U\boldsymbol{n}$, resulting in

$$\nabla_{\mathcal{S}}\boldsymbol{v} = U\nabla_{\mathcal{S}}\boldsymbol{n} + \boldsymbol{n} \otimes \nabla_{\mathcal{S}}U = -U\boldsymbol{L} + \boldsymbol{n} \otimes \nabla_{\mathcal{S}}U, \tag{4.172}$$

which yields

$$\nabla_{\mathcal{S}}((\nabla_{\mathcal{S}}\boldsymbol{v})^{\top}\boldsymbol{n}) = \nabla_{\mathcal{S}}\nabla_{\mathcal{S}}U. \tag{4.173}$$

Using $\nabla_{\mathcal{S}}((\nabla_{\mathcal{S}}\boldsymbol{v})^{\top}\boldsymbol{n})$ and $\nabla_{\mathcal{S}}\boldsymbol{v}$ from (4.173) and (4.172), and regarding the property (4.16), (4.171) can be expressed as

$$\begin{aligned}\operatorname{tr}\dot{\boldsymbol{L}} &= \operatorname{tr}(U\boldsymbol{L}^2) + \operatorname{tr}(\nabla_{\mathcal{S}}\nabla_{\mathcal{S}}U) = \operatorname{tr}(\boldsymbol{L}^2)U + \Delta_{\mathcal{S}}U \\ &= (4H^2 - 2K)U + \Delta_{\mathcal{S}}U. \end{aligned} \tag{4.174}$$

Substituting (4.174) in (4.170) delivers the normal variation $\dot{H}_n$ of the mean curvature H given by

$$\dot{H}_n = (2H^2 - K)U + \tfrac{1}{2}\Delta_{\mathcal{S}}U. \tag{4.175}$$

Now, consider the tangential contribution $\boldsymbol{v} = \boldsymbol{v}_t$ of the variation. According to the property $\boldsymbol{v}_t \cdot \boldsymbol{n} = 0$ and the identity $(4.12)_2$, it follows that

$$(\nabla_{\mathcal{S}}\boldsymbol{v}_t)^{\top}\boldsymbol{n} = -(\nabla_{\mathcal{S}}\boldsymbol{n})^{\top}\boldsymbol{v}_t. \tag{4.176}$$

Using the definition of the curvature tensor $\boldsymbol{L}$ in (4.13) and its symmetry, (4.176) becomes

$$(\nabla_{\mathcal{S}}\boldsymbol{v}_t)^{\top}\boldsymbol{n} = \boldsymbol{L}\boldsymbol{v}_t. \tag{4.177}$$

Substituting $(\nabla_{\mathcal{S}}\boldsymbol{v}_t)^{\top}\boldsymbol{n}$ from (4.177) into the expression (4.171) for $(\operatorname{tr}\dot{\boldsymbol{L}})$ and subsequently in (4.170) delivers the tangential contribution of the variation of the mean curvature $\dot{H}_t$ as

$$\dot{H}_t = \tfrac{1}{2}\operatorname{tr}(\nabla_{\mathcal{S}}(\boldsymbol{L}\boldsymbol{v}_t) - \boldsymbol{L}\nabla_{\mathcal{S}}\boldsymbol{v}_t). \tag{4.178}$$

Using the definition $\boldsymbol{L} = -\nabla_{\mathcal{S}}\boldsymbol{n}$ of the curvature tensor, it can be concluded that [167]

$$\nabla_{\mathcal{S}}(\boldsymbol{L}\boldsymbol{v}_t) = (\nabla_{\mathcal{S}}\boldsymbol{L})\boldsymbol{v}_t + \boldsymbol{L}\nabla_{\mathcal{S}}\boldsymbol{v}_t, \tag{4.179}$$

which, upon its substitution in (4.178), and in view of Noll [167] and the definition of the mean curvature H in $(4.15)_1$, results in

$$\dot{H}_t = \tfrac{1}{2}\mathrm{tr}\,[(\nabla_{\mathcal{S}}\boldsymbol{L})\boldsymbol{v}_t] = \tfrac{1}{2}[\nabla_{\mathcal{S}}(\mathrm{tr}\,\boldsymbol{L})] \cdot \boldsymbol{v}_t = \nabla_{\mathcal{S}}H \cdot \boldsymbol{v}_t. \tag{4.180}$$

The normal and tangential contributions $\dot{H}_n$ and $\dot{H}_t$ of the variation of the mean curvature H can eventually be combined delivering

$$\begin{aligned}\dot{H} &= \dot{H}_n + \dot{H}_t \\ &= (2H^2 - K)U + \tfrac{1}{2}\Delta_{\mathcal{S}}U + \nabla_{\mathcal{S}}H \cdot \boldsymbol{v}_t.\end{aligned} \tag{4.181}$$

- **Virtual areal Jacobian:**

Variation of the virtual areal Jacobian $\jmath_\varepsilon$ is needed for deriving the variation of a surface integral. It is well known that areal and volumetric Jabobians are related through

$$\jmath_\varepsilon = J_\varepsilon|\boldsymbol{F}_\varepsilon^{-\top}\boldsymbol{n}|. \tag{4.182}$$

Differentiating (4.182) with respect to ε at $\varepsilon = 0$ yields

$$\dot{\jmath} = \dot{J}|\boldsymbol{F}^{-\top}\boldsymbol{n}| + J\dot{\overline{|\boldsymbol{F}_\varepsilon^{-\top}\boldsymbol{n}|}}_{\varepsilon=0}, \tag{4.183}$$

which upon substitution of $\dot{J}$, $\boldsymbol{F}^{-\top}$, J, and $\dot{\overline{|\boldsymbol{F}_\varepsilon^{-\top}\boldsymbol{n}|}}_{\varepsilon=0}$ from (4.154), (4.148), (4.155), and (4.160) simplifies to

$$\begin{aligned}\dot{\jmath} &= \operatorname{div}\boldsymbol{v} - (\nabla\boldsymbol{v})^{\top}\boldsymbol{n}\cdot\boldsymbol{n}\\ &= (\nabla\boldsymbol{v})^{\top}\cdot\boldsymbol{P} = \operatorname{tr}\left((\nabla\boldsymbol{v})\boldsymbol{P}\right)\\ &= \operatorname{div}_{\mathcal{S}}\boldsymbol{v}.\end{aligned}\tag{4.184}$$

Finally, using the decomposition (4.36), the identity $(4.12)_1$, and the definition $(4.15)_1$ of the mean curvature H, it follows

$$\begin{aligned}\dot{\jmath} &= \operatorname{div}_{\mathcal{S}}\boldsymbol{v}_t + \operatorname{div}_{\mathcal{S}}(U\boldsymbol{n})\\ &= \operatorname{div}_{\mathcal{S}}\boldsymbol{v}_t - 2HU.\end{aligned}\tag{4.185}$$

- **Surface integral of a spatial field:**

Various extensive quantities emerge as surface integrals of spatial fields. Consider Γ, the integral of an arbitrary spatial field γ defined on $\mathcal{S}$ as

$$\Gamma = \int_{\mathcal{S}}\gamma.\tag{4.186}$$

In calculating the variation $\dot{\Gamma}$ of Γ, variation of both integrand γ and the boundary of the integral $\mathcal{S}$ must be included, i.e.

$$\dot{\Gamma} = \dot{\overline{\int_{\mathcal{S}}\gamma}} = \lim_{\varepsilon\to 0}\frac{1}{\varepsilon}\Big(\int_{\mathcal{S}_\varepsilon}\gamma_\varepsilon - \int_{\mathcal{S}}\gamma\Big).\tag{4.187}$$

Using the change of variable, integral over $\mathcal{S}_\varepsilon$ can be transferred into integral over $\mathcal{S}$. Next, using the variation of the areal Jacobian $\jmath$ in (4.185), it can be concluded

$$\begin{aligned}
\dot{\Gamma} &= \lim_{\varepsilon \to 0} \frac{1}{\varepsilon} \Big(\int_{\mathcal{S}} \gamma_\varepsilon \jmath_\varepsilon - \int_{\mathcal{S}} \gamma \Big) \\
&= \int_{\mathcal{S}} \lim_{\varepsilon \to 0} \frac{(\gamma_\varepsilon \jmath_\varepsilon - \gamma_\varepsilon) + (\gamma_\varepsilon - \gamma)}{\varepsilon} \\
&= \int_{\mathcal{S}} \big(\gamma \dot{\jmath} + \dot{\gamma} \big) \\
&= \int_{\mathcal{S}} [\dot{\gamma} + \gamma(\mathrm{div}_{\mathcal{S}} \boldsymbol{v}_t - 2HU)]. \qquad (4.188)
\end{aligned}$$

Lineal quantities

In this section, variations of various quantities defined on the boundary $\mathcal{C}$ are derived.

- **Virtual lineal stretch:**

Consider an infinitesimal material element on the curve $\mathcal{C}$ with $\boldsymbol{e}$ being the unit tangent to that. Then, the lineal stretch defined as

$$\lambda_\varepsilon = |\boldsymbol{F}_\varepsilon \boldsymbol{e}| \qquad (4.189)$$

describes the evolution of the ratio of the the infinitesimal material line element and its original length under variation $\boldsymbol{v}$. Using the identity $|\boldsymbol{F}_\varepsilon \boldsymbol{e}|^2 = (\boldsymbol{F}_\varepsilon \boldsymbol{e}) \cdot (\boldsymbol{F}_\varepsilon \boldsymbol{e})$, variation of λ_ε can be derived as

$$\begin{aligned}
\dot{\lambda} = \dot{\overline{|\boldsymbol{F}_\varepsilon \boldsymbol{e}|}}_{\varepsilon=0} &= \left[\frac{(\dot{\overline{\boldsymbol{F}_\varepsilon}} \boldsymbol{e}) \cdot (\boldsymbol{F}_\varepsilon \boldsymbol{e})}{|\boldsymbol{F}_\varepsilon \boldsymbol{e}|} \right]_{\varepsilon=0} \\
&= \frac{(\dot{\boldsymbol{F}} \boldsymbol{e}) \cdot (\boldsymbol{F} \boldsymbol{e})}{|\boldsymbol{F} \boldsymbol{e}|} \qquad (4.190)
\end{aligned}$$

which, upon substituting $\dot{\boldsymbol{F}}$ and $\boldsymbol{F}$ from (4.146) and (4.147), can be expressed as

$$\dot{\lambda} = \boldsymbol{e} \cdot (\nabla \boldsymbol{v})\boldsymbol{e}. \tag{4.191}$$

Evidently, $(\nabla \boldsymbol{v})\boldsymbol{e}$ represents the directional derivative of $\boldsymbol{v}$ in $\boldsymbol{e}$ direction, i.e.

$$(\nabla \boldsymbol{v})\boldsymbol{e} = \frac{\partial \boldsymbol{v}}{\partial s} = \boldsymbol{v}'. \tag{4.192}$$

Lastly, using (4.192) in (4.190) results in

$$\dot{\lambda} = \boldsymbol{v}' \cdot \boldsymbol{e}. \tag{4.193}$$

- **Unit tangent:**

The variations of various lineal quantities such as the curvature, the curvature derivative, and the geodesic curvatures involve the variation of the unit tangent $\boldsymbol{e}$. To determine the variation $\dot{\boldsymbol{e}}$ of $\boldsymbol{e}$, it is necessary to calculate the derivative of the virtual unit tangent $\boldsymbol{e}_\varepsilon$ convecting with the boundary $\mathcal{C}_\varepsilon$ as

$$\boldsymbol{e}_\varepsilon = \frac{\boldsymbol{F}_\varepsilon \boldsymbol{e}}{|\boldsymbol{F}_\varepsilon \boldsymbol{e}|}. \tag{4.194}$$

Thus

$$\begin{aligned} \dot{\boldsymbol{e}} &= \left[\frac{|\boldsymbol{F}_\varepsilon \boldsymbol{e}|(\dot{\overline{\boldsymbol{F}_\varepsilon}} \boldsymbol{e}) - \dot{\overline{|\boldsymbol{F}_\varepsilon \boldsymbol{e}|}}(\boldsymbol{F}_\varepsilon \boldsymbol{e})}{|\boldsymbol{F}_\varepsilon \boldsymbol{e}|^2} \right]_{\varepsilon=0} \\ &= \frac{|\boldsymbol{F}\boldsymbol{e}|(\dot{\boldsymbol{F}}\boldsymbol{e}) - \dot{\overline{|\boldsymbol{F}_\varepsilon \boldsymbol{e}|}}_{\varepsilon=0}(\boldsymbol{F}\boldsymbol{e})}{|\boldsymbol{F}\boldsymbol{e}|^2}. \end{aligned} \tag{4.195}$$

Regarding (4.190), $\dot{\overline{|\boldsymbol{F}_\varepsilon \boldsymbol{e}|}}_{\varepsilon=0}$ is equal to variation of the lineal stretch $\dot{\lambda}$ given in (4.193). Also, $\dot{\boldsymbol{F}}$ and $\boldsymbol{F}$ can be substituted from (4.146) and (4.147) into (4.195) leading to

$$\begin{aligned}\dot{\boldsymbol{e}} &= (\nabla \boldsymbol{v})\boldsymbol{e} - (\boldsymbol{v}' \cdot \boldsymbol{e})\boldsymbol{e} \\ &= \boldsymbol{v}' - (\boldsymbol{v}' \cdot \boldsymbol{e})\boldsymbol{e}. \qquad (4.196)\end{aligned}$$

- **Arclength derivative of a spatial field:**

Arclength derivatives present in some lineal quantities, such as the curvature $\boldsymbol{\kappa} = \boldsymbol{e}'$ and the curvature derivative κ'. Suppose that ξ represents a general spatial field on the curve $\mathcal{C}$. Following the definition of the first variation in (4.144) and using $\dot{\lambda}$ from (4.193), the variation $\dot{\overline{\xi'}}$ is calculated as

$$\begin{aligned}\dot{\overline{\xi'}} &= \lim_{\varepsilon\to 0} \frac{1}{\varepsilon}\Big(\frac{\partial \xi_\varepsilon}{\partial s_\varepsilon} - \frac{\partial \xi}{\partial s}\Big) \\ &= \lim_{\varepsilon\to 0} \frac{1}{\varepsilon}\Big(\frac{\partial \xi_\varepsilon}{\partial s}\frac{\partial s}{\partial s_\varepsilon} - \frac{\partial \xi}{\partial s}\Big) \\ &= \lim_{\varepsilon\to 0} \frac{1}{\varepsilon}\Big(\frac{\partial \xi_\varepsilon}{\partial s}\frac{\partial s}{\partial s_\varepsilon} - \frac{\partial \xi_\varepsilon}{\partial s} + \frac{\partial \xi_\varepsilon}{\partial s} - \frac{\partial \xi}{\partial s}\Big) \\ &= \Big(\lim_{\varepsilon\to 0}\frac{\partial \xi_\varepsilon}{\partial s}\Big)\Big[\lim_{\varepsilon\to 0}\frac{1}{\varepsilon}\Big(\frac{\partial s}{\partial s_\varepsilon} - 1\Big)\Big] + \frac{\partial}{\partial s}\Big[\lim_{\varepsilon\to 0}\Big(\frac{\xi_\varepsilon - \xi}{\varepsilon}\Big)\Big] \\ &= \frac{\partial \xi}{\partial s}\dot{\overline{(\lambda^{-1})}} + \frac{\partial \dot{\xi}}{\partial s} \\ &= -\dot{\lambda}\xi' + \frac{\partial \dot{\xi}}{\partial s} \\ &= (\dot{\xi})' - (\boldsymbol{v}' \cdot \boldsymbol{e})\xi'. \qquad (4.197)\end{aligned}$$

- **Curvature vector and (scalar) curvature:**

According to the definition (4.21) of the curvature vector $\boldsymbol{\kappa} = \boldsymbol{e}'$, variation $\dot{\boldsymbol{\kappa}}$ of the curvature vector $\boldsymbol{\kappa}$ can be expressed using the identity (4.197) as

$$\dot{\boldsymbol{\kappa}} = (\dot{\boldsymbol{e}})' - (\boldsymbol{v}' \cdot \boldsymbol{e})\boldsymbol{\kappa}, \tag{4.198}$$

which, upon substitution of variation $\dot{\boldsymbol{e}}$ of the unit tangent $\boldsymbol{e}$ from (4.196), can be expanded as

$$\dot{\boldsymbol{\kappa}} = (\boldsymbol{v}' - (\boldsymbol{v}' \cdot \boldsymbol{e})\boldsymbol{e})' - (\boldsymbol{v}' \cdot \boldsymbol{e})\boldsymbol{\kappa}. \tag{4.199}$$

In addition, using the definition (4.23) of the scalar curvature κ, it follows that

$$\dot{\kappa} = \kappa^{-1}(\dot{\boldsymbol{\kappa}} \cdot \boldsymbol{\kappa}). \tag{4.200}$$

Using $\dot{\boldsymbol{\kappa}}$ from (4.199) yields

$$\dot{\kappa} = \kappa^{-1}(\boldsymbol{v}' - (\boldsymbol{v}' \cdot \boldsymbol{e})\boldsymbol{e})' \cdot \boldsymbol{\kappa} - (\boldsymbol{v}' \cdot \boldsymbol{e})\kappa. \tag{4.201}$$

- **Curvature derivative:**

The variation $\dot{\overline{\kappa'}}$ of the curvature derivative κ' can be easily calculated using the general variation of the derivative of a spatial field given in (4.197) and the variation $\dot{\kappa}$ of the curvature κ in (4.201) as

$$\dot{\overline{\kappa'}} = \big(\kappa^{-1}(\boldsymbol{v}' - (\boldsymbol{v}' \cdot \boldsymbol{e})\boldsymbol{e})' \cdot \boldsymbol{\kappa} - (\boldsymbol{v}' \cdot \boldsymbol{e})\kappa\big)' - (\boldsymbol{v}' \cdot \boldsymbol{e})\kappa'. \tag{4.202}$$

- **Geodesic curvature:**

Variation $\dot{\kappa}_g$ can be obtained using $(4.24)_2$ as

$$\dot{\kappa}_g = -\dot{\boldsymbol{\kappa}} \cdot \boldsymbol{\nu} - \boldsymbol{\kappa} \cdot \dot{\boldsymbol{\nu}}. \tag{4.203}$$

Regarding (4.21), the curvature vector $\boldsymbol{\kappa}$ in (4.203) can be replaced by its normal and tangential components leading to

$$\dot{\kappa}_g = -\dot{\boldsymbol{\kappa}} \cdot \boldsymbol{\nu} - \kappa_n \boldsymbol{n} \cdot \dot{\boldsymbol{\nu}} + \kappa_g \boldsymbol{\nu} \cdot \dot{\boldsymbol{\nu}}. \tag{4.204}$$

Since $\boldsymbol{\nu}$ is unit vector and perpendicular to $\boldsymbol{n}$, it follows that

$$\dot{\boldsymbol{\nu}} \cdot \boldsymbol{\nu} = 0, \quad \boldsymbol{n} \cdot \dot{\boldsymbol{\nu}} = -\dot{\boldsymbol{n}} \cdot \boldsymbol{\nu}. \tag{4.205}$$

Substituting (4.205) into (4.204) results in

$$\dot{\kappa}_g = \kappa_n \dot{\boldsymbol{n}} \cdot \boldsymbol{\nu} - \dot{\boldsymbol{\kappa}} \cdot \boldsymbol{\nu}, \tag{4.206}$$

which, in view of the variations $\dot{\boldsymbol{n}}$ and $\dot{\boldsymbol{\kappa}}$ in (4.161) and (4.199), and alternative definition $(4.24)_2$ of κ_g, can be written as

$$\dot{\kappa}_g = -\kappa_n (\nabla_{\mathcal{S}} \boldsymbol{v})^{\top} \boldsymbol{n} \cdot \boldsymbol{\nu} - (\boldsymbol{v}' - (\boldsymbol{v}' \cdot \boldsymbol{e})\boldsymbol{e})' \cdot \boldsymbol{\nu} - \kappa_g (\boldsymbol{v}' \cdot \boldsymbol{e}). \tag{4.207}$$

Considering the decomposition (4.36) of the variation $\boldsymbol{v}$ and regarding the relations (4.172) and (4.177), the term $(\nabla_{\mathcal{S}} \boldsymbol{v})^{\top} \boldsymbol{n}$ in (4.207) can advantageously be expressed as

$$(\nabla_{\mathcal{S}} \boldsymbol{v})^{\top} \boldsymbol{n} = \nabla_{\mathcal{S}} U + \boldsymbol{L} \boldsymbol{v}_t, \tag{4.208}$$

which can be substituted in (4.207) delivering

$$\dot{\kappa}_g = -\kappa_n \boldsymbol{\nu} \cdot \boldsymbol{L} \boldsymbol{v}_t - \kappa_n \nabla_{\mathcal{S}} U \cdot \boldsymbol{\nu} - (\boldsymbol{v}' - (\boldsymbol{v}' \cdot \boldsymbol{e})\boldsymbol{e})' \cdot \boldsymbol{\nu} - \kappa_g (\boldsymbol{v}' \cdot \boldsymbol{e}). \tag{4.209}$$

- **Curve integral of a spatial field:**

Extensive lineal quantities usually emerge as the curve integrals. Consider the curve integral Ξ of a generic spatial field ξ defined on the curve $\mathcal{C}$ as

$$\Xi = \int_{\mathcal{C}} \xi. \tag{4.210}$$

Similar to the variation of a surface integral Γ of a spatial field γ defined on the surface $\mathcal{S}$, variation of the curve integral Ξ of the spatial field ξ on $\mathcal{C}$ involves variations of both the boundary of the integral and the integrand. Thus, the variation $\dot{\Xi}$ can be expressed as

$$\dot{\Xi} = \dot{\overline{\int_{\mathcal{C}} \xi}} = \lim_{\varepsilon \to 0} \frac{1}{\varepsilon} \Big(\int_{\mathcal{C}_\varepsilon} \xi_\varepsilon - \int_{\mathcal{C}} \xi \Big). \tag{4.211}$$

Using the change of variable, integral over $\mathcal{C}_\varepsilon$ can be transferred into integral over $\mathcal{C}$. Thus, using the variation of λ in (4.193), it follows that

$$\begin{aligned} \dot{\Xi} &= \lim_{\varepsilon \to 0} \frac{1}{\varepsilon} \Big(\int_{\mathcal{C}} \xi_\varepsilon \lambda_\varepsilon - \int_{\mathcal{C}} \xi \Big) \\ &= \int_{\mathcal{C}} \lim_{\varepsilon \to 0} \frac{(\xi_\varepsilon \lambda_\varepsilon - \xi_\varepsilon) + (\xi_\varepsilon - \xi)}{\varepsilon} \\ &= \int_{\mathcal{C}} (\xi \dot{\lambda} + \dot{\xi}) \\ &= \int_{\mathcal{C}} (\dot{\xi} + \xi \boldsymbol{v}' \cdot \boldsymbol{e}). \end{aligned} \tag{4.212}$$

Variations of the geometrical quantities based on the parameterization of the surface and boundary

In this section, variations of different geometrical quantities required in our analysis in Section 4.7 are derived. Section 4.7 includes the parametric descriptions of various quantities are expressed in terms of the spatial point $\boldsymbol{x}(r, \theta)$ parametrized by coordinates r and θ. Calculating the first variation of such quantities easily relies on the straightforward differentiation with respect to the variation parameter ε at $\varepsilon = 0$, while r and θ have no variations. Thus, variation and partial derivatives with respect to r and θ can readily commute.

- **Areal Jacobian:**

Areal Jacobian $|\boldsymbol{x}_r \times \boldsymbol{x}_\theta|$ emerges in the surface integrals over the domain $\mathcal{D}$ of the reference configuration. In view of the property $|\boldsymbol{x}_r \times \boldsymbol{x}_\theta|^2 = (\boldsymbol{x}_r \times \boldsymbol{x}_\theta) \cdot (\boldsymbol{x}_r \times \boldsymbol{x}_\theta)$ and the definition (4.65) of the unit normal $\boldsymbol{n}$, it follows that

$$\begin{aligned} \dot{\overline{|\boldsymbol{x}_r \times \boldsymbol{x}_\theta|}} &= \boldsymbol{n} \cdot (\dot{\overline{\boldsymbol{x}_r \times \boldsymbol{x}_\theta}}) \\ &= \boldsymbol{n} \cdot (\boldsymbol{v}_r \times \boldsymbol{x}_\theta + \boldsymbol{x}_r \times \boldsymbol{v}_\theta) \\ &= (\boldsymbol{x}_\theta \times \boldsymbol{n}) \cdot \boldsymbol{v}_r - (\boldsymbol{x}_r \times \boldsymbol{n}) \cdot \boldsymbol{v}_\theta. \end{aligned} \tag{4.213}$$

- **Unit normal:**

Based on the definition (4.65) of the unit normal $\boldsymbol{n}$, its variation $\dot{\boldsymbol{n}}$ can be derived as

$$\dot{\boldsymbol{n}} = \frac{(\dot{\overline{\boldsymbol{x}_r \times \boldsymbol{x}_\theta}})}{|\boldsymbol{x}_r \times \boldsymbol{x}_\theta|} - \frac{\dot{\overline{|\boldsymbol{x}_r \times \boldsymbol{x}_\theta|}}}{|\boldsymbol{x}_r \times \boldsymbol{x}_\theta|}\boldsymbol{n}, \tag{4.214}$$

which, upon substituting $\dot{\overline{|\boldsymbol{x}_r \times \boldsymbol{x}_\theta|}}$ from (4.213), leads to

$$\dot{\boldsymbol{n}} = \frac{1}{|\boldsymbol{x}_r \times \boldsymbol{x}_\theta|}\Big\{\boldsymbol{v}_r \times \boldsymbol{x}_\theta + \boldsymbol{x}_r \times \boldsymbol{v}_\theta - \big[(\boldsymbol{x}_\theta \times \boldsymbol{n}) \cdot \boldsymbol{v}_r - (\boldsymbol{x}_r \times \boldsymbol{n}) \cdot \boldsymbol{v}_\theta\big]\boldsymbol{n}\Big\}. \tag{4.215}$$

- **Mean curvature:**

Variation $\dot{H}$ of the mean curvature H can be derived using the parametric expression (4.63) of the mean curvature. Lengthy but straightforward differentiation of

$(4.66)_1$ with respect to variation parameter ε at $\varepsilon = 0$ and substituting the variations $\dot{\overline{|\boldsymbol{x}_r \times \boldsymbol{x}_\theta|}}$ and $\dot{\boldsymbol{n}}$ from (4.213) and (4.215) yield

$$
\begin{aligned}
\dot{H} = \frac{1}{2|\boldsymbol{x}_r \times \boldsymbol{x}_\theta|^2} \Bigg\{ & |\boldsymbol{x}_\theta|^2 \boldsymbol{n} \cdot \boldsymbol{v}_{rr} + \Bigg[|\boldsymbol{x}_r \times \boldsymbol{x}_\theta| (\boldsymbol{n} \times \boldsymbol{n}_\theta) - 3\boldsymbol{n} \cdot (\boldsymbol{x}_\theta \times \boldsymbol{n}_r)(\boldsymbol{x}_\theta \times \boldsymbol{n}) \\
& - 3\boldsymbol{n} \cdot (\boldsymbol{n}_\theta \times \boldsymbol{x}_r)(\boldsymbol{x}_\theta \times \boldsymbol{n}) + \boldsymbol{x}_r(\boldsymbol{n} \cdot \boldsymbol{x}_{\theta\theta} - \boldsymbol{x}_\theta \cdot \boldsymbol{n}_\theta) + \boldsymbol{x}_\theta(\boldsymbol{x}_\theta \cdot \boldsymbol{n}_r - \boldsymbol{n} \cdot \boldsymbol{x}_{r\theta}) \\
& + \left(\boldsymbol{x}_\theta \cdot \boldsymbol{x}_{r\theta} - \boldsymbol{x}_r \cdot \boldsymbol{x}_{\theta\theta} - \frac{|\boldsymbol{x}_r \times \boldsymbol{x}_\theta|_r}{|\boldsymbol{x}_r \times \boldsymbol{x}_\theta|} |\boldsymbol{x}_\theta|^2 + \frac{|\boldsymbol{x}_r \times \boldsymbol{x}_\theta|_\theta}{|\boldsymbol{x}_r \times \boldsymbol{x}_\theta|} (\boldsymbol{x}_r \cdot \boldsymbol{x}_\theta) \right) \boldsymbol{n} \\
& - |\boldsymbol{x}_\theta|^2 \boldsymbol{n}_r + (\boldsymbol{x}_r \cdot \boldsymbol{x}_\theta) \boldsymbol{n}_\theta \Bigg] \cdot \boldsymbol{v}_r - 2(\boldsymbol{x}_r \cdot \boldsymbol{x}_\theta) \boldsymbol{n} \cdot \boldsymbol{v}_{r\theta} \\
& + \Bigg[|\boldsymbol{x}_r \times \boldsymbol{x}_\theta| (\boldsymbol{n}_r \times \boldsymbol{n}) + 3\boldsymbol{n} \cdot (\boldsymbol{x}_\theta \times \boldsymbol{n}_r)(\boldsymbol{x}_r \times \boldsymbol{n}) + 3\boldsymbol{n} \cdot (\boldsymbol{n}_\theta \times \boldsymbol{x}_r)(\boldsymbol{x}_r \times \boldsymbol{n}) \\
& + \boldsymbol{x}_r(\boldsymbol{x}_r \cdot \boldsymbol{n}_\theta - \boldsymbol{x}_{r\theta} \cdot \boldsymbol{n}) + \boldsymbol{x}_\theta(\boldsymbol{x}_{rr} \cdot \boldsymbol{n} - \boldsymbol{x}_r \cdot \boldsymbol{n}_r) \\
& + \left(\boldsymbol{x}_r \cdot \boldsymbol{x}_{r\theta} - \boldsymbol{x}_\theta \cdot \boldsymbol{x}_{rr} + \frac{|\boldsymbol{x}_r \times \boldsymbol{x}_\theta|_r}{|\boldsymbol{x}_r \times \boldsymbol{x}_\theta|} (\boldsymbol{x}_\theta \cdot \boldsymbol{x}_r) - \frac{|\boldsymbol{x}_r \times \boldsymbol{x}_\theta|_\theta}{|\boldsymbol{x}_r \times \boldsymbol{x}_\theta|} |\boldsymbol{x}_r|^2 \right) \boldsymbol{n} \\
& + (\boldsymbol{x}_r \cdot \boldsymbol{x}_\theta) \boldsymbol{n}_r - |\boldsymbol{x}_r|^2 \boldsymbol{n}_\theta \Bigg] \cdot \boldsymbol{v}_\theta + |\boldsymbol{x}_r|^2 \boldsymbol{n} \cdot \boldsymbol{v}_{\theta\theta} \Bigg\}. \qquad (4.216)
\end{aligned}
$$

It is worth-mentioning that the superficial variations $\dot{\overline{|\boldsymbol{x}_r \times \boldsymbol{x}_\theta|}}$, $\dot{\boldsymbol{n}}$, and $\dot{H}$ given in (4.213), (4.215), and (4.216) are valid for any general—orthogonal or non-orthogonal—curvilinear coordinate system. Thus, the polar coordinates r and θ can be replaced by any other curvilinear coordinates.

- **Lineal Jacobian:**

The lineal Jacobian $|\boldsymbol{x}_\theta|_{r=R}$ emerges in the curve integrals over $\partial\mathcal{D}$. Based on the definition $(|\boldsymbol{x}_\theta|^2)_{r=R} = (\boldsymbol{x}_\theta \cdot \boldsymbol{x}_\theta)_{r=R}$, it can be concluded

$$
\dot{\overline{|\boldsymbol{x}_\theta|}}_{r=R} = \left(\frac{\boldsymbol{v}_\theta \cdot \boldsymbol{x}_\theta}{|\boldsymbol{x}_\theta|} \right)_{r=R}, \qquad (4.217)
$$

which upon use of the inextensibility constraint (4.67) reduces to

$$\dot{\overline{|\boldsymbol{x}_\theta|}}_{r=R} = \frac{(\boldsymbol{v}_\theta \cdot \boldsymbol{x}_\theta)_{r=R}}{R}. \tag{4.218}$$

- **Curvature:**

Variation of the scalar curvature κ can be determined using its parametric description in $(4.66)_1$ as

$$\dot{\kappa} = \left(\frac{\dot{\overline{|\boldsymbol{x}_\theta \times \boldsymbol{x}_{\theta\theta}|}}}{|\boldsymbol{x}_\theta|^3} - \frac{3|\boldsymbol{x}_\theta \times \boldsymbol{x}_{\theta\theta}|\dot{\overline{|\boldsymbol{x}_\theta|}}}{|\boldsymbol{x}_\theta|^4} \right)_{r=R}. \tag{4.219}$$

Regarding the property $|\boldsymbol{x}_\theta \times \boldsymbol{x}_{\theta\theta}|^2 = (\boldsymbol{x}_\theta \times \boldsymbol{x}_{\theta\theta}) \cdot (\boldsymbol{x}_\theta \times \boldsymbol{x}_{\theta\theta})$, it follows that

$$\begin{aligned}
\dot{\overline{|\boldsymbol{x}_\theta \times \boldsymbol{x}_{\theta\theta}|}} &= \frac{\dot{\overline{(\boldsymbol{x}_\theta \times \boldsymbol{x}_{\theta\theta})}} \cdot (\boldsymbol{x}_\theta \times \boldsymbol{x}_{\theta\theta})}{|\boldsymbol{x}_\theta \times \boldsymbol{x}_{\theta\theta}|} \\
&= \frac{(\boldsymbol{v}_\theta \times \boldsymbol{x}_{\theta\theta} + \boldsymbol{x}_\theta \times \boldsymbol{v}_{\theta\theta}) \cdot (\boldsymbol{x}_\theta \times \boldsymbol{x}_{\theta\theta})}{|\boldsymbol{x}_\theta \times \boldsymbol{x}_{\theta\theta}|} \\
&= \frac{(\boldsymbol{v}_\theta \cdot \boldsymbol{x}_\theta)|\boldsymbol{x}_{\theta\theta}|^2 - (\boldsymbol{v}_\theta \cdot \boldsymbol{x}_{\theta\theta})(\boldsymbol{x}_{\theta\theta} \cdot \boldsymbol{x}_\theta)}{|\boldsymbol{x}_\theta \times \boldsymbol{x}_{\theta\theta}|} \\
&\quad + \frac{|\boldsymbol{x}_\theta|^2(\boldsymbol{v}_{\theta\theta} \cdot \boldsymbol{x}_{\theta\theta}) - (\boldsymbol{x}_\theta \cdot \boldsymbol{x}_{\theta\theta})(\boldsymbol{v}_{\theta\theta} \cdot \boldsymbol{x}_\theta)}{|\boldsymbol{x}_\theta \times \boldsymbol{x}_{\theta\theta}|}.
\end{aligned} \tag{4.220}$$

Substituting $\dot{\overline{|\boldsymbol{x}_\theta|}}_{r=R}$ and $\dot{\overline{|\boldsymbol{x}_\theta \times \boldsymbol{x}_{\theta\theta}|}}$ from (4.217) and (4.220) into (4.219), and in view of the constraint (4.67) and the subsequent conditions (4.68), the variation $\dot{\kappa}$ in (4.219) takes the form

$$\dot{\kappa} = \left(\frac{1}{R^2} \frac{\boldsymbol{v}_{\theta\theta} \cdot \boldsymbol{x}_{\theta\theta}}{|\boldsymbol{x}_{\theta\theta}|} - 2\frac{|\boldsymbol{x}_{\theta\theta}|}{R^4}(\boldsymbol{v}_\theta \cdot \boldsymbol{x}_\theta) \right)_{r=R}. \tag{4.221}$$

- **Curvature derivative:**

Using the parametric definition $(4.66)_2$ of κ' and the expression (4.217) of $\dot{\overline{|\boldsymbol{x}_\theta|}}_{r=R}$, it can be concluded that

$$
\begin{aligned}
\dot{\overline{\kappa'}} &= \left(\frac{(\dot{\kappa})_\theta |\boldsymbol{x}_\theta| - \dot{\overline{|\boldsymbol{x}_\theta|}}\kappa_\theta}{|\boldsymbol{x}_\theta|^2}\right)_{r=R} \\
&= \left(\frac{(\dot{\kappa})_\theta}{|\boldsymbol{x}_\theta|} - (\boldsymbol{v}_\theta \cdot \boldsymbol{x}_\theta)\frac{\kappa_\theta}{|\boldsymbol{x}_\theta|^3}\right)_{r=R},
\end{aligned}
\tag{4.222}
$$

which, using the variation $\dot{\kappa}$ in (4.219) and regarding the constraint (4.67), can be expressed as

$$
\begin{aligned}
\dot{\overline{\kappa'}} = \Bigg\{ &\frac{1}{R^3}\frac{\boldsymbol{x}_{\theta\theta}}{|\boldsymbol{x}_{\theta\theta}|} \cdot \boldsymbol{v}_{\theta\theta\theta} + \left(\frac{1}{R^3}\frac{\boldsymbol{x}_{\theta\theta\theta}}{|\boldsymbol{x}_{\theta\theta}|} - \frac{|\boldsymbol{x}_{\theta\theta}|_\theta \boldsymbol{x}_{\theta\theta}}{R^3|\boldsymbol{x}_{\theta\theta}|^2} - \frac{2|\boldsymbol{x}_{\theta\theta}|\boldsymbol{x}_\theta}{R^5}\right) \cdot \boldsymbol{v}_{\theta\theta} \\
&- \frac{1}{R^5}\left(3|\boldsymbol{x}_{\theta\theta}|_\theta \boldsymbol{x}_\theta + 2|\boldsymbol{x}_{\theta\theta}|\boldsymbol{x}_{\theta\theta}\right) \cdot \boldsymbol{v}_\theta \Bigg\}_{r=R}.
\end{aligned}
\tag{4.223}
$$

- **Geodesic curvature:**

Using the parametric description $(4.66)_4$ of the geodesic curvature κ_g, it follows that

$$
\begin{aligned}
\dot{\kappa}_g = \Bigg\{ &\frac{1}{|\boldsymbol{x}_\theta|^3}\big[\dot{\boldsymbol{n}} \cdot (\boldsymbol{x}_\theta \times \boldsymbol{x}_{\theta\theta}) + \boldsymbol{n} \cdot (\boldsymbol{v}_\theta \times \boldsymbol{x}_{\theta\theta}) + \boldsymbol{n} \cdot (\boldsymbol{x}_\theta \times \boldsymbol{v}_{\theta\theta})\big] \\
&- \frac{3\dot{\overline{|\boldsymbol{x}_\theta|}}\big[\boldsymbol{n} \cdot (\boldsymbol{x}_\theta \times \boldsymbol{x}_{\theta\theta})\big]}{|\boldsymbol{x}_\theta|^4} \Bigg\}_{r=R}.
\end{aligned}
\tag{4.224}
$$

By substituting $\dot{\boldsymbol{n}}$ and $\dot{\overline{|\boldsymbol{x}_\theta|}}$ from (4.215) and (4.217), using the constraint (4.67) and the subsequent properties (4.68), and in view of the vector identity $(\mathbf{a}\times\mathbf{b})\cdot(\mathbf{c}\times\mathbf{d}) =$

$(\mathbf{a}\cdot\mathbf{c})(\mathbf{b}\cdot\mathbf{d})-(\mathbf{a}\cdot\mathbf{d})(\mathbf{b}\cdot\mathbf{c})$, the expression of $\dot{\kappa}_g$ in (4.224) can be expanded as

$$\begin{aligned}\dot{\kappa}_g = \frac{1}{R^3}\Bigg\{ & \frac{-1}{|\boldsymbol{x}_r\times\boldsymbol{x}_\theta|}\Big[R^2\boldsymbol{x}_{\theta\theta}+\big(\boldsymbol{n}\cdot(\boldsymbol{x}_\theta\times\boldsymbol{x}_{\theta\theta})\big)(\boldsymbol{x}_\theta\times\boldsymbol{n})\Big]\cdot\boldsymbol{v}_r \\ & +\Bigg(\frac{1}{|\boldsymbol{x}_r\times\boldsymbol{x}_\theta|}\big[(\boldsymbol{x}_r\cdot\boldsymbol{x}_\theta)\boldsymbol{x}_{\theta\theta}-(\boldsymbol{x}_r\cdot\boldsymbol{x}_{\theta\theta})\boldsymbol{x}_\theta+\big(\boldsymbol{n}\cdot(\boldsymbol{x}_\theta\times\boldsymbol{x}_{\theta\theta})\big)(\boldsymbol{x}_r\times\boldsymbol{n})\big] \\ & \quad +(\boldsymbol{x}_{\theta\theta}\times\boldsymbol{n})-\frac{3}{R^2}\big(\boldsymbol{n}\cdot(\boldsymbol{x}_\theta\times\boldsymbol{x}_{\theta\theta})\big)\boldsymbol{x}_\theta\Bigg)\cdot\boldsymbol{v}_\theta+(\boldsymbol{n}\times\boldsymbol{x}_\theta)\cdot\boldsymbol{v}_{\theta\theta}\Bigg\}_{r=R}. \end{aligned} \tag{4.225}$$

4.11.2 General solution of the PDE (4.106)

In this section, it is proved that the general solution of the fourth-order PDE in (4.106) as

$$\Delta^2 w-\zeta^2\Delta w=0 \qquad \text{on } \mathcal{R}, \tag{4.226}$$

is in the form given in (4.122).

To begin with, consider the change of variable

$$y(\rho,\theta):=\Delta w, \tag{4.227}$$

by which, (4.226) simplifies to the second-order PDE

$$\Delta y-\zeta^2 y=0 \qquad \text{on } \mathcal{R}. \tag{4.228}$$

Using the separation of variables $y(\rho,\theta)=\Omega(\rho)\Theta(\theta)$ and in view of the periodicity condition $\Theta(\theta)=\Theta(\theta+2\pi n)$, $\forall n\in\mathbb{N}$, it is easy to show that

$$\left.\begin{aligned}&\Theta''+n^2\Theta=0,\\ &\rho^2\Omega''+\rho\Omega'-(n^2+\zeta^2\rho^2)\Omega=0.\end{aligned}\right\} \tag{4.229}$$

From $(4.229)_1$, it follows that $\sin(n\theta)$ and $\cos(n\theta)$ are two solutions of $\Theta(\theta)$. Also by change of variable $\gamma := \zeta\rho$ and defining $Y(\gamma) := \Omega(\rho)$, $(4.229)_2$ changes to

$$\gamma^2 Y'' + \gamma Y' - (n^2 + \gamma^2)Y = 0, \tag{4.230}$$

which is the modified Bessel equation with the bounded solution $I_n(\gamma)$. Thus, the general solution for $y(\rho, \theta)$ is expressed as

$$y(\rho,\theta) = \alpha_0 I_0(\zeta\rho) + \sum_{n=1}^{\infty} \big[\alpha_n I_n(\zeta\rho)\cos(n\theta) + \beta_n I_n(\zeta\rho)\sin(n\theta)\big], \tag{4.231}$$

with α_n and β_n ($n \in \mathbb{N}$) being unknown coefficients. Notice that, the modified Bessel function of the second kind is excluded from the solution because it is singular at $\rho = 0$. Substituting the solution (4.231) back into (4.227) leads to

$$\Delta w = \alpha_0 I_0(\zeta\rho) + \sum_{n=1}^{\infty} \big[\alpha_n I_n(\zeta\rho)\cos(n\theta) + \beta_n I_n(\zeta\rho)\sin(n\theta)\big]. \tag{4.232}$$

In view of the change of variable $\gamma = \zeta\rho$, the Fourier expansion of w is

$$w(\rho,\theta) = W_0(\gamma) + \sum_{n=1}^{\infty} \big[\hat{W}_n(\gamma)\cos(n\theta) + \check{W}_n(\gamma)\sin(n\theta)\big]. \tag{4.233}$$

Substituting the expansion (4.233) in (4.232) yields

$$W_0'' + \gamma^{-1} W_0' = \tilde{\alpha}_0 I_0(\gamma), \tag{4.234}$$

and

$$\left.\begin{aligned} \hat{W}_n'' + \gamma^{-1}\hat{W}_n' - n^2\gamma^{-2}\hat{W}_n &= \tilde{\alpha}_n I_n(\gamma), \\ \check{W}_n'' + \gamma^{-1}\check{W}_n' - n^2\gamma^{-2}\check{W}_n &= \tilde{\beta}_n I_n(\gamma), \end{aligned}\right\} \tag{4.235}$$

where $\tilde{\alpha}_n = \zeta^{-2}\alpha_n$ and $\tilde{\beta}_n = \zeta^{-2}\beta_n$.

To solve the nonhomogeneous linear ODE's (4.234) and (4.235), we use the method of variation of parameters [168].

Let start from the system of equations (4.235). Obviously, $W_n^1 = \gamma^n$ and $W_n^2 = \gamma^{-n}$ are two independent solutions of the homogeneous equations in (4.235). Thus, following the method of variation of parameters, the general solution of (4.235) is given as

$$\left.\begin{aligned} \hat{W}_n(\gamma) &= \hat{C}_n^1(\gamma)\gamma^n + \hat{C}_n^2(\gamma)\gamma^{-n}, \\ \check{W}_n(\gamma) &= \check{C}_n^1(\gamma)\gamma^n + \check{C}_n^2(\gamma)\gamma^{-n}, \end{aligned}\right\} \tag{4.236}$$

where

$$\left.\begin{aligned} \hat{C}_n^1(\gamma) &= -\tilde{\alpha}_n \int \frac{\gamma^{-n}}{W(W_n^1, W_n^2)} I_n(\gamma)\,\mathrm{d}\gamma + \hat{c}_n^1, \\ \hat{C}_n^2(\gamma) &= \tilde{\alpha}_n \int \frac{\gamma^{n}}{W(W_n^1, W_n^2)} I_n(\gamma)\,\mathrm{d}\gamma + \hat{c}_n^2, \\ \check{C}_n^1(\gamma) &= -\tilde{\beta}_n \int \frac{\gamma^{-n}}{W(W_n^1, W_n^2)} I_n(\gamma)\,\mathrm{d}\gamma + \check{c}_n^1, \\ \check{C}_n^2(\gamma) &= \tilde{\beta}_n \int \frac{\gamma^{n}}{W(W_n^1, W_n^2)} I_n(\gamma)\,\mathrm{d}\gamma + \check{c}_n^2, \end{aligned}\right\} \tag{4.237}$$

which, upon substituting the Wronskian

$$W(W_n^1, W_n^2) = \begin{vmatrix} W_n^1 & W_n^2 \\ (W_n^1)' & (W_n^2)' \end{vmatrix} = -2n\gamma^{-1},$$

simplify to

$$\left.\begin{aligned} \hat{C}_n^1(\gamma) &= \frac{\tilde{\alpha}_n}{2n} \int \gamma^{1-n} I_n(\gamma)\,\mathrm{d}\gamma + \hat{c}_n^1, \quad & \hat{C}_n^2(\gamma) &= -\frac{\tilde{\alpha}_n}{2n} \int \gamma^{1+n} I_n(\gamma)\,\mathrm{d}\gamma + \hat{c}_n^2, \\ \check{C}_n^1(\gamma) &= \frac{\tilde{\beta}_n}{2n} \int \gamma^{1-n} I_n(\gamma)\,\mathrm{d}\gamma + \check{c}_n^1, \quad & \check{C}_n^2(\gamma) &= -\frac{\tilde{\beta}_n}{2n} \int \gamma^{1+n} I_n(\gamma)\,\mathrm{d}\gamma + \check{c}_n^2, \end{aligned}\right\} \tag{4.238}$$

where $\hat{c}_n^1$, $\hat{c}_n^2$, $\check{c}_n^1$, and $\check{c}_n^2$ are integration constants. In view of the integration properties of the modified Bessel functions, it follows

$$\left.\begin{aligned} \hat{C}_n^1(\gamma) &= \frac{\tilde{\alpha}_n \gamma^{1-n}}{2n} I_{n-1}(\gamma) + \hat{c}_n^1, \quad \hat{C}_n^2(\gamma) = -\frac{\tilde{\alpha}_n \gamma^{1+n}}{2n} I_{n+1}(\gamma) + \hat{c}_n^2, \\ \check{C}_n^1(\gamma) &= \frac{\tilde{\beta}_n \gamma^{1-n}}{2n} I_{n-1}(\gamma) + \check{c}_n^1, \quad \check{C}_n^2(\gamma) = -\frac{\tilde{\beta}_n \gamma^{1+n}}{2n} I_{n+1}(\gamma) + \check{c}_n^2. \end{aligned}\right\} \tag{4.239}$$

Substituting the coefficients (4.239) into the general solution (4.236) yields

$$\left.\begin{aligned} \hat{W}_n(\gamma) &= \hat{c}_n^1 \gamma^n + \hat{c}_n^2 \gamma^{-n} + \frac{\tilde{\alpha}_n \gamma}{2n}\big(I_{n-1}(\gamma) - I_{n+1}(\gamma)\big), \\ \check{W}_n(\gamma) &= \check{c}_n^1 \gamma^n + \check{c}_n^2 \gamma^{-n} + \frac{\tilde{\beta}_n \gamma}{2n}\big(I_{n-1}(\gamma) - I_{n+1}(\gamma)\big), \end{aligned}\right\} \tag{4.240}$$

where, in view of the property $I_n(\gamma) = \frac{\gamma}{2n}\big(I_{n-1}(\gamma) - I_{n+1}(\gamma)\big)$, simplify to

$$\left.\begin{aligned} \hat{W}_n(\gamma) &= \hat{c}_n^1 \gamma^n + \hat{c}_n^2 \gamma^{-n} + \tilde{\alpha}_n I_n(\gamma), \\ \check{W}_n(\gamma) &= \check{c}_n^1 \gamma^n + \check{c}_n^2 \gamma^{-n} + \tilde{\beta}_n I_n(\gamma). \end{aligned}\right\} \tag{4.241}$$

Notice that the solution γ^{-n} must be excluded as it is singular at $\gamma = 0$. Hence,

$$\left.\begin{aligned} \hat{W}_n(\gamma) &= \hat{c}_n^1 \gamma^n + \tilde{\alpha}_n I_n(\gamma), \\ \check{W}_n(\gamma) &= \check{c}_n^1 \gamma^n + \tilde{\beta}_n I_n(\gamma). \end{aligned}\right\} \tag{4.242}$$

Now, we consider the nonhomogeneous equation (4.234). The homogeneous solutions of (4.234) are $W_0^1 = \ln\gamma$ and $W_0^2 = 1$. Similarly, the general solution (4.234) is given by

$$W_0(\gamma) = C_0^1(\gamma)\ln\gamma + C_0^2(\gamma), \tag{4.243}$$

where $C_0^1(\gamma)$ and $C_0^2(\gamma)$ are given as

$$\left.\begin{aligned} C_0^1(\gamma) &= -\tilde{\alpha}_0 \int \frac{1}{W(W_0^1, W_0^2)} I_0(\gamma)\,\mathrm{d}\gamma + c_0^1, \\ C_0^2(\gamma) &= \tilde{\alpha}_0 \int \frac{\ln\gamma}{W(W_0^1, W_0^2)} I_0(\gamma)\,\mathrm{d}\gamma + c_0^2, \end{aligned}\right\} \tag{4.244}$$

which, upon substituting the Wronskian

$$W(W_0^1, W_0^2) = \begin{vmatrix} W_0^1 & W_0^2 \\ (W_0^1)' & (W_0^2)' \end{vmatrix} = -\gamma^{-1},$$

simplify to

$$\left.\begin{aligned} C_0^1(\gamma) &= \tilde{\alpha}_0 \int \gamma I_0(\gamma)\,\mathrm{d}\gamma + c_0^1, \\ C_0^2(\gamma) &= -\tilde{\alpha}_0 \int \gamma(\ln\gamma) I_0(\gamma)\,\mathrm{d}\gamma + c_0^2, \end{aligned}\right\} \tag{4.245}$$

where c_0^1 and c_0^2 are two integration constants. Equations (4.245), using the integration properties of the modified Bessel functions, can be simplified to

$$\left.\begin{aligned} C_0^1(\gamma) &= \tilde{\alpha}_0 \gamma I_1(\gamma) + c_0^1, \\ C_0^2(\gamma) &= \tilde{\alpha}_0 I_0(\gamma) - \tilde{\alpha}_0 \gamma(\ln\gamma) I_1(\gamma) + c_0^2. \end{aligned}\right\} \tag{4.246}$$

Substituting the coefficients (4.246) back into the general solution (4.243) yields

$$W_0(\gamma) = c_0^2 + c_0^1 \ln\gamma + \tilde{\alpha}_0 I_0(\gamma), \tag{4.247}$$

where upon excluding the singular term $(\ln\gamma)$ reduces to

$$W_0(\gamma) = c_0^2 + \tilde{\alpha}_0 I_0(\gamma). \tag{4.248}$$

Finally, on substituting $\hat{W}_n(\gamma)$ and $\check{W}_n(\gamma)$ from (4.242) and $W_0(\gamma)$ from (4.248) into the expression of $w(\gamma,\theta)$ in (4.233), and defining

$$\left.\begin{aligned} &c_0 := c_0^2, \quad a_0 := \tilde{\alpha}_0, \quad a_n := \tilde{\alpha}_n, \\ &b_n := \tilde{\beta}_n, \quad c_n := \zeta^n \hat{c}_n^1, \quad d_n := \zeta^n \check{c}_n^1, \end{aligned}\right\} \tag{4.249}$$

the solution for the PDE (4.106) is obtained as

$$\begin{aligned} w(\rho,\theta) = c_0 + a_0 I_0(\zeta\rho) + \sum_{n=1}^{\infty} \big(c_n\rho^n + a_n I_n(\zeta\rho)\big)\cos(n\theta) \\ + \sum_{n=1}^{\infty} \big(d_n\rho^n + b_n I_n(\zeta\rho)\big)\sin(n\theta). \end{aligned} \tag{4.250}$$

4.11.3 Coefficients A_0^1 and A_0^2 and the matrix $[A]_n$

The coefficients A_0^1 and A_0^2 and the matrix $[A]_n = [A_n^{11}\ A_n^{12}; A_n^{21}\ A_n^{22}]$ in (4.123) are

$$\begin{aligned} A_0^1 &= -\frac{\eta}{4}\big(\zeta^3 I_0'''(\zeta) + \zeta^2 I_0''(\zeta)\big) + (\frac{\eta}{4}+\nu)\zeta I_0'(\zeta), \\ A_0^2 &= \frac{\eta}{4}\zeta^2 I_0''(\zeta) + (\frac{\eta}{4}+\bar{\eta})\zeta I_0'(\zeta), \\ A_n^{11} &= -\frac{\eta}{4}\big(\zeta^3 I_n'''(\zeta) + \zeta^2 I_n''(\zeta)\big) + (\frac{\eta}{4}+\nu)\zeta I_n'(\zeta) \\ &\quad + (\frac{\eta}{4}-\bar{\eta})n^2\zeta I_n'(\zeta) + n^4 I_n(\zeta) - \big(\nu+1-\bar{\eta}+\frac{\eta}{2}\big)n^2 I_n(\zeta), \\ A_n^{12} &= -\frac{\eta}{4}n(n-1)^2 + (\frac{\eta}{4}+\nu)n + (\frac{\eta}{4}-\bar{\eta})n^3 + n^4 - \big(\nu+1-\bar{\eta}+\frac{\eta}{2}\big)n^2, \\ A_n^{21} &= \frac{\eta}{4}\zeta^2 I_n''(\zeta) + (\frac{\eta}{4}+\bar{\eta})\big(\zeta I_n'(\zeta) - n^2 I_n(\zeta)\big), \\ A_n^{22} &= \bar{\eta}n(1-n). \end{aligned} \tag{4.251}$$

CHAPTER 5
Stability of discoidal high-density lipoprotein particles

5.1 Preface

Motivated by the ongoing desire for characterizing configurations of discoidal HDL particles, in Chapter 4, methods of continuum mechanics were applied to formulate equilibrium conditions for such particles possessing general configurations. In recent simulations and experiments [92, 93, 94, 95, 96, 94, 97, 50], besides the trivial shape (i.e., the usual flat circular shape) of discoidal HDL particles, two interesting nontrivial shapes are observed: nonplanar saddle-like and planar elliptic. In this chapter, it is hypothesized that these nontrivial shapes may reflect post-buckled configurations of discoidal HDL particles after instability in their trivial configuration. Towards verification of this hypothesis, based on the linearized formulations derived in Chapter 4, and relying on the second-variation condition, the linear stability of discoidal HDL particles in their trivial state is studied. Connections between the instability modes and the observed nontrivial shapes of discoidal HDL particles are made. This chapter is reproduced from the published paper

M. Maleki and E. Fried, "Stability of discoidal high-density lipoprotein particles," *Soft Matter*, vol. 9, pp. 9991–9998, 2013.

with permission from The Royal Society of Chemistry, and from the coauthor Prof. Eliot Fried.

5.2 Abstract

Motivated by experimental and numerical studies revealing that discoidal high-density lipoprotein (HDL) particles may adopt flat elliptical and nonplanar saddle-like configurations, it is hypothesized that these might represent stabilized configurations of initially unstable flat circular particles. A variational description is developed to explore the stability of a flat circular discoidal HDL particle. While the lipid bilayer is modeled as two-dimensional fluid film endowed with surface tension and bending elasticity, the apoA-I belt is modeled as one-dimensional inextensible twist-free chain endowed with bending elasticity. Stability is investigated using the second variation of the underlying energy functional. Various planar and nonplanar instability modes are predicted and corresponding nondimensional critical values of salient dimensionless parameters are obtained. The results predict that the first planar and nonplanar unstable modes occur due to in-plane elliptical and transverse saddle-like perturbations. Based on available data, detailed stability diagrams indicate the range of input parameters for which a flat circular discoidal HDL particle is linearly stable or unstable.

5.3 Introduction

The packaging and transport of water-insoluble cholesterol in the bloodstream are mediated by lipoprotein particles. In “reverse cholesterol transport,” high-density lipoprotein (HDL) particles scavenge cholesterol from tissues and other types of lipoprotein particles and deliver it to the liver for excretion into bile or other use. A comprehensive understanding of the biophysical basis for the vasculoprotective functionalities of HDL particles is essential to developing effective strategies to prevent, diagnose, and treat atherosclerosis. However, as Vuorela et al. [90] observe: "*The functionality of HDL has remained elusive, and even its structure is not well understood.*"

During reverse cholesterol transport, an HDL particle sustains shape transitions that are accompanied by changes in the conformation of its apolipoprotein building block apoA-I. Davidson & Silva [89] explain that the functionality of apoA-I is linked to its conformational variations and emphasize the need to understand the diverse range of conformations that it adopts in its lipid-free and lipid-bound forms. A discoidal HDL particle consists of a lipid bilayer bound by an apoA-I chain. Camont et al. [169] argue that the low lipid content and high surface fluidity of discoidal HDL particles induces conformational changes of apoA-I that result in enhanced exposure to its aqueous surroundings and, thus, in an increased capacity to acquire blood lipids. Using all-atom molecular dynamics (MD) simulations, Catte et al. [91] predict that assembling a flat circular HDL particle from a lipid-free apoA-I chain involves the formation of intermediate nonplanar, twisted, saddle-like particles. Coarse-grained molecular dynamics simulations of Shih et al. [5, 170] and experiments of Silva et al. [171], Miyazaki et al. [95], and Huang et al. [172] confirm this prediction. In addition, experimental results of Skar-Gislinge et al. [97] reveal that HDL particles exhibit an intrinsic tendency to adopt planar, elliptical configurations.

Simulations have provided valuable insight regarding the molecular interactions that govern the assembly and dynamics of discoidal HDL particles. However, the small time steps needed to correctly capture the highest frequency of molecular vibrations and preserve numerical accuracy make it difficult to access time scales long enough to determine equilibria or draw conclusions regarding stability. For these purposes, continuum models provide a valuable complement to simulations. In particular, continuum models have been used with remarkable success to determine equilibria and study stability in biomembranes and biomolecules.

Inspired by the aforementioned experiments and simulations, a continuum mechanical model for the equilibrium and stability of a flat circular HDL particle is presented. Guided by prevalent continuum models of biomembranes and biomolecules, the bilayer is treated as a two-dimensional fluid film endowed with surface tension and resistance to bending and the apoA-I chain as a one-dimensional inextensible, twist-free, elastic filament endowed with resistance to bending. The bilayer and apoA-I chain are required to be perfectly bonded, in which case the boundary of the fluid film and the elastic filament must have the same shape. A variational description of the equilibrium of a discoidal HDL particle is provided. A flat, circular shape is chosen as a reference configuration. To study the linear stability of the reference shape, infinitesimal perturbations involving both planar and transverse components are considered. Such perturbations can be caused by thermal fluctuations of the lipid bilayer or the apoA-I chain or by interactions between the HDL particle and its environment. Closed-form analytical solutions for the linearized equilibrium conditions are obtained and stability is explored via the second-variation condition. In addition, available values of the physical parameters that enter the model are used to determine the range of inputs under which a flat, circular HDL particle is linearly stable or unstable. Lastly, connections between our result and previous experimental measurements and numerical simulations are made.

5.4 Energetics of a discoidal HDL particle

Geometrically, a discoidal HDL particle is treated as a smooth, orientable surface $\mathcal{S}$ with boundary $\mathcal{C} = \partial\mathcal{S}$. The interior and boundary of $\mathcal{S}$ correspond, respectively, to the bilayer and apoA-I components of the particle. Following convention, H and K denote the mean and Gaussian curvatures of $\mathcal{S}$ and κ denotes the curvature of $\mathcal{C}$.

To capture the energetics of the bilayer, $\mathcal{S}$ is endowed with a uniform surface tension σ and an areal bending-energy density

$$\psi = \tfrac{1}{2}\mu H^2 + \bar{\mu}K, \tag{5.1}$$

of the type put forth by Canham [21] and Helfrich [22], where $\mu > 0$ and $\bar{\mu}$ are the splay and saddle-splay moduli. The relevance of spontaneous curvature, which ordinarily appears in the Canham–Helfrich model, to discoidal HDL particles has yet to be investigated and, thus, is omitted from (5.1).

To capture the energetics of the apoA-I chain, $\mathcal{C}$ is endowed with a lineal bending-energy density φ depending on the curvature κ of $\mathcal{C}$ and its arclength derivative κ'. The latter dependence is included to account for the energetic cost of large, localized curvature variations associated with kinks on the apolipoprotein chain discussed by Brouillette et al. [156] and Klon et al. [157]. For simplicity, it is assumed that

$$\varphi = \tfrac{1}{2}\alpha\kappa^2 + \tfrac{1}{2}\beta(\kappa')^2, \tag{5.2}$$

where $\alpha > 0$ is the constant flexural rigidity of $\mathcal{C}$ and $\beta \geq 0$ is a higher-order generalization thereof. Since $\mathcal{C}$ is closed, including a quadratic coupling term proportional to $2\kappa\kappa' = (\kappa^2)'$ in φ would not alter the net potential energy and no generality is lost by neglecting such a contribution. The particular choice (5.2) of φ is a special case of a general expression for the lineal free-energy density of a polymer chain proposed by Zhang et al. [173], who allow for arbitrary dependence on κ, κ', and the torsion τ of $\mathcal{C}$. Granted the foregoing assumption and that external forces associated with gravity, van der Waals interactions, or flow-related forces are negligible, the net potential-energy of a discoidal HDL particle is given by

$$\mathcal{E} = \int_{\mathcal{S}} (\sigma + \psi) + \int_{\mathcal{C}} \varphi. \tag{5.3}$$

As a surface with boundary, $\mathcal{S}$ has Euler characteristic equal to unity. On using (5.1) and (5.2) in (5.3) and applying the Gauss–Bonnet theorem (taking into consideration that $\mathcal{C}$ is assumed to be smooth), the net potential-energy $\mathcal{E}$ becomes

$$\mathcal{E} = \mathcal{E}_a + \mathcal{E}_l + 2\pi\bar{\mu}, \tag{5.4}$$

where

$$\mathcal{E}_a = \int_{\mathcal{S}} (\sigma + \tfrac{1}{2}\mu H^2) \tag{5.5}$$

and

$$\mathcal{E}_l = \int_{\mathcal{C}} \big(\tfrac{1}{2}\alpha\kappa^2 + \tfrac{1}{2}\beta(\kappa')^2 - \bar{\mu}\kappa_g\big), \tag{5.6}$$

denote the effective areal and lineal potential energies, with κ_g being the geodesic curvature of $\mathcal{C}$. Without loss of generality, the additive constant $2\pi\bar{\mu}$ in (5.4) is disregarded hereafter.

The assumed inextensibility of the apoA-I chain is imposed by working with the augmented net potential-energy

$$\mathcal{F} = \mathcal{E}_a + \mathcal{E}_l + \int_{\mathcal{C}} \lambda, \tag{5.7}$$

where λ is an unknown Lagrange multiplier.

5.5 Parameterization and nondimensionization

Let $\mathcal{D} = \{(r, \theta) \in \mathbb{R}^2 : 0 \leq r \leq R, 0 \leq \theta \leq 2\pi\}$ denote the disk of radius R. The surface and boundary of a discoidal HDL particle can then be described by a smooth function

$$\boldsymbol{x} : \mathcal{D} \to \mathbb{R}^3. \tag{5.8}$$

Due to the inextensibility of $\mathcal{C}$, $\boldsymbol{x}$ must satisfy

$$|\boldsymbol{x}_\theta(R, \theta)| = R, \quad 0 \leq \theta \leq 2\pi. \tag{5.9}$$

With this choice, the bilayer and apoA-I chain are represented by

$$\boldsymbol{x}(r, \theta), \quad 0 \leq r < R, \quad 0 \leq \theta \leq 2\pi, \tag{5.10}$$

and

$$\boldsymbol{x}(R, \theta), \quad 0 \leq \theta \leq 2\pi. \tag{5.11}$$

On determining expressions for the geometrical objects H, κ, κ', and κ_g consistent with the parametrization (5.10)–(5.11), the augmented net potential-energy $\mathcal{F}$ defined in (5.7) can be expressed as a functional of $\boldsymbol{x}$.

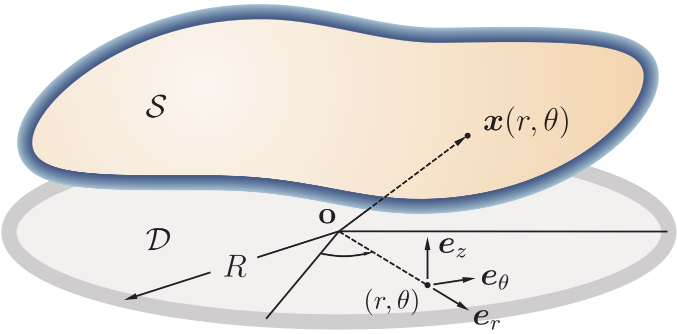

Figure 5–1: Schematic of a slightly perturbed discoidal HDL particle and its flat circular reference configuration (in grays). The transverse deformation is exaggerated for illustrative purposes.

It is convenient to present results in dimensionless form via the change of variables

$$\boldsymbol{x}(r,\theta) = R\boldsymbol{\xi}(\rho,\theta), \quad r = R\rho, \tag{5.12}$$

in which case the dimensionless reference domain is a disk of radius unity denoted by $\mathcal{R}$. In addition, it is convenient to introduce the following group of dimensionless quantities

$$\big(\mathcal{H}, \eta, \bar{\eta}, \nu, \iota, \epsilon\big) := \Big(\frac{\mathcal{F}R}{\alpha}, \frac{\mu R}{\alpha}, \frac{\bar{\mu}R}{\alpha}, \frac{\sigma R^3}{\alpha}, \frac{\lambda R^2}{\alpha}, \frac{\beta}{\alpha R^2}\Big). \tag{5.13}$$

In particular, the dimensionless counterpart $\mathcal{H}$ of the augmented net potential energy defined (5.7) takes the form

$$\begin{aligned}\mathcal{H} = \int_0^{2\pi}\int_0^1 (\nu + \tfrac{1}{2}\eta R^2 H^2)|\boldsymbol{\xi}_\rho \times \boldsymbol{\xi}_\theta| \,\mathrm{d}\rho\,\mathrm{d}\theta \\ + \int_0^{2\pi} \big(\tfrac{1}{2}R^2\kappa^2 + \tfrac{1}{2}\epsilon R^4(\kappa')^2 - \bar{\eta}R\kappa_g + \iota\big)|\boldsymbol{\xi}_\theta|_{\rho=1}\,\mathrm{d}\theta.\end{aligned} \tag{5.14}$$

For brevity, the adjective 'dimensionless' is dropped hereafter. To obtain linearized equilibrium equations and study the stability of a discoidal HDL particle, it suffices to use an infinitesimal displacement approximation in which the position of a generic point on $\mathcal{S}$ is given by (5.12), with

$$\boldsymbol{\xi}(\rho,\theta) = \mathbf{o} + (\rho + u(\rho,\theta))\boldsymbol{e}_r + v(\rho,\theta)\boldsymbol{e}_\theta + w(\rho,\theta)\boldsymbol{e}_z, \tag{5.15}$$

where $\mathbf{o}$ indicates the origin of the reference disk and u, v, and w are the components of $\boldsymbol{\xi}$ in $\boldsymbol{e}_r$, $\boldsymbol{e}_\theta$, and $\boldsymbol{e}_z$ directions, respectively (Fig. 5–1). The inextensibility condition (5.9) becomes

$$|\boldsymbol{\xi}_\theta(1,\theta)| = 1, \quad 0 \le \theta \le 2\pi. \tag{5.16}$$

The expansion (5.15) can be used to express (5.14) componentwise. The linearized equilibrium conditions arise on expanding all terms in (5.14) up to the second order of u, v, w, including their partial derivatives. For brevity, the intermediate calculations are suppressed.

5.6 Equilibrium conditions

At equilibrium, the first variation $\dot{\mathcal{H}}$ of the functional $\mathcal{H}$ in (5.14) vanishes. Notice that a superposed dot indicates the first variation. Imposing the requirement $\dot{\mathcal{H}} = 0$ yields the partial-differential equation

$$\Delta^2 w - \zeta^2 \Delta w = 0 \qquad \text{on } \mathcal{R}, \tag{5.17}$$

with Δ the Laplacian on $\mathcal{R}$ and $\zeta = 2\sqrt{\nu/\eta}$, and boundary conditions

$$\begin{aligned}\Big[(\iota + \nu - \tfrac{1}{2}) + \nu(u + v_\theta) + \tfrac{1}{2}(2u + 5u_{\theta\theta} + 2u_{\theta\theta\theta\theta} - v_\theta)& \\ - \epsilon\big(u_{\theta\theta} + 2u_{\theta\theta\theta\theta} + u_{\theta\theta\theta\theta\theta\theta}\big) - \big(\iota(u_\theta - v)\big)_\theta\Big]_{\rho=1} &= 0,\end{aligned} \tag{5.18}$$

$$\big[\iota_\theta + (\iota + \nu - \tfrac{1}{2})(u_\theta - v)\big]_{\rho=1} = 0, \tag{5.19}$$

$$\Big[-\frac{\eta}{4}(\Delta w)_\rho + \nu w_\rho + \tfrac{1}{2}(3w_{\theta\theta} + 2w_{\theta\theta\theta\theta}) - \bar{\eta}(w_{\theta\theta} - w_{\rho\theta\theta}) - (\iota w_\theta)_\theta\Big]_{\rho=1} = 0, \quad (5.20)$$

$$\Big[\frac{\eta}{4}\Delta w + \bar{\eta}(w_\rho + w_{\theta\theta})\Big]_{\rho=1} = 0. \quad (5.21)$$

Moreover, the linearized version of the inextensibility condition (5.16) requires that

$$(u + v_\theta)_{\rho=1} = 0. \quad (5.22)$$

The equilibrium condition (5.17), which governs the local geometry of the lipid bilayer, is the linearized version of the shape equation familiar from works on vesicles. The boundary conditions (5.18), (5.19), and (5.20) express force balance on $\mathcal{C}$ in the $\boldsymbol{e}_r$, $\boldsymbol{e}_\theta$, and $\boldsymbol{e}_z$ directions, respectively. The remaining boundary condition (5.21) involves the slope of the edge in the $\boldsymbol{e}_r$-direction and, thus, expresses moment balance on $\mathcal{C}$.

Up to the order considered, the partial-differential equation (5.17) imposes no restrictions on the in-plane displacements u and v. Hence, w and the in-plane components u and v are coupled only on the boundary of $\mathcal{R}$. Also, u and v are absent from the boundary conditions (5.20) and (5.21). Thus, (5.17) and the associated boundary conditions (5.20) and (5.21) may be used to determine w, independently. Satisfaction of (5.17) and (5.18)–(5.21) at the trivial solution ($u = v = w = 0$) results in a relation,

$$\iota = \tfrac{1}{2} - \nu, \quad (5.23)$$

for the Lagrange multiplier λ which is analogous to a result obtained by Giomi & Mahadevan [101] in their work on soap films bound by inextensible, elastic filaments.

Next, using (5.23) in (5.19) yields

$$\iota = \text{constant}. \tag{5.24}$$

The $\boldsymbol{e}_\theta$-component of force balance on the boundary of a discoidal HDL particle therefore requires that the Lagrange multiplier ι be uniform.

5.7 Solving the system of equations

Along with conditions (5.23) and (5.24), the partial-differential equation (5.17) and boundary conditions (5.20) and (5.21), suffice to completely determine the transverse displacement w. In addition, using (5.23) in (5.18) yields

$$\big[u + 2u_{\theta\theta} + u_{\theta\theta\theta\theta} + \nu(u_{\theta\theta} + u) - \epsilon(u_{\theta\theta} + 2u_{\theta\theta\theta\theta} + u_{\theta\theta\theta\theta\theta\theta})\big]_{\rho=1} = 0, \tag{5.25}$$

which ensures the in-plane balance of forces at the boundary and should be accompanied by (5.22) (or an equivalent integrated version thereof).

5.7.1 In-plane deformation

Equation (5.25) is an ordinary-differential equation with constant coefficients. In view of the periodicity of u (i.e., $u(1,\theta) = u(1,\theta + 2\pi k)$, $\forall k \in \mathbb{Z}$), (5.25) admits a representation of the form

$$u(1,\theta) = U\sin(m\theta) \quad (m \in \mathbb{Z}). \tag{5.26}$$

Substitution of (5.26) in (5.25) yields a characteristic equation

$$(m^2 - 1)\big[(m^2 - 1) + m^2(m^2 - 1)\epsilon - \nu\big] = 0. \tag{5.27}$$

One solution of (5.27) is $m^2 = 1$, which corresponds to the planar rigid body translation and is of no physical interest. Otherwise, (5.27) yields a critical value,

$$\nu_m^{\mathrm{i}} = m^2 - 1 + m^2(m^2 - 1)\epsilon, \tag{5.28}$$

of ν for each planar mode m. Granted that $\epsilon \geq 0$, the lowest critical value of ν corresponds to $m = 2$ and is given by

$$\nu_{\mathrm{c}}^{\mathrm{i}} = \nu_2^{\mathrm{i}} = 3 + 12\epsilon. \tag{5.29}$$

The value $\nu_{\mathrm{c}}^{\mathrm{i}} = 3$ arising for $\epsilon = 0$ is consistent with the results obtained by Chen & Fried [162] for a circular soap film bound by an inextensible, elastic filament.

5.7.2 Transverse displacement

Modulo a rigid translation, the general solution of the partial-differential equation (5.17) is

$$\begin{aligned} w(\rho, \theta) = a_0 I_0(\zeta\rho) + \sum_{n=1}^{\infty} \big(c_n \rho^n + a_n I_n(\zeta\rho)\big) \cos(n\theta) \\ + \sum_{n=1}^{\infty} \big(d_n \rho^n + b_n I_n(\zeta\rho)\big) \sin(n\theta), \end{aligned} \tag{5.30}$$

where I_i, $i \in \mathbb{N}$, is a modified Bessel function of the first kind. Substituting (5.30) into the boundary conditions (5.20) and (5.21) and invoking (5.23) and (5.24) results in an eigenvalue problem leading to the dispersion relation

$$\begin{aligned}
\Big[-\frac{\eta}{4}\big(\zeta^3 I_n'''(\zeta)+\zeta^2 I_n''(\zeta)\big)+(\frac{\eta}{4}+\nu)\zeta I_n'(\zeta) \\
+(\frac{\eta}{4}-\bar\eta)n^2\zeta I_n'(\zeta)+n^4 I_n(\zeta)-(\nu+1-\bar\eta+\frac{\eta}{2})n^2 I_n(\zeta)\Big]\big[\bar\eta n(1-n)\big] \\
-\Big[-\frac{\eta}{4}n(n-1)^2+(\frac{\eta}{4}+\nu)n+(\frac{\eta}{4}-\bar\eta)n^3+n^4-(\nu+1-\bar\eta+\frac{\eta}{2})n^2\Big] \\
\Big[\frac{\eta}{4}\zeta^2 I_n''(\zeta)+(\frac{\eta}{4}+\bar\eta)\big(\zeta I_n'(\zeta)-n^2 I_n(\zeta)\big)\Big]=0. \quad (5.31)
\end{aligned}$$

The terms involving c_1 and d_1 in (5.30) represent rigid body rotations about the diameter of domain $\mathcal{R}$ and, thus, are physically irrelevant. In addition, the requirements $a_0 = a_1 = b_1 = 0$ must be met to satisfy the boundary conditions (5.20) and (5.21) for $n = 0$ and $n = 1$. Thus, $n = 2$ is the first nontrivial mode of the transverse deformation w. Due to its complexity, (5.31) will be studied numerically and discussed in Section 5.9. Whereas ν is treated as a control parameter, η and $\bar\eta$ are treated as known input parameters. The solution of (5.31), which distinguishes the critical surface tension for each transverse mode n, is denoted by ν_n^{t}. Thus, w can be written as

$$w(\rho,\theta)=\sum_{n=1}^{\infty}\omega_n(\rho)\Theta_n(\theta), \quad (5.32)$$

with

$$\left.\begin{aligned}
\omega_n(\rho) &= I_n(\zeta\rho)+\gamma_n\rho^n, \\
\Theta_n(\theta) &= a_n\cos n\theta+b_n\sin n\theta,
\end{aligned}\right\} \quad (5.33)$$

and

$$\gamma_n=\frac{\frac{\eta}{4}\zeta^2 I_n''(\zeta)+(\frac{\eta}{4}+\bar\eta)\big(\zeta I_n'(\zeta)-n^2 I_n(\zeta)\big)}{\bar\eta n(n-1)}. \quad (5.34)$$

5.8 Stability of a flat circular HDL particle

The stability of the equilibrium configuration can be addressed by checking the sign of the second variation $\ddot{\mathcal{H}}$ of the functional $\mathcal{H}$. Consistent with the notation for the first variation, a superposed double dot indicates the second variation. The quantity $\ddot{\mathcal{H}}$ can be decomposed into a sum

$$\ddot{\mathcal{H}} = \ddot{\mathcal{H}}_{\mathrm{i}} + \ddot{\mathcal{H}}_{\mathrm{t}}, \tag{5.35}$$

of a purely planar component

$$\ddot{\mathcal{H}}_{\mathrm{i}} = \int_0^{2\pi} \big[(\nu+1)\dot{u} + (\nu+2-\epsilon)\dot{u}_{\theta\theta} + (1-2\epsilon)\dot{u}_{\theta\theta\theta\theta} + \dot{u}_{\theta\theta\theta\theta\theta\theta}\big]\dot{u}\,\mathrm{d}\theta \tag{5.36}$$

and a purely transverse component

$$\begin{aligned}\ddot{\mathcal{H}}_{\mathrm{t}} = {} & \int_0^{2\pi}\int_0^1 \Big[\frac{\eta}{4}\Delta^2\dot{w} - \nu\Delta\dot{w}\Big]\dot{w}\rho\,\mathrm{d}\rho\,\mathrm{d}\theta \\ & + \int_0^{2\pi} \Big[\big(\nu + \frac{\eta}{4}\big)\dot{w}_{\rho} - \frac{\eta}{4}\dot{w}_{\rho\rho} - \frac{\eta}{4}\dot{w}_{\rho\rho\rho} \\ & + (\nu + 1 - \bar{\eta} + \frac{\eta}{2})\dot{w}_{\theta\theta} + \big(\bar{\eta} - \frac{\eta}{4}\big)\dot{w}_{\rho\theta\theta} + \dot{w}_{\theta\theta\theta\theta}\Big]\dot{w}\,\mathrm{d}\theta \\ & + \int_0^{2\pi} \Big[\big(\frac{\eta}{4} + \bar{\eta}\big)\dot{w}_{\rho} + \frac{\eta}{4}\dot{w}_{\rho\rho} + \big(\frac{\eta}{4} + \bar{\eta}\big)\dot{w}_{\theta\theta}\Big]\dot{w}_{\rho}\,\mathrm{d}\theta.\end{aligned} \tag{5.37}$$

5.8.1 Planar and transverse modes

The decoupling of the planar and transverse displacements in (5.35) enables separate studies of the stability of a discoidal HDL particle to planar and transverse perturbations.

Planar stability requires that

$$\ddot{\mathcal{H}}_{\mathrm{i}} > 0. \tag{5.38}$$

Using a Fourier expansion, the in-plane variation $\dot{u}$ may be expressed as

$$\dot{u}(1,\theta) = \sum_{m=1}^{\infty} f_m \sin m\theta, \tag{5.39}$$

which, on substitution into (5.38), yields

$$\sum_{m=1}^{\infty} f_m^2 (m^2-1)\big[(m^2-1) + m^2(m^2-1)\epsilon - \nu\big] > 0. \tag{5.40}$$

Since the variation $\dot{u}$ is arbitrary, the coefficients f_m in (5.39) are independent and each term of the summand in (5.40) must separately satisfy the inequality (5.40). In response to planar perturbations, a flat, circular HDL particle therefore obeys

$$\left.\begin{aligned} \nu < \nu_m^{\mathrm{i}} : &\quad \text{stable,} \\ \nu > \nu_m^{\mathrm{i}} : &\quad \text{unstable,} \end{aligned}\right\} \tag{5.41}$$

with ν_m^{i} given in (5.28).

Transverse stability requires that

$$\ddot{\mathcal{H}}_{\mathrm{t}} > 0. \tag{5.42}$$

Similar to the strategy used to investigate stability with respect to planar perturbations, a general transverse variation $\dot{w}$ can be expanded in a Fourier series. However, since the coefficients of each mode in the Fourier expansion of $\dot{w}$ are independent, it is, without loss of generality, possible to consider

$$\dot{w}(\rho,\theta) = \chi_n(\rho)\cos(n\theta), \quad n \in \mathbb{N}, \tag{5.43}$$

with χ_n being an arbitrary function. Determination of conditions necessary and sufficient to ensure (5.42) for χ_n arbitrary appears to be challenging. An alternative approach invokes the Rayleigh–Ritz variational method, in which χ_n is approximated by sum of known functions multiplied by unknown coefficients. The known functions must satisfy the geometrical boundary conditions but may otherwise be chosen arbitrarily. Guided by the structure of the general solution (5.30), consider the *Ansatz*

$$\chi_n(\rho) = g_n\rho^n + h_n I_n(\zeta\rho), \tag{5.44}$$

where g_n and h_n are independent unknown coefficients. Substitution of (5.44) in (5.43), and subsequently in (5.42), and evaluating the relevant integrals yields

$$\ddot{\mathcal{H}}_{\mathrm{t}} = \frac{\pi}{2}[V]^{\top}[M][V] > 0, \tag{5.45}$$

for each n, with $[V] = [g_n \; h_n]^{\top}$ and $[M]$ a 2×2 matrix provided in the Appendix. The condition necessary and sufficient for (5.45) to be satisfied is that $[M]$ be positive-definite, namely that its components obey

$$M_{11} > 0, \quad M_{11}M_{22} > (M_{12})^2. \tag{5.46}$$

As a consequence of $(5.46)_1$, it follows that

$$\nu < n(n+1) - 2n\bar{\eta}. \tag{5.47}$$

Due to its complexity, $(5.46)_2$ will be studied numerically and discussed in Section 5.9.

5.8.2 Onset of instability

The onset of instability corresponds to the vanishing of the second variation $\ddot{\mathcal{H}}$ of $\mathcal{H}$. It can be shown that the critical values $\nu_n^{\rm i}$ and $\nu_n^{\rm t}$ of the surface tension correspond, respectively, to the onset of the planar and transverse instability. For $\nu = \nu_n^{\rm i}$ and $\nu = \nu_n^{\rm t}$, the solutions (5.26) and (5.32) can be used in (5.36) and (5.37), respectively. Specifically, for each m and n, $\dot{u}$ and $\dot{w}$ can be expressed as

$$\left.\begin{aligned} \dot{u}(1,\theta) &= \dot{U}\sin(m\theta), \\ \dot{w}(\rho,\theta) &= \omega_n(\rho)(\dot{a}_n\cos n\theta + \dot{b}_n\sin n\theta), \end{aligned}\right\} \tag{5.48}$$

where $\dot{U}$, $\dot{a}_n$, and $\dot{b}_n$ are the variations of the coefficients U, a_n, and b_n. Regarding $(5.48)_1$ and (5.25), it is readily observed that $\ddot{\mathcal{H}}_{\rm i}$ vanishes identically. Thus, (5.27) determines the planar instability requirement and delivers the critical surface tension $\nu_m^{\rm i}$ given in (5.28). Also, in view of $(5.48)_2$ and the equilibrium conditions (5.17), (5.20), and (5.21), $\ddot{\mathcal{H}}_{\rm t}$ vanishes. Thus, the dispersion relation (5.31) furnishes the condition necessary for the onset of transverse instability.

The connection between the stability conditions (5.46) and the critical value $\nu_n^{\rm t}$ at the onset of instability will be discussed in the next section.

5.9 Numerical results and discussion

Results from numerical studies based on the model are described next. Regarding the various input parameters, it seems reasonable to fix some of them. In particular, the splay modulus μ and the bounding loop bending stiffness α are kept fixed, unless mentioned otherwise. Due to the lack of data for the bending stiffness or persistence length of apoA-I, existing data for the persistence length of apolipoprotein C-II

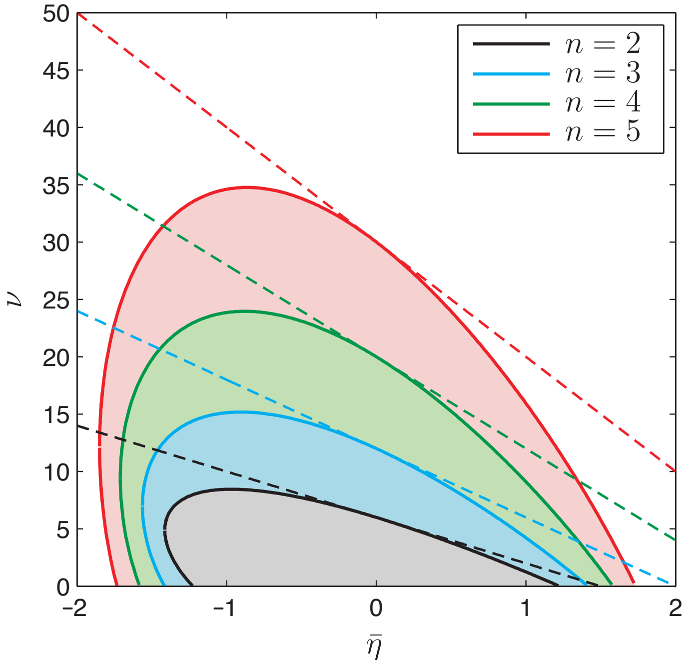

Figure 5–2: Stability plane showing the domains where a flat circular discoidal HDL particle is stable or unstable under transverse perturbations. Solid lines show ν_n^{t}, namely the solution of the dispersion equation (5.31). Regions below the dashed lines are the domains where the stability requirement $(5.46)_1$ is met.

chains, which are another common component of lipoprotein particles, are used. The input parameters are merely used to illustrate the primary features of the problem; modest deviations from their exact values should not significantly affect the nature of the stability. Hatters et al. [164] report that the persistence length of apolipoprotein C-II is approximately 36 nm, which corresponds to a bending stiffness of (36 nm)k_BT, with k_B Boltzmann's constant and T the absolute temperature. Assuming a double-belt apolipoprotein structure for the bounding loop yields $\alpha \sim$ (70 nm)k_BT. A representative value $\mu \approx 0.5 \times 10^{-19}$ J is used for the splay modulus of a lipid bilayer [163] and it is assumed [50, 51, 52, 53, 54, 55] that the reference HDL particle

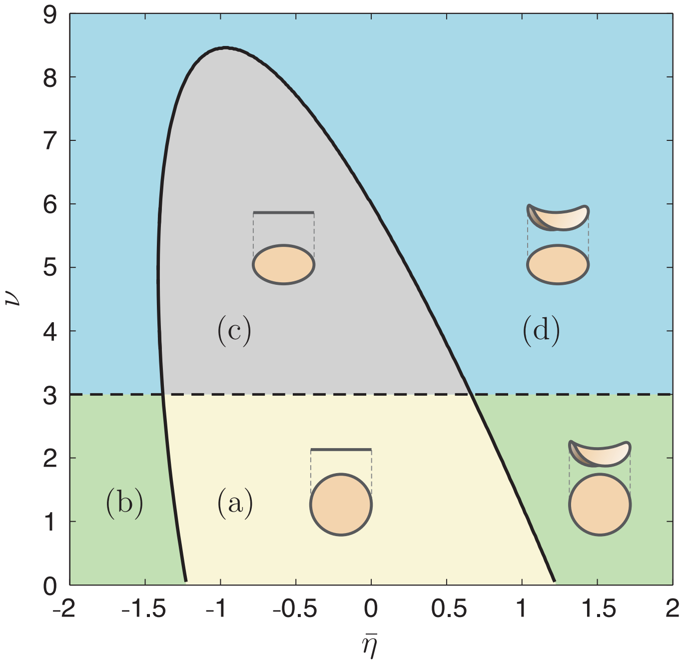

Figure 5–3: Stability plane for a flat circular HDL particle subjected to transverse ($n = 2$) and planar ($m = 2$) perturbations, including four distinct regions (a)–(d). While the solid line shows the variation of $\nu_2^{\rm t}$, the dashed line shows $\nu_2^{\rm i} = 3$ for $\epsilon = 0$ (as provided in (5.29)). Also depicted are side and top views of post-buckled configurations corresponding to the regions (a)–(d).

has diameter $2R \approx 10$ nm. With these choices, $(5.13)_2$ yields $\eta \approx 0.83$. It thus seems reasonable to use $\eta = 1$.

Figure 5–2 depicts the transverse stability of a flat circular HDL particle for different values of the surface tension ν and the saddle-splay modulus $\bar{\eta}$. Only the first four modes are considered. The solid lines indicate the variation of the critical surface tension $\nu_n^{\rm t}$ with $\bar{\eta}$ for each mode, obtained from the dispersion relation (5.31). The numerical technique used to solve the dispersion relation (31) involves systematically checking the sign of its left-hand side for wide ranges of the input parameters $\bar{\eta}$ and ν. Careful numerical checks have been performed to ensure the accuracy of the

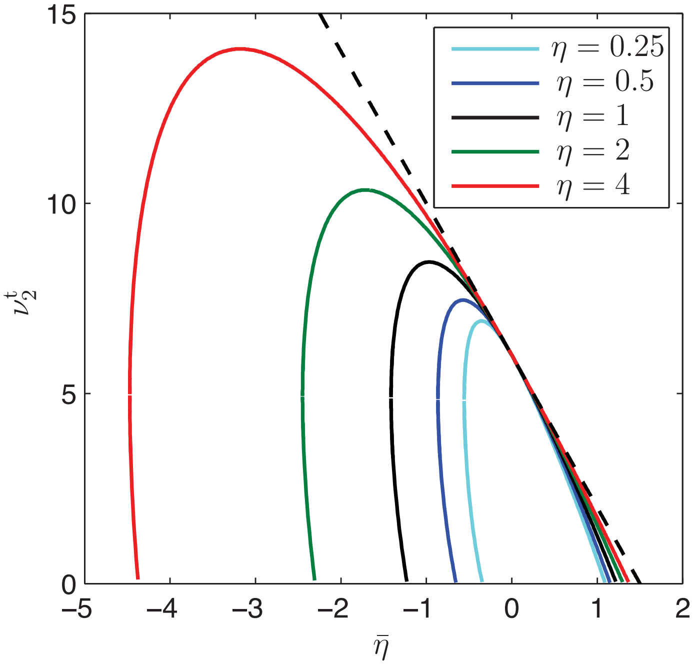

Figure 5–4: Effect of η on the variation of the critical surface tension $\nu_2^{\rm t}$ with $\bar{\eta}$. Requirement $(5.46)_1$ is met in the region below the dashed line.

solution. For various values of ν and $\bar{\eta}$ in the stability plane, the second variation condition (5.46) has been used to carefully determine the nature of stability in different regions of the $(\nu, \bar{\eta})$-plane. Whereas the necessary condition $(5.46)_1$ limits the stable domain to the region below the dashed lines, $(5.46)_2$ limits the stable domain exactly into the region enclosed by each solid line. The intersection of $(5.46)_1$ and $(5.46)_2$ determines the shaded region enclosed by each solid line as the domain where a flat circular HDL particle is stable under a transverse perturbation with mode n. Outside each enclosed region, the particle is unstable under a perturbation with mode n. Evidently, the solid lines correspond to the onset of instability, namely the point at which an exchange of stability occurs. Interestingly, for each n, the stable region for mode n is contained in the stable region of mode $n+1$. It is therefore evident that within the stable region for $n = 2$ the particle is stable with respect to all higher modes. It is also found that, within the stable region enclosed by each solid line, stability is enhanced by negative values of the saddle-splay modulus $\bar{\eta}$, as the stable domain for $\bar{\eta} < 0$ is larger than that for $\bar{\eta} > 0$. Finally, it is noteworthy that, while the dispersion relation (5.31) has two roots for sufficiently large negative $\bar{\eta}$, it otherwise has only one root.

Figure 5–3 depicts the stability plane of a flat circular HDL particle under transverse (saddle-like) and planar (elliptical) perturbations. While the solid line corresponds to ν_2^{t}, the dashed line corresponds to $\nu_2^{\mathrm{i}} = 3$ for $\epsilon = 0$ (given in (5.29)). For other values of $\epsilon \geq 0$, the dashed line is merely shifted upward while remaining straight and horizontal. According to (5.41), in the region below the dashed line, a planar discoidal HDL particle is stable. The intersection of the transverse and planar stable and unstable regions determines four distinct regions. In region (a), a discoidal HDL particle is stable under both transverse and planar perturbations. Thus, a flat, circular particle should be observable only for values of ν and $\bar{\eta}$ in region (a). In region (b), a discoidal HDL particle is stable under planar perturbations but is destabilized by transverse saddle-like perturbations. In region (c), a discoidal HDL particle is stable under transverse perturbations but is unstable to planar perturbations. Thus, for values of ν and $\bar{\eta}$ in region (c), a noncircular flat HDL particle should be observed. Lastly, in region (d), a discoidal HDL particle is unstable under both transverse and planar perturbations. Hence, for values of ν and $\bar{\eta}$ in region (d), flat and saddle-like HDL particles with circular projections onto the reference plane are not observable. To aid in visualizing the various possibilities, schematic configurations of a discoidal HDL particle in regions (a)–(d) are also provided in Figure 5–3. However, it should be emphasized that the linear analysis presented here is unable to exactly predict final post-buckled configurations involving large distortions. The schematic configurations provided in Figure 5–3 are merely based on the stability/instability of a circular flat HDL particle under elliptic and transverse saddle-like perturbations.

So far, it has been assumed that the dimensionless parameter η is fixed while allowing the other dimensionless parameters ν and $\bar{\eta}$ to vary. Regarding $(5.13)_2$, if the radius R is held fixed, the constancy of η requires that the ratio μ/α of the splay modulus μ of the lipid bilayer and the bending rigidity α of the apoA-I chain to be constant. However, to have a more complete picture of the results, considering different values of η reveals the influence of μ or α on the stability of discoidal HDL particles. Particularly, the effect of α, due to lack of information on the bending modulus of apoA-I, seems essential. The variation of the critical surface tension ν_2^{t} with $\bar{\eta}$ has been obtained for different values of η and is plotted in Fig. 5–4. On increasing η, the region confined between each curve and the horizontal axis is magnified and extends toward more negative values of $\bar{\eta}$. For larger values of μ or smaller values of α, the domain of stability for a discoidal HDL particle therefore grows.

5.10 Concluding remarks

Simulations of Catte et al. [91] reveal that gradually removing lipid molecules from discoidal HDL particles induces a transition from planar circular to nonplanar saddle-like configurations. Since the length of the apoA-I chain does not change during the depletion of lipid molecules from the bilayer of an HDL particle, decreasing the number of lipid molecules while keeping the surface area of HDL particle fixed should increase the average spacing between neighboring lipid molecules and, hence, the tension on the surface of particle. This is analogous to increasing the distance between the lipid molecules in each leaflet of the bilayer by imposing an areal stretch. It is evident from the results of Figs. 5–2 and 5–3 that increasing the surface tension ν diminishes the range of stable values for the saddle-splay modulus $\bar{\eta}$ and favors instability. For $\nu > \nu_{\mathrm{c}}^{\mathrm{i}}$, with $\nu_{\mathrm{c}}^{\mathrm{i}}$ given in (5.29), a flat circular HDL particle loses its shape under in-plane perturbations. Similarly, for values of the surface tension $\nu > \nu_n^{\mathrm{t}}$, a flat circular HDL particle becomes unstable to transverse perturbations. To reiterate, the first planar and nonplanar unstable modes correspond respectively to planar elliptical and nonplanar saddle-like shapes.

Although the linear analysis performed here is incapable of specifying the final shape that a discoidal HDL particle might adopt, our results, the simulations of Catte et al. [91] and Shih et al. [5, 170], and the experimental observations of Silva et al. [171], Miyazaki et al. [95], Huang et al. [172], and Skar-Gislinge et al. [97], suggest that the observed planar elliptical and nonplanar saddle-like shapes of discoidal HDL particles might represent stabilized post-buckled configurations of initially-flat circular particles which have become unstable due to identical types of perturbation—i.e., the planar elliptic (mode $m = 2$) and nonplanar saddle-like (mode $n = 2$). This hypothesis is based on a longstanding tradition of analogous observations in structural mechanics, a tradition wherein linearized stability analysis predicts the critical or buckling conditions under which a structure adopts a nontrivial configuration, usually a configuration with the same mode shape of the driving perturbation. The linearized analysis presented in this paper determines conditions necessary for instability of a flat circular HDL particle. Nevertheless, a comprehensive understanding of the equilibrium and stability of discoidal HDL particles requires a nonlinear analysis capable of determining nontrivial configurations involving large distortions [174].

An important next step would be to compare the predictions of the linearized analysis to results from experiments or numerical simulations. The numerical results presented here predict the stability of a flat circular HDL particle for tentative values of the salient dimensionless parameters. Although the qualitative features of these results should not change significantly for modest deviations from parameter values, access to more realistic values for these parameters would naturally allow for more accurate predictions. For example, the bending rigidity α of the apoA-I chain is unavailable and has been approximated by the a reported value for apolipoprotein C-II. Also, the surface tension σ (and perhaps the bending moduli μ and $\bar{\mu}$) may vary with the composition of the lipid bilayer and the number density of lipid molecules, which are sensitive to experimental conditions and assumptions underlying simulations. The existing simulations [91, 5, 170] and experiments [171, 95, 172, 97] do not provide quantitative information guidelines for comparisons. Further experiments or simulations designed to evaluate the underlying physical parameters and to determine the conditions under which flat noncircular and saddle-like configurations arise therefore seem worthy of the required effort.

5.11 Appendix

The components of the matrix $[M]$ in (5.45) are

$$
\begin{aligned}
M_{11} &= 2n(n-1)\big(-2n\bar{\eta} - \nu + n(n+1)\big),\\
M_{12} = M_{21} &= (\eta/4)\big(\zeta I_n'(\zeta)(n^2+n+1)\\
&\quad - I_n(\zeta)n^2(n+2) + \zeta^2 I_n''(\zeta)(n-1) - \zeta^3 I_n'''(\zeta)\big)\\
&\quad + \bar{\eta}(1-n)\big(2n\zeta I_n'(\zeta) + 2n^2 I_n(\zeta)\big)\\
&\quad + \nu\big(\zeta I_n'(\zeta) + nI_n(\zeta)(1-2n)\big) + 2n^2(n^2-1)I_n(\zeta),\\
M_{22} &= (\eta/4)\big(2\zeta^2(I_n'(\zeta))^2 + 2\zeta^3 I_n'(\zeta)I_n''(\zeta) + 2\zeta I_n'(\zeta)I_n(\zeta)\\
&\quad - 4n^2 I_n^2(\zeta) - 2\zeta^2 I_n''(\zeta)I_n(\zeta) - 2\zeta^3 I_n'''(\zeta)I_n(\zeta)\big)\\
&\quad + \bar{\eta}\big(2\zeta^2(I_n'(\zeta))^2 - 4n^2\zeta I_n(\zeta)I_n'(\zeta) + 2n^2 I_n^2(\zeta)\big)\\
&\quad + \nu\big(2\zeta I_n'(\zeta)I_n(\zeta) - 2n^2 I_n^2(\zeta)\big) + 2n^2(n^2-1)I_n^2(\zeta).
\end{aligned}
\tag{5.49}
$$

CHAPTER 6
Concluding remarks

In this chapter, the key conclusions and original contributions of the thesis are provided. Also, possible future extensions are outlined.

6.1 Conclusions

This thesis presented continuum-based modeling and analysis of lipid bilayers. Two applications were considered: multiphase vesicles and discoidal HDL particles.

- **Mechanical modeling of lipid bilayer**

First, the origins of spontaneous curvature in lipid bilayers were considered. Guided by Zurlo [63] and Deseri et al. [64], the lipid bilayer was considered as a three-dimensional shell-like structure. As a natural choice, the spontaneous state (the state, at which the lipid bilayer midsurface exhibits a particular spontaneous curvature tensor), was considered as a reference configuration. A comprehensive description of the kinematics of the lipid bilayer under a general deformation was presented. Effect of leaflets coherency in the local and global forms (area compatibility) were considered. The material symmetry of the lipid bilayer concerning its in-plane isotropy and fluidity was studied and a proof leading to the representation theorem of the volumetric energy density was provided. Geometrical expressions of the kinematical invariants appearing in the volumetric energy density were given. The volumetric incompressibility of lipid bilayer was highlighted, along with its effect on thickness changes of the lipid bilayer under stretch or bending. Adopting the Coleman–Noll [131] procedure and using the volumetric energy density, general relations for the stress in the lipid bilayer were derived.

The areal energy density of a lipid bilayer with spontaneous curvature was derived after the dimension reduction procedure involving integration of the volumetric energy density across the lipid bilayer thickness. Attention was paid to deformations in which the areal stretch exhibits mild changes on the midsurface. The areal energy density, in general, is a function of the spatial (observed) mean and Gaussian curvatures H and K, the spontaneous counterparts $H_\circ$ and $K_\circ$ of those quantities, and the areal stretch J of the midsurface. Based on the derived stress relations, an alternative explanation for the bending moduli in terms of areal stiffness and tension was given. The limiting case under which the areal energy density reduces to an expression of Canham–Helfrich type was studied. An important observation—also, just recently observed by Seguin and Fried [66] based on a microphysical approach—was that the Canham–Helfrich type energy, apart from the spontaneous mean curvature $H_\circ$ also involves the spontaneous Gaussian curvature $K_\circ$. The effect of leaflet asymmetry was also studied. While leaflet asymmetry may contribute to a nonzero spontaneous curvature (e.g., through different molecular geometries of the leaflets), the constitutive asymmetry (i.e., the different mechanical responses of the leaflets) must also be considered. It was revealed that the constitutive asymmetry can emerge as a secondary contribution H_c to the spontaneous mean curvature $H_\circ$, combining together to yield a net spontaneous curvature H_sp.

- **Mechanics of multiphase lipid vesicles**

The equilibrium of two-phase vesicles was explored in the context of a simple continuum model. Two classes of configurations were studied. In the first class, a two-phase vesicle consists of multiple lipid domains budded from the host lipid membrane. The second class involves ground-state configuration, in which the multiple domains have coalesced and formed a single, large vesicle of pure phase. Inspired by numerous configurations observed in the existing experimental studies of two-phase vesicles, each lipid domain was assumed to be a spherical cap. While multidomain configurations form rapidly (over time intervals on the order of seconds), ground-state configurations take considerably longer (over time intervals up to the order of hours) to form. Accordingly, it was assumed that the enclosed volume of vesicle in a multidomain configuration is fixed, as the solvent does not have enough time to diffuse across the membrane over relevant time scales. However, volume changes were allowed for ground-state configurations. In this case, guided by Seifert [23], the osmotic pressure inside the vesicle was allowed to change with the volume of vesicle in accord with the van't Hoff [154] relation. For both classes of configurations, geometrical compatibility and force balance were satisfied across the junctions of lipid domains. The force balance, as observed previously by Baumgart et al. [3, 76], Allain and Ben Amar [77], and Tian et al. [86], links the line tension at the interface with the surface tensions of the lipid domains. The surface tension in spherical lipid bilayers depends on the osmotic pressure through the Young–Laplace equation (e.g., see [88, 76, 81, 151, 152]). Thus, as opposed to the common treatment of line tension in multiphase vesicles, the line tension was considered as a dependent variable while the osmotic pressure was chosen as a control parameter.

In multidomain configurations with fixed volume, the osmotic pressure cannot contribute to the net potential energy of a vesicle through a change of volume. However, it can indirectly change the energy through the lineal contribution in which the line tension depends on the osmotic pressure. Our results showed that higher osmotic pressure increases the net potential energy of multidomain configurations and also its energy difference with that of the configuration with coalesced domains. As a result, it was concluded that the osmotic pressure increase may facilitate coalescence of lipid domains.

Next, equilibrium of a two-phase vesicle in ground states were considered. For different values of the osmotic pressure $\Pi_\circ$, variations of the net potential energy were explored in different possible configurations characterized by the radius of contact circle of two domains. The results indicated the existence of at most two minimum energy states. The first minimum energy state corresponds to a pinched-off configuration where two lipid domains resemble complete spheres. The other state corresponds to a complete sphere configuration where two lipid domains have same radii of curvatures and, together, form a complete spherical vesicle. Emphasis was placed on the role of a critical osmotic pressure Π_c below which the complete sphere configuration is the only minimum energy state. However, above Π_c, both minimum energy states may exist and these states are separated by an energy barrier. These two minimum energy states may be considered as ground states. For osmotic pressures $\Pi_\circ$ greater than Π_c, it was proposed that whether a vesicle takes the pinched-off or complete sphere configuration can be determined based on the excess radius of the vesicle before the phase separation. Accordingly, a critical excess radius depending on the initial osmotic pressure was identified.

- **Equilibrium and stability of discoidal HDL particles**

A model for investigating the equilibrium and stability analysis of discoidal HDL particles was developed. Inspired from the shape and the general assembly of discoidal HDL particles, a simple mathematical model was proposed. The model includes a smooth material surface (representing the lipid bilayer) bound on its edge by an inextensible material curve (representing the double-belt apoA-I). Based on physical justifications, it was assumed that the surface and curve are perfectly bonded at their interface. The energy of an isolated discoidal HDL particle was associated with the surface tension (or energy per unit area) and bending energy of the lipid bilayer and the flexural energy of double-belt apoA-I. In addition, the relevant dimensionless parameters were identified.

Based on a variational approach and adopting a direct, geometrical formulation, the general nonlinear equilibrium equations were derived and physically interpreted. It was revealed that, while on the surface the local equilibrium is governed by the conventional shape equation, the equilibrium of the boundary is governed by four distinct equations expressing the local force and moment balances. It was also explained how the formulation might easily be adapted for the case in which the lipid bilayer is locally inextensible. Next, an alternative presentation for formulating the problem in a parameterized form was generated. For that purpose, the conventional flat circular configuration of an HDL particle was used to parametrize a general configuration in the observed space. The parametric counterparts of equilibrium equations on the surface and boundary were derived. In addition, confining attention to deformations involving small slopes, the relevant linearized versions of equilibrium equations of a flat circular HDL particle were obtained. It was shown that the transverse (out of plane) and in-plane deformations of a flat circular HDL particle are decoupled in the small-slope regime. The closed-form analytical solutions were provided for the linearized equations for different deformational modes. Two dispersion relations were identified as requirements for satisfaction of the equilibrium conditions on the boundary in the in-plane and transverse directions. Physically, these relations indicate conditions necessary for existence of nontrivial solutions.

Next, the stability of discoidal HDL particles was investigated. The main motivation for this investigation was recent experimental observations and simulations [92, 93, 94, 95, 96, 94, 97, 50] revealing that discoidal HDL particles can adopt nontrivial configurations involving nonplanar saddle-like and planar elliptical shapes. It was hypothesized that these nontrivial shapes may represent post-buckled configurations of a flat circular HDL particle. To confirm this hypotheis, the linear stability of a flat circular HDL particle was explored. First, using a second variation analysis, both transverse and planar stabilities were studied. While an exact analysis was performed for the planar stability, analysis of the transverse stability was assisted using the approximate Rayleigh–Ritz variational method. Conditions necessary and sufficient for linear stability were presented. It was shown that the first planar and transverse instability modes are planar elliptical and nonplanar saddle-like, respectively. In addition, motivated by the recent work of Giomi and Mahadevan [101], a simple energy comparison method was used for the linear stability analysis. In this method, the sign of energy change under small perturbations was used to determine whether or not a flat circular HDL particle is stable.

Detailed numerical results were provided for the equilibrium and stability in the small-slope regime. It was observed that the dimensionless splay and saddle-splay moduli η and $\bar{\eta}$ and the surface tension ν play important physical roles. Transverse and planar stabilities were investigated for wide ranges of input parameters and different deformational modes. Particularly, for a fixed value of dimensionless parameter η, stable and unstable regions of the $(\bar{\eta}, \nu)$-plane were detected. It was shown that the loci of stability changes exactly coincide with those corresponding to the roots of the relevant dispersion relations. As a general observation, it was revealed that at each fixed value of $\bar{\eta}$, increasing the dimensionless parameter ν (or equivalently increasing the surface tension σ) until the critical values $\nu_{\mathrm{c}}^{\mathrm{i}}$ and $\nu_{\mathrm{c}}^{\mathrm{t}}$ leads, respectively, to loss of stability under in-plane and transverse perturbations, although exceptions exist for large magnitudes of negative $\bar{\eta}$. Hence, the results suggest possible shape transitions from flat circular to flat elliptic or nonplanar saddle-like shapes. It was shown that the stable domain for negative $\bar{\eta}$ is larger than that associated with positive values of $\bar{\eta}$. Also, it was observed that larger values of η favor more transverse stability. The efficacy of the energy comparison method was examined in comparison with the second variation analysis. It was concluded that for small magnitudes of $\bar{\eta}$ or large values of η, the energy comparison method is an efficient tool for analysis of transverse stability. For planar stability, its result matches nicely with that of the second variation analysis.

6.2 Original contributions to knowledge

Original contributions of this thesis are:

1. The general stress relation within a lipid bilayer were derived based on a hyperelastic model consistent with in-plane isotropy and fluidity of lipid bilayer.
2. A dimensionally-reduced areal energy density was derived for lipid bilayers with spontaneous curvature. Also, the connection with the existing and highly popular Canham–Helfrich model incorporating spontaneous curvature was established.
3. The presented model justifies the appearance of spontaneous curvature in the Canham–Helfrich model in a clear and rational way. Apart from the conventional spontaneous mean curvature, the dimensionally-reduced energy density contains a spontaneous Gaussian curvature. Also, the effect of differences between the constitutive descriptions of the leaflets on the spontaneous mean curvature in the Canham–Helfrich type energy density was discussed.
4. Equilibrium of multidomain and ground-state configurations of a two-phase vesicle were studied using a simple mechanical model.
5. The effect of osmotic pressure on the energy of a multidomain configuration was studied. The proposed model predicts two pinched-off and complete sphere shapes as the ground-state configurations of a two-phase vesicle.
6. The importance of a critical osmotic pressure and a critical excess radius of a vesicle before phase separation on the ground-state shape of a two-phase vesicle was clarified.

7. A continuum mechanical model was developed to explore the equilibrium and stability of discoidal HDL particles.
8. Using the variational approach and a direct, geometrically-based formulation, the equilibrium conditions of a discoidal HDL particle under general nonlinear distortion were derived.
9. An alternative formulation based on a parametrization of the surface and boundary of a discoidal HDL particle was derived. Accordingly, the equilibrium conditions were reformulated in parametrized form.
10. The linearized equilibrium conditions were derived based on the small-slope approximation (about the flat circular shape). It was shown that the transverse and in-plane equilibria of a discoidal HDL particle decouple in the linearized formulation. Different deformational mode shapes were identified and closed-form solutions to the linearized equilibrium conditions were given.
11. The linear stability analysis for a flat circular HDL particle was developed using the second variation of the energy functional. Also, a simple energy comparison method was used to study linear stability.
12. Numerical investigations were provided for linear stability of a flat circular HDL particle. Various stable and unstable regions (of input dimensionless parameters) with respect to small transverse and planar perturbations were detected. Nonplanar saddle-like and planar elliptic mode shapes were identified as the first transverse and planar instability modes. The critical conditions for such instabilities were obtained.

13. Qualitative connections between the presented instability results and the nontrivial saddle-like or flat elliptic shapes observed in the existing simulations and experiments were made. Consistent with the first saddle-like and flat elliptic instability modes predicted by the presented stability analysis, it was hypothesized that the observed nontrivial shapes of a discoidal HDL particle in the simulations and experiments might be post-buckled states of destabilized flat circular HDL particles.

6.3 Future works

Following issues can be addressed in future works:

1. The role of constitutively-induced spontaneous curvature can be addressed experimentally or numerically.
2. The effect of spontaneous Gaussian curvature $K_\circ$ can be studied in nonuniform lipid systems such as multiphase vesicles.
3. The importance of critical osmotic pressure Π_c and critical excess radius can be confirmed experimentally or by numerical simulation.
4. Stability of discoidal HDL particles can be addressed by numerical simulations or experimentally and quantitative comparisons with the presented results can be performed.
5. Experiments or MD simulations can be used to determine the surface tension and bending moduli of lipid bilayer in a discoidal HDL particle. In addition, to best of the author's knowledge, the bending stiffness or persistence length of apoA-I chain is not yet measured. Upon provision of more realistic values of

these input parameters, the presented results on the stability of discoidal HDL particles can be refined.

6. The presented parametrized description and the variational setting provide a useful platform for implementation of numerical tools such as finite-element method.

References

[1] H. T. McMahon and J. L. Gallop, "Membrane curvature and mechanisms of dynamic cell membrane remodelling," *Nature*, vol. 438, no. 7068, pp. 590–596, 2005.

[2] S. Semrau and T. Schmidt, "Membrane heterogeneity–from lipid domains to curvature effects," *Soft Matter*, vol. 5, no. 17, pp. 3174–3186, 2009.

[3] T. Baumgart, S. T. Hess, and W. W. Webb, "Imaging coexisting fluid domains in biomembrane models coupling curvature and line tension," *Nature*, vol. 425, no. 6960, pp. 821–824, 2003.

[4] A. J. García-Sáez, S. Chiantia, and P. Schwille, "Effect of line tension on the lateral organization of lipid membranes," *Journal of Biological Chemistry*, vol. 282, no. 46, pp. 33537–33544, 2007.

[5] A. Y. Shih, A. Arkhipov, P. L. Freddolino, S. G. Sligar, and K. Schulten, "Assembly of lipids and proteins into lipoprotein particles," *The Journal of Physical Chemistry B*, vol. 111, no. 38, pp. 11095–11104, 2007.

[6] C. Tanford, *The Hydrophobic Effect: Formation of Micelles and Biological Membranes 2d Ed*. J. Wiley., 1980.

[7] D. D. Lasic, "The mechanism of vesicle formation," *Biochemical Journal*, vol. 256, no. 1, pp. 1–11, 1988.

[8] S. May, "A molecular model for the line tension of lipid membranes," *The European Physical Journal E*, vol. 3, no. 1, pp. 37–44, 2000.

[9] F. Y. Jiang, Y. Bouret, and J. T. Kindt, "Molecular dynamics simulations of the lipid bilayer edge," *Biophysical Journal*, vol. 87, no. 1, pp. 182–192, 2004.

[10] P. M. Kasson and V. S. Pande, "Molecular dynamics simulation of lipid reorientation at bilayer edges," *Biophysical Journal*, vol. 86, no. 6, pp. 3744–3749, 2004.

[11] A. M. Smith, M. Vinchurkar, N. Gronbech-Jensen, and A. N. Parikh, "Order at the edge of the bilayer: Membrane remodeling at the edge of a planar supported bilayer is accompanied by a localized phase change," *Journal of the American Chemical Society*, vol. 132, no. 27, pp. 9320–9327, 2010.

[12] T. Y. Tsong, "Electroporation of cell membranes," *Biophysical Journal*, vol. 60, no. 2, pp. 297–306, 1991.

[13] P. Marmottant and S. Hilgenfeldt, "Controlled vesicle deformation and lysis by single oscillating bubbles," *Nature*, vol. 423, no. 6936, pp. 153–156, 2003.

[14] P. Fromherz, C. Röcker, and D. Rüppel, "From discoid micelles to spherical vesicles. the concept of edge activity," *Faraday Discussions of the Chemical Society*, vol. 81, pp. 39–48, 1986.

[15] W. Neu and J. Neu, "Mechanism of irreversible electroporation in cells: Insight from the models," in *Irreversible Electroporation* (B. Rubinsky, ed.), Series in Biomedical Engineering, pp. 85–122, Springer Berlin Heidelberg, 2010.

[16] J. F. Nagle and S. Tristram-Nagle, "Structure of lipid bilayers," *Biochimica et Biophysica Acta (BBA)-Reviews on Biomembranes*, vol. 1469, no. 3, pp. 159–195, 2000.

[17] J. Liu and J. C. Conboy, "1,2-diacyl-phosphatidylcholine flip-flop measured directly by sum-frequency vibrational spectroscopy," *Biophysical Journal*, vol. 89, no. 4, pp. 2522–2532, 2005.

[18] M. Bloom, E. Evans, and O. G. Mouritsen, "Physical properties of the fluid lipid-bilayer component of cell membranes: a perspective," *Quarterly Reviews of Biophysics*, vol. 24, no. 03, pp. 293–397, 1991.

[19] S. May, "Protein-induced bilayer deformations: the lipid tilt degree of freedom," *European Biophysics Journal*, vol. 29, no. 1, pp. 17–28, 2000.

[20] A. Lee, "Lipid–protein interactions in biological membranes: a structural perspective," *Biochimica et Biophysica Acta (BBA)-Biomembranes*, vol. 1612, no. 1, pp. 1–40, 2003.

[21] P. B. Canham, "The minimum energy of bending as a possible explanation of the biconcave shape of the human red blood cell," *Journal of Theoretical Biology*, vol. 26, no. 1, pp. 61–81, 1970.

[22] W. Helfrich, "Elastic properties of lipid bilayers: theory and possible experiments.," *Zeitschrift für Naturforschung. Teil C: Biochemie, Biophysik, Biologie, Virologie*, vol. 28, no. 11, pp. 693–703, 1973.

[23] U. Seifert, "Configurations of fluid membranes and vesicles," *Advances in Physics*, vol. 46, no. 1, pp. 13–137, 1997.

[24] H.-G. Döbereiner, O. Selchow, and R. Lipowsky, "Spontaneous curvature of fluid vesicles induced by trans-bilayer sugar asymmetry," *European Biophysics Journal*, vol. 28, no. 2, pp. 174–178, 1999.

[25] R. J. Mashl and R. F. Bruinsma, "Spontaneous-curvature theory of clathrin-coated membranes," *Biophysical Journal*, vol. 74, no. 6, pp. 2862–2875, 1998.

[26] A. Agrawal and D. J. Steigmann, "Modeling protein-mediated morphology in biomembranes," *Biomechanics and Modeling in Mechanobiology*, vol. 8, no. 5, pp. 371–379, 2009.

[27] P. L. Luisi and P. Walde, *Giant Vesicles: Perspectives in Supramolecular Chemistry*, vol. 22. Wiley, Chichester, 2000.

[28] T. M. Allen and P. R. Cullis, "Drug delivery systems: entering the mainstream," *Science*, vol. 303, no. 5665, pp. 1818–1822, 2004.

[29] A. A Attama, "SLN, NLC, LDC: state of the art in drug and active delivery," *Recent Patents on Drug Delivery & Formulation*, vol. 5, no. 3, pp. 178–187, 2011.

[30] A. Samad, Y. Sultana, and M. Aqil, "Liposomal drug delivery systems: an update review," *Current Drug Delivery*, vol. 4, no. 4, pp. 297–305, 2007.

[31] R. Banerjee, "Liposomes: applications in medicine," *Journal of Biomaterials Applications*, vol. 16, no. 1, pp. 3–21, 2001.

[32] N. Latif and B. K. Bachhawat, "Liposomes in immunology," *Journal of Biosciences*, vol. 6, no. 4, pp. 491–502, 1984.

[33] G. Gregoriadis, I. Gursel, M. Gursel, and B. McCormack, "Liposomes as immunological adjuvants and vaccine carriers," *Journal of Controlled Release*, vol. 41, no. 1, pp. 49–56, 1996.

[34] A. Gómez-Hens and J. Manuel Fernández-Romero, "The role of liposomes in analytical processes," *Trac-Trends in Analytical Chemistry*, vol. 24, no. 1, pp. 9–19, 2005.

[35] K. A. Edwards and A. J. Baeumner, "Liposomes in analyses," *Talanta*, vol. 68, no. 5, pp. 1421–1431, 2006.

[36] M. Yanagisawa, M. Imai, and T. Taniguchi, "Shape deformation of ternary vesicles coupled with phase separation," *Physical Review Letters*, vol. 100, no. 14, p. 148102, 2008.

[37] L. Rajendran and K. Simons, "Lipid rafts and membrane dynamics," *Journal of Cell Science*, vol. 118, no. 6, pp. 1099–1102, 2005.

[38] E. L. Elson, E. Fried, J. E. Dolbow, and G. M. Genin, "Phase separation in biological membranes: integration of theory and experiment," *Annual Review of Biophysics*, vol. 39, pp. 207–226, 2010.

[39] J. Hjort Ipsen, G. Karlström, O. Mourtisen, H. Wennerström, and M. Zuckermann, "Phase equilibria in the phosphatidylcholine-cholesterol system," *Biochimica et Biophysica Acta (BBA)-Biomembranes*, vol. 905, no. 1, pp. 162–172, 1987.

[40] J. H. Ipsen, O. G. Mouritsen, and M. J. Zuckermann, "Theory of thermal anomalies in the specific heat of lipid bilayers containing cholesterol," *Biophysical Journal*, vol. 56, no. 4, pp. 661–667, 1989.

[41] D. Lingwood and K. Simons, "Lipid rafts as a membrane-organizing principle," *Science*, vol. 327, no. 5961, pp. 46–50, 2010.

[42] K. Simons and M. J. Gerl, "Revitalizing membrane rafts: new tools and insights," *Nature Reviews Molecular Cell Biology*, vol. 11, no. 10, pp. 688–699, 2010.

[43] v. d. F. Goot and T. Harder, "Raft membrane domains: from a liquid-ordered membrane phase to a site of pathogen attack," in *Seminars in Immunology*, vol. 13, pp. 89–97, Elsevier, 2001.

[44] A. Ono and E. O. Freed, "Role of lipid rafts in virus replication," *Advances in Virus Research*, vol. 64, pp. 311–358, 2005.

[45] K. Simons, R. Ehehalt, *et al.*, "Cholesterol, lipid rafts, and disease," *Journal of Clinical Investigation*, vol. 110, no. 5, pp. 597–603, 2002.

[46] A. S. Shaw, "Lipid rafts: now you see them, now you don't," *Nature Immunology*, vol. 7, no. 11, pp. 1139–1142, 2006.

[47] S. Munro, "Lipid rafts: elusive or illusive?," *Cell*, vol. 115, no. 4, pp. 377–388, 2003.

[48] S. L. Veatch and S. L. Keller, "Separation of liquid phases in giant vesicles of ternary mixtures of phospholipids and cholesterol," *Biophysical Journal*, vol. 85, no. 5, pp. 3074–3083, 2003.

[49] H. S. Sul and J. Storch, "Cholesterol and lipoproteins: Synthesis, transport, and metabolism," in *Biochemical, Physiological, and Molecular Aspects of Human Nutrition (2nd Edition)* (M. H. Stipanuk and M. A. Caudill, eds.), pp. 388–415, Elsevier, 2012.

[50] M. Miyazaki, Y. Tajima, Y. Ishihama, T. Handa, and M. Nakano, "Effect of phospholipid composition on discoidal HDL formation," *Biochimica et Biophysica Acta (BBA)-Biomembranes*, vol. 1828, pp. 1340–1346, 2013.

[51] D. Atkinson, M. A. F. Davis, and R. B. Leslie, "The structure of a high density lipoprotein (HDL_3) from porcine plasma," *Proceedings of the Royal Society of London. Series B. Biological Sciences*, vol. 186, no. 1083, pp. 165–180, 1974.

[52] P. J. Blanche, E. L. Gong, T. M. Forte, and A. V. Nichols, "Characterization of human high-density lipoproteins by gradient gel electrophoresis," *Biochimica et Biophysica Acta (BBA)-Lipids and Lipid Metabolism*, vol. 665, no. 3, pp. 408–419, 1981.

[53] C. G. Brouillette and G. M. Anantharamaiah, "Structural models of human apolipoprotein A-I," *Biochimica et Biophysica Acta (BBA)-Lipids and Lipid Metabolism*, vol. 1256, no. 2, pp. 103–129, 1995.

[54] P. Barter, J. Kastelein, A. Nunn, and R. Hobbs, "High density lipoproteins (HDLs) and atherosclerosis; the unanswered questions," *Atherosclerosis*, vol. 168, no. 2, pp. 195–211, 2003.

[55] L. Li, J. Chen, V. K. Mishra, J. A. Kurtz, D. Cao, A. E. Klon, S. C. Harvey, G. M. Anantharamaiah, and J. P. Segrest, "Double belt structure of discoidal

high density lipoproteins: molecular basis for size heterogeneity," *Journal of Molecular Biology*, vol. 343, no. 5, pp. 1293–1311, 2004.

[56] M. C. Phillips, "New insights into the determination of HDL structure by apolipoproteins," *Journal of Lipid Research*, vol. 54, no. 8, pp. 2034–2048, 2013.

[57] E. A. Evans, "Bending resistance and chemically induced moments in membrane bilayers," *Biophysical Journal*, vol. 14, pp. 923–931, 1974.

[58] R. E. Goldstein and S. Leibler, "Structural phase transitions of interacting membranes," *Physical Review A*, vol. 40, no. 2, p. 1025, 1989.

[59] R. Lipowsky and E. Sackmann, *Structure and Dynamics of Membranes: I. From Cells to Vesicles/II. Generic and Specific Interactions*, vol. 1. Access Online via Elsevier, 1995.

[60] S. Safran, *Statistical Thermodynamics of Surfaces, Interfaces, and Membranes.* Westview Press, Boulder, 2003.

[61] J. T. Jenkins, "The equations of mechanical equilibrium of a model membrane," *SIAM Journal on Applied Mathematics*, vol. 32, no. 4, pp. 755–764, 1977.

[62] D. Steigmann, "Fluid films with curvature elasticity," *Archive for Rational Mechanics and Analysis*, vol. 150, no. 2, pp. 127–152, 1999.

[63] G. Zurlo, *Material and geometric phase transitions in biological membranes.* Ph.D. Dissertation, Università di Pisa, 2006.

[64] L. Deseri, M. D. Piccioni, and G. Zurlo, "Derivation of a new free energy for biological membranes," *Continuum Mechanics and Thermodynamics*, vol. 20, no. 5, pp. 255–273, 2008.

[65] L. Deseri and G. Zurlo, "The stretching elasticity of biomembranes determines their line tension and bending rigidity," *Biomechanics and Modeling in Mechanobiology (DOI: 10.1007/s10237-013-0478-z)*, 2013.

[66] B. Seguin and E. Fried, "Microphysical derivation of the Canham–Helfrich free-energy density," *Journal of Mathematical Biology (DOI: 10.1007/s00285-013-0647-9)*, 2013.

[67] B. Seguin and E. Fried, "Statistical foundations of liquid-crystal theory. i: Discrete systems of rod-like molecules," *Archive for Rational Mechanics and Analysis*, vol. 206, no. 3, pp. 1039–1072, 2012.

[68] D. Steigmann, "A model for lipid membranes with tilt and distension based on three-dimensional liquid crystal theory," *International Journal of Non-Linear Mechanics*, vol. 56, pp. 61–70, 2013.

[69] L. Foret, "A simple mechanism of raft formation in two-component fluid membranes," *Europhysics Letters*, vol. 71, no. 3, p. 508, 2005.

[70] M. S. Turner, P. Sens, and N. D. Socci, "Nonequilibrium raftlike membrane domains under continuous recycling," *Physical Review Letters*, vol. 95, no. 16, p. 168301, 2005.

[71] V. Frolov, Y. A. Chizmadzhev, F. Cohen, and J. Zimmerberg, "entropic traps in the kinetics of phase separation in multicomponent membranes stabilize nanodomains," *Biophysical Journal*, vol. 91, no. 1, pp. 189–205, 2006.

[72] M. Yanagisawa, M. Imai, T. Masui, S. Komura, and T. Ohta, "Growth dynamics of domains in ternary fluid vesicles," *Biophysical Journal*, vol. 92, no. 1, pp. 115–125, 2007.

[73] J. Gómez, F. Sagués, and R. Reigada, "Actively maintained lipid nanodomains in biomembranes," *Physical Review E*, vol. 77, no. 2, p. 021907, 2008.

[74] F. Jülicher and R. Lipowsky, "Domain-induced budding of vesicles," *Physical Review letters*, vol. 70, no. 19, p. 2964, 1993.

[75] F. Jülicher and R. Lipowsky, "Shape transformations of vesicles with intramembrane domains," *Physical Review E*, vol. 53, no. 3, p. 2670, 1996.

[76] T. Baumgart, S. Das, W. Webb, and J. Jenkins, "Membrane elasticity in giant vesicles with fluid phase coexistence," *Biophysical Journal*, vol. 89, no. 2, pp. 1067–1080, 2005.

[77] J.-M. Allain and M. B. Amar, "Budding and fission of a multiphase vesicle," *The European Physical Journal E*, vol. 20, no. 4, pp. 409–420, 2006.

[78] A. Agrawal and D. J. Steigmann, "Coexistent fluid-phase equilibria in biomembranes with bending elasticity," *Journal of Elasticity*, vol. 93, no. 1, pp. 63–80, 2008.

[79] S. Semrau, T. Idema, L. Holtzer, T. Schmidt, and C. Storm, "Accurate determination of elastic parameters for multicomponent membranes," *Physical Review Letters*, vol. 100, no. 8, p. 088101, 2008.

[80] B. Božič and J. Majhenc, "Macroscopic properties of phospholipid vesicles with a contact angle between the membrane domains," *Chem Phys Chem*, vol. 10, no. 16, pp. 2862–2870, 2009.

[81] T. Idema and C. Storm, "Analytical expressions for the shape of axisymmetric membranes with multiple domains," *The European Physical Journal E*, vol. 34, no. 7, pp. 1–10, 2011.

[82] J.-B. Fournier and M. B. Amar, "Effective creases and contact angles between membrane domains with high spontaneous curvature," *The European Physical Journal E*, vol. 21, no. 1, pp. 11–17, 2006.

[83] S. L. Das and J. T. Jenkins, "A higher-order boundary layer analysis for lipid vesicles with two fluid domains," *Journal of Fluid Mechanics*, vol. 597, no. 1, pp. 429–448, 2008.

[84] M. Trejo and M. B. Amar, "Effective line tension and contact angles between membrane domains in biphasic vesicles," *The European Physical Journal E*, vol. 34, no. 1, p. 8, 2011.

[85] S. Semrau, T. Idema, T. Schmidt, and C. Storm, "Membrane-mediated interactions measured using membrane domains," *Biophysical Journal*, vol. 96, no. 12, pp. 4906–4915, 2009.

[86] A. Tian, C. Johnson, W. Wang, and T. Baumgart, "Line tension at fluid membrane domain boundaries measured by micropipette aspiration," *Physical Review Letters*, vol. 98, no. 20, p. 208102, 2007.

[87] J. B. Hutchison, R. M. Weis, and A. D. Dinsmore, "Change of line tension in phase-separated vesicles upon protein binding," *Langmuir*, vol. 28, no. 11, pp. 5176–5181, 2012.

[88] J.-M. Allain and M. Ben Amar, "Biphasic vesicle: instability induced by adsorption of proteins," *Physica A: Statistical Mechanics and its Applications*, vol. 337, no. 3, pp. 531–545, 2004.

[89] W. S. Davidson and R. A. G. D. Silva, “Apolipoprotein structural organization in high density lipoproteins: belts, bundles, hinges and hairpins,” *Current Opinion in Lipidology*, vol. 16, no. 3, pp. 295–300, 2005.

[90] T. Vuorela, A. Catte, P. S. Niemelä, A. Hall, M. T. Hyvönen, S.-J. Marrink, M. Karttunen, and I. Vattulainen, “Role of lipids in spheroidal high density lipoproteins,” *PLoS Computational Biology*, vol. 6, no. 10, p. e1000964, 2010.

[91] A. Catte, J. C. Patterson, M. K. Jones, W. Gray Jerome, D. Bashtovyy, Z. Su, F. Gu, J. Chen, M. P. Aliste, S. C. Harvey, L. Li, G. Weinstein, and J. P. Segrest, “Novel changes in discoidal high density lipoprotein morphology: a molecular dynamics study,” *Biophysical Journal*, vol. 90, no. 12, pp. 4345–4360, 2006.

[92] A. Y. Shih, S. G. Sligar, and K. Schulten, “Maturation of high-density lipoproteins,” *Journal of The Royal Society Interface*, vol. 6, no. 39, pp. 863–871, 2009.

[93] M. K. Jones, A. Catte, L. Li, and J. P. Segrest, “Dynamics of activation of lecithin: cholesterol acyltransferase by apolipoprotein A-I,” *Biochemistry*, vol. 48, no. 47, pp. 11196–11210, 2009.

[94] F. Gu, M. K. Jones, J. Chen, J. C. Patterson, A. Catte, W. G. Jerome, L. Li, and J. P. Segrest, “Structures of discoidal high density lipoproteins: a combined computational-experimental approach,” *Journal of Biological Chemistry*, vol. 285, no. 7, pp. 4652–4665, 2010.

[95] M. Miyazaki, M. Nakano, M. Fukuda, and T. Handa, “Smaller discoidal high-density lipoprotein particles form saddle surfaces, but not planar bilayers,” *Biochemistry*, vol. 48, no. 32, pp. 7756–7763, 2009.

[96] M. Miyazaki, Y. Tajima, T. Handa, and M. Nakano, “Static and dynamic characterization of nanodiscs with apolipoprotein ai and its model peptide,” *The Journal of Physical Chemistry B*, vol. 114, no. 38, pp. 12376–12382, 2010.

[97] N. Skar-Gislinge, J. B. Simonsen, K. Mortensen, R. Feidenhans’l, S. G. Sligar, B. L. Møller, T. Bjørnholm, and L. Arleth, “Elliptical structure of phospholipid bilayer nanodiscs encapsulated by scaffold proteins: casting the roles of the lipids and the protein,” *Journal of the American Chemical Society*, vol. 132, no. 39, pp. 13713–13722, 2010.

[98] R. Kamien, "The geometry of soft materials: A primer," *Reviews of Modern Physics*, vol. 74, pp. 953–971, 2002.

[99] Z. Tu and Z. Ou-Yang, "Elastic theory of low-dimensional continua and its applications in bio- and nano-structures," *Journal of Computational and Theoretical Nanoscience*, vol. 5, pp. 422–448, 2008.

[100] D. Swigon, "The mathematics of dna structure, mechanics, and dynamics," in *Mathematics of DNA Structure, Function and Interactions* (C. Benham, S. Harvey, W. Olson, D. Sumners, and D. Swigon, eds.), pp. 293–320, Springer, 2009.

[101] L. Giomi and L. Mahadevan, "Minimal surfaces bounded by elastic lines," *Proceedings of the Royal Society A: Mathematical, Physical and Engineering Science*, vol. 468, no. 2143, pp. 1851–1864, 2012.

[102] R. Harrison and G. G. Lunt, *Biological membranes: their structure and function.* Blackie, Glasgow, 1975.

[103] P. L. Yeagle, *Cell membrane features. Encyclopedia of Life Sciences.* Wiley, Chichester, 2001.

[104] M. S. Bretscher, "Membrane structure: some general principles," *Science*, vol. 181, no. 4100, pp. 622–629, 1973.

[105] Y.-H. M. Chan and S. G. Boxer, "Model membrane systems and their applications," *Current opinion in chemical biology*, vol. 11, no. 6, pp. 581–587, 2007.

[106] C. Peetla, A. Stine, and V. Labhasetwar, "Biophysical interactions with model lipid membranes: applications in drug discovery and drug delivery," *Molecular pharmaceutics*, vol. 6, no. 5, pp. 1264–1276, 2009.

[107] K. Tsumoto, S.-i. M. Nomura, Y. Nakatani, and K. Yoshikawa, "Giant liposome as a biochemical reactor: transcription of dna and transportation by laser tweezers," *Langmuir*, vol. 17, no. 23, pp. 7225–7228, 2001.

[108] A. Fischer, A. Franco, and T. Oberholzer, "Giant vesicles as microreactors for enzymatic mrna synthesis," *ChemBioChem*, vol. 3, no. 5, pp. 409–417, 2002.

[109] M. Michel, M. Winterhalter, L. Darbois, J. Hemmerle, J. C. Voegel, P. Schaaf, and V. Ball, "Giant liposome microreactors for controlled production of calcium phosphate crystals," *Langmuir*, vol. 20, no. 15, pp. 6127–6133, 2004.

[110] D. M. Vriezema, M. Comellas Aragonès, J. A. Elemans, J. J. Cornelissen, A. E. Rowan, and R. J. Nolte, "Self-assembled nanoreactors," *Chemical Reviews*, vol. 105, no. 4, pp. 1445–1490, 2005.

[111] R. Lipowsky, "The morphology of lipid membranes," *Current Opinion in Structural Biology*, vol. 5, no. 4, pp. 531–540, 1995.

[112] E. Cosserat and F. Cosserat, *Théorie des corps déformables.* A. Hermann, Paris, 1909.

[113] S. Germain, *Recherches sur la Théorie des Surfaces Élastique.* Huzard-Courcier, Paris, 1821.

[114] S. D. Poisson, "Mémoire sur les surfaces élastiques," *Mém. Cl. Sci. Mathém. Phys. Inst. de France 2nd*, pp. 167–225, 1812.

[115] J. C. Nitsche, *Periodic surfaces that are extremal for energy functionals containing curvature functions.* In: Davis HT, Nitsche JCC (ed) Statistical thermodynamics and differential geometry of microstructured materials (The IMA volumes in mathematics and its applications), Springer, 1993.

[116] D. Steigmann, E. Baesu, R. E. Rudd, J. Belak, and M. McElfresh, "On the variational theory of cell-membrane equilibria," *Interfaces and Free Boundaries*, vol. 5, no. 4, pp. 357–366, 2003.

[117] J. N. Israelachvili, *Intermolecular and surface forces: revised third edition.* Academic press, 2011.

[118] W. Wintz, H.-G. Döbereiner, and U. Seifert, "Starfish vesicles," *Europhysics Letters*, vol. 33, no. 5, p. 403, 1996.

[119] M. Mutz and D. Bensimon, "Observation of toroidal vesicles," *Physical Review A*, vol. 43, no. 8, p. 4525, 1991.

[120] X. Michalet and D. Bensimon, "Observation of stable shapes and conformal diffusion in genus 2 vesicles," *Science*, vol. 269, no. 5224, pp. 666–668, 1995.

[121] G. R. Kirchhoff, “Über das gleichgewicht und bewegungen einer elastischen scheibe,” *J reine angew Math*, vol. 40, pp. 51–88, 1850.

[122] T. M. Fischer, “Bending stiffness of lipid bilayers. I. bilayer couple or single-layer bending?,” *Biophysical Journal*, vol. 63, no. 5, pp. 1328–1335, 1992.

[123] B. Bozic, S. Svetina, B. Zeks, and R. Waugh, “Role of lamellar membrane structure in tether formation from bilayer vesicles,” *Biophysical Journal*, vol. 61, no. 4, pp. 963–973, 1992.

[124] W. Wiese, W. Harbich, and W. Helfrich, “Budding of lipid bilayer vesicles and flat membranes,” *Journal of Physics: Condensed Matter*, vol. 4, no. 7, p. 1647, 1992.

[125] M. E. Gurtin, E. Fried, and L. Anand, *The mechanics and thermodynamics of continua*. Cambridge University Press, 2010.

[126] M. Luckey, *Membrane structural biology: with biochemical and biophysical foundations*. Cambridge University Press, 2008.

[127] P. Janmey and P. Kinnunen, “Biophysical properties of lipids and dynamic membranes,” *Trends in Cell Biology*, vol. 16, no. 10, pp. 538–546, 2006.

[128] P. F. Devaux and R. Morris, “Transmembrane asymmetry and lateral domains in biological membranes,” *Traffic*, vol. 5, no. 4, pp. 241–246, 2004.

[129] Q.-S. Zheng, “Two-dimensional tensor function representation for all kinds of material symmetry,” *Proceedings of the Royal Society of London. Series A: Mathematical and Physical Sciences*, vol. 443, no. 1917, pp. 127–138, 1993.

[130] A. E. Green and J. E. Adkins, *Large elastic deformations*. Clarendon Press Oxford, 1970.

[131] B. D. Coleman and W. Noll, “The thermodynamics of elastic materials with heat conduction and viscosity,” *Archive for Rational Mechanics and Analysis*, vol. 13, no. 1, pp. 167–178, 1963.

[132] P. G. Ciarlet, “An introduction to differential geometry with applications to elasticity,” *Journal of Elasticity*, vol. 78, no. 1-3, pp. 1–215, 2005.

[133] J. G. Simmonds, “The strain energy density of rubber-like shells,” *International Journal of Solids and Structures*, vol. 21, no. 1, pp. 67–77, 1985.

[134] H. Stumpf and J. Makowski, “On large strain deformations of shells,” *Acta Mechanica*, vol. 65, no. 1-4, pp. 153–168, 1986.

[135] L. Taber, “Large elastic deformation of shear deformable shells of revolution: theory and analysis,” *Journal of Applied Mechanics*, vol. 54, p. 578, 1987.

[136] L. A. Taber, “On a theory for large elastic deformation of shells of revolution including torsion and thick-shell effects,” *International Journal of Solids and Structures*, vol. 24, no. 9, pp. 973–985, 1988.

[137] L. A. Taber, “Comparison of elasticity and shell theory results for large deformation of rubberlike shells,” *International Journal of Non-Linear Mechanics*, vol. 24, no. 3, pp. 237–249, 1989.

[138] R. F. Yükseler, “Strain energy density of rubber-like shells of arbitrary geometry,” *Journal of Elastomers and Plastics*, vol. 37, no. 3, pp. 247–257, 2005.

[139] M. Hilgers and A. Pipkin, “Energy-minimizing deformations of elastic sheets with bending stiffness,” *Journal of Elasticity*, vol. 31, no. 2, pp. 125–139, 1993.

[140] M. Hilgers and A. Pipkin, “Bending energy of highly elastic membranes II,” *Quarterly of Applied Mathematics*, vol. 54, no. 2, pp. 307–316, 1996.

[141] E. Fried and M. E. Gurtin, “Thermomechanics of the interface between a body and its environment,” *Continuum Mechanics and Thermodynamics*, vol. 19, no. 5, pp. 253–271, 2007.

[142] R. Lipowsky, “Budding of membranes induced by intramembrane domains,” *Journal de Physique II*, vol. 2, no. 10, pp. 1825–1840, 1992.

[143] T. Taniguchi, “Shape deformation and phase separation dynamics of two-component vesicles,” *Physical Review Letters*, vol. 76, no. 23, p. 4444, 1996.

[144] T. S. Ursell, W. S. Klug, and R. Phillips, “Morphology and interaction between lipid domains,” *Proceedings of the National Academy of Sciences*, vol. 106, no. 32, pp. 13301–13306, 2009.

[145] M. Imai and Y. Sakuma, “Shape deformations of multicomponent vesicles,” *Advances in Planar Lipid Bilayers and Liposomes, vol. 12*, pp. 41–78, 2010.

[146] N. F. Morales-Penningston, J. Wu, E. R. Farkas, S. L. Goh, T. M. Konyakhina, J. Y. Zheng, W. W. Webb, and G. W. Feigenson, “Guv preparation

and imaging: Minimizing artifacts," *Biochimica et Biophysica Acta (BBA)-Biomembranes*, vol. 1798, no. 7, pp. 1324–1332, 2010.

[147] P. I. Kuzmin, S. A. Akimov, Y. A. Chizmadzhev, J. Zimmerberg, and F. S. Cohen, "Line tension and interaction energies of membrane rafts calculated from lipid splay and tilt," *Biophysical Journal*, vol. 88, no. 2, pp. 1120–1133, 2005.

[148] S. A. Akimov, P. I. Kuzmin, J. Zimmerberg, and F. S. Cohen, "Lateral tension increases the line tension between two domains in a lipid bilayer membrane," *Physical Review E*, vol. 75, no. 1, p. 011919, 2007.

[149] K. B. Towles and N. Dan, "Line tension and coalescence in heterogeneous membranes," *Langmuir*, vol. 23, no. 26, pp. 13053–13058, 2007.

[150] K. B. Towles and N. Dan, "Coupling between line tension and domain contact angle in heterogeneous membranes," *Biochimica et Biophysica Acta (BBA)-Biomembranes*, vol. 1778, no. 4, pp. 1190–1195, 2008.

[151] Z.-c. Ou-Yang and W. Helfrich, "Instability and deformation of a spherical vesicle by pressure," *Physical Review Letters*, vol. 59, no. 21, pp. 2486–2488, 1987.

[152] Z.-c. Ou-Yang and W. Helfrich, "Bending energy of vesicle membranes: General expressions for the first, second, and third variation of the shape energy and applications to spheres and cylinders," *Physical Review A*, vol. 39, no. 10, p. 5280, 1989.

[153] U. Seifert, K. Berndl, and R. Lipowsky, "Shape transformations of vesicles: Phase diagram for spontaneous-curvature and bilayer-coupling models," *Physical Review A*, vol. 44, no. 2, pp. 1182–1202, 1991.

[154] J. H. van't Hoff, "Die rolle des osmotischen druckes in der analogie zwischen lösungen und gasen," *Z. phys. Chemie*, vol. 1, pp. 481–508, 1887.

[155] M. Maleki and E. Fried, "Stability of discoidal high-density lipoprotein particles," *Soft Matter*, vol. 9, pp. 9991–9998, 2013.

[156] C. G. Brouillette, G. M. Anantharamaiah, J. A. Engler, and D. W. Borhani, "Structural models of human apolipoprotein AI: a critical analysis and review," *Biochimica et Biophysica Acta (BBA)-Molecular and Cell Biology of Lipids*, vol. 1531, no. 1, pp. 4–46, 2001.

[157] A. E. Klon, J. P. Segrest, and S. C. Harvey, "Comparative models for human apolipoprotein AI bound to lipid in discoidal high-density lipoprotein particles," *Biochemistry*, vol. 41, no. 36, pp. 10895–10905, 2002.

[158] M. E. Gurtin and A. I. Murdoch, "A continuum theory of elastic material surfaces," *Archive for Rational Mechanics and Analysis*, vol. 57, no. 4, pp. 291–323, 1975.

[159] O. Farago and P. Pincus, "Statistical mechanics of bilayer membrane with a fixed projected area," *Journal of Chemical Physics*, vol. 120, no. 6, pp. 2934–2950, 2004.

[160] M. Maleki, B. Seguin, and E. Fried, "Kinematics, material symmetry, and energy densities for lipid bilayers with spontaneous curvature," *Biomechanics and Modeling in Mechanobiology*, vol. 12, pp. 997–1017, 2013.

[161] Z. Tu and Z. Ou-Yang, "A geometric theory on the elasticity of biomembranes," *Journal of Physics A: Mathematical and General*, vol. 37, no. 47, pp. 11407–11429, 2004.

[162] Y.-c. Chen and E. Fried, "Stability and bifurcation of a soap film spanning a flexible loop," *Journal of Elasticity (DOI: 10.1007/s10659-013-9458-x)*, 2013.

[163] D. Marsh, "Elastic curvature constants of lipid monolayers and bilayers," *Chemistry and Physics of Lipids*, vol. 144, no. 2, pp. 146–159, 2006.

[164] D. M. Hatters, C. A. MacRaild, R. Daniels, W. S. Gosal, N. H. Thomson, J. A. Jones, J. J. Davis, C. E. MacPhee, C. M. Dobson, and G. J. Howlett, "The circularization of amyloid fibrils formed by apolipoprotein C-II," *Biophysical Journal*, vol. 85, no. 6, pp. 3979–3990, 2003.

[165] R. L. Fosdick and E. G. Virga, "A variational proof of the stress theorem of cauchy," *Archive for Rational Mechanics and Analysis*, vol. 105, no. 2, pp. 95–103, 1989.

[166] R. Rosso and E. G. Virga, "Adhesive borders of lipid membranes," *Proceedings of the Royal Society of London. Series A: Mathematical, Physical and Engineering Sciences*, vol. 455, no. 1992, pp. 4145–4168, 1999.

[167] W. Noll, *Finite-Dimensional Spaces: Algebra, Geometry, and Analysis, Volume I.* Martinus Nijhoff Publishers, 1987.

[168] A. I. Kiselev, M. L. Krasnov, and G. I. Makarenko, *Ordinary differential equations (translated by Primrose EJF).* Frederick Ungar Publishing Co., 1967.

[169] L. Camont, M. J. Chapman, and A. Kontush, "Biological activities of HDL subpopulations and their relevance to cardiovascular disease," *Trends in Molecular Medicine*, vol. 17, no. 10, pp. 594–603, 2011.

[170] A. Y. Shih, P. L. Freddolino, A. Arkhipov, and K. Schulten, "Assembly of lipoprotein particles revealed by coarse-grained molecular dynamics simulations," *Journal of Structural Biology*, vol. 157, no. 3, pp. 579–592, 2007.

[171] R. A. G. D. Silva, G. M. Hilliard, L. Li, J. P. Segrest, and W. S. Davidson, "A mass spectrometric determination of the conformation of dimeric apolipoprotein AI in discoidal high density lipoproteins," *Biochemistry*, vol. 44, no. 24, pp. 8600–8607, 2005.

[172] R. Huang, R. A. G. D. Silva, W. Gray Jerome, A. Kontush, M. J. Chapman, L. K. Curtiss, T. J. Hodges, and W. S. Davidson, "Apolipoprotein AI structural organization in high-density lipoproteins isolated from human plasma," *Nature Structural & Molecular Biology*, vol. 18, no. 4, pp. 416–422, 2011.

[173] S. Zhang, X. Zuo, M. Xia, S. Zhao, and E. Zhang, "General equilibrium shape equations of polymer chains," *Physical Review E*, vol. 70, no. 5, p. 051902, 2004.

[174] M. Maleki and E. Fried, "Equilibrium of discoidal high-density lipoprotein particles," (in preparation).